

Electronic Correlations and Topology in Graphene Moiré Multilayers and InAs/GaSb-Derivative Systems

Thesis by
Robert Michael Polski

In Partial Fulfillment of the Requirements for the
Degree of
Doctor of Philosophy

The logo for the California Institute of Technology (Caltech), featuring the word "Caltech" in a bold, orange, sans-serif font.

CALIFORNIA INSTITUTE OF TECHNOLOGY
Pasadena, California

2023
Defended August 15, 2022

© 2023

Robert Michael Polski
ORCID: 0000-0003-0887-8099

Some rights reserved. This thesis is distributed under a Creative Commons Attribution-NonCommercial 4.0 International Public License (CC BY-NC 4.0).

ACKNOWLEDGEMENTS

I would like to first acknowledge my advisor, Stevan Nadj-Perge, for his enthusiastic mentorship, faith, and support. I hugely appreciate his vision, technical insights, love for science, and the many discussions we have had. I won't forget his steadfast, tenacious approach to finding the underlying truth and meaning in our results. From when I first arrived at Caltech, I quickly noticed his devotion to his graduate students and projects, and I appreciated his approach's tender balance between providing guidance and allowing for freedom and creativity. These commendable mentor qualities inspired my own research efforts and those of my fellow group members. Working with him has been the experience of a lifetime.

I also want to thank the other members of the Nadj-Perge group, particularly, the two people I worked with most. Harpreet Arora and Yiran Zhang, you are the most hard working, capable people I've worked with, and none of this journey would have worked out as well without you. Harpreet, you were an astounding mentor and a wonderful person to work with. I don't think I will ever forget the day you asked me to join the group, our first sighting of the quantum Hall effect in graphene, and the philosophical conversations we would get into while waiting for fridges to work. You were largely responsible for what I know about van der Waals materials and cleanroom fabrication, and your persistence to see something genuinely new and fit things into the bigger picture always kept me going. Yiran, your work ethic and fearlessness will take you far. Since you joined the group, you learned so rapidly that you became, in no time, the master at van der Waals fabrication. You always kept experiments moving, helped provide a wide range of things to measure, and were always open for conversations to hash out physics details. Your unwavering spirit and the many conversations we had, physics-related and otherwise, kept me sane and on my toes. To all the others in the group since I've been here: Youngjoon Choi, Hyunjin Kim, Jeannette Kemmer, Soudabeh Mashhadi, Hechen Ren, Ding Zhong, Lingyuan Kong, Houxin Zhou, and others who have worked with us, thank you for the countless ways you have contributed to make the journey engaging and enjoyable. You have both challenged me and welcomed me by creating a productive, cordial, and helpful atmosphere. It has been a pleasure working with and talking with each and every one of you.

I have benefited greatly from working with many more collaborators from around Caltech and elsewhere. Particularly I'd like to recognize our theory collaborators:

Alex Thomson, Cyprian Lewandowski, Étienne Lantagne-Hurtubise, Yang Peng, Jason Alicea, Gil Refeal, and Felix von Oppen. Your insight always helped push our experiments to the next level. I'd also like to thank Minh Binh-Nguyen who provided devices, insight, and guidance for the InAs/GaSb project. Another group of people I'd like to thank are the KNI staff I have worked with: Guy Derose, Alex Wertheim, Matthew Hunt, and Nathan Lee. You helped me immensely by setting me up and teaching me cleanroom fabrication and microscopy techniques. Marcus Teague, Jacob Bagley, Jiaqing Wang, and Nai-Chang Yeh, I appreciate your support during the first part of my PhD. Jennifer Blankenship and Christy Jenstead, you have always been there for administrative and moral support, for a laugh, and for guidance through the fog of graduate school. I would also like to thank Jason Alicea, Keith Schwab, and Joseph Falson for being on my defense committee and for Michael Roukes's and Dave Hsieh's support on my candidacy committee.

Finally, I'd like to thank my family. Ashley, you have been the most important part of my life, a friend through both good and hard times, and my steadfast supporter. It has been a long journey for both of us (medical school and now residency are no joke), but I can't help being amazed by the growth we've been through together. Thank you for your consistent love, for having an open ear, and for the joy it has been to occasionally decompress, take a hike, climb, or go on an adventure with you. These moments kept me going through the hard times. Particularly during the moments of writing, you and our puppy Moose have been exceptionally bright spots in my life. To my mom, dad, sister, and grandparents, you have always been supportive of my goals and kept me going. Thank you for your love and for putting up with me being gone for so long through this process. I always deeply appreciated your phone calls and words of encouragement. To my other family, Lynn, Dan, Zach, and Allie Reichert, along with Omi and Papa, thank you for always providing a listening ear, interesting questions, a safe haven away from work, and a constant source of love and support. To Sandy and Nan, who housed me during the final steps of my PhD, thank you so much. You will always be family to me. To all the others among friends, family, and colleagues not mentioned (there are too many to count) who have enriched my life throughout the PhD process, thank you. You have helped make me the person I am and are the reason I'm here today.

ABSTRACT

Twisted bilayer graphene (TBG) near the magic angle exhibits a wide variety of correlated and topological phases such as superconductivity, correlated insulators, and orbital ferromagnetism. We show using electrical transport measurements that adding a layer of tungsten diselenide in proximity to twisted bilayer graphene stabilizes superconductivity to twist angles significantly below the magic angle despite the disappearance of correlated insulators and insulators at full moiré filling. These findings—along with our report of a relationship between superconductivity and symmetry breaking Fermi surface reconstruction—suggest constraints on theories of the origin of superconductivity in TBG. In the context of this TBG-tungsten diselenide system, we study how the correlated phases evolve over a wide twist angle range and classify them into a hierarchy based on where they occur relative to the magic angle (or where bands have been maximally flattened). While effects such as orbital ferromagnetism near one electron per moiré unit cell and gapped correlated insulators only exist in close proximity to the magic angle, superconductivity and high-temperature cascade transitions survive in a wider twist angle range.

We also analyze the structures of twisted trilayer, quadrilayer, and pentalayer graphene (and all proximitized to tungsten diselenide) near their respective theoretical magic angles, revealing robust electron- and hole-side superconductivity in each heterostructure. We additionally find previously unreported insulating states in twisted trilayer and quadrilayer graphene along with an enlarged filling range of superconductivity in pentalayer. Our studies on twisted graphene multilayers beyond two layers allow us to generalize the correlated physics found in TBG and consider the role of the additional bands introduced.

In the last part of this thesis, we measure the two-dimensional topological insulator candidate system InAs/GaSb with added stoichiometric impurities. Previous studies in pure InAs/GaSb structures have revealed low bulk resistivity and edge states that arise from trivial effects which can be easily mistaken for topological effects. Due, in part, to the strain effects of Indium impurities added to GaSb, our results show high bulk resistivity. We also, due to the wide gate-tunability in our devices, are able to measure the expected spin-orbit-split valence band structure. Our development of highly tunable InAs/GaSb-derivative structures paves the way for another look at two-dimensional topological insulator behavior in these systems and for their integration into superconducting devices.

PUBLISHED CONTENT AND CONTRIBUTIONS

Manuscripts covered in this thesis:

Arora, H. S.*, Polski, R.*, Zhang, Y.*, Thomson, A., Choi, Y., Kim, H., Lin, Z., Wilson, I. Z., Xu, X., Chu, J.-H., Watanabe, K., Taniguchi, T., Alicea, J. & Nadj-Perge, S. Superconductivity in metallic twisted bilayer graphene stabilized by WSe₂. *Nature* **583**, 379-384. ISSN: 0028-0836. arXiv: [2002.03003](https://arxiv.org/abs/2002.03003). <https://www.nature.com/articles/s41586-020-2473-8> (2020). H.S.A., R.P., Y.Z., and S.N.-P. designed the experiment. R.P. performed the measurements. H.S.A., R.P., and S.N.-P. analyzed the data. R.P. co-wrote the manuscript with input from other authors.

Zhang, Y.*, Polski, R.*, Lewandowski, C., Thomson, A., Peng, Y., Choi, Y., Kim, H., Watanabe, K., Taniguchi, T., Alicea, J., von Oppen, F., Refael, G., Nadj-Perge, S. Promotion of superconductivity in magic-angle graphene multilayers. *Science* **377**, 1538-1543. ISSN: 2375-2548. arXiv: [2112.09270](https://arxiv.org/abs/2112.09270) <https://www.science.org/doi/10.1126/science.abn8585> (2022). R.P. and Y.Z. performed the measurements, fabricated the devices, and analyzed the data, with input and materials provided by others. R.P. co-wrote the manuscript with input from other authors.

Polski, R.*, Zhang, Y.*, Peng, Y., Arora, H. S., Choi, Y., Kim, H., Watanabe, K., Taniguchi, T., Refael, G., von Oppen, F., Nadj-Perge, S. Hierarchy of symmetry breaking correlated phases in twisted bilayer graphene. arXiv: [2205.05225](https://arxiv.org/abs/2205.05225) (2022). R.P. and Y.Z. performed the measurements, fabricated devices, and analyzed the data, with input and materials provided by others. R.P. co-wrote the manuscript with input from other authors.

Zhang, Y., Polski, R., Thomson, A., Lantagne-Hurtubise, É., Lewandowski, C., Zhou, H., Watanabe, K., Taniguchi, T., Alicea, J., Nadj-Perge, S. Enhanced superconductivity in spin-orbit proximitized bilayer graphene. *Nature*, in press. ISSN: 0028-0836. arXiv: [2205.05087](https://arxiv.org/abs/2205.05087) (2022). Y.Z., R.P., and H.Z. performed the measurements, fabricated the devices, and analyzed the data. R.P. co-wrote the manuscript with input from other authors.

Polski, R., Zhang, Y., Nguyen, B.-M., Nadj-Perge, S. Large bulk resistivity and split valence band structure in stoichiometrically doped InAs/GaSb quantum wells. Manuscript in preparation. R.P. and Y.Z. performed the measurements. R.P. analyzed the data. R.P. co-wrote the manuscript with input from other authors.

* indicates co-first authorship

Other contributed manuscripts

- Choi, Y., Kemmer, J., Peng, Y., Thomson, A., Arora, H. S., Polski, R., Ren, H., Alicea, J., Refael, G., Watanabe, K., Taniguchi, T., Nadj-Perge, S. Electronic correlations in twisted bilayer graphene near the magic angle. *Nature Physics* **15**, 1174-1180. ISSN: 1745-2473. arXiv: [1901.02997](https://arxiv.org/abs/1901.02997). <https://www.nature.com/articles/s41567-019-0606-5> (2019).
- Seyler, K. L., de la Torre, A., Porter, Z., Zoghlin, E., Polski, R., Nguyen, M., Nadj-Perge, S., Wilson, S. D., Hsieh, D. Spin-orbit-enhanced magnetic surface second-harmonic generation in Sr₂IrO₄. *Physical Review B* **102**, 201113(R). ISSN: 2469-9969. arXiv: [2011.11662](https://arxiv.org/abs/2011.11662). <https://journals.aps.org/prb/abstract/10.1103/PhysRevB.102.201113> (2020).
- Choi, Y., Kim, H., Peng, Y., Thomson, A., Lewandowski, C., Polski, R., Zhang, Y., Arora, H. S., Watanabe, K., Taniguchi, T., Alicea, J., Nadj-Perge, S. Correlation-driven topological phases in magic-angle twisted bilayer graphene. *Nature* **589**, 536-541. ISSN: 0028-0836. arXiv: [2008.11746](https://arxiv.org/abs/2008.11746). <https://www.nature.com/articles/s41586-020-03159-7> (2021).
- Choi, Y., Kim, H., Lewandowski, C., Peng, Y., Thomson, A., Polski, R., Zhang, Y., Watanabe, K., Taniguchi, T., Alicea, J., Nadj-Perge, S. Interaction-driven band flattening and correlated phases in twisted bilayer graphene. *Nature Physics* **17**, 1375-1381. ISSN: 1745-2473. arXiv: [2102.02209](https://arxiv.org/abs/2102.02209). <https://www.nature.com/articles/s41567-021-01359-0> (2021).
- Kim, H., Choi, Y., Lewandowski, C., Thomson, A., Zhang, Y., Polski, R., Watanabe, K., Taniguchi, T., Alicea, J., Nadj-Perge, S. Evidence for unconventional superconductivity in twisted trilayer graphene. *Nature* **606**, 494-500. ISSN: 0028-0836. arXiv: [2109.12127](https://arxiv.org/abs/2109.12127). <https://www.nature.com/articles/s41586-022-04715-z> (2022).

TABLE OF CONTENTS

Acknowledgements	iii
Abstract	v
Published Content and Contributions	vi
Table of Contents	vii
List of Illustrations	x
List of Tables	xxxi
List of Acronyms	xxxii
Preface	1
Chapter I: Introduction	3
1.1 Graphene, a model system for condensed matter physics	3
1.2 Electron correlations	6
1.3 Van der Waals heterostructures	10
1.4 Moiré patterns, the continuum model, and the magic angle	12
1.5 Superconductivity: conventional vs. unconventional	18
1.6 Spin-orbit coupling	20
1.7 Topology in graphene systems	22
Chapter II: Device design and characterization	26
2.1 Fabrication	26
2.2 Electrical transport measurements	32
2.3 Dilution fridge setup and electronics	38
Chapter III: Superconductivity stabilized in twisted bilayer graphene-WSe ₂ heterostructures	42
3.1 Twisted bilayer graphene picked up with WSe ₂	42
3.2 Superconductivity in devices with twist angles as low as 0.79°	44
3.3 Disappearing correlated insulators and full-filling gaps at low twist angles	48
3.4 Weak antilocalization measurements in TBG-WSe ₂	52
3.5 Landau Fans	54
3.6 Discussion on spin-orbit coupling effects	55
Chapter IV: Hierarchy of correlations in twisted bilayer graphene-WSe ₂ heterostructures	61
4.1 Devices studied	61
4.2 Correlated phases at a range of twist angles	62
4.3 Link between superconductivity and Fermi surface reconstruction	63
4.4 Notes on the effects of adding WSe ₂ and disorder	65
4.5 High-temperature features at a range of twist angles	67
4.6 Strong correlations and a ferromagnetic state at 1.10°	70
4.7 Ten band Hartree-Fock model for TBG near $\nu = 1$	74
Chapter V: Promotion of superconductivity in magic-angle graphene multilayers	77

5.1 Alternating twisted multilayer graphene heterostructures	77
5.2 Introduction to the devices measured	80
5.3 Gaps in TTG and TQG	86
5.4 Superconducting regions	88
5.5 Hall density analysis	90
5.6 Superconductivity extended to $\nu \approx 5$ in TPG	93
Chapter VI: Topology and band engineering in InAs/GaSb-derivative structures	101
6.1 Introduction to 2D topological insulators (2DTIs)	101
6.2 InAs/GaSb, a topological insulator candidate	103
6.3 InAs/ $\text{In}_x\text{Ga}_{1-x}\text{Sb}$ and $\text{InAs}_{1-x}\text{Sb}_x/\text{In}_y\text{Ga}_{1-y}\text{Sb}$ impurity doped systems	111
6.4 8-band Kane model band structure including strain	114
6.5 Effective model for the valence band Fermi surface area	118
Chapter VII: Outlook	124
7.1 Twisted moiré heterostructure devices	124
7.2 Superconductivity stabilization in other graphene systems	125
7.3 InAs/GaSb-derivative Josephson junction devices	129
Bibliography	134
Appendix A: Chapter 4 Supplementary Data: Hierarchy of correlations in twisted bilayer graphene-WSe ₂ heterostructures	155
Appendix B: Chapter 5 Supplementary Data: Ascendance of superconduc- tivity in magic-angle graphene multilayers	162
B.1 Determining T_c and Hall density	162
B.2 Figures	163

LIST OF ILLUSTRATIONS

<i>Number</i>	<i>Page</i>
1.1 The structure of graphene, a hexagonal lattice with lattice constant of 0.246 nm. The primitive lattice vectors are shown as \mathbf{a}_1 and \mathbf{a}_2 . Each unit cell (orange oval) contains two atoms, often denoted as the A and B sublattices.	4
1.2 The low-energy band structure of graphene, showing Dirac cones that are colored red/blue for \mathbf{K}/\mathbf{K}' points in the Brillouin zone.	5
1.3 Example spin-correlated phases. (a) An antiferromagnetic state and (b) a ferromagnetic state on a square lattice of localized electrons.	8
1.4 Schematic of energy splitting between spin-up (red) and spin-down (blue) parabolic itinerant bands.	9
1.5 Ball and stick model from a planview (a) and a side view (b) of a TMDC, which contains one transition metal (blue) and two chalcogen atoms (orange) per unit cell. Some of the most typical examples are the semiconducting materials WSe ₂ , WS ₂ , MoS ₂ , and MoSe ₂	11
1.6 A device consisting of pre-fabricated Au electrodes, with a flake of Fe ₃ GeTe ₂ and a flake of NbSe ₂ stacked so that the resistance of the junction between them could be measured.	12
1.7 Examples of a ball and stick model of TBG (a), and a scanning tunneling microscope topography image of TBG (b). A moiré unit cell is displayed as green hexagon in (a), and the black lines in (b) mark another way to construct a moiré unit cell. (b) is taken from our paper [10].	13
1.8 Schematic depiction of band structures in TBG. (a) Two monolayer graphene Brillouin zones twisted by an angle θ and the resulting mini-Brillouin zone (mBZ) for the moiré lattice. (b) Two uncoupled Dirac cones that occur at the dots in (a). (c) When coupling is included, and (d) when the coupling is included and the twist angle is near the magic angle.	16

1.9	Continuum model TBG band structure for twist angles above and below the magic angle, showing the flattening near the magic angle. Note that the x-axes represent momentum \mathbf{k} following the mini Brillouin zone shown in the left inset.	18
1.10	Uemura plot of superconducting critical temperature T_c vs. Fermi temperature T_F for a range of materials, including TBG. Reprinted from [20], with permission from the copyright holder, Springer Nature.	20
1.11	An schematic of the energy splitting involved in spin-orbit coupling, where opposite spins/momenta are split, but the reversing both leads to the same energy.	21
1.12	A depiction of the two time-reversed (opposite) paths electrons scattering off defects.	22
1.13	The energy of the massive Dirac Hamiltonian (pink) with blue vectors representing the vector $\mathbf{d}(\mathbf{k})$	25
2.1	Flakes of van der Waals materials exfoliated onto SiO_2 in preparation for making a TBG-WSe ₂ device. The red lines on graphene outline the two pieces that are rotated with respect to each other in the final device.	28
2.2	An example polymer stamp, showing a pre-cut PDMS square that supports the thin PC film, which is attached to the slide using scotch tape with a window cut out.	29
2.3	A transfer setup used to make van der Waals stacks.	29
2.4	Flake-by-flake polymer dry stacking technique. (a)–(e) The stacking process used for a TBG-WSe ₂ device. (f) The stack (except for the bottom hBN) picked up on the polymer stamp, using the flakes from Fig. 2.1. The top hBN (blue), WSe ₂ (pink), and two graphene pieces (red) are outlined.	30
2.5	A finished TBG-WSe ₂ device, with contacts and etched into a Hall bar. The orange stripe behind the device is a thin Au backgate.	33
2.6	Demonstration of four-point measurements made on a Hall bar.	34
2.7	Demonstration of the resistance measured in a 2D system at high enough magnetic fields to display the quantum Hall effect.	36

2.8	Schematic Landau level energy and fan diagrams. (a) Energy structure of Landau levels in a Dirac cone. The spacing between the Landau levels can be changed with magnetic field, and electron density tunes the Fermi level up or down. (b) Example Landau fan schematic for monolayer graphene. (c) Example Landau fan schematic for TBG at $\theta = 1.1^\circ$, showing the fan originating from the dispersive bands after full filling (green) and a fan originating from half filling with a degeneracy of 2.	37
2.9	Figures showing the Oxford Triton with all the thermal shields on (a), and showing the plates at each temperature stage (b).	39
2.10	Picture of the filter boxes (lids are also placed over the PCBs) loaded onto the mixing chamber plate.	40
2.11	Pictures of the sample puck open, showing the PCB in the out-of-plane field orientation (a), and closed (b).	41
3.1	A schematic model of the devices studied in this chapter and the next, TBG picked up with WSe ₂ and encapsulated in hBN.	43
3.2	Ball and stick models for the graphene (a) and WSe ₂ (b) crystals, viewed from the top for size comparison. Shown is the lattice constant for each crystal.	44
3.3	Optical images of devices D1–D4. Electrodes that are used in the measurements and corresponding twisted angles are labeled for each device. The ones marked with blue lines are used for measuring Hall conductance in Fig. 3.13. The scale bar in each panel corresponds to 15 μm	45
3.4	The R_{xx} plot recorded vs. temperature and ν for device D1 at 0.97°	46
3.5	R_{xx} vs. T and ν for measured contact pairs with 0.87° (a) and 0.79° (b) twist angles.	46
3.6	Fraunhofer-like patterns for the 0.97° region at $\nu = -2.4$ (a), 0.87° region at $\nu = 1.96$ (b), and 0.79° region at $\nu = 2.3$	48
3.7	Additional data from device D1 (0.97°). (a) Fraunhofer-like pattern for electron doping, at $\nu = 1.58$. (b), (c) Additional Fraunhofer-like pattern for hole doping, $\nu = -2.1$ (b), and $\nu = -2.5$ (c).	48

- 3.8 Additional temperature data for device D1 (0.97°). (a) R_{xx} as a function of ν and Temperature up to 10 K. (b) Temperature dependence of R_{xx} for $\nu = 2$ and $\nu = 3$ showing insulating behaviour. (c) At other partial integer filling factors R_{xx} increases with temperature, consistent with metallic behavior. 49
- 3.9 Larger-temperature-range data showing R_{xx} as a function of filling factor ν , for $\theta = 0.87^\circ$ (a), (b) and $\theta = 0.79^\circ$ (c), (d). Line cuts shown in (b) are taken from the same data set as (a), and line cuts shown in (d) are taken from (c). (e) Conductance vs. $1/T$ for full filling $\nu = \pm 4$ extracted from the data in (a) (blue and black) and (c) (cyan and gray). The behavior for $\theta = 0.79^\circ$ shows much smaller variation in temperature. (f) Conductance vs. $1/T$ for partial filling factors $\nu = +2, +3$ (shown with activated gap measurements) for 0.97° showing insulating behavior. In contrast, the inset shows that for 0.87° , partial fillings $\nu = 1, 2$ show metallic behavior. 50
- 3.10 Activated gap measurements for the $\nu = \pm 4$ full filling gaps in device D3 at 1.04° . The higher temperatures required for this measurement were enabled by measuring this sample in a Quantum Design PPMS system with continuous temperature regulation from 1.7–300 K. Inset: activated gap measurements of the correlated states at $\nu = \pm 2$. 51
- 3.11 Additional data for device D4 (0.80°). (a) R_{xx} as a function of ν and temperature to 2 K, revealing a superconducting pocket over the range of $2 < \nu < 3.2$ and resistance at full filling ($\nu = |4|$) less than at the charge neutrality point. (b) Current vs. voltage at $\nu = 2.79$, at temperatures from 50 mK to 900 mK, in 50 mK steps. The main plot is on the log scale in both axes, revealing a BKT transition temperature near 250 mK. Inset: I-V dependence for the same temperatures. (c) Fraunhofer-like pattern for D4 at $\nu = 2.40$ 52

- 3.12 WAL data measured in D4 ($\theta = 0.80^\circ$). (a) R_{xx} as a function of backgate voltage, V_{bg} , for the 0.80° contacts of D4. The black line shows the voltage range used in the flat bands, which corresponds to the plots in (b)–(d). The red line, from the dispersive bands, corresponds to plots in (e), (f). (b) The change in conductivity, relative to the 0 mT point, as a function of magnetic field ($\Delta\sigma$) taken at the mentioned range of gate voltage at 25 mK. (c), (d) show averaged data from (b) for different field ranges. The data in (e), (f) show a WAL peak in the dispersive bands near $V_{bg} = -6$ V (red line in (a)). Data in (e) was taken at 25 mK. In (f), the data points at each temperature are offset by $0.1 e^2/h$ for clarity. 53
- 3.13 Longitudinal resistance R_{xx} as a function of magnetic field and ν for the four regions of twist angle 0.97° (a), 0.87° (b), 0.79° (c), and 0.80° (d). Here the dominant sequence in the Landau fan is $\pm 2, \pm 4, \pm 6, \pm 8, \pm 10$, as labeled in (b). After ± 10 , we find a sequence of $\pm 14, \pm 18$, and ± 22 , which can also be accounted for by the SOI, as shown in Fig. 3.17. These mentioned Landau levels up to ± 22 are marked by white lines in each plot. Additional slopes are found in (a) corresponding to Landau levels $-1, +3, -12$, as well as short segments corresponding to $+5$ and $+7$ that disappear as the field increases. In (b), (c) we find Landau level $+3$, but in (c) $+22$ seems to be missing. The odd levels are all marked with green lines. 55
- 3.14 Hall conductance for devices D1 ($\theta = 0.97^\circ$, panel (a)) and D2 ($\theta = 0.79^\circ$, panel (b)) showing quantized steps around the CNP with steps corresponding to $\pm 2, \pm 4$ and ± 6 (in units of e^2/h) being pronounced down to 1.5 T. The less developed $3e^2/h$ step has also been observed. 56

- 3.15 Continuum-model results for valley K that include Ising and Rashba spin-orbit coupling at 0.87° (a)–(c) and 0.79° (d)–(f) twist angles. (a), (d) Band structure along the high-symmetry directions of the Brillouin zone indicated in the inset. The line colour represents the out-of-plane spin projection, $\langle S_z \rangle$, and the dotted horizontal line denotes the chemical potential corresponding to $\nu = +2$. (b), (c) and (e), (f) Energy of the upper pair of flat conduction bands, including spin-orbit coupling. Coloured lines show the Fermi surfaces at $\nu = +2$, with the colour indicating the in-plane spin projection. The out-of-plane projection is largely constant along these surfaces and may therefore be deduced from (a), (d). Black lines correspond to the Fermi surface without SOI effects. The large spin-orbit-induced Fermi-surface deformation visible here reflects the flatness of the bands near the Fermi energy. 57
- 3.16 Continuum model band structure calculations for different SOI parameters. (a), (c), (f), (h) Flat-band energies similar to Fig. 3.15. (b), (d), (e), (g), (i), (j) $\nu = +2$ Fermi surfaces. We consider the cases where no SOI is present along with cases where only Ising, only Kane-Mele, and only Rashba are present. In (c)–(j), the non-zero SOI parameter is set to 3 meV. In (c), the bands possess an out-of-plane spin polarization ($\langle S^z \rangle$), which is displayed in colour as per the inset. In (i) and (j), the colour of the Fermi surfaces indicates the expectation value of the in-plane spin according to the wheel above (i). All other parameter sets have a zero in-plane spin projection. 58

- 3.17 Simulated Landau fan diagrams with SOI. (a), (c) Color plot of the phenomenologically broadened density of states as a function of energy squared in $(\text{meV})^2$ (roughly equivalent to the electron density that is gate-tuned in the experiment) and the magnetic field in Tesla. (b), (d) The spectrum without taking broadening effects into account. Blue and red lines correspond to levels originating proximate to the $+\mathbf{K}$ and $-\mathbf{K}$ valleys, respectively. The parameters considered are $(\tilde{\lambda}_I, \tilde{\lambda}_R, \tilde{\lambda}_{\text{KM}}) = (3, 4, 0)$ meV with a broadening $\Gamma = 0.22$ meV and (a), (b) and $(\tilde{\lambda}_I, \tilde{\lambda}_R, \tilde{\lambda}_{\text{KM}}) = (1.5, 2.5, 2)$ meV with a broadening $\Gamma = 0.15$ meV (c), (d). We note that the Landau level sequence and energy levels on the hole-doped side are identical to those shown here for (a) and (b). When both $\tilde{\lambda}_I$ and $\tilde{\lambda}_{\text{KM}}$ are nonzero, as in (c) and (d), a slightly different Landau-level sequence is generically obtained at negative energies relative to the CNP. 60
- 4.1 Device overview and optical images. (a) Schematic of the devices and example stack of flakes before cleanroom processing, showing the twist angle angle between the graphene and bottom hBN, showing no obvious alignment. (b)–(e) Optical images of finished devices. 62
- 4.2 Phase diagram, focusing particularly on superconductivity. (Top) Phase diagram as a function of twist angle, indicating the regions which exhibit the anomalous Hall effect (AHE) due to ferromagnetism, $\nu = +2$ correlated insulators (CI), superconductivity (SC), and symmetry breaking cascade effects as deduced from R_{xx} peaks and Hall density resets. The cascade and superconductivity start to disappear on either side of the diagram, as indicated by the fading bar color. (Bottom) Critical temperatures T_c of superconductivity for both holes and electrons (squares indicate 50% R_n and the error bars 10% and 90% R_n ; for more details, see Fig. A.1). The gradient-filled domes are guides to the eye. 63
- 4.3 Hall density vs. ν . Flavor symmetry breaking correlations manifest as Hall density resets (as seen clearly for 1.04° – 1.23° on the hole side, indicated by colored arrows) and occasionally as singularities or hole-like regions (as seen at 1.10° and 0.97° on the electron side). 64

- 4.4 Widths of charge-neutrality peaks δn . The full-width half-max used for this plot is shown in the inset for the 1.10° data point with T_c of 1.59 K (red) and the 1.23° point (pink). Listed next to each data point is the maximum T_c measured for the twist angle, and the color corresponds to whether the superconductivity was on the hole (blue) or electron (red) side. 66
- 4.5 Data for device D3 at 0.88° . (a) A ν -T diagram of R_{xx} . (b) Linecuts at base temperature of R_{xx} for different contacts (colors corresponding to the inset) show little variation over a range of several μm . (c) Applying an electric field (D) shows no obvious D-field dependence. 66
- 4.6 Pomeranchuk-effect phase transition peak fits. (a) Example of a peak fit at $\nu \approx 1$ for a device at twist angle 0.88° . (b) R_{xx} peak positions near filling factor $\nu \approx 1$ as a function of temperature for devices with various twist angles. The vertical colored lines represent the $\nu = 1$ filling factor for the respectively colored twist angle data. (c), (d) Fit parameters $\Delta\mu$ and $\Delta\gamma$ representing change in the chemical potential and specific heat, respectively, for the phase transition represented by the R_{xx} peaks in (b). Error bars are 95% confidence intervals. The hollow square for 0.95° was set to the same $\Delta\gamma$ value as the 0.97° device due to the unconstrained $\Delta\gamma$ value for the data points. 67
- 4.7 $\frac{d\rho}{dT}$ resistivity derivative data. (a), (b) $\frac{d\rho}{dT}$ 2D diagrams for devices at twist angles 0.88° and 1.10° , respectively. R_{xx} peaks corresponding to Pomeranchuk-like transitions are shown with black dots, superconducting (SC) pockets are shown with arrows, and the magenta lines are guides to the eye representing the approximate regions of T-linear resistivity. The green lines reveal the inflection points in ρ . (c) The resistivity slope $\frac{d\rho}{dT}$ for a range of twist angles, where red(blue) is for electrons(holes). The values come from the average derivative over the area spanned by $1.5 < \nu < 1.8$ ($-2 < \nu < -1.6$) for electrons (holes) and $15 < T < 38$ (error bars are the standard deviations). Device D4, twist angle 1.10° is represented by hollow squares. 69

4.8	Data for the 1.10° region of D1. (a) Linecuts for a range of temperatures shown in the colorbar. (b) R_{xx} of the hole-side superconductivity dome, along with a linecut at $\nu = -2.16$ (right inset) and Fraunhofer-like pattern (left inset, $\nu = -2.3$). (c) Temperature dependence of the charge neutrality point and $nu = 2$ peaks, showing the activated gap behavior at $\nu = 2$	70
4.9	R_{xx} data focusing around $\nu = 1$. (a) R_{xx} vs. ν and T on the electron side for D1 at 1.10° . (b) A zoom into panel (a) around $\nu = 1$, revealing the switching behavior of the resistance. (c) Dense line-cut plots near $\nu = 1$, showing that the evolution of R_{xx} maxima above 10 K (magenta line) are distinct from the ferromagnetic peak.	71
4.10	R_{xy} hysteresis data. (a) Hysteresis loops taken at $\nu = 0.9$ at a range of temperatures. Inset: the resistance jump ΔR_{xy} of hysteresis loops measured vs. B and T. (b) ΔR_{xy} measured as a function of ν and B at 1.5 K. For each ν , the line results from sweeping B up and down. (c) $\Delta R_{xy}^\nu = R_{xy}^{\nu\uparrow} - R_{xy}^{\nu\downarrow}$ measured as a function of the sweeping parameter ν and B, which was held constant.	71
4.11	More details on hysteresis. (a) ΔR_{xy} vs. B and ν around filling factor 1 measured at 3.5 K. (b) Hysteresis loops measured at filling factors marked by arrows in (a). (c)-(e) Hysteresis loops as a function of ν and B. (c) The 3D perspective of (d) (ν sweep forward is solid, backward is dashed) and (e) (B sweep forward is solid, backward sweep is dashed). The density sweep in (d) was measured at 30 mT, after cycling to 200 mT to align the domains. (f) Pulses of B and ν showing reproducible switching of magnetic state, with bit-like switching of R_{xy}	73
4.12	Hall effect and Chern number behavior near $\nu = 1$. (a) Hall density vs. ν measured at 0.5 T (the value shown is antisymmetrized $[R_{xy}(0.5T) - R_{xy}(-0.5T)]/2$). (b), (c) Magnetic field and ν dependence of R_{xy} and R_{xx} measured at 3 K. (c) contains dotted lines representing the $C = -1, +1, +3$. $C = -1$ and $+3$ lines originated from $\nu = 0.95$	74

4.13	Ten-band model calculations. (a)–(d) The band structure obtained for each spin and mini-valley (K, K') flavor for the case of broken $C_2\mathcal{T}$ symmetry at $\nu \approx 0.81$. The K_\uparrow flavor, which is nearly filled, preserves the Dirac-like band structure (a), whereas the other three flavors have a $C_2\mathcal{T}$ -broken mass (b)–(d). The gray planes represent the chemical potential. (e)–(h) Berry curvature Ω_{k_x, k_y} for the conduction flat band in the K_\uparrow flavor (e) and for K_\downarrow (f)–(h), where the Berry curvature is concentrated above the Γ pocket. The Fermi surface is plotted as a dotted circle.	75
5.1	Schematics of the alternating twisted trilayer (a), quadrilayer (b), and pentalayer (c) graphene studied.	77
5.2	The non-interacting band structures calculated based on the continuum model for TTG (a), TQG (b), and TPG (c) near their respective magic angles. The colors represent the eigenstates associated with the flat bands (blue), Dirac cones (yellow), and dispersive TBG-like bands (red). On the left side of each diagram is the band structure with $D/\epsilon_0 = 0$, and the right side shows finite field $D/\epsilon_0 \approx 0.4$ V/nm.	78
5.3	R_{xx} linecuts for TTG device D1 (a), TQG device D2 (b), and TPG device D3 (c) at a range of temperatures (25 mK, every 0.25 K from 0.25 to 2 K, and then every 1 K from 3 to 7 K. The cuts were taken at constant D fields of $D/\epsilon_0 = 0.22$ V/nm (a), -0.15 V/nm (b), and 0 V/nm (c).	81
5.4	R_{xx} measurements as a function of ν and electric displacement field D for TTG (a), TQG (b), and TPG (c).	82
5.5	Leftmost optical images are devices D1–D3. The scale bar in each panel is 5 μm . R_{xx} 2D diagrams (n – D) shown in the middle are obtained from electrodes marked with the corresponding colored lines. The electrodes marked with purple lines were used for measuring R_{xx} in the other figures of the text. Rightmost plots were taken at $V_{\text{tg}} = 0$ V (along the grey dashed lines in the n – D plots). All three devices have a high degree of homogeneity in twist angle with the same superconducting filling range and $ \nu = 4$ carrier density for multiple contacts.	83

- 5.6 Landau fans of multilayer devices. (a)–(f) R_{xx} measured as a function of B field and ν from trilayer to pentalayer. The main sequences of the fan diagrams are labelled below the R_{xx} plots. Landau levels from the dispersive bands are visible as R_{xx} oscillations at low B fields in the fan diagrams. (g)–(m) R_{xy} measured as a function of B field and ν from trilayer to pentalayer. Below the 2D plots, we show Hall conductance linecuts around $|\nu| = 4$. The layer number n determines the resulting quantization. Since the dispersive bands of n -layer magic-angle graphene consist of $n - 2$ Dirac-like cones (at low energies), the $|\nu| = 4$ quantization is therefore expected to follow monolayer graphene sequence multiplied by $n - 2$. The plateaus in TTG and TQG clearly show this trend, while in TPG only the first plateau is observed. These observations however confirm the number of layers in each sample. 84
- 5.7 Measurements of the $\nu \approx 2$ insulator in TTG through linecuts (a), and equivalent 2D diagram (b). Activation gap measurement (c), and D dependence (d). 86
- 5.8 Magnetic field dependence of the TTG insulating state under out-of-plane magnetic field (a) and in-plane magnetic field (b). Linecuts at the bottom of (b) are for clarity. 87
- 5.9 The R_{xx} gap behavior at charge neutrality in TQG revealed with temperature linecuts (a), and a D -temperature diagram (b). (c) Experimentally derived gaps with respect to D and (d) TQG continuum-model gaps. U is the top-bottom layer potential used. 88
- 5.10 (a)–(d) Ginzburg–Landau coherence lengths ξ_{GL} (for details on determining ξ_{GL} , see Section B.1) versus ν for all three devices around $\nu = -2$ —and for $\nu = +2$ for TPG (d)—superimposed on the R_{xx} versus T and ν plots. (e) ξ_{GL} and moiré wavelength L_M versus twist angle of different layers, suggesting a possible relation between the two length scales. 88

- 5.11 Critical temperature T_c is indicated by a dashed line that delineates 10% of the normal state resistance (see Section B.1 for details). T_c is maximized at finite D fields. Overall, superconductivity is suppressed more easily with D as the layer number is increased for both hole ((a)–(c)) and electron (Fig. B.2) doping. (d) Theoretical calculations of the inverse of the flat-band bandwidth for twisted trilayer, quadrilayer, and pentalayer graphene as a function of D/ϵ_0 (top) and potential difference U (bottom). For a fixed D , the bandwidth of the flat bands is larger for systems with more layers, but when expressed as a function of U , the flat-band broadening follows a similar trend across the different structures. 89
- 5.12 Comparison of Hall and longitudinal resistance in tri- and quadrilayer graphene devices. (a), (b) D field and ν dependence of R_{xx} (top) and Hall density (bottom, measured at $B = 0.9$ T) for TTG. Purple and grey dashed lines mark the filling factors where flavor symmetry-breaking transitions associated with $|\nu| = 2$ and $|\nu| = 3$ happen, respectively. The yellow line in (a) delineates the evolution of the vHs. (c), (d) Same for TQG (bottom, measured at $B = 1.5$ T). The superconducting T_c reaches its maximum (orange dot in (d)) exactly at the position of the vHs. When present, flavor symmetry-breaking transitions around $|\nu| \approx 3$ coincide with the termination of superconductivity. By contrast, superconductivity extends much further in the absence of a $|\nu| \approx 3$ reset (c). 91
- 5.13 TPG device Hall density and phase diagram. (a) Hall density as a function of ν and D . (b) Schematic of features in the phase diagram of TPG, mapping out the cascade (present at low D but not present at high D), van Hove singularities, superconducting boundary, and $|\nu_{\text{flat}}| = 4$ Hall density resets. Sketches of the DOS around $\nu = +2$ for different D fields are shown on the right. The middle panel illustrates the flavor symmetry polarization observed in regions that support superconductivity. Flavor symmetry is preserved at higher D fields, as shown in the top and bottom panels. 92
- 5.14 Electron-side superconductivity in TPG. (a), (b) 2D plots of R_{xx} and Hall density n_H , respectively, showing the extent of superconductivity, how it evolves with D and is associated with features in panel (b). (c), Fraunhofer-like pattern taken at the yellow point in (a). 93

5.15	Observation of a vHs near $\nu = 6$. R_{xx} (a) and R_{xy} (b) for large ν in TPG at $D = 0$. The purple arrows show the vHs located in the dispersive TBG-like band near its half-filling point ($\nu \approx 6$), which is shown in the band structure of (e). The same vHs is also present in TQG (d), which also has a dispersive TBG-like band (compare to Fig. 5.14b).	94
5.16	Depiction of different approximation schemes used to understand the role of interactions in TPG. Note that the Hartree correction shifts the flat band (purple) up in energy, and the chemical potential (for a given ν) consequently also shifts upward. Cascaded bands (bands that are totally filled as a result of symmetry breaking) in (c) and (d) are shown in green. (d) corresponds to a minimal model of Hartree and Fock effects characterized by a Hartree shift (Δ_H) and a Fock gap (Δ_F).	95
5.17	A schematic of the three bands contributing to ν . Superconductivity is expected in cascaded flat bands (blue). The schematic depicts scenario (ii), where the dispersive bands collect charge, keeping the flat bands from filling until $n\nu \approx 5$, where superconductivity ends.	96
5.18	Model calculations, including interactions, of band filling. (a) Partial filling of each subsystem versus total filling ν for a fixed dielectric constant $\epsilon = 11.15$. Here, solid (dashed) lines correspond to a cascaded (uncascaded) solution with the cascade solution enabling higher filling of the flat-band subsystem. (b) Similar to (a) but the solid (dashed) lines correspond to a solution at potential difference $U = 0$ meV ($U = 34$ meV). Finite D allows the flat bands to fill more quickly. (c) filling of the flat-band subsystem as function of the Hartree and Fock terms, holding total ν constant. While (a), (b) are calculated using the model shown in panel (b), (c) of Fig. 5.16, (c) is calculated using the minimal Hartree-Fock model of panel (d) in Fig. 5.16.	97
5.19	TPG measurements near $\nu = 4$. R_{xx} (top panel) and Hall density (bottom panel) measurements measured at D shown in the figure.	98
5.20	The D -dependence near $\nu = 4$. (a) R_{xx} vs. ν and D , showing the linecuts where (b)–(g) are taken from. (b)–(g) ν vs. temperature at a selected value of D , showing the evolution near $\nu \approx 4$	99

6.1	A schematic of a 2D topological insulator, demonstrating the inverted band structure with protected helical edge states. The close-up shows the spin polarization of the edge states in opposite directions, and the axes in the plot track the energy E , of the conduction and valence bands along the sample width x	103
6.2	Schematics of the double quantum wells studied. Adapted from Ref. [185].	104
6.3	Schematic diagrams InAs/GaSb uncoupled/coupled quantum well band structure. (a) Uncoupled overlapping InAs and GaSb quantum wells and (b) coupled quantum wells with anticrossing points at finite k and spin-orbit coupling. The green lines represent the predicted topologically protected edge states of opposite spin and momentum combinations.	104
6.4	An electrostatic capacitance model that is a first approximation to the InAs/GaSb double quantum well's behavior under top and back gates. (a) shows a circuit schematic, and (b), (c) show the relevant parameters for the model, which are described in the text	107
6.5	2D gate plots of electron and hole densities. (a) $n - p$, (b) n , and (c) $-p$, using the capacitance model. The color bar is the same in all plots, except plot (b) has the p contribution removed. (c) has the n contribution removed. The band schematics plotted next to (a) reveal the general behavior of the bands and chemical potential at various points in the phase diagram.	109
6.6	Landau fan of an InAs/GaSb device VA18-034 showing electron-like/InAs behavior on the right and hole-like behavior on the left, with some evidence of mixing/inverted bands.	110
6.7	VA19-014 R_{xx} characterization. (a) R_{xx} plot measured with respect to topgate voltage V_{tg} and backgate voltage V_{bg} . (b) Linecuts from (a) on a linear scale and log scale in the inset.	111
6.8	Comparing 2D Landau diagrams with constant- n lines. (a) 2D gate diagram taken at 2 T to show the Landau levels of constant n on the right side. (b) 2d gate diagram taken at 5 T to clarify the Landau level behavior.	112
6.9	Landau fan diagrams. (a) R_{xx} and (b) R_{xy} Landau fan diagrams for two different values of V_{bg} , taken by sweeping V_{tg}	113

6.10	Fourier transforms (y-axis densities n and p are derived from $2f_{1/Be}/h$) of the data in Fig. 6.9(a), (b).	113
6.11	$k \cdot p$ calculation details. (a) The 1D lattice in the growth direction used in the 8-band calculations. Each point has its own Hamiltonian with the appropriate material parameters, and they are linked through the k_z variable. (b) The resulting band structure without including strain effects yet.	115
6.12	The $k \cdot p$ 8-band model calculation with strain included for $\text{InAs}_{0.913}\text{Sb}_{0.087}/\text{In}_{0.33}\text{Ga}_{0.67}\text{Sb}$ at two levels of band overlap corresponding to $k_{cross} = 0.2$ and 0.16 nm^{-1} . The positive side of the k axis refers to k in the [100] direction, and the negative side to the [110] direction.	117
6.13	Fermi surface properties deduced from the $k \cdot p$ model with $k_{cross} = 0.2 \text{ nm}^{-1}$. (a) displays the Fermi surface areas. The red and magenta curves are for the heavy and light electron bands, respectively, and the black and blue are for heavy and light holes, respectively. (b), (c) The effective masses calculated from (a) for holes and electrons.	118
6.14	Modified quadratic band structure now introducing a heavy and light hole band along with heavy and light electron bands. The light electron band and heavy hole band start at a certain energy E_2 , whereas the heavy hole and light electron bands start at the band gap, which is approximately where μ is. We have just included the part above μ for the sake of better identifying these as parabolas and for the sake of the definition of E_g	119
6.15	Plots of the Fourier transforms of the SdH oscillations (represented as Fermi surface area), along with the capacitance model (right side lines) and split-band effective model (left side lines) fits to the data. Taken for V_{tg} linecuts at two V_{bg} points.	121
6.16	The four quadratic bands used in the effective model and the Fermi level (black line) as seen at three different V_{tg} points for $V_{bg} = -0.4V$	122

- 6.17 Results for a VA18-040 Hallbar. (a) A 2D topgate and backgate map of longitudinal resistance. (b) Hybridization gaps derived from the 8-band $k \cdot p$ model for the approximate range of electron-hole band overlap (top of hole band minus bottom of electron band) seen in experiment. (c) SdH oscillations-derived Fermi surface areas for a linecut at $V_{bg} = -2$ V. The colored lines were calculated from the same models as in Fig. 6.15, but with parameters $C_b = 0.06$, $C_t = 0.08$, $C_m = 1.62 \mu\text{F}/\text{cm}^2$, $E_s = 4$ meV, and the same effective masses except for $m_{h,\text{light}} = 0.14m_0$ in the valence band and $m_h = 0.1m_0$ in the conduction band. 123
- 6.18 In-plane field dependent topgate curves for Hallbar devices with the structure of (a) VA19-014 and (b) VA18-040. 123
- 7.1 2D R_{xx} plot vs. D and n . The left schematics show the setup of WSe₂ on top of BBG and the direction holes are pulled with each sign of D field. 126
- 7.2 Superconductivity characterization under changes in temperature and magnetic field. (a) Temperature linecuts at $D/\epsilon_0 = 1$ V/nm, showing BKT behavior (right bottom inset) with a transition temperature 260 mK (green), along with R_{xx} vs. temperature at $n = -5.75 \times 10^{11}$ cm⁻² (upper left inset). (b) Fraunhofer-like pattern at $D/\epsilon_0 = 0.9$ V/nm and $n = -5.05 \times 10^{11}$ cm⁻². 127
- 7.3 Anomalous magnetic-field dependence of superconductivity. (a) A map of the superconducting dome showing the dependence of R_{xx} on in-plane field (B_{\parallel} in the y -axis, left) and n . The zero-field T_c curve vs. n is plotted alongside (right y -axis). (b) Critical in-plane field normalized by the Pauli critical field, as a function of temperature normalized by T_c (inset is un-normalized data). Each curve was taken at a different density, and the solid lines are fit curves. (c) The Pauli violation ratio at a number of densities, with error bars being the standard deviation of the model fits. The doping trend of the PVR is well captured by a model (blue line in the inset) taking into account fixed Ising SOC together with doping-dependent Rashba SOC and constant orbital depairing 127

7.4	Landau fans and corresponding Fourier transforms. (a), (b) Landau fans measured for BBG-WSe ₂ at $D/\epsilon_0 = 1$ V/nm and -1 V/nm, respectively. (c), (d) matching normalized Fourier transforms. (e), (f) R_{xx} plots at the same D along with Fermi surface schematics. . . .	128
7.5	Geometry of Josephson junction devices fabricated from InAs/GaSb-derivative quantum well wafers. Shown are the Al electrodes (gray) and quantum well (orange).	130
7.6	I - V curves for two representative devices: (a) from VA20-004 with dimensions $L = 0.15 \mu\text{m}$ and $W = 4 \mu\text{m}$, and (b) from VA21-010 with dimensions $L = 0.3 \mu\text{m}$ and $W = 2 \mu\text{m}$	131
7.7	Fraunhofer patterns measured for two Josephson junctions. (a) Dev 3 from VA20-004 and (b) Dev 2 from VA21-010. The Dynes-Fulton-based estimates, derived from the Fraunhofer patterns above, of current density along the width of the Josephson junctions are shown in the lower panels.	132
7.8	Critical current vs. gate voltage. $I_c R_n$ (a) and dV/dI data (b) for Josephson junction device 013 from VA21-010 ($L = 0.3 \mu\text{m}$ and $W = 4 \mu\text{m}$) showing topgate dependence. The saturation of the critical current left of $V_{tg} = -7\text{V}$ is likely due to screening in the gate.	133
7.9	Changing critical current with topgate and backgate. (a) dV/dI data for Josephson junction 212 from VA21-010 ($L = 0.2 \mu\text{m}$ and $W = 4 \mu\text{m}$) showing I_c from 0 to ~ 50 nA as the topgate is tuned. (b) dV/dI and (c) resistance taken at 50 mT to kill superconductivity, showing modulation with back gate.	133

- A.1 Figures in the left column show the high-temperature (to 40 K) R_{xx} vs. the moiré filling factor for a number of devices across the angle range. The corresponding figures in the right column reduce the temperature range to emphasize the correlated insulators and superconductivity appearing at low temperature. (b) shows extracted T_c on the hole side for each of the angles represented here. The resistance was much larger for device D1 at 1.10° , as well as another device D4 at the same twist angle, so the y-axis for these curves is on the right of the plot. The extreme sensitivity of the correlations and superconductivity to the twist angle, cleanliness, homogeneity, and other factors occasionally results in different T_c values for devices of the same angle. (l), The electron-side superconductivity T_c values. T_c was derived from 50% R_n , where R_n is defined as the intersection of line fits to the highly sloped region and the normal region just above the transition (line fits shown for selected curves as dashed black lines). The same method was used to determine the error-bars at 10% and 90% R_n in Fig. 4.2. 156
- A.2 More detailed Hall density data for the mentioned devices, taken at the the range of temperatures displayed in (b). The only deviation from these panels is in (a), where the lowest-temperature curve was measured at 50 mK instead of 25 mK. The inset of (a) displays the $\nu \approx -2$ region for the 0.88° device as it evolves at temperatures up to 5 K, revealing the appearance of the feature mentioned in the main text and Fig. 4.3, which corresponds with the onset of hole-side superconductivity. This small feature, indicative of the onset of a cascade, survives to only around 2 K. The rest of the panels reveal clear cascades, where the Hall density returns to near 0, at both $\nu = -2$ and $+2$ at low temperatures. 157

- A.3 R_{xx} measured as a function of magnetic field B and moiré filling factor ν for a collection of twist angles. One can see high-resistance states near $\nu = 2$ just near the magic angle (0.97° to 1.15°) and near $\nu = 1$ only in a very small range near 1.10° (by 1.04° , it is already disappearing, and it is gone at 1.15° here). On the edge of the magic angle, (such as at 0.97°) the $\nu = 2$ state develops with a small magnetic field. The hole-side $\nu = -2$ insulator is always smaller than the electron-side $\nu = 2$ insulator, and it is not fully developed at 0 magnetic field in these diagrams. The noisy features commonly seen for $|\nu| > 3$ and occasionally for other values of ν at high field are likely due to contact/geometry effects near the insulating states. . . . 158
- A.4 Linear-in-T behavior of TBG. (a)–(g) Derivatives of resistivity with respect to temperature up to 40 K for twist angles from 0.95° to 1.23° . (h) Selected linecuts of R_{xx} vs. temperature for the 1.04° twist angle (filling factor values also shown as coloured lines in (d)). The linecuts show the broad positive-curvature zone near charge neutrality (black line), the linear resistivity that persists down to a few Kelvin (although often blocked by a correlated insulator, superconducting, or other symmetry-broken state at low temperatures) near $|\nu| = 2$ (red and blue lines), and the super-linear low temperature to sub-linear high temperature states at $|\nu| > 2$ (purple and orange lines), which have large transition regions that prevent linear behavior until high temperatures. The curve at $\nu = -2.826$ (purple) shows an example where the higher-temperature positive-curvature zone is seen as the superconducting dome is phasing out (small T_c). 159
- A.5 Other signatures of ferromagnetism in TBG. (a) ΔR_{xy} vs. B and ν around filling factor 1 measured with twist angle 1.04° in device D1 at 1.5K. (b) Line cut of R_{xy} versus B at $\nu = 0.87$ (red arrow) for the same device. (c) Temperature dependence of another device D9, twist angle 0.99° , showing evidence of switching behavior (similar to that seen in Fig. 4.9b) and therefore possible ferromagnetism near $\nu = 1$. Bad contacts prevented us from measuring R_{xy} data in this device. 160

- A.6 Comparison of two devices at 1.10° . (a), (c) R_{xx} and R_{xy} versus filling factor and magnetic field up to 8 T for D1. (b) Schematics showing correlated Chern insulators (bold blue lines) and zero-field competing Chern insulators (red lines) at the magic angle. (d) Hall conductance showing well-quantized Chern insulators emanating from charge neutrality (broadest plateaus at $C = \pm 4$), $\nu = \pm 1$ ($C = \pm 3$) and $\nu = \pm 2$ ($C = \pm 2$). (e), (f) Landau fan of D4 and schematic of visible Landau levels along with correlated Chern insulators (bold lines). Notice the fan around charge neutrality does not show the usual clear 4-fold degeneracy preference represented by a wider Landau level plateau in (a), and the fan emanating from $\nu = 1$ persists to lower fields. This variance in magnetic field dependence reveals the sensitivity of the symmetry-broken states near 1.10° , particularly near $\nu = 1$. (g), (h) T-dependence of D4 at high and low temperatures, respectively. Contrast this with the T-dependence of D1 in Fig. 4.8 and Fig. A.1. . 161
- B.1 Magnetic field dependence of twisted multilayer graphene samples. Column (a) shows R_{xx} versus ν and D phase diagrams, and the green dots indicate the positions where the corresponding I versus B plots shown in (b) are measured for D1–D3. Column (c) shows the critical current I_c versus ν at the optimal D fields for D1–D3. Column (d) shows R_{xx} versus ν and B around $\nu = -2$ for D1–D3, highlighting the high critical magnetic fields in these systems. Superconductivity in the twisted graphene multilayers has a higher B_c (~ 0.8 T or higher) than in TBG. . 163
- B.2 D - T dependence of multilayer samples. (a)–(c) R_{xx} as a function of T and D field for D1–D3 at filling factor $\nu = +2.2$, $+2.4$, and $+3.2$, respectively. Superconducting T_c is indicated by a dashed line that delineates 10% of the normal state resistance (see section B.1 for details). (d)–(e) T_c/T_c^{max} versus potential energy difference U for TTG, TQG, and TPG around hole-side (d) and electron-side (e) optimal doping, respectively. U is converted from D using $U = 0.1 \times (n - 1) \times 0.33 \text{ nm} \times eD$, where e is the electron charge and $n - 1$ is the number of graphene interfaces. . 164

- B.3 Data for the second TQG device with twist angle $\theta \approx 1.64^\circ$. (a) R_{xx} and (b) Hall density versus filling factor ν and displacement field D . Yellow lines in (a) track the evolution of vHs features in Hall density. R_{xx} versus ν and temperature measured at $D/\epsilon_0 = -0.29 \text{ V nm}^{-1}$ (c) and -0.17 V nm^{-1} (d). (e) R_{xx} Landau fan measured at zero D field. (f) R_{xx} versus ν measured at zero D field and zero magnetic field. R_{xy} phase diagram measurements (b) and the Landau fan (e) reveal more correlated behavior ($|\nu| < 4$) than the TQG device at 1.80° twist angle. 165
- B.4 Detailed tracking of Hall density for multilayer samples. Hall density (a)–(c) and R_{xx} (d)–(f) as a function of ν and D for TTG, TQG, and TPG. Hall density maps are measured at $B = 0.9 \text{ T}$, 1.5 T , and 1.5 T , respectively. Yellow lines in (d)–(f) track the evolution of vHs/‘gap’ features where Hall density changes sign. Examples are shown of Hall density near the cascade transition reset (g), the vHs (h), and the ‘gap’ (i) following the definitions in Ref. [127]. Filling ranges for the line cuts are marked by the corresponding colored dashed lines in (a), (c). 166
- B.5 R_{xx} as a function of ν and D measured at different temperatures. Plots for TTG (a)–(c), TQG (d)–(f), and TPG (g)–(i). Grey lines track the evolution of the vHs/‘gap’ features. (j) The plot on the left shows a line cut of R_{xx} versus D at charge neutrality for TQG. The plot on the right shows corresponding density of states (DOS) at charge-neutrality point (CNP) calculated using non-interacting continuum model. In the regions where DOS is high, resistance is expected to be low and vice versa. (k) Equivalent plots as in (j) for TPG. 167
- B.6 Detailed Hall effect and temperature dependence data for TPG. (a) Hall density versus D and ν at $B = 0.5 \text{ T}$. (b) Line cuts from (a). Panels below zoom in on the evolution of Hall density resets near $|\nu| = 4$. (c) and (d) Hall density versus D and ν measured at $B = 1.5 \text{ T}$ (c) and 3 T (d), with respective line cuts shown in (f) and (g). (e) R_{xx} versus D and ν measured at $T = 1.5 \text{ K}$, $B = 0.5 \text{ T}$ (line cuts are shown in (h)). From all the above line cuts, Hall density resets and R_{xx} resistive features consistently exist around $\nu = +4$ 168

LIST OF TABLES

<i>Number</i>	<i>Page</i>
A.1 Device Table. The superconducting transition temperatures (SC T_c), $\nu = 2$ correlated insulator (CI) gap, and $\nu = 1$ correlated state parameters measured for the devices used to plot the phase diagram in Fig. 4.2 sorted by twist angle.	155

LIST OF ACRONYMS

- 2DTI** 2-dimensional topological insulator
- BBG** Bernal bilayer graphene
- BCS** Refers to the discoverers of the traditional theory of superconductivity and its discoverers, Bardeen, Cooper, and Schrieffer
- BEC** Bose-Einstein condensate
- CNP** Charge neutrality point
- hBN** Hexagonal boron nitride
- IPA** Isopropyl alcohol
- NMP** N-methyl-2-pyrrolidinone, a solvent
- PC** Poly(bisphenol A carbonate) or polycarbonate, a polymer used for fabrication
- PDMS** Polydimethylsiloxane, a polymer used for fabrication
- PMMA** Polymethyl methacrylate, another polymer
- SdH** Shubnikov de Haas, referring to resistance oscillations associated with Landau levels
- SOC** Spin-orbit coupling
- SOI** Spin-orbit interaction
- STM** Scanning tunneling microscope
- TBG** Twisted bilayer graphene
- TMDC** Transition metal dichalcogenide
- TPG** Twisted pentalayer graphene
- TQG** Twisted quadrilayer graphene
- TTG** Twisted trilayer graphene
- vHs** van Hove singularity, diverging density of states resulting from a band edge or saddle point
- WAL** Weak antilocalization

PREFACE

This thesis covers the unifying theme of correlations and topology in two-dimensional electronic systems studied using electrical transport measurements. The two general classes of study covered here are twisted graphene moiré heterostructures and Indium Arsenide/Gallium Antimonide (InAs/GaSb)-derivative quantum wells. While an attempt has been made to relate the two topics, some of the standard language, fabrication considerations, and goals in the two classes of electronic systems are different enough to warrant separate sections. The layout is generally as follows.

Although the introductory material in Chapters 1 and 2 includes sections particularly relevant to graphene moiré heterostructures, many of the topics apply more generally to other 2D systems and offer a foundation for the work on InAs/GaSb systems. After the introductory chapters, the discussion turns to twisted bilayer graphene in Chapters 3 and 4, in which we reveal the twisted bilayer graphene-tungsten diselenide (WSe_2) system, the presence of superconductivity down to low twist angles, and delve into a broader look at twist angle dependence and correlated phases. Chapter 5 studies alternating twisted multilayer graphene structures with three, four, and five layers. Near each respective magic angle, we find superconductivity and study the unique properties in each system. Chapter 6 offers more introductory material on two-dimensional topological insulators and electron-hole band structure calculations that are relevant for the purpose of studying InAs/GaSb quantum wells. The result is the specific application to our measurements on $\text{InAs}_{1-x}\text{Sb}_x/\text{In}_y\text{Ga}_{1-y}\text{Sb}$ quantum wells with stoichiometric doping of Sb and In. Finally, Chapter 7 provides a promising overlook on future studies in both graphene-based heterostructures and InAs/GaSb-derivative quantum wells. Data is included on Bernal bilayer graphene- WSe_2 heterostructures and InAs/GaSb Josephson junctions to highlight relevant issues we have begun to explore.

In the work here, we have made our best attempt to harmoniously merge experiment with theoretical underpinnings, while focusing also on reproducibility in our experiments. Emphasis should always be placed on observations and trends that are generally seen in a number of devices rather than possible outliers. While we have made our best attempts in this direction, we realize the potential for complicating factors such as the still-unknown role of WSe_2 in our graphene systems. Discussions on twist angle inhomogeneity, measurements of disorder, and long-wavelength commensurate structures have also been included. When discussing theory, we have

made explicit attempts to avoid overly simplistic binaries (such as that superconductivity must arise from either weak-coupling unconventional phonon-based mechanisms or high- T_c -cuprate-like mechanisms) while providing constraints in future theoretical endeavors. We also provide fairly comprehensive data from our twisted graphene heterostructure measurements in the hope that the data provided will lend researchers further guidance in theory development.

“To doubt everything or to believe everything are two equally convenient solutions; both dispense with the necessity of reflection.”

Henri Poincaré

“Nothing in life is to be feared, it is only to be understood. Now is the time to understand more, so that we may fear less.”

Marie Curie

Chapter 1

INTRODUCTION

Experimental fields thrive on model systems. A sufficiently simple, but interesting, model system allows for easy experimental manipulation, respectable theoretical approximations, and a somewhat idealized basis of understanding onto which we can add more complex effects. Thus a model system can result in close theory-experiment collaborations and a scientific spirit of competition assisted by a host of different approaches to the subject. Even if a model system evades direct application, the refinement of theoretical understanding provided by its study can have immense practical consequences. Biologists have long understood and popularized this concept of model systems, and it has served an important role in the field of condensed matter physics. As geneticists have the model organism *Drosophila melanogaster* and neuroscientists have *Caenorhabditis elegans*, condensed matter physicists have graphene.

Just considering the naturally occurring forms of graphene, we find a world of physics (and applications) that has produced thousands of papers and still has surprising findings appearing after decades of study. Furthermore, adding the more artificial degree of freedom of rotational misalignment while stacking, we find a dazzling array of new effects. Since the twisted graphene structures inherit some of the experimental and theoretical capabilities of the original graphene system, the study of these new structures offer a promising route to probe the convoluted physics of strong electron correlations, topological band structure effects in materials, and unconventional superconductivity.

1.1 Graphene, a model system for condensed matter physics

Monolayer graphene consists of carbon atoms arranged into a simple but nontrivial 2D planar crystal structure consisting of a triangular lattice with a two-atom basis (the hexagonal lattice, shown in Fig. 1.1). Since carbon atoms have 4 electrons, and each atom in graphene forms three traditional covalent bonds, the extra electron per atom forms a π bond that stretches across the crystal, allowing for high electrical conductivity. When the details are worked out, the π -bonds result in a simple low-energy form of the electron energy dispersion, which is what we call the energy levels available in the lattice according to the electron wavelengths, or wavevectors

k. The low-energy Hamiltonian is [1]

$$H = \hbar v_F (\tau \sigma_x, \sigma_y) \cdot \mathbf{k} = \hbar v_F \begin{pmatrix} 0 & \tau k_x - i k_y \\ \tau k_x + i k_y & 0 \end{pmatrix} \quad (1.1)$$

where (σ_x, σ_y) represents a 2D vector of Pauli matrices operating on the sublattice basis, \mathbf{k} is the wavevector (k_x, k_y) , and τ is a valley index equal to +1 for the \mathbf{K} valley and -1 for the \mathbf{K}' valley. This Hamiltonian is the Dirac equation for massless particles such as light, only with a velocity $v_F = 1 \times 10^6$ m/s that is reduced by a factor of 300 from the speed of light. The energy eigenvalues derived from Eq. (1.1) take the linear, isotropic form $E = \pm \hbar v_F k$. Note that the Dirac cones, as they are called, emanate from distinct points (called valleys) \mathbf{K} and \mathbf{K}' , relative to which the vector \mathbf{k} is measured (see Fig. 1.2). This Dirac cone band structure also makes the system practical for experimentalists due to the semimetallic behavior across the accessible energy levels and the access to both electron- and hole-like behavior. Following Fig. 1.2, adding electrons fills energy levels above the plane of Dirac cone vertices up to what is called the Fermi level (the energy to which electrons are filled). Dropping the Fermi level below the plane is equivalent to adding holes. The

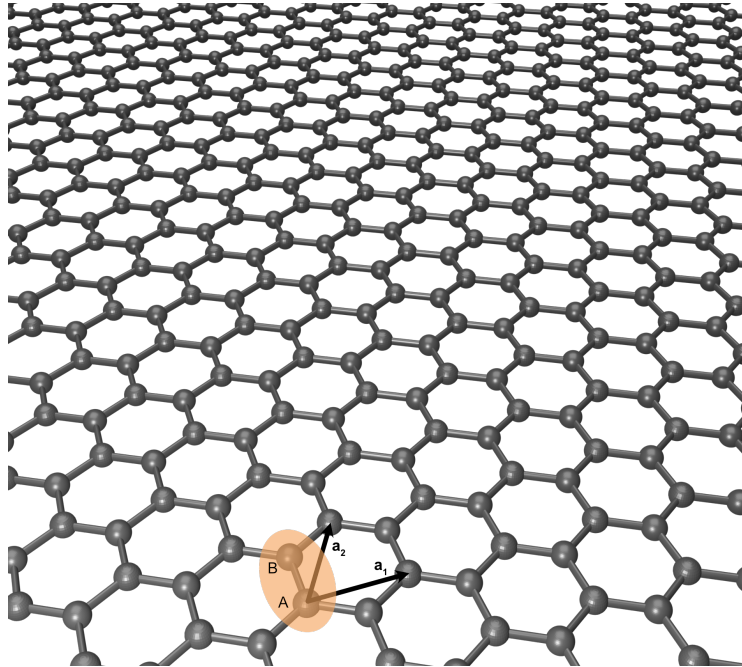


Figure 1.1: The structure of graphene, a hexagonal lattice with lattice constant of 0.246 nm. The primitive lattice vectors are shown as \mathbf{a}_1 and \mathbf{a}_1 . Each unit cell (orange oval) contains two atoms, often denoted as the A and B sublattices.

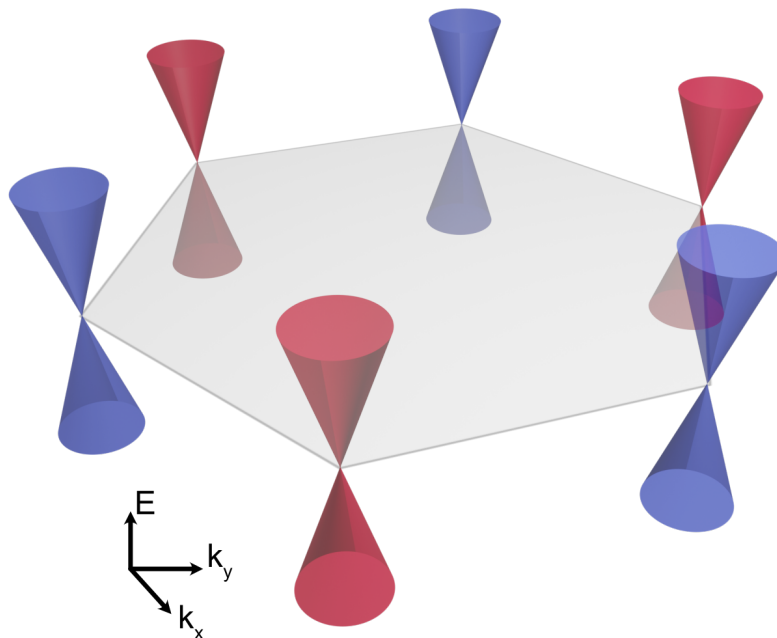


Figure 1.2: The low-energy band structure of graphene, showing Dirac cones that are colored red/blue for \mathbf{K}/\mathbf{K}' points in the Brillouin zone.

fact that energy levels are available from energies below to above the cone vertices makes the structure semimetallic.

Graphene research rapidly developed after the pragmatic discovery that one can isolate high-quality monolayer graphene with a simple Scotch-tape exfoliation technique [2, 3], which favorably contrasts with the expensive growth methods required for most high-quality 2D electron systems. This technique works for a host of so-called van der Waals materials, which consist of planar layers of material loosely connected by van der Waals forces. Due to an additional stacking technique developed more recently (described below), device mobility has been reported in the range of 1 million $\text{cm}^2/(\text{V}\cdot\text{s})$. This is comparable to other high-quality materials grown using molecular beam epitaxy, the pinnacle of material growth techniques in terms of purity and control.

The 2D, atomically thin nature of graphene allows for high electron and hole density tunability with a voltage applied to a capacitive gate separated from the graphene layer by a dielectric. Without gate-tunability, one would need to resort to chemical doping and new samples fabricated and tested for each electron/hole density, as is done for many of the high-temperature superconductors. Graphene, on the other

hand, can be tuned in-situ to have very low electron densities (which in such a thin, low heat-capacity system has fascinating practical implications [4]) and high densities, with resistivities in easily measured tens of Ω to $k\Omega$ ranges. Furthermore, the close proximity of the electron and hole energy bands and the more nuanced effect of chirality allow for the experimental study of unique behaviors such as Klein tunneling, where electrons travel unimpeded through a potential barrier [5]. The 2D electrons also lend themselves to study by methods such as scanning tunneling microscopy since the graphene layer can be left exposed in a pristine fashion. When adding the fabrication conveniences discussed later and graphene's amenability in heterostructures of multiple materials, it is easy to see the vast playground of effects available to graphene researchers.

1.2 Electron correlations

The equation and pictures above describe the single-particle physics of graphene. Most well known solid-state materials, like the standard semiconductors of Si and GaAs, can be largely understood by considering how individual electrons act in the periodic potential of the ionic lattice. The researcher can calculate the energy levels, or band structure, available to electrons and then consider how the electrons fill those levels and respond to the experimental stimuli. This picture, however, conveniently neglects the energetic effects of the electrons on each other, except for possibly some renormalized terms such as mass. While electron-electron correlations often result in small quantitative changes to the band structure—but ultimately no qualitative differences—their effects can restructure the lattice or produce new orders such as ferromagnetism and superconductivity. Changes to the band structure can result in gaps where they were previously unexpected or polarization favoring certain types of electron. These and a host of other phases—some exotic, elusive, and highly sought-after—arise from the complex effects of the Coulomb interaction when considering effects such as spin and localized vs. delocalized (itinerant) electrons.

There are a few effects worth mentioning since they are directly relevant to the discussion or provide context to the future discussion of the complicated effects of interactions in twisted multilayer graphene. In general, Coulomb interactions are included by accounting for the potential energy between pairs of electrons at positions \mathbf{r}_i and \mathbf{r}_j :

$$H_C = \frac{1}{2} \sum_{i \neq j} \frac{e^2}{4\pi\epsilon|\mathbf{r}_i - \mathbf{r}_j|} \quad (1.2)$$

where ϵ is the dielectric constant that varies depending on the sample geometry. While in general this interaction term is complicated to implement, Hartree-Fock theory provides a mean-field approach for correcting the single-particle band structure [6]. If one uses a Slater determinant wavefunction of the electrons and a variational approach to optimize the energy, the Coulomb interaction breaks into two terms. The first is the Hartree term:

$$V_H(\mathbf{r}) = \int d\mathbf{r}' \frac{e^2}{4\pi\epsilon|\mathbf{r} - \mathbf{r}'|} \sum_{\sigma'} \sum_j^{occ} |\psi_j(\mathbf{r}', \sigma')|^2. \quad (1.3)$$

Hartree correlations account for the Coulomb interaction of the averaged electron density for all occupied electrons, regardless of spin species σ' . Since it is easier to incorporate with a self-consistent approach, it serves as a good first approximation to accounting for correlations in the band structure. When electrons are localized (or clustered), as in twisted graphene systems, this term will generally become significant and favor distributing electrons away from localized points. The Fock (or exchange) term is:

$$- \int d\mathbf{r}' \frac{e^2}{4\pi\epsilon|\mathbf{r} - \mathbf{r}'|} \sum_{\sigma'} \sum_j^{occ} \psi_j^*(\mathbf{r}', \sigma') \psi_j(\mathbf{r}, \sigma) \psi_i(\mathbf{r}', \sigma') \quad (1.4)$$

$$= \sum_{\sigma'} \int d\mathbf{r}' V_{ex}(\mathbf{r}, \mathbf{r}', \sigma, \sigma') \psi_i(\mathbf{r}', \sigma'). \quad (1.5)$$

This term accounts for interactions between electrons of different spin species (σ, σ'), and it involves a more complicated integral operator than the simpler Hartree term $V_H(\mathbf{r})\psi_i(\mathbf{r}, \sigma)$. The complicated nature of the Fock term means that it usually involves more approximations and assumptions. However, it can be responsible for sizeable effects, such as exchange-induced gaps that completely polarize bands. Hartree and Fock terms are both relevant in twisted graphene systems. It is worth noting that the Hartree term generally produces continuous changes in the band structure as the electron density is changed, and the Fock term introduces gaps and can split spin/valley species, which is relevant for ferromagnetism and correlated insulators.

The interaction integrals above can occasionally be simplified to an interaction strength term U (or sometimes a few different terms). There are a few useful toy models that incorporate an interaction term U . The first is a lattice of localized

electron sites, in which electrons are penalized for being on the same site, as a result of Coulomb repulsion. Depending on the other energetic terms, such as the kinetic energy and spin-spin interactions, this system tends to favor different ordered states. The first one is widely studied through the Hubbard Hamiltonian [7], which considers just the kinetic energy from hopping between sites and the on-site Coulomb interaction. When the system is half filled, an antiferromagnetic ground state is favored (Fig. 1.3a). Although electrons are not forbidden from hopping to the nearest-neighbor sites, they are energetically disfavored by the increase in energy U from two electrons being on the same site. Since the electrons are frozen, this state is insulating. This insulator, called a Mott insulator, is an example of how insulators can form due to electron interactions instead of the usual scenario where a single-particle band is filled.

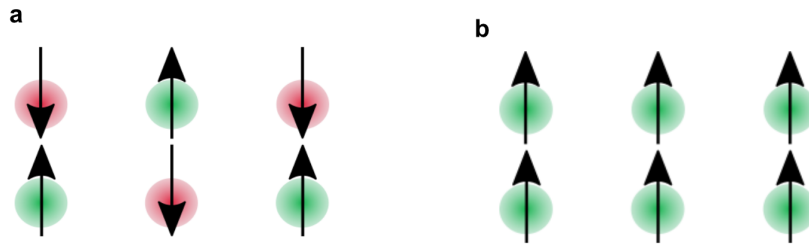


Figure 1.3: Example spin-correlated phases. (a) An antiferromagnetic state and (b) a ferromagnetic state on a square lattice of localized electrons.

Spin-spin interactions tend to favor ferromagnetism (Fig. 1.3b), where a single spin species is favored. Although the picture in Fig. 1.3b represents spins localized onto a lattice, it is useful to consider the so-called Stoner model of ferromagnetism in itinerant (mobile) electrons. The model considers spin-up $n_{\mathbf{k},\uparrow}$ and spin-down $n_{\mathbf{k},\downarrow}$ Bloch electron number operators, where \mathbf{k} and \mathbf{k}' are the wavevectors [8]. The interaction looks like

$$H_{int} = \frac{U}{N} \sum_{\mathbf{k}, \mathbf{k}'} n_{\mathbf{k},\uparrow} n_{\mathbf{k}',\downarrow}. \quad (1.6)$$

The number of electrons in the up state can be determined with

$$\langle n_{\uparrow} \rangle = \int_0^{\infty} N(E) f[E(\mathbf{k}, \uparrow)] dE, \quad (1.7)$$

where $D(E)$ is the density of states (here assumed to be about the same for up and down spins for simplicity), and f is the Fermi-Dirac distribution function. A similar equation applies for $\langle n_{\downarrow} \rangle$. If we assume the presence of a small external magnetic field B for the purpose of calculating spin susceptibility, the U term can be seen as an additional internal magnetic field, further favoring spin polarization. The energy of up- and down-spin electrons can be represented as follows (and shown in Fig. 1.4)

$$E(\mathbf{k}, \uparrow) = E(\mathbf{k}) - \mu_B B + U \langle n_{\downarrow} \rangle \quad (1.8)$$

$$E(\mathbf{k}, \downarrow) = E(\mathbf{k}) + \mu_B B + U \langle n_{\uparrow} \rangle. \quad (1.9)$$

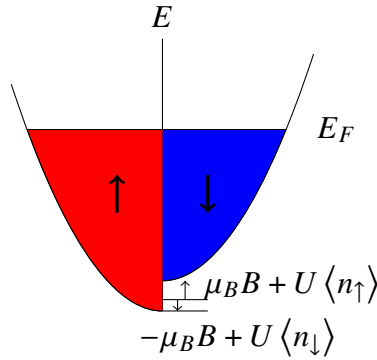


Figure 1.4: Schematic of energy splitting between spin-up (red) and spin-down (blue) parabolic itinerant bands.

$E(\mathbf{k})$ here is just the energy before magnetic field and interactions. Then we can calculate the magnetic moment

$$M = \mu_B (\langle n_{\uparrow} \rangle - \langle n_{\downarrow} \rangle) \quad (1.10)$$

$$= \mu_B \int_0^{\infty} \{f[E - \mu_B B + U \langle n_{\downarrow} \rangle] - f[E + \mu_B B + U \langle n_{\uparrow} \rangle]\} N(E) dE. \quad (1.11)$$

This is solved by taking the limit of $T \rightarrow 0$ and small B , so that the change about the Fermi energy E_F is small, the density of states is approximately constant there, and the Fermi-Dirac distributions just pick out the states filled up to E_F

$$M \stackrel{T \rightarrow 0}{=} \mu_B N(E_F) [E_F + \mu_B B - U \langle n_{\downarrow} \rangle - (E_F - \mu_B B - U \langle n_{\uparrow} \rangle)] \quad (1.12)$$

$$= \mu_B N(E_F) \left[2\mu_B B + U \frac{M}{\mu_B} \right]. \quad (1.13)$$

If we move terms and calculate the spin susceptibility χ , we get

$$\chi = \frac{M}{B} = \frac{2\mu_B^2 N(E_F)}{1 - UN(E_F)}, \quad (1.14)$$

which is reminiscent of the Curie-Weiss form for ferromagnetism that shows a diverging term as $T \rightarrow T_c$. The divergence indicates the onset of ferromagnetism and gives us the Stoner Criterion for the development of itinerant ferromagnetism,

$$UN(E_F) > 1. \quad (1.15)$$

Increasing interactions U or the density of states at the Fermi level $N(E_F)$ can result in ferromagnetism. Since $N(E_F)$ is larger for flat bands (many energy levels concentrated in a small range of energy levels), the idea behind the Stoner criterion provides the context of why flat-band electron systems are interesting places to search for correlated phases. Theories of superconductivity also follow the qualitative trend where high interaction strength and density of states lead to the development of a superconducting gap.

The naturally derived monolayer and Bernal bilayer graphene materials add to the study of electron correlations by introducing valley degeneracy. However, previous studies of correlated effects in graphene occurred at high magnetic fields [9], where the quantum Hall effect flattens energy levels into highly degenerate Landau levels that allow for interactions to dominate. Spin ferromagnetic, canted anti-ferromagnetic, and other effects have been observed as a consequence, and the picture gets more rich and complicated with bilayer graphene. However, twisted multilayer graphene structures can be tuned to have flat bands without high magnetic fields, resulting in a more rich phase diagram without requiring high magnetic fields.

1.3 Van der Waals heterostructures

Studying electron-electron correlations in van der Waals materials has been aided by the fact that van der Waals materials of different character, layer number, and orientation can be cleanly stacked on top of each other, forming van der Waals heterostructures. The experimenter has access to naturally metallic, insulating, semiconducting (like many of the transition metal dichalcogenides (TMDCs) shown in Fig. 1.5), magnetic, and superconducting layers that can result in electron systems with enhanced properties when compared to single-crystal samples. And high-

quality crystals can be found through exfoliation techniques involving the repeated application of tape to a bulk crystal and subsequent transfer to Si/SiO₂ substrates.

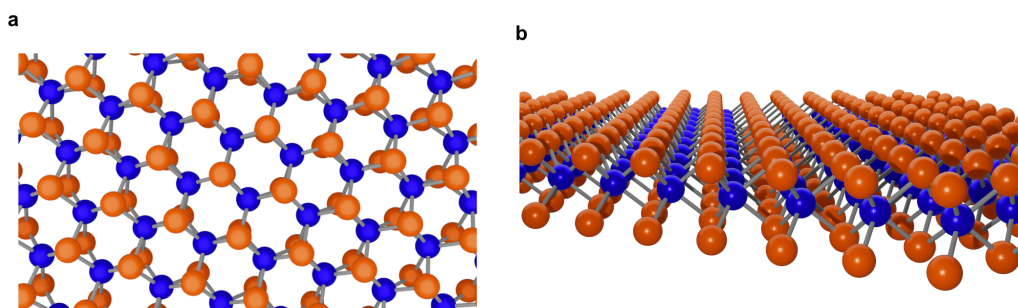


Figure 1.5: Ball and stick model from a planview (a) and a side view (b) of a TMDC, which contains one transition metal (blue) and two chalcogen atoms (orange) per unit cell. Some of the most typical examples are the semiconducting materials WSe₂, WS₂, MoS₂, and MoSe₂.

The van der Waals crystals vary in cleanliness, ease of use, and applicability in heterostructures. For instance, some have vacancies, dopants, and other inhomogeneities, whereas others tend to oxidize quickly in ambient conditions, and others tend to form large Schottky barriers when contacted with metals. Furthermore, the properties of heterostructures can largely rely on the details behind transferring the flakes into interfaces and the geometry of contact formation and device etching.

An example device is shown in Fig. 1.6, which consists of a van der Waals interface between a superconductor (NbSe₂) and a ferromagnet (Fe₃GeTe₂), with pre-patterned gold contacts that the two flakes were placed onto and an insulating hexagonal boron nitride (hBN) flake encapsulating the structure. While van der Waals heterostructures such as this introduce a vast potential for unique and clean interfaces between dissimilar materials, the properties rely heavily on the details of fabrication and individual material properties. For instance, the mentioned ferromagnet-superconductor interface is plagued by the fact that NbSe₂ and Fe₃GeTe₂ are both sensitive to oxidation and degradation from chemical baths. Furthermore, NbSe₂ has a high failure rate in the standard sequential stack pickup technique described in the next chapter, and is consequently often exposed to further polymer residues. Fe₃GeTe₂ rarely exfoliates into large crystals of thickness < 5 nm.

Graphene and hBN crystals are air-stable and easy to exfoliate into sizeable flakes (30–100+ μm features). Graphene monolayers are easily detected optically, and



Figure 1.6: A device consisting of pre-fabricated Au electrodes, with a flake of Fe_3GeTe_2 and a flake of NbSe_2 stacked so that the resistance of the junction between them could be measured.

when we use proper polymer pick-up techniques, fabrication temperatures, and encapsulation, we can make devices of high mobility. The hBN layer, which is structured the same as graphene except for having alternating atoms of boron and nitrogen and a slightly larger lattice constant, isolates graphene from charge puddles inherent in SiO_2 and provides a flat surface for the metallic graphene. Both graphene and hBN are also amenable to fabrication steps after stacking the layers together, such as electron beam lithography, etching, and metal deposition. Top and back gates can be easily fabricated in graphene/hBN heterostructures that can capacitively induce electron densities on the order of 10^{13} cm^{-2} .

1.4 Moiré patterns, the continuum model, and the magic angle

A moiré pattern forms when two spatially oscillating patterns of similar wavelength become nearly aligned. When this happens, a larger-wavelength beating pattern emerges, which is seen in the common example of trying to take a picture of a TV screen (stripes form when the pixels of the camera and pixels of the TV nearly match). In two-dimensional crystals, either a slightly different lattice constant or a twist offset between layers can lead to a new large-wavelength lattice.

Two graphene pieces can form a moiré pattern when they are stacked on each other with a small rotational offset—or twist angle—between them, as shown in Fig. 1.7a. Twisted bilayer graphene (TBG) forms a lattice with a twist-angle-dependent spacing L_M between unit cells, following

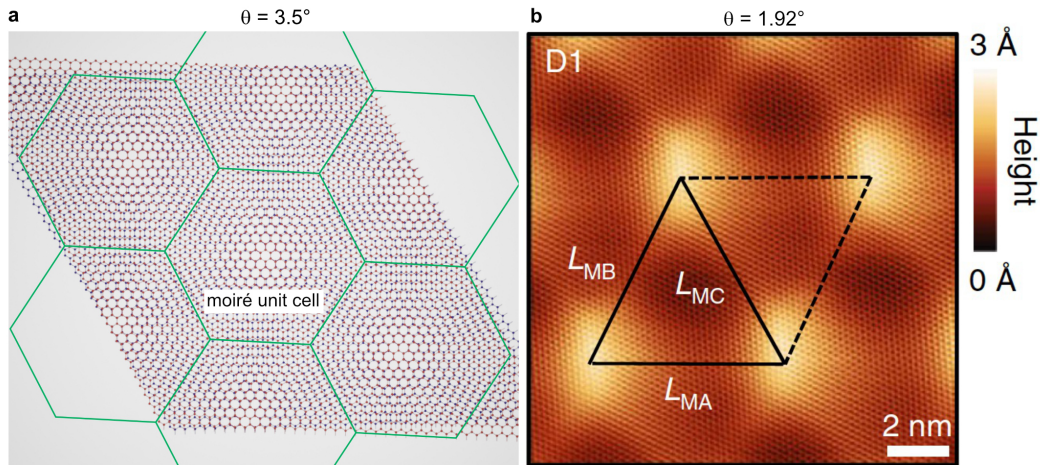


Figure 1.7: Examples of a ball and stick model of TBG (a), and a scanning tunneling microscope topography image of TBG (b). A moiré unit cell is displayed as green hexagon in (a), and the black lines in (b) mark another way to construct a moiré unit cell. (b) is taken from our paper [10].

$$L_M = \frac{a}{2 \sin(\theta/2)}, \quad (1.16)$$

which leads to a unit cell area

$$A_M = \frac{\sqrt{3}a^2}{8 \sin^2(\theta/2)}. \quad (1.17)$$

Whereas graphene atoms are spaced apart by 0.142 nm, and the lattice constant is 0.246 nm, unit cells for twist angles near 1° are spaced about $L_M \approx 14$ nm apart. The unit cell size theoretically will increase infinitely as the twist angle approaches 0 (although practically, the two graphene sheets will relax for small enough twist angles). The size of the unit cells is small enough that Coulomb interactions between sites are sizeable compared to the bandwidths we are dealing with— $e^2/(4\pi\epsilon L_M) \sim 10$ s of meV. However, the unit cells are large enough that they can be filled using gate-induced doping, which can produce densities of electrons $n > 10^{13} \text{ cm}^{-2}$. In the case of graphene, filling each moiré unit cell with four electrons is particularly relevant because this fills the (four-fold) spin and valley degenerate bands and reveals insulators that are expected with single-particle calculations. In the case of about 1° , that corresponds to $n = 4/A_M \approx 2.3 \times 10^{12} \text{ cm}^{-2}$, well within the abilities of gating in van der Waals materials. The scales involved here open up a range of

possibilities since atomic lattices rarely get beyond the atomic scale, and fabrication techniques get very difficult below 100 nm.

A topography image taken with a scanning tunneling microscope (STM), shown in Fig. 1.7b, shows a TBG moiré pattern for the twist angle of 1.92° , with a unit cell spacing of ~ 7 nm, while the smaller, weaker lattice of the top graphene layer can also be seen. Since scanning tunneling microscope topography also takes into account electronic local density of states, the image also reveals periodic electron accumulation, which occurs where the graphene lattices overlap almost perfectly—called the AA sites since the A sublattices on both layers are aligned. On the other hand, AB and BA sites (occurring at the vertices of the green hexagons in Fig. 1.7a and the center of the triangles in Fig. 1.7b), where only half of the graphene atoms overlap with opposite sublattices stacked on top of each other, tend to have less electron density.

Another system exhibiting moiré patterns is the graphene-hBN interface. Due to hBN's large band gap, pairing it with graphene mostly reveals the metallic properties of the graphene layers, usually without perturbation from the hBN layers. However, graphene and hBN can align if stacked at nearly the same twist angle, creating a moiré pattern. Two main effects occur in this instance. First, the two elements in hBN introduce a sublattice asymmetry that was not present in the all-carbon graphene lattice. This tends to open an insulating gap at the charge neutrality point (~ 0 electron and hole density). Second, the slight difference in lattice constants results in a moiré pattern with a maximum wavelength of about 15 nm. When four electrons fill each moiré unit cell, the behavior turns insulating again, indicating the filling of the bands for the larger-wavelength unit cell in a similar fashion as what happens in TBG.

Turning again to twisted bilayer graphene, modeling a moiré pattern at small twist angles is a difficult task if approaching from an *ab initio* approach based on atomic positions, due to the large amount of atoms in each moiré unit cell, on the order of thousands. However, the so-called continuum model [11, 12] was developed based on the low-energy Dirac Hamiltonian of graphene and is widely used as a first approach to the single-particle band structure of graphene. The concept starts with the Hamiltonians of the top and bottom graphene layers along with a tunneling term that couples the two layers,

$$H_{cont} = H_t + H_b + H_{tun}. \quad (1.18)$$

Here it is convenient to use a second-quantized description, where $\psi_{t/b}(\mathbf{k})$ and $\psi_{t/b}^\dagger(\mathbf{k})$ are the annihilation and creation operators for the top/bottom layers, respectively. These are actually eight-component spinors accounting for sublattice, spin, and valley degrees of freedom (unless there are assumed degeneracies). The intralayer terms are the Dirac Hamiltonian rotated symmetrically in opposite directions by $\theta/2$

$$H_{t/b} = \int d\mathbf{k} \psi_{t/b}^\dagger(\mathbf{k}) h_{t/b}(\mathbf{k}) \psi_{t/b}(\mathbf{k}) \quad (1.19)$$

where the integral represents the sum over \mathbf{k} states for the total energy (also allowing for coupling between different \mathbf{k}), although we are mostly concerned with the \mathbf{k} dependent Hamiltonian

$$h_{t/b}(\mathbf{k}) = -\hbar v_F R_z(\pm\theta/2) [k_x \tau_z \sigma_x + k_y \sigma_y] R_z^{-1}(\pm\theta/2) \quad (1.20)$$

where σ_i are Pauli matrices acting on sublattice indices, and τ_i Pauli matrices act on the valley indices. The negative sign only introduces a phase factor compared to Eq. (1.1) that we can ignore. We assume from here on that we can ignore valley coupling (which works for the single-particle picture but perhaps not when interactions are included), so we focus on one valley \mathbf{K} , or $\tau_z = 1$. The rotation can be applied to either the \mathbf{k} or sublattice σ terms, so we apply it to the sublattice, obtaining for the two layers

$$h_t(\mathbf{k}) = -\hbar v_F e^{i\theta\sigma_z/4} \mathbf{k} \cdot \boldsymbol{\sigma} e^{-i\theta\sigma_z/4} \quad h_b(\mathbf{k}) = -\hbar v_F e^{i\theta\sigma_z/4} \mathbf{k} \cdot \boldsymbol{\sigma} e^{-i\theta\sigma_z/4}. \quad (1.21)$$

Modeling the layers without interlayer tunneling essentially models two Dirac cones separated by a twist-angle dependent wavevector $K_\theta \propto \sin(\theta/2)$, with a simple schematic shown in Fig. 1.8a,b. The next step is to consider the interlayer tunneling H_{tun} , which tends to induce level repulsion, as shown in Fig. 1.8c. This term couples operators from top and bottom layers with offset momenta \mathbf{q}_ℓ , corresponding to the reciprocal lattice vectors of the moiré lattice

$$H_{tun} = \sum_{\ell=1,2,3} \int d\mathbf{k} \psi_t^\dagger(\mathbf{k}) T_\ell \psi_b(\mathbf{k} + \mathbf{q}_\ell) + h.c. \quad (1.22)$$

where

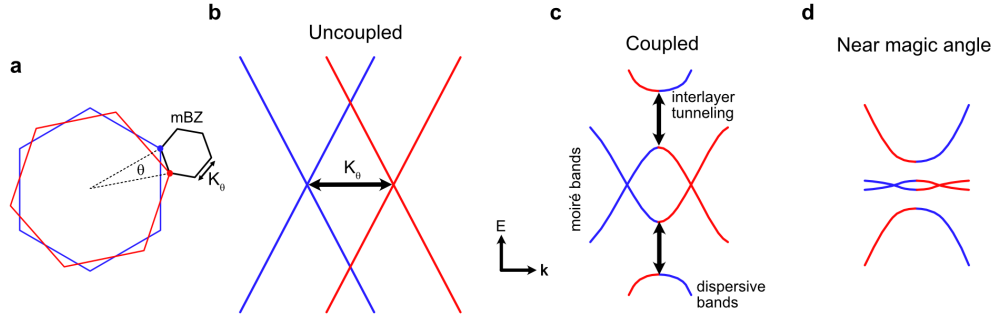


Figure 1.8: Schematic depiction of band structures in TBG. (a) Two monolayer graphene Brillouin zones twisted by an angle θ and the resulting mini-Brillouin zone (mBZ) for the moiré lattice. (b) Two uncoupled Dirac cones that occur at the dots in (a). (c) When coupling is included, and (d) when the coupling is included and the twist angle is near the magic angle.

$$\mathbf{q}_\ell = k_\theta \left(-\sin \left[\frac{2\pi}{3} (\ell - 1) \right] \hat{x} + \cos \left[\frac{2\pi}{3} (\ell - 1) \right] \hat{y} \right), \quad k_\theta = \frac{4\pi}{3a} 2 \sin(\theta/2), \quad (1.23)$$

and (using $\sigma_\pm = (\sigma_x \pm i\sigma_y)/2$)

$$T_\ell = w_{AA} + w_{AB} \left(e^{-2\pi i(\ell-1)/3} \sigma_+ + e^{2\pi i(\ell-1)/3} \sigma_- \right). \quad (1.24)$$

There are two coupling parameters w_{AA} and w_{AB} , which correspond to interlayer tunneling at AA and AB sites, respectively. TBG at low angles tends to relax, resulting in slightly larger AB-type regions and smaller AA-type regions [13], so we have generally used $w_{AA} = 55$ meV and $w_{AB} = 105$ meV. This choice of parameters results in the correct magic angle $\sim 1.1^\circ$ and experimentally matches the gaps between moiré bands and dispersive bands.

The Hamiltonian is practically solved by noting that $\psi_{t/b}(\mathbf{k})$ can be represented in a Bloch basis, expanded into an extended zone scheme by adding more Hamiltonian components with wavevector $\mathbf{k} + \mathbf{G}$ (for reciprocal lattice vector \mathbf{G}) and coupling them. The final Hamiltonian matrix looks like the following

$$\left(\begin{array}{ccc|ccc} h_t(\mathbf{k}) & & & & & \\ & h_t(\mathbf{k} + \mathbf{G}_1) & & & & \\ & & \ddots & & & \\ \hline & & & T & & \\ & & & & h_b(\mathbf{k}) & \\ & & & & & h_b(\mathbf{k} + \mathbf{G}_2) \\ & & & & & \ddots \\ T^\dagger & & & & & \end{array} \right) \quad (1.25)$$

where each point of a lattice of reciprocal vectors (made large enough to assure convergence) constitutes another row and column corresponding to its respective intralayer Hamiltonian on the diagonal. The interlayer elements T then couple terms between layers and with varying by momenta q_ℓ , matching the condition of Eq. (1.22). This is usually schematically represented as

$$h_{TBG}(\mathbf{k}) = \begin{pmatrix} h_t(\mathbf{k}) & T \\ T^\dagger & h_b(\mathbf{k}) \end{pmatrix}. \quad (1.26)$$

The continuum model, since one can continuously tune the twist angle and since it works at small angles, predicts a special result. At certain twist angles the Fermi velocity becomes zero, and the low-energy bands flatten considerably. The Fermi velocity can be approximated [11] based on the dimensionless ratios $\eta = w_{AA}/w_{AB}$ and $\alpha = \frac{w_{AB}}{v_F k_\theta}$, where v_F is the original monolayer graphene Fermi velocity 10^6 m/s. The low-energy continuum model Fermi velocity is, then, approximately

$$v_{cont} = \frac{1 - 3\alpha^2}{1 + 3\alpha^2(1 + \eta^2)} v_F. \quad (1.27)$$

So the points with zero Fermi velocity are controlled by α , the ratio of the AB hopping to the Moiré wavevector—or the separation between Dirac cones—which is proportional to θ . Although there are multiple twist angles with vanishing Fermi velocity, only one is practically accessible for TBG, and it is around 1.1° . Fig. 1.9 shows how the continuum model bands drastically flatten when lowering the twist angle and then widen as the angle is further lowered. The flat bands also meet the higher-energy dispersive bands below a certain angle $\sim 0.8^\circ$. It is worth noting briefly that the bands in magic-angle TBG, as measured by STM, are not as flat as suggested by the continuum model, due to correlations [10, 14].

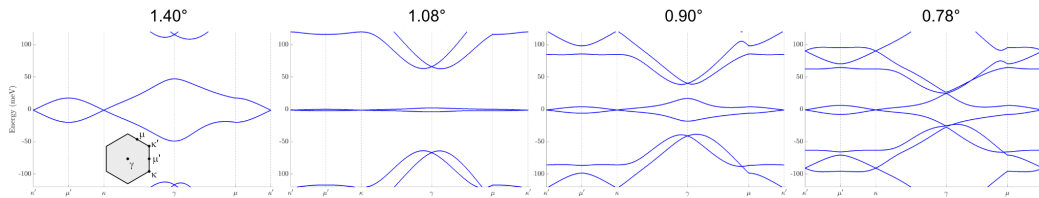


Figure 1.9: Continuum model TBG band structure for twist angles above and below the magic angle, showing the flattening near the magic angle. Note that the x-axes represent momentum \mathbf{k} following the mini Brillouin zone shown in the left inset.

1.5 Superconductivity: conventional vs. unconventional

Superconductivity is generally recognized by its characteristic features of zero resistance, an energy gap (observed with optics and other energy spectroscopy techniques), strong diamagnetism (cancelling out magnetic fields in the superconducting area), and macroscopic phase coherence (visible in Josephson junctions). The traditional theory of superconductivity—outlined in 1957 by Bardeen, Cooper, and Schrieffer [15] and thus often called BCS superconductivity—provides a useful foundation from which to understand these basic experimental phenomena. Many basic elemental materials, such as aluminum, titanium, tin, and mercury, act as conventional BCS superconductors, typically only at very low temperatures. However, BCS theory fails to account for the range of features more recently associated with complex unconventional superconducting systems, most notably high-temperature superconductivity [16] and its association with other electron correlations.

The BCS theory of superconductivity generally applies to Cooper pairs of one spin-up and one spin-down electron, with an isotropic (s-wave, spin-singlet) pairing potential and a limit to the critical temperature T_c that is directly related to the density of states at the Fermi level $N(E_F)$ and the strength of the pairing potential V [17]:

$$k_B T_c = 1.13 \hbar \omega_c e^{-\frac{1}{N(E_F)V}} \quad (1.28)$$

where k_B is Boltzmann's constant and ω_c is the cutoff frequency of the attractive pairing interaction. The pairing gap at zero temperature Δ results from a similar equation to Eq. (1.28), and the two can be related by a multiplicative constant $\Delta = 1.764 k_B T_c$. However, these equations assume the weak-coupling condition, i.e., $N(E_F)V \ll 1$. Conventional superconductivity arises from a pairing potential due to phonons mediating an attractive electron-electron interactions. Thus, a

conventional BCS-like superconductor will show the strongest superconductivity when the density of states and electron-phonon coupling are high.

The coherence length ξ also has a BCS weak-coupling prediction:

$$\xi = \frac{\hbar v_F}{\pi \Delta}. \quad (1.29)$$

It can also be directly empirically determined—since it represents a maximum vortex length scale in an out-of-plane magnetic field—with the equation derived from Ginzburg-Landau theory

$$T_c/T_{c0} = 1 - (2\pi\xi^2/\Phi_0)B_\perp \quad (1.30)$$

where $\Phi_0 = h/(2e)$. It is most often determined by the slope of the T_c vs. B curve close to the critical temperature.

This leaves us several routes by which we can classify superconductivity as unconventional. Superconductivity could possibly form an anisotropic pairing gap, as in the d-wave pairing observed in cuprate superconductors [18]. The Cooper pairs could form a spin-aligned triplet or other configurations as opposed to the spin-neutral singlet state. The mechanism mediating Cooper pairs could be due to electron-electron or spin-based interactions as opposed to the traditional phonons. The bound pairs could also be more exotic than traditional Cooper pairs [19].

Strong-coupling superconductivity would violate the equations above and could even imply approaching the Bose-Einstein condensate (BEC) regime with an extended phase space of tightly paired electrons [21], particularly with residual effects at temperatures higher than T_c . In many high- T_c superconductors, this manifests as a pseudogap. The degree of coupling can be estimated with the dimensionless constant Δ/E_F , which approximately converts to the more experimentally attainable T_c/T_F , where E_F and $T_F = E_F/k_B$ are the Fermi energy and Fermi temperature, respectively, and are directly related to the total number of electrons in the system. So-called Uemura plots [22], such as in Fig. 1.10 showing T_c plotted vs. T_F for known superconductors, are insightful since previously recognized unconventional superconductors fall toward the top left of the diagram (as opposed to conventional superconductors, which tend toward the bottom right of the diagram) [20, 23, 24]. A high T_c/T_F ratio was one of the first indicators of unconventional superconductivity

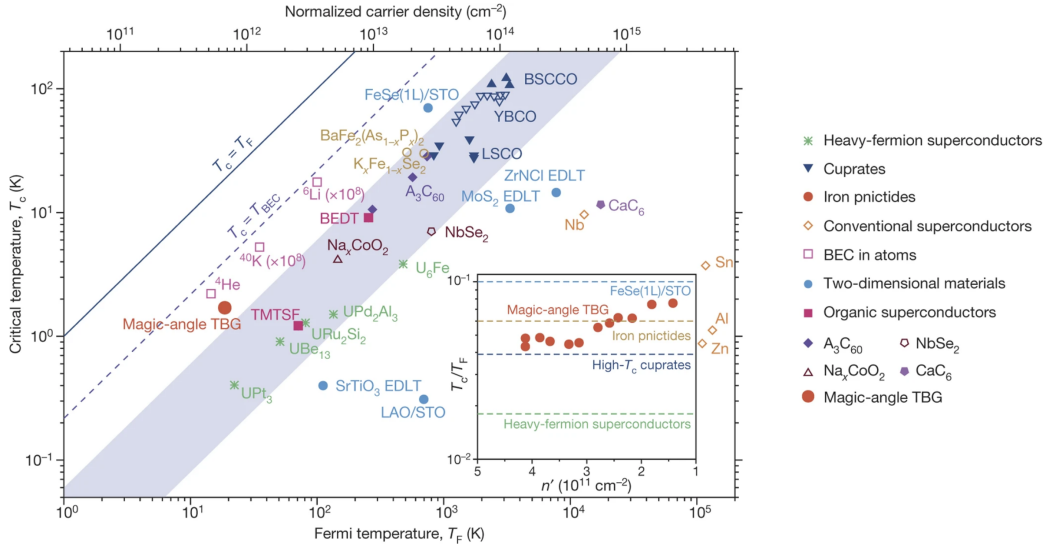


Figure 1.10: Uemura plot of superconducting critical temperature T_c vs. Fermi temperature T_F for a range of materials, including TBG. Reprinted from [20], with permission from the copyright holder, Springer Nature.

in TBG [20], leading to theoretical interest and continued debate on the mechanism behind superconductivity in TBG and other twisted moiré materials.

Since tightly-bound pairs in strong-coupling superconductors can be susceptible to phase fluctuations, coherence lengths also tend to be smaller than weak-coupling BCS superconductors, so comparison to Eq. (1.29) can be another useful measure indicating strong-coupling or non-BCS superconductors.

Any mixture of these and other measures of unconventional superconductivity provide fertile grounds for more fully understanding superconductivity, particularly when observations are paired with other correlated effects. Graphene moiré systems' advantages, in terms of fabrication and doping, provide useful experimental testing grounds for theories of unconventional superconductivity.

1.6 Spin-orbit coupling

Spin-orbit coupling (SOC) is an energetic contribution to electrons resulting from the interaction between the spin of the electron and effective magnetic fields from the lattice or orbital angular momentum. It generally splits electrons of one particular spin species into two separate energy levels of opposite momenta. One can also switch between the two levels by flipping the spin of the electron (Fig. 1.11). An intuitive picture of SOC comes from considering an out-of-plane (\hat{z} direction)

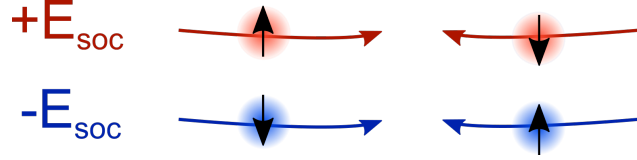


Figure 1.11: An schematic of the energy splitting involved in spin-orbit coupling, where opposite spins/momenta are split, but the reversing both leads to the same energy.

electric field E induced by an asymmetric lattice. Due to relativity, moving electrons interpret the field as magnetic field, and the energetic coupling to spins is

$$H_{\text{Rashba}} = -\frac{g\hbar E}{4c^2 m_e^2} (\mathbf{s} \times \mathbf{p}) \cdot \hat{\mathbf{z}} \quad (1.31)$$

where the g -factor is $g \approx 2$ for a bare electron, c is the speed of light, m_e is the mass of an electron, \mathbf{s} is the electron spin vector, and \mathbf{p} is the momentum. This is called the Rashba effect, and it generally splits in-plane spins. In graphene, due to the association of momentum with valley and sublattice degrees of freedom, this can be represented as

$$H_{\text{Rashba}} = \frac{\lambda_R}{2} (\tau_z \sigma_x s_y - \sigma_y s_x), \quad (1.32)$$

with τ_i and σ_i being Pauli matrices acting on the valley and sublattice states, respectively, and where λ_R represents the energy splitting.

Another relevant SOC term in 2D systems, considered for graphene in Ref. [25], is called the Kane-Mele SOC:

$$H_{\text{Kane-Mele}} = \frac{\lambda_{KM}}{2} \tau_z \sigma_z s_z. \quad (1.33)$$

And the other relevant term to graphene and TMDCs is called Ising SOC, and it couples out-of-plane spins to valley (momentum):

$$H_{\text{Ising}} = \frac{\lambda_I}{2} \tau_z s_z. \quad (1.34)$$

A well know feature that results from spin-orbit coupling is the weak antilocalization (WAL) effect, a distinct conductivity peak at low temperatures and magnetic fields. An explanation of the effect follows from a simple argument that can be found in

more detail in [26]. Electrons bounce randomly off random defects in a material. In materials with favorable amounts of defects and at temperatures low enough for the electrons to maintain phase coherence, an effect called weak localization occurs. Electrons that travel in opposite paths, returning to their origin, tend to constructively interfere. Conductivity, as a result suffers since it is favorable for electrons to return rather than traveling through the material. The interference is jumbled, however, by a magnetic field, resulting in a distinct conductivity dip at zero magnetic field.

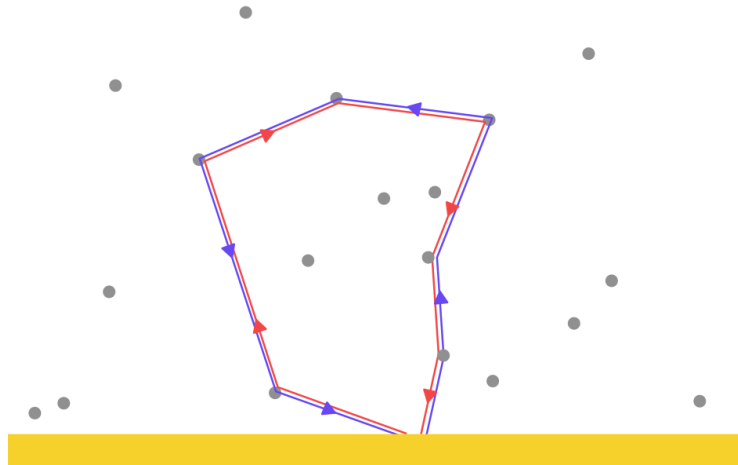


Figure 1.12: A depiction of the two time-reversed (opposite) paths electrons scattering off defects.

In systems with SOC, the opposite effect occurs. When SOC is strong, the spin of an electron will get randomized when travelling along the path shown in Fig. 1.12. However, electrons on the time-reversed path will experience the opposite spin rotation, resulting in destructive interference. In this case, small magnetic fields decrease the conductivity, resulting in a conductivity peak at zero magnetic field. The peak is generally on the order of $\lesssim e^2/h$.

1.7 Topology in graphene systems

Graphene has been at the forefront of theoretical interest not only for the reasons stated above, but also for its close connection to topology in condensed matter systems. One of the first widely recognized examples is found in the Haldane model [27], which revealed a globally time-reversal symmetric topological insulator state by introducing locally varying magnetic fields in a graphene lattice. Later, around the time of the experimental discovery of graphene, Kane and Mele realized [25] that spin-orbit coupling in graphene could induce the quantum spin Hall effect in graphene, characterized by a gap in the bulk of a sample paired with topologically

protected helical edge states (where current of spin \uparrow goes in one direction and current of spin \downarrow in the opposite direction). Topological edge states should be insensitive to disorder and reveal quantized conductance according to a Chern number C multiplied by the quantum of conductance e^2/h . However, graphene's intrinsic spin-orbit coupling is very small, precluding the quantum spin Hall effect. Further efforts to find topologically nontrivial states through induced spin-orbit coupling [28–30] and ferromagnetism [31] have not yet turned up unambiguous experimental signatures of topological states in monolayer graphene although bilayer graphene may show more promise [32].

However, further insights into the topology of graphene come from another method of modifying the Hamiltonian, which is relevant for the discussion of TBG: instead of a spin-orbit gap, an added sublattice mass (a term that energetically favors atoms on one sublattice of the graphene over the other) to the Dirac Hamiltonian in Eq. (1.1) introduces an analytic example of topology in the graphene system [33]. This results in a Hamiltonian of the form

$$\hat{H} = \hbar v_F (\tau \sigma_x, \sigma_y) \cdot \mathbf{k} + m \sigma_z = \begin{pmatrix} m & \hbar v_F (\tau k_x - i k_y) \\ \hbar v_F (\tau k_x + i k_y) & -m \end{pmatrix}. \quad (1.35)$$

This Hamiltonian has the modified energies $E = \pm \sqrt{\hbar^2 v_F^2 k^2 + m^2}$ and therefore quadratic electron and hole bands separated by the gap of $2m$.

The relevant quantity for calculating the topological character of the band structure is the Berry Curvature, defined as

$$\Omega(\mathbf{k}) = -\text{Im} \nabla_{\mathbf{k}} \times \langle u_{\mathbf{k}} | \nabla_{\mathbf{k}} u_{\mathbf{k}} \rangle \cdot \hat{\mathbf{z}} = -2 \text{Im} \left\langle \frac{\partial u_{\mathbf{k}}}{\partial k_x} \middle| \frac{\partial u_{\mathbf{k}}}{\partial k_y} \right\rangle \quad (1.36)$$

where the last equality works for $\Omega(\mathbf{k})$ in the $\hat{\mathbf{z}}$ direction for a 2D system, and $u_{\mathbf{k}}$ is the Bloch basis function for the underlying Bloch wavefunction $\psi_{\mathbf{k}}(\mathbf{r}) = u_{\mathbf{k}} e^{i\mathbf{k} \cdot \mathbf{r}}$, which in this case is the eigenvectors of the Hamiltonian.

Whereas the Berry curvature is 0 for states of the massless Dirac Hamiltonian, except for singularities at the \mathbf{K} and \mathbf{K}' points, a more complex function is found for the eigenvectors of the massive Dirac Hamiltonian in Eq. (1.35) [34]:

$$\Omega(\mathbf{k}) = \pm \tau \frac{\hbar^2 v_F^2 m}{2(m^2 + \hbar^2 v_F^2 k^2)^{3/2}} \quad (1.37)$$

where the \pm sign out front refers to electrons(+) or holes(-).

Integrating the Berry curvature gives us the Chern number:

$$C = \frac{1}{2\pi} \int \Omega(\mathbf{k}) d^2\mathbf{k} = \frac{\tau \hbar^2 v_F^2 m}{2} \int_{k=0}^{k \rightarrow \infty} \frac{k dk}{(m^2 + \hbar^2 v_F^2 k^2)^{3/2}} = \pm \frac{\tau}{2}. \quad (1.38)$$

Note that here the integral should be over the Brillouin zone, and the Dirac Hamiltonian only applies in the low energy limit. However, the denominator quickly disappears at large k . This calculation can be thought of with a more intuitive picture when we are dealing with a 2-level Hamiltonian that can be represented in terms of Pauli matrices $\hat{H} = \sum_{i=x,y,z} d_i(\mathbf{k}) \sigma_i$. The Chern number derivation from Berry curvature can be represented in terms of a 3D unit vector $\hat{\mathbf{d}}(\mathbf{k}) = \mathbf{d}(\mathbf{k})/|\mathbf{d}(\mathbf{k})|$ in terms of the equation

$$C = \frac{1}{4\pi} \int \hat{\mathbf{d}} \cdot \left(\frac{\partial \hat{\mathbf{d}}}{\partial k_x} \times \frac{\partial \hat{\mathbf{d}}}{\partial k_y} \right) d^2\mathbf{k} \quad (1.39)$$

which simply counts the times $\hat{\mathbf{d}}$ wraps around the surface of a sphere in the integral [35]. In our case with $\mathbf{d}(\mathbf{k}) = (\hbar v_F \tau k_x, \hbar v_F k_y, m)$, the unit vector $\hat{\mathbf{d}}$ points in the \hat{z} direction at $\mathbf{k} = 0$, and it points in the $x - y$ plane when k_x or $k_y \rightarrow \infty$, as shown in Fig. 1.13. The vector thus wraps around half a sphere over the integrated space, giving us the result in Eq. (1.38) and geometrically demonstrating the connection to topology.

The calculation in Eq. (1.38) captures the general behavior of massive Dirac fermions, in which the Chern number is opposite in sign for conduction vs. valence bands and for opposite valleys (but the Chern number is spin-invariant). Since Dirac points come in pairs (here spin- and valley-degenerate pairs, and mini-valleys in TBG [36]), the Chern number will always be an integer. Even though a sublattice mass can be added to graphene experimentally with aligned hBN, the degeneracy of graphene's valleys causes the overall Chern number to inherently cancel out, leaving a non-topological gap.

Nevertheless, experiments can show signatures of the Berry curvature through the valley Hall effect [34, 37]. And with the right combination of band flattening and symmetry breaking—which causes favorable polarization of one flavor—the nonzero Chern number can represent itself in an orbital ferromagnet, as we will see later in twisted bilayer graphene.

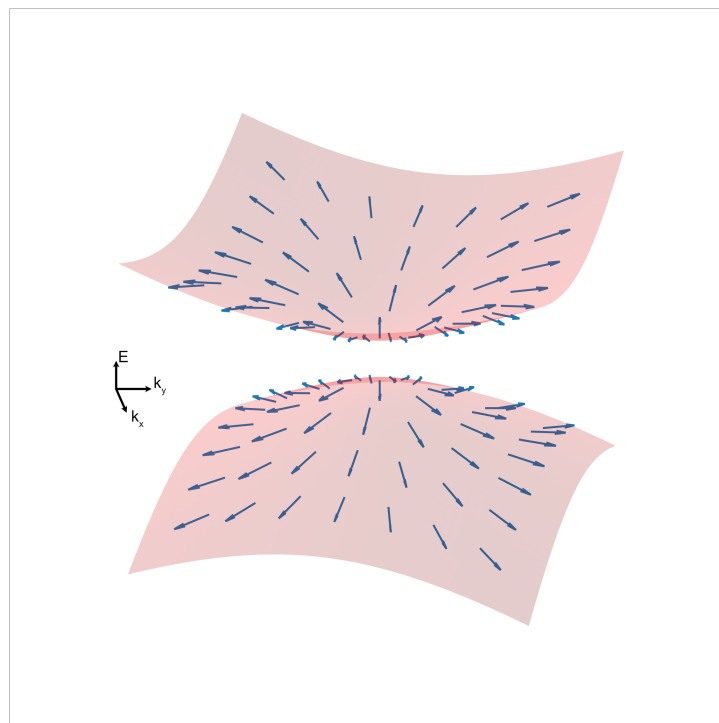


Figure 1.13: The energy of the massive Dirac Hamiltonian (pink) with blue vectors representing the vector $\mathbf{d}(\mathbf{k})$.

DEVICE DESIGN AND CHARACTERIZATION

This thesis largely discusses measurements of electrical transport properties, or electrical resistance, of 2D materials. When we are considering van der Waals materials, there are important details in the fabrication procedure to allow for high-quality measurements. These details are particularly relevant to the fabrication of TBG when considering types of disorder present, so fabrication procedures are discussed first in this chapter. Secondly, this chapter discusses measurement equipment and protocols, with a brief discussion of Landau levels, which are heavily used in analysis, and the setup of our Oxford Triton dilution refrigerator.

2.1 Fabrication

Van der Waals dry stacking technique

Since the original isolation of monolayer van der Waals materials [2, 3], stacking techniques for graphene have improved dramatically. In particular, when insulating hBN is used as a substrate [38], the atomic flatness significantly reduces the strain and charge impurities induced by substrates like SiO₂ [39]. In addition, the less graphene is exposed to solvents and polymers, the better the device quality. Thus, the next big step was discovering a way to fabricate devices without exposing the graphene layer to any polymer or solvent [40]. In this method, a polymer is used to sequentially pick up a flake of each material, and the stack of flakes is dropped onto the substrate by melting the polymer. Contacts are then made by etching through the graphene layer and subsequent metal deposition. Only the top hBN is exposed to solvents and polymers, leaving the encapsulated graphene pristine. Furthermore, the application of temperatures $>110^\circ\text{C}$ while depositing or peeling flakes off of their substrates tends to push impurities (which appear as bubbles in optical images) out of the interfaces between flakes [41]. These bubble impurities plague device quality, so devices are generally made by etching devices out of bubble-free areas.

For moiré heterostructures, an additional procedural step makes precise control over twist angle possible [42]. Due to the strong adhesion of graphene to hBN and its tendency to tear, a single graphene flake can be split into multiple pieces, which can be picked up one by one. Since the flake consists of a single crystal, twisting between pickup steps can allow for control at the level of $\sim 0.1^\circ$. Small-angle

twisted moiré structures present a problem due to the tendency of the interface to relax toward a non-twisted configuration as a result of the low friction of van der Waals materials. TBG, in particular, has been reported to relax with the application of high temperatures [20]. From our fabrication experience, we found that TBG at $\leq 1.5^\circ$ is more prone to relaxation when many stacking steps are involved, when high temperatures ($> 100^\circ \text{C}$) are used during stacking steps, and when stacking occurs in a quick and uncontrolled manner. This, unfortunately, means that bubble impurities appear in our devices more often than when we use high-temperature stacking steps; however, we can usually make large enough areas for devices when we use large graphene flakes and slow, controlled transfer steps.

Before optimizing our technique, devices would often show disorder-broadened features in measurements, and superconductivity did not reliably appear. Conversations with other research groups also confirmed our struggles at getting reproducible results, with a report or two of only one superconducting device out of ten. Often times, these devices involve multiple contacts, with different levels of impurity and inhomogeneity for each one. TBG papers have also revealed a range of behaviors [20, 43–53]. This is likely due in part to the fact that TBG naturally displays sizeable twist angle inhomogeneity on the level of $\sim 100 \text{ nm}$ [54], even for groups that have honed the fabrication process enough to reliably make superconducting devices. Additionally, the similarity of lattice constants in graphene and hBN could result in accidental commensurate lattices from alignment or moiré-in-moiré conditions that result from more complex three-layer alignment [55, 56]. Thus the explicit symmetry breaking involved in these alignment conditions could change the device behavior.

The mentioned complications result in a lack of reproducibility in TBG devices, so we have made attempts to base the bulk of our work on findings that are reproduced in multiple devices, while not overly weighing details that may be device dependent. And, after honing our fabrication technique, we see superconductivity in multiple contacts in a majority of devices. We suppose the reproducibility we see could be assisted, to some degree, by the included tungsten diselenide (WSe_2) in our devices, which seems to reduce disorder in TBG. STM measurements also support the reduction in disorder [57].

The devices used in the following two chapters consist of TBG with a WSe_2 monolayer stacked on top, with encapsulating hBN layers on the top and bottom, as shown in Fig. 3.1. The stack is deposited onto a pre-deposited Au back gate. We opted to

avoid picking up an additional graphite layer for a back gate since this would increase the stacking steps, and thus the potential for strain and relaxation induced by the relatively violent process of stacking. The general process we used for assembling a stack of van der Waals materials is outlined below.

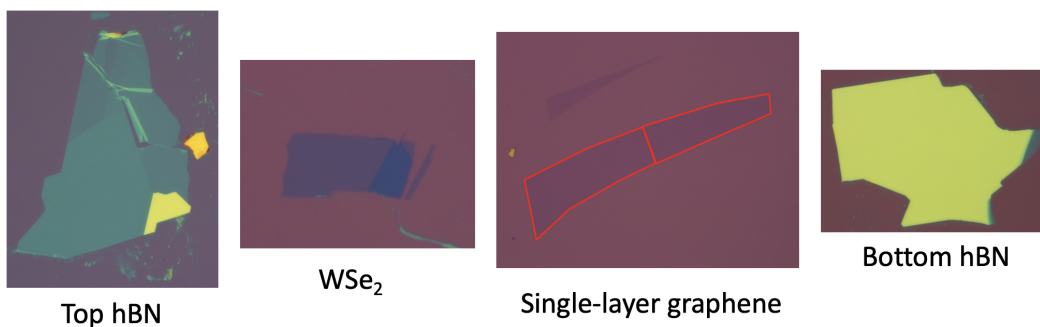


Figure 2.1: Flakes of van der Waals materials exfoliated onto SiO_2 in preparation for making a TBG- WSe_2 device. The red lines on graphene outline the two pieces that are rotated with respect to each other in the final device.

1. **Exfoliation:** Apply a bulk crystal of the desired type to scotch tape. Then stick and peel the tape repeatedly to create a thin, even layer of flakes across the tape. Stick the tape onto a Si substrate with about 300 nm SiO_2 (to enhance the contrast and make the flakes visible), and peel off slowly. After this exfoliation step, flakes are found by searching around the Si chip using optical microscopy. A few tips can be used to get large, thin flakes. For instance, a light oxygen plasma cleaning of the Si/ SiO_2 substrate can help with finding large monolayer graphene flakes. Generally, using large facets of bulk crystals, being generous with the amount of bulk crystal used, and light application of heat ($\sim 100^\circ\text{C}$ for <5 minutes) can help in some instances. We repeat this exfoliation and flake searching step for each material before starting the stack assembly. Examples of each flake in a TBG- WSe_2 device are shown in Fig. 2.1.
2. **Polymer pickup of the top hBN:** A good top hBN flake is large enough to cover the remaining flakes, and thick enough to provide structure but not so thick as to obscure the other flakes in the stack. We used flakes in the range of 10–30 nm thick for the top hBN. The polymer pickup technique requires a polymer that will reliably pick up the first hBN flake but will melt at accessible temperatures. A thin film of poly(bisphenol A carbonate) (PC)



Figure 2.2: An example polymer stamp, showing a pre-cut PDMS square that supports the thin PC film, which is attached to the slide using scotch tape with a window cut out.

supported by polydimethylsiloxane (PDMS) on a glass slide Fig. 2.2. A PC thin film is produced by dissolving the polymer into a solvent, such as N-methyl-2-pyrrolidinone (NMP) until it forms a viscous liquid. After placing a few drops on a glass slide, slipping another slide across the first slide, and letting the two slides harden, the PC forms a dry thin film. We can then cut and pick up the film with scotch tape. A window in the scotch tape allows us to stretch the PC over a PDMS stamp. After a curing step at 104°C for 9 minutes, we can use the polymer stamp to pick up the hBN flake.

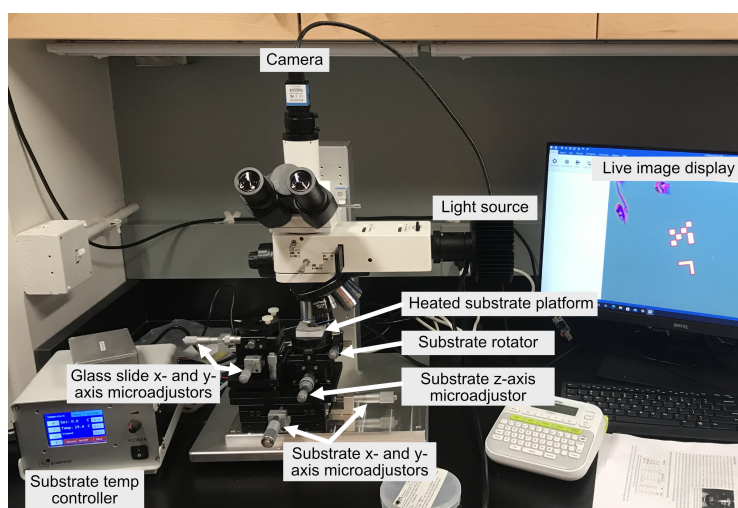


Figure 2.3: A transfer setup used to make van der Waals stacks.

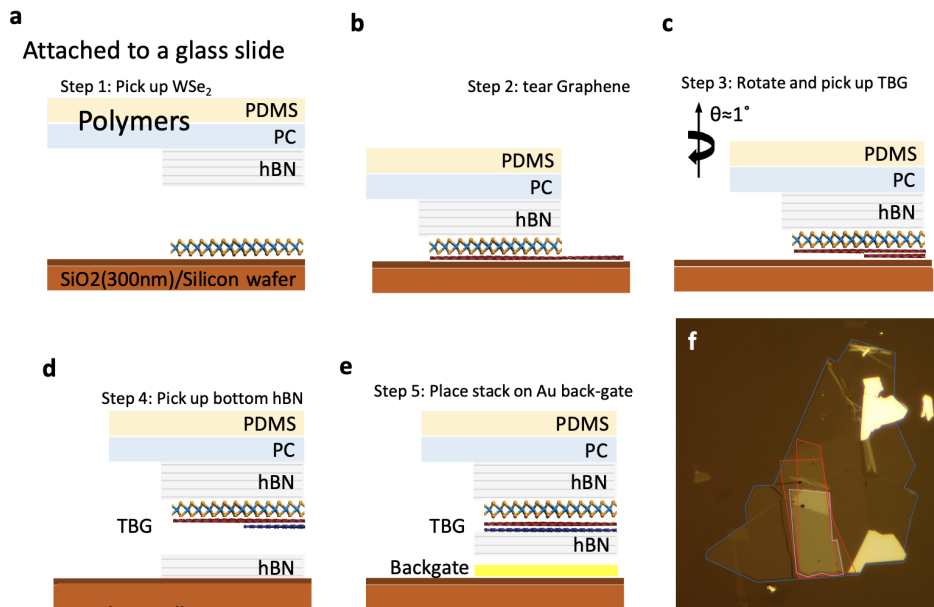


Figure 2.4: Flake-by-flake polymer dry stacking technique. (a)–(e) The stacking process used for a TBG-WSe₂ device. (f) The stack (except for the bottom hBN) picked up on the polymer stamp, using the flakes from Fig. 2.1. The top hBN (blue), WSe₂ (pink), and two graphene pieces (red) are outlined.

- Stack assembly:** The degrees of freedom necessary for assembling a stack of van der Waals materials (including twisting for moiré structures) are: x-, y-, and z-axis control of the substrate relative to the polymer stamp slide, independent tuning of the microscope focus, accurate twist control of the substrate, and (optional but convenient) x- and y-axis control of the polymer stamp slide. The substrate holder also needs to have temperature control up to at least 180° C. We used a commercially produced transfer setup (HQ Graphene), shown in Fig. 2.3. The polymer stamp is used to subsequently pick up the top hBN, followed by monolayer WSe₂, the two graphene flakes, and a bottom hBN flake (30–70 nm thick to avoid over-etching in further steps), as shown in Fig. 2.4. As the polymer stamp is lowered over each van der Waals flake, the polymer contact to the substrate forms a line that propagates as the polymer stamp is raised or lowered. When the line propagates across the flake and then retracts, the flake is picked up and added to the stack that adheres to the bottom of the polymer stamp. When picking up flakes for twisted devices, we used a temperature of $\sim 90^\circ$ C for each pickup step. Slight temperature increases and decreases allow for slow and steady propagation of the polymer contact line across the flake that is being picked up. While in the next chapter

[46], the graphene flake was torn to make twisted structures, in the following chapters [53, 58], the graphene flake was first cut into pieces with a Pt-Ir STM tip attached to a glass slide to allow for clean pickup of each piece. For TBG, first the top flake of graphene is picked up. Then the substrate is rotated to about $1.1\text{--}1.3^\circ$ (overshooting the target angle slightly to allow for relaxation), and the second flake is picked up.

4. **Deposition and cleaning:** Finally, to complete the stacking step, the stamp containing the finished stamp is lowered onto a substrate, a degenerately doped Si/SiO₂ chip pre-patterned with Au lithography markers for optically designing devices and with a Au gate. While lower the stack onto the substrate, the temperature is set to 150°C . Then, the temperature is raised to 170°C to melt the PC, and the stamp is lifted. Leftover polymer residue can be removed in a 10-minute NMP bath.

For three-, four-, and five-layer devices, the process of twisting and stacking graphene flakes is just repeated for extra pieces of the graphene flake. The rest of the steps remain the same.

Contact deposition and etching

The next steps involve the use of micro- and nano-fabrication tools available in the Kavli Nanoscience Institute (KNI).

1. **Electron-beam lithography:** Each step of lithography is first prepared by spin-coating polymethyl methacrylate (PMMA, more specifically 950 PMMA A4) at 1500 rpm followed by a low-temperature bake of 110°C for 90 s. We use dedicated electron-beam lithography machines (Raith EBPG 5000+ or 5200) at 100 kV, beam currents in the range of 1–100 nA, and a dosage of $1100\text{--}1300\ \mu\text{C}/\text{cm}^2$, depending on feature size. We construct our Hall bar lithography patterns to avoid feature sizes $\lesssim 1\ \mu\text{m}$ and fillet edges to avoid sharp corners, which reduces cracks in the PMMA. After lithography, we use a methyl isobutyl ketone (MIBK)/isopropyl alcohol (IPA) solution to develop the patterns and remove the PMMA from the exposed area. In the first lithography step, we set up a pattern for the contacts and contact pads.
2. **Contact etch:** We use an RF reactive ion plasma etch system (Plasmatherm RIE) to etch our devices made of van der Waals materials since it has a

controllable etch rate. We first use a light O₂ etch (30 W, 20 sccm O₂ flow rate, 50 mTorr chamber pressure for 1 minute) to clean off any residual PMMA from the contact area. Then, a CHF₃/O₂ etch step is used (60 W, 40 sccm CHF₃/4 sccm O₂, 40 mTorr) to remove the top hBN, graphene, and a little of the bottom hBN from the contact area. We found hBN to etch at a rate of approximately 25-40 nm/minute, with graphene and WSe₂ areas etching at a slightly slower rate. We periodically checked the etch optically to avoid over-etching.

3. **Metal evaporation and liftoff:** The sequential etching through hBN-encapsulated graphene and subsequent electron-beam evaporation allows for reliable effective one-dimensional contacts to graphene [40]. In our process, as opposed to Ref. [40], we achieve contacts in one lithography step. This both avoids an unnecessary lithography step and possible PMMA and solvent-based contamination of the contacts since the metal is deposited immediately after etching. We use a Kurt J. Lesker Labline electron-beam evaporator to evaporate metals for contacts and gates. We deposit 5 nm Ti followed by usually 100 nm of Au. We found more reliable contacts by depositing only after achieving base pressures $< 1 \times 10^{-7}$ torr.
4. **Device geometry etch:** After the contacts are deposited, we shape the device into a multi-contact Hall bar (e.g., see Fig. 2.5 for a device after the contact deposition and geometry etch steps) by first performing a lithography step that exposes an area around the contacts and outside the outline of a Hall bar geometry. Note that the Hall bar is defined in a bubble-free region. After lithography, the device is etched using the same CHF₃/O₂ etch recipe as before, but for longer to etch down to the SiO₂.

This was occasionally supplemented by an extra lithography step and the deposition of a Ti/Au topgate before the final device geometry etch step. The topgate was necessary for three-, four-, and five-layer graphene moiré structures in order to control the electric field.

2.2 Electrical transport measurements

The types of measurements mostly discussed here involve the study of how electrons move through condensed matter systems, or electrical transport. The quantity of interest is the resistance of a material. The theoretical picture comes from modelling

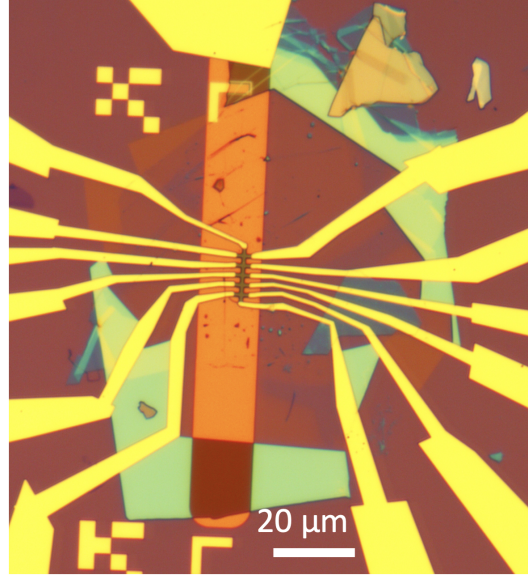


Figure 2.5: A finished TBG-WSe₂ device, with contacts and etched into a Hall bar. The orange stripe behind the device is a thin Au backgate.

low-energy excitations imposed on the material by an excitation voltage and derive the resulting current. When considered at low temperatures, the current depends on energetic states being available near the Fermi energy E_F (the point where electrons are filled up to), the velocity of states near the Fermi energy, and a consideration of scattering mechanisms. A first-order approach comes from Boltzmann transport theory [8], given a two-dimensional band structure with energy $\epsilon(\mathbf{k})$ and current density \mathbf{j} flowing through the material along the electric field \mathbf{E} , we get

$$\mathbf{j} = \frac{e}{(2\pi)^2} \int d\mathbf{k} \mathbf{v}(\mathbf{k}) \left(-\frac{\partial f^0}{\partial \epsilon(\mathbf{k})} \phi(\mathbf{k}) \right) = \frac{e}{(2\pi)^2} \int d\mathbf{k} \mathbf{v}(\mathbf{k}) \left(-\frac{\partial f^0}{\partial \epsilon(\mathbf{k})} e\mathbf{E} \cdot \mathbf{v}(\mathbf{k}) \tau(\mathbf{k}) \right) \quad (2.1)$$

where $\mathbf{v}(\mathbf{k}) = \frac{1}{\hbar} \frac{d\epsilon}{d\mathbf{v}(\mathbf{k})}$ is the group velocity of electrons derived from the band structure, $-\frac{\partial f^0(\mathbf{k})}{\partial \epsilon(\mathbf{k})} \phi(\mathbf{k})$ is the perturbed Boltzmann distribution function that tells us which electron states are occupied. f^0 is the equilibrium Fermi-Dirac distribution function. $\phi(\mathbf{k}) = e\mathbf{E} \cdot \mathbf{v}(\mathbf{k}) \tau(\mathbf{k})$ is the perturbation potential consisting of the electric field with consideration of scattering mechanisms through a relaxation time $\tau(\mathbf{k})$, which could be due to material defects, electron-phonon coupling, and electron-electron coupling. This can be simplified very roughly by assuming temperature approaches zero, resulting in $-\frac{\partial f^0(\mathbf{k})}{\partial \epsilon(\mathbf{k})}$ becoming very sharp and selecting a single energy E_F out of the integral. If we also convert the integral over \mathbf{k} into an integral

over ϵ , we include the density of states at the Fermi surface $N(E_F)$ to get (along one direction x , so paying attention only to j_x and E_x components of current and electric field)

$$\sigma = \frac{j_x}{E_x} \sim e^2 \langle v_F^2 \rangle_x \langle \tau \rangle N(E_F) \quad (2.2)$$

where $\sigma = 1/\rho$ is the conductivity (and ρ is the resistivity), $\langle v_F^2 \rangle_x$ is a sort of averaged Fermi velocity favoring the x direction, and $\langle \tau \rangle$ is an averaged scattering time. Although this analysis is very rough, it gets the point across that the conductivity is highest when the band structure allows for high Fermi velocity and density of states. If the band contains a gap, $N(E_F) \rightarrow 0$ in the gap and the material is insulating, which results in very low conductivity. Scattering mechanisms tend to decrease the scattering time τ and reduce the conductivity, and higher temperature tends to blur the states about the Fermi energy by broadening $-\frac{\partial f^0(k)}{\partial \epsilon(k)}$ by a factor of roughly $k_B T$, where k_B is Boltzmann's constant. Thus low temperatures more closely reveal the band structure since the energy scales we work with are of order \lesssim a few meV, and 1 K corresponds to broadening of order 0.1 meV.

Although electrical transport measures quantities that are theoretically somewhat convoluted to relate to the band structure $\epsilon(\mathbf{k})$, the simplicity of the electrical setup allows for easy fabrication and placement of the device into well isolated fridges. In addition, the measurements can sometimes have relatively simple interpretations, such as zero resistivity in superconductors, and serve as a starting point for many practical devices, such as Josephson junctions and transistors.

The Hall bar device

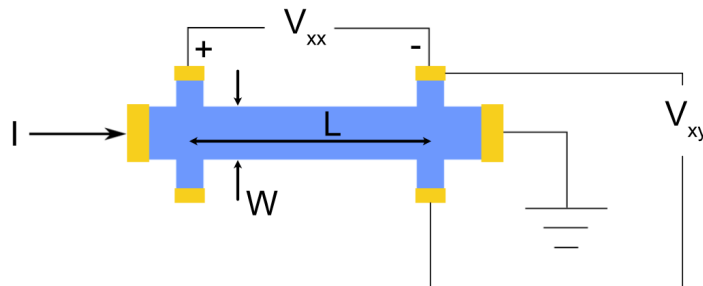


Figure 2.6: Demonstration of four-point measurements made on a Hall bar.

More practically, measurements are performed in an idealized geometry such as the

Hall bar (Fig. 2.6) where the geometry allows for nearly constant electric field down the length of the device L . The contacts on either side of the device allow for a four-point measurement where they are seen as probing the voltage in the rectangular section of the geometry. This is done by supplying a current I and measuring the longitudinal resistance as $R_{xx} = V_{xx}/I$. Four-point measurements in most cases do not contribute contact resistance to the measurement of V_{xx} and thus are useful for low-resistance measurements (as in measurements of superconductors). In two-dimensional devices, sometimes one refers to the resistivity $\rho_{xx} = R_{xx}W/L$, where the units are sometimes referred to as Ω/square since it is the resistance if the sample was shaped like a square where $W = L$.

The other form of measurements, mostly relevant under magnetic fields, result from transverse accumulation of electrons in the device. $R_{xy} = V_{xy}/I$ is useful for determining the density of carriers in the device through the Hall effect: $n_{\text{Hall}} = \frac{B}{R_{xy}e}$. Hall effect measurements can also reveal the effect of magnetization (in that case called the anomalous Hall effect). Although some may use the convention that positive R_{xy} results from hole carriers (negative n), we will generally use the opposite convention: positive R_{xy} results from electron carriers.

Landau levels

A useful technique in two-dimensional transport measurements is enabled when we apply a large out-of-plane magnetic field to the device. If the sample is clean enough, electrons inside the device effectively form orbits and localize, resulting in an insulating bulk. However, electrons along the edges of the device form one-dimensional chiral edge states that disfavor backscattering, resulting in longitudinal $R_{xx} \approx 0$ (Fig. 2.7). R_{xy} measurements using contacts on opposite sides of the device also result in quantized resistance $R_{xy} = \frac{h}{Ce^2}$ where C is an integer representing the number of edge states and is also related to the topology of the system. The number of edge states depends on both magnetic field B and the density of electrons in the system n . This effect is called the integer quantum Hall effect.

The explanation for this behavior results from the quantized energy levels that result from electrons in cyclotron orbits, which in the case of quadratic bands is

$$E = \hbar\omega_c(N + 1/2) \quad (2.3)$$

where $\omega_c = eB/m^*$, m^* is the effective mass, and N is an integer. In monolayer graphene, due to the Dirac cone dispersion, the equivalent equation is

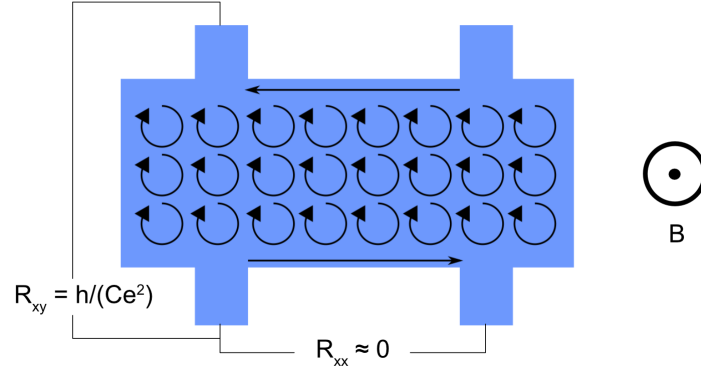


Figure 2.7: Demonstration of the resistance measured in a 2D system at high enough magnetic fields to display the quantum Hall effect.

$$E = \hbar\omega_D \text{sgn}(N)\sqrt{|N|} \quad (2.4)$$

where $\omega_D = v_F\sqrt{2eB/\hbar}$ is the cyclotron frequency for Dirac bands. As the Fermi energy is changed in the system, these energy levels (called Landau levels) are filled sequentially. For a schematic, see Fig. 2.8a. When the Fermi energy is placed on a Landau level, there is a high density of states that allows for conduction of electrons and quick filling of the Landau level. However, when in the gap between the Landau levels, the quantum Hall effect picture described above causes electrons in the bulk to localize while edge states dominate the transport. Thus, oscillations in R_{xx} are seen as a result of tuning the either electron density n (which fills sequential Landau levels) or the spacing of the Landau levels through B . The resulting trajectory of Landau level gaps in n - B parameter space is represented in the following simple relationship

$$\frac{n}{n_0} = C \frac{\phi}{\phi_0} \quad (2.5)$$

where $n_0 = 1/A$ is a normalization factor involving area A that is ultimately canceled out, $\phi = B \cdot A$ is the magnetic flux, $\phi_0 = h/e$ is the magnetic flux quantum, and C is the integer factor mentioned above. When both n and B can be tuned while measuring R_{xx} , a fan-like diagram results (Fig. 2.8b, c). Each Landau level gap has a slope corresponding to h/Ce , and the values of C present depend on the degeneracy of the system. For a monolayer of graphene, C takes the values $\pm 4(N + 1/2)$ with $N = 0, 1, 2, \dots$, or a sequence of $\pm 2, \pm 6, \pm 10$, etc. (Fig. 2.8b). The factor of

$1/2$ in the equation is unique to graphene and results from the π Berry phase [59, 60]. A bare Bernal bilayer of graphene returns $C = \pm 4N$ where $N = 1, 2, 3 \dots$, or a sequence of $\pm 4, \pm 8, \pm 12$, etc. In both cases, the separation of C values by 4 represents the fourfold spin and valley degeneracy. It is also important to note that the origin of the fans is at the base of the band, where the band is unfilled. In the case of graphene that is the charge neutrality point at $n = 0$. Often, intermediate Landau levels are seen at large magnetic fields, due to the magnetic field breaking the degeneracies of the system.

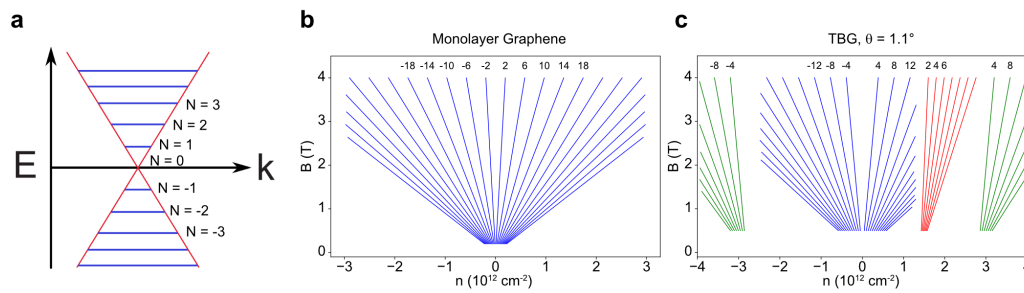


Figure 2.8: Schematic Landau level energy and fan diagrams. (a) Energy structure of Landau levels in a Dirac cone. The spacing between the Landau levels can be changed with magnetic field, and electron density tunes the Fermi level up or down. (b) Example Landau fan schematic for monolayer graphene. (c) Example Landau fan schematic for TBG at $\theta = 1.1^\circ$, showing the fan originating from the dispersive bands after full filling (green) and a fan originating from half filling with a degeneracy of 2.

TBG fan diagrams are slightly more complex because most often one of two cases prevails.

1. Naively, TBG is just two separate sheets of monolayer graphene. If interlayer coupling is relatively small, which is the case in large-angle TBG, the degeneracy from the added layer leads to twice the indices of monolayer graphene, or a sequence of $\pm 4, \pm 12, \pm 20$, and this is observed in TBG with twist angle 1.8° [61], for example.
2. When the twist angle of TBG is reduced to near the magic angle or below, there are a few more considerations. The expected picture should be very similar to the case above since, despite strong interlayer coupling, there is still a supposed eight-fold degeneracy of spin, valley, and mini-valley. However, a

four-fold degenerate sequence matching Bernal bilayer graphene is generally seen experimentally [20, 43], likely due to an instability to strain effects [62]. The main way to tell TBG apart from Bernal bilayer graphene is through the satellite fans originating from the fully filled bands at 4 electrons or holes per moiré unit cell and possibly from 2 electrons or holes per moiré unit cell or other correlated insulator states. Interestingly, when fans are visible at 2 electrons per moiré unit cell, the sequence has two-fold degeneracy: ± 2 , ± 4 , ± 6 , etc. See Fig. 2.8c for an example schematic with both full-filling satellite fans and a fan from positive half filling.

Finally, if electron density n is hard to determine, it is useful to measure the frequency of the oscillations as B is varied with constant n . Usually these oscillations in $R_{xx}(B)$ are referred to as Shubnikov-de Haas (SdH) oscillations, and they can be measured even before the quantization in the quantum Hall effect sets in. The important relationship is [6]

$$\Delta\left(\frac{1}{B}\right) = \frac{2\pi e}{\hbar A_F} \quad (2.6)$$

where A_F is the Fermi surface area, and $\Delta(1/B)$ is the period of oscillations. The common way to measure the Fermi surface area involves taking the Fourier transform of R_{xx} measurements represented in the variable $1/B$, leading to frequencies $f_{1/B} = \frac{\hbar A_F}{2\pi e}$. For the case of an isotropic 2D Fermi surface, $A_F = \pi k_F^2$, and $k_F^2 = 4\pi n/g$, where g is the degeneracy of the bands. This leads to $n = (ge/h)f_{1/B}$, which will be referred to again in Section 6.3.

2.3 Dilution fridge setup and electronics

In this thesis, nearly all the measurements have been performed in our bottom-loading Oxford Triton dilution fridge (Fig. 2.9). The dilution fridge uses a multi-stage cooling system, with the final stage utilizing a pumping action on a mixture of He^3 and He^4 isotopes to reach a base temperature of about 20–25 mK. The plate containing the mixture, and thus the lowest temperature stage, is the mixing chamber plate. The fridge is equipped with 48 DC lines and a uniaxial superconducting magnet that can reach up to 8 T. Since the base temperature is in a sort of equilibrium point for the fridge—where no extra heaters have to be applied—and since the low temperatures are generally favorable for measurements, data reported here is generally taken at the base temperature unless otherwise stated.

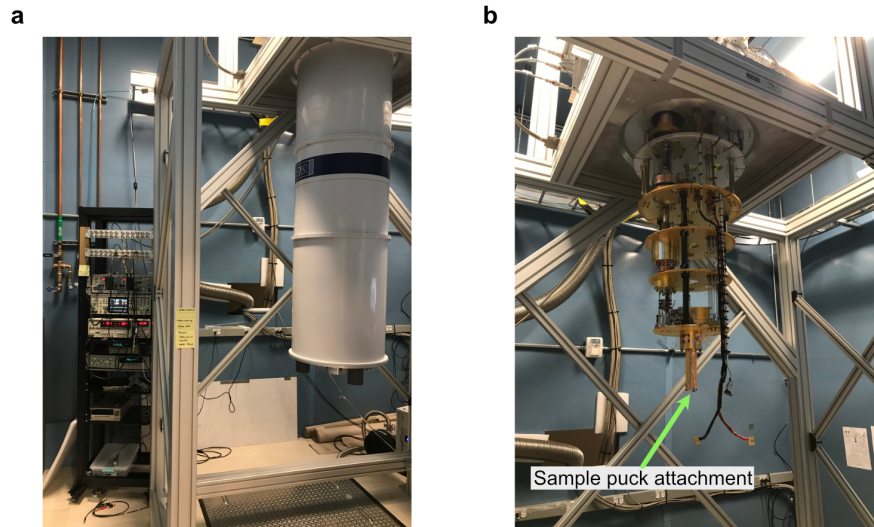


Figure 2.9: Figures showing the Oxford Triton with all the thermal shields on (a), and showing the plates at each temperature stage (b).

Our dilution fridge uses multiple temperature stages, with fully-encapsulating shields thermally anchored to each stage, to minimize heat transfer through thermal radiation. However, one source of radiation still needs to be suppressed: transmission through the wires to the device [63]. Unless filtering is applied, the electron temperature will be significantly higher than the base temperature of the fridge. For DC measurements taken below kHz frequencies, the general approach involves repeated thermalization steps and low-temperature passive filtering of frequencies outside of the range used.

For the filtering used on our fridge, we largely followed the setup of Ref. [64], although we did not implement high-frequency filtering beyond the π and RC filters. Our setup has been thermalized by first installing an extra 5 m of constantan (a copper-nickel alloy with low thermal conductivity) twisted pair cables (in addition to ~ 2 m already installed), which is wound around and glued with GE varnish onto oxygen-free copper cylinders that are bolted to each stage of the fridge. The slightly resistive nature of the constantan wires ($\sim 66 \Omega/\text{m}$) causes a small amount of attenuation at each stage.

For high-frequency filtering, we first used three different passive π filters in series, which filter out bands of 200 MHz–4 GHz (Mini-circuits LFCN-80+), 2–7 GHz (LFCN-1400+), and 7–18 GHz (LFCN-5000+). Since the stop-band range of the LFCN-80+ is where many modern microwave electronics transmit, we included two

π filters of that range for each line. Then, we used a two-pole RC filter, consisting of 1 k Ω resistors cylindrical MELF-type resistors known to retain resistivity to low temperatures and 1–10 nF C0G/NP0 ceramic capacitors. Most lines use 1 nF capacitors, resulting in a low-pass cutoff frequency of about 159 kHz, whereas a few lines use 10 nF capacitors, resulting in a cutoff frequency of about 16 kHz. Since devices measured, the lines, and current-limiting resistors add extra resistivity to the circuit and consequently increase the time constant of the filters, this range allowed for noise filtering with reasonable time constants. The components for each of the 48 lines were arranged on surface-mount PCBs enclosed in custom-made gold-plated oxygen-free copper boxes attached to the mixing chamber plate (Fig. 2.10). Each PCB was supplied with plenty of grounding/thermalization anchors through screws to the copper boxes. Between the filtering boxes and the connection to the sample puck, the wires were protected with copper braiding and copper plates. Additional VLFX-80+ π filters were added between the room-temperature electronics and the fridge for further filtering.

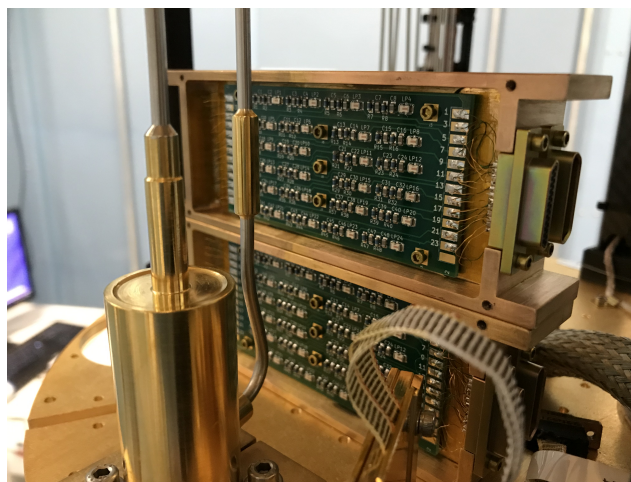


Figure 2.10: Picture of the filter boxes (lids are also placed over the PCBs) loaded onto the mixing chamber plate.

The sample PCB is loaded into an encapsulated puck, shown in Fig. 2.11. Parts were fabricated out of oxygen-free copper and coated with gold to thermalize the sample and position it such that an out-of-plane magnetic field can be applied. An additional piece was constructed for holding the sample in an in-plane magnetic field orientation.

For the vast majority of measurements, lock-in amplifiers were used, specifically Stanford Research models 830 and 865a. Frequencies of 7–20 Hz allowed for the

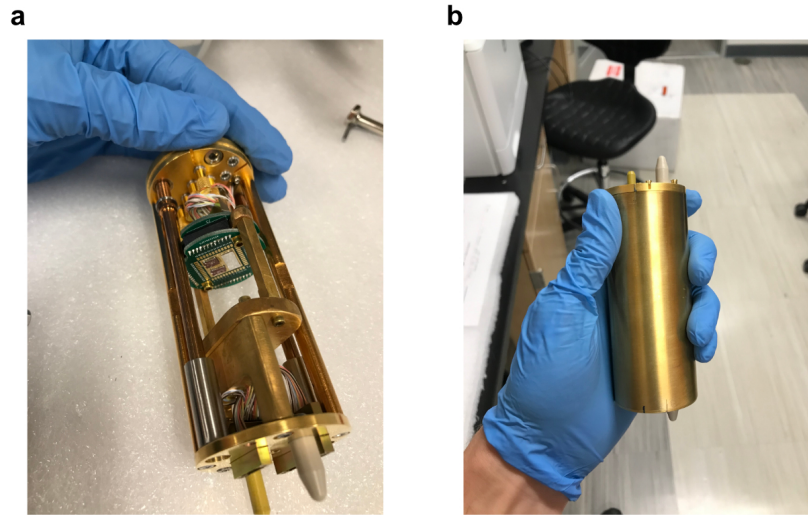


Figure 2.11: Pictures of the sample puck open, showing the PCB in the out-of-plane field orientation (a), and closed (b).

low-noise filtering that lock-in amplifiers can provide while remaining in the DC limit. Generally, in graphene samples, 0.5–1 nA was used, maintained by a series 30 k Ω –10 M Ω resistor added to the line. Gate voltages were supplied by Stanford Research SIM928 battery-supplied isolated voltage sources, and occasionally these sources provided offset biases that, when added with a summing amplifier (Stanford Research SIM980), allowed for dV/dI measurements.

SUPERCONDUCTIVITY STABILIZED IN TWISTED BILAYER GRAPHENE-WSE₂ HETEROSTRUCTURES

Twisted bilayer graphene (TBG) around the magic angle of $\sim 1.1^\circ$ is now well known for exhibiting a rich phase diagram of correlated insulating, superconducting, ferromagnetic, and topological phases [20, 43, 44, 65–67]. While these phases have been further studied for a number of devices with both electrical transport measurements [45, 47–50, 52, 68–70] and scanning probe measurements [10, 14, 54, 57, 71–75], the origins, interplay, and specific symmetry breaking mechanisms of the phases are still elusive, particularly for the superconducting state. We modified the traditional TBG heterostructure by picking up TBG with a monolayer of tungsten diselenide (WSe₂), widely known to proximitize spin-orbit coupling into monolayer [28, 29, 76] and bilayer graphene [32, 77], in order to study which phases are stabilized and which are suppressed. To our surprise, the superconducting phase is stabilized and persists when correlated insulating states disappear, and even as the non-correlated moiré-induced gaps disappears. This contrasts with the standard picture, where superconductivity and correlated insulators have been observed only for angles within $\pm 0.1^\circ$ from the magic-angle value of 1.1° .

3.1 Twisted bilayer graphene picked up with WSe₂

To get an idea of why changing the surrounding layers of graphene could be beneficial for studying TBG, we point out that the physics of the correlated phases in TBG is already known to be strongly affected by the dielectric environment. In particular, since insulating hexagonal boron nitride (hBN) and graphene exhibit similar crystal lattices, the relative alignment between the hBN and TBG is critical. For example, a ferromagnetic state near $\nu = +3$ was observed in devices where hBN aligns with TBG [66, 67]. However, in such devices the band structure of the flat bands is strongly altered [67], and superconductivity—typically observed when hBN and TBG are misaligned—is absent. Recent work using a very thin hBN layer separating a back gate from TBG additionally suggests that electrostatic screening plays a role in the appearance of insulating and superconducting states [47] (see also Ref. [48]). These experiments exemplify the effects of hBN layers on the phase diagram in hBN-TBG-hBN structures and highlight the importance of understanding how microscopic details of the dielectric environment alter the properties of correlated phases.

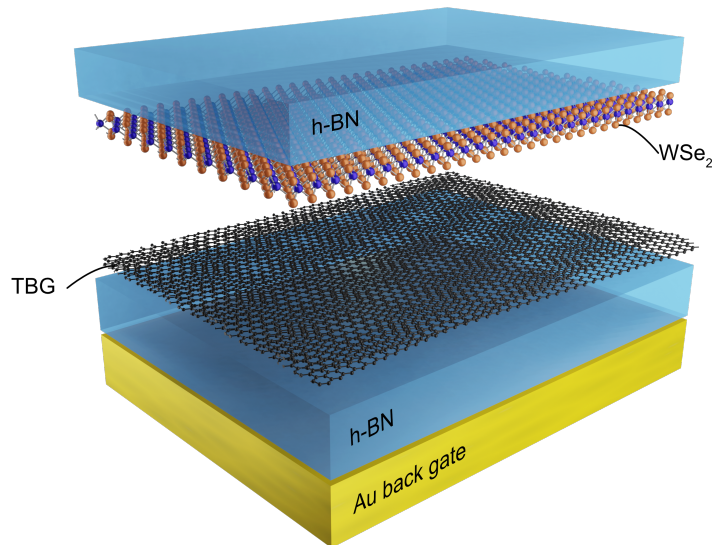


Figure 3.1: A schematic model of the devices studied in this chapter and the next, TBG picked up with WSe_2 and encapsulated in hBN.

Here, instead of the usual hBN-TBG-hBN structures, we investigate devices made from hBN-TBG- WSe_2 -hBN van der Waals stacks in which a monolayer of WSe_2 resides between the top hBN and TBG (Fig. 3.1). The WSe_2 has been grown by the groups of X. Xu and J.-H. Chu [46]. Like hBN, flakes of transition metal dichalcogenides, such as WSe_2 , can be used as high-quality insulating dielectrics for graphene-based devices [78]; however, the two van der Waals dielectrics differ in several ways that may alter the TBG band structure. First, unlike hBN, the WSe_2 and graphene lattice constants differ significantly (0.353 nm for WSe_2 and 0.246 nm for graphene, Fig. 3.2). This mismatch implies that the moiré pattern formed between TBG and WSe_2 has a maximum lattice constant ~ 1 nm—much smaller than that formed in small-angle TBG (> 10 nm). Second, it is well-established that WSe_2 can induce a spin-orbit interaction (SOI) in graphene via van der Waals proximity [29, 32, 76, 77]. And finally, due to hybridization effects, WSe_2 may also change both the Fermi velocity of the proximitized graphene sheet and the system’s phonon spectrum, although we have not found direct evidence of these changes so far. We chose to use monolayer WSe_2 in particular because of its large band gap [79] that allows applying a large range of gate voltages. It has also been suggested previously that a monolayer induces larger spin-orbit coupling in graphene compared to few-layer WSe_2 [29].

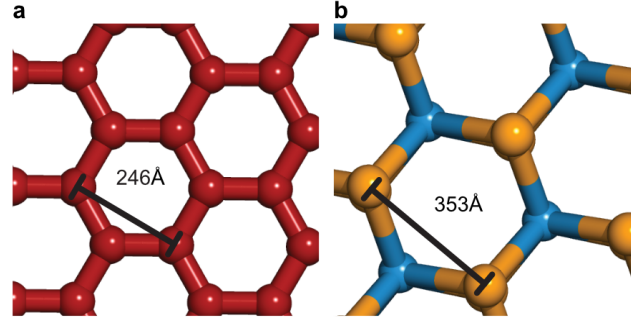


Figure 3.2: Ball and stick models for the graphene (a) and WSe₂ (b) crystals, viewed from the top for size comparison. Shown is the lattice constant for each crystal.

3.2 Superconductivity in devices with twist angles as low as 0.79°

We have studied four TBG-WSe₂ devices and concentrate mostly on two of them (see Fig. 3.10 and Fig. 3.11 for data from two additional devices). Optical images of the four devices are shown in Fig. 3.3. The device bottom hBN thicknesses for D1, D2, D3, and D4 are 62 nm, 40 nm, 48 nm, and 56 nm, respectively. All four devices were stacked and then placed on pre-defined Au back gates (orange area in Fig. 3.3). D4 differs from the other devices since it features monolayer WSe₂ on both the top and bottom of the device. Surprisingly, we find robust superconductivity in all studied TBG-WSe₂ structures, even for twist angles far outside of the previously established range.

Fig. 3.4 shows a representative phase diagram of longitudinal resistance R_{xx} with respect to temperature and moiré filling factor ν . ν represents the number of electrons per moiré unit cell, and negative ν represents holes per moiré unit cell. Due to the spin and valley degeneracy (fourfold degeneracy), there is an expected band gap at $\nu = \pm 4$.

The conversion from backgate voltage to filling factor ν relies on the determination of the twist angle, and the details of the twist angle determination are important to our claims. First, note that the Moiré unit cell depends on the twist angle according to 1.17 (where we have simplified using the small-angle approximation)

$$A_M \approx \frac{\sqrt{3}a^2}{2\theta}. \quad (3.1)$$

Since $\nu = 4$ corresponds to a fully filled moiré unit cell, we can derive the twist angle θ by relating the electron density at full filling to the moiré unit cell area $n_{\text{full}} = 4/A_M$, which results in

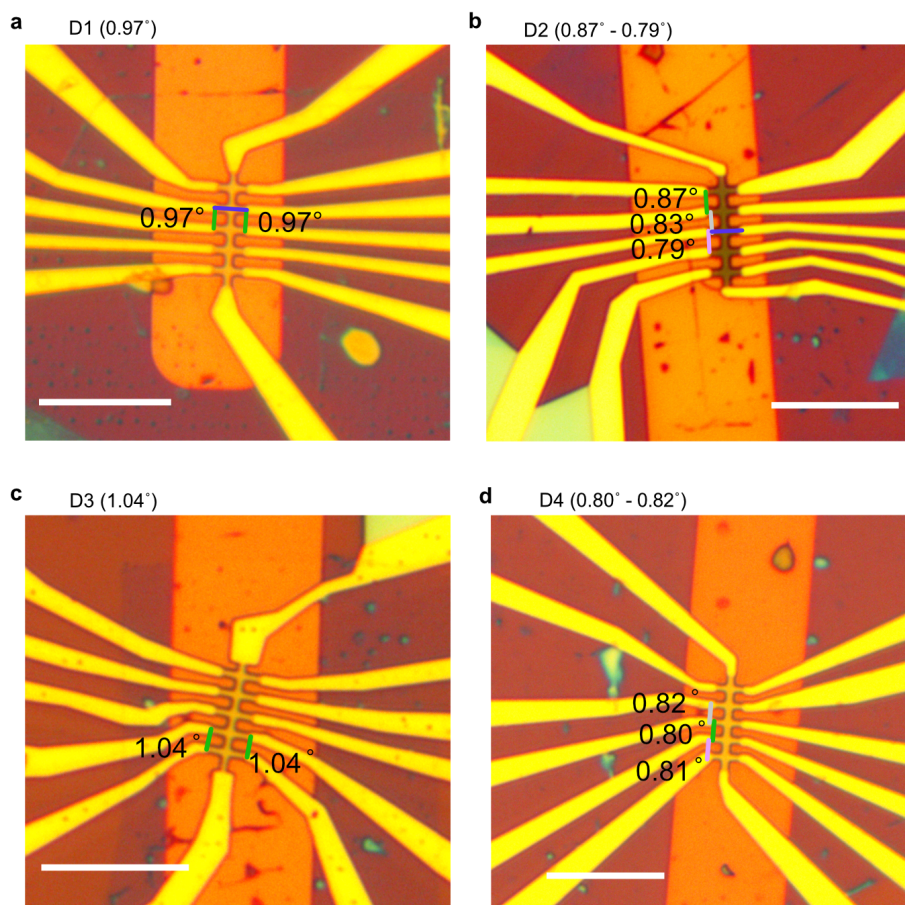


Figure 3.3: Optical images of devices D1–D4. Electrodes that are used in the measurements and corresponding twisted angles are labeled for each device. The ones marked with blue lines are used for measuring Hall conductance in Fig. 3.13. The scale bar in each panel corresponds to $15 \mu\text{m}$.

$$\theta^2 \approx \frac{\sqrt{3}a^2}{8}n_{\text{full}}, \quad (3.2)$$

where $a = 0.246 \text{ nm}$ is the lattice constant of graphene, and θ is in radians. n_{full} can be determined roughly by using the geometric capacitance between the gate and graphene of $C = \epsilon_r \epsilon_0 / d$, where C is the capacitance per unit area, $\epsilon_r \approx 3$ is the dielectric constant of hBN, and d is the bottom hBN thickness (determined optically or using atomic force microscopy). Then the backgate voltage applied can be converted to electron density with $n = CV_{bg}$. When the x-axis of a plot such as Fig. 3.4 has been converted to density, the position of the full-filling insulators can be roughly determined, which gives us n_{full} .

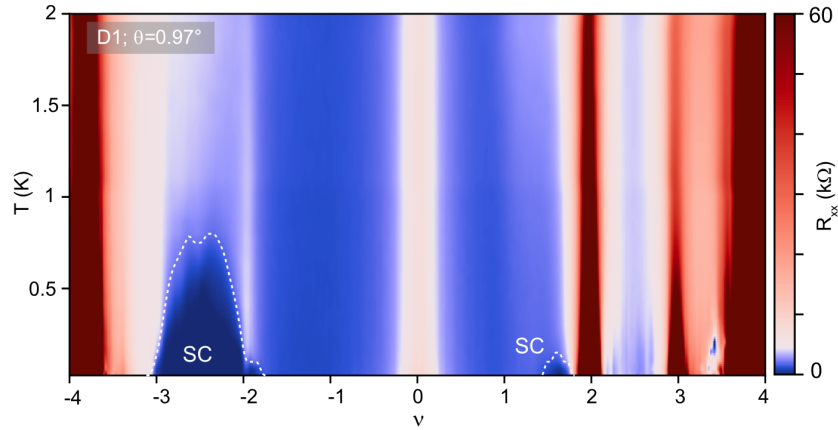


Figure 3.4: The R_{xx} plot recorded vs. temperature and ν for device D1 at 0.97° .

However, this only roughly determines the twist angle, and using Landau levels is much more accurate. Landau fan diagrams plotted as R_{xx} oscillations vs. V_{bg} and magnetic field B allow us to accurately determine, first, the backgate capacitance by fitting lines to the resistance minima about $\nu = 0$ that make up the Landau level sequence of TBG. This avoids the problem of the approximate ϵ_r value of hBN and inaccuracy in thickness determination. Then, fitting lines to Landau fans originating from the full-filling points (and optimally also from half-filling insulators) allow extrapolation to n_{full} , ultimately resulting in twist angle accuracy of about $0.01\text{--}0.02^\circ$.

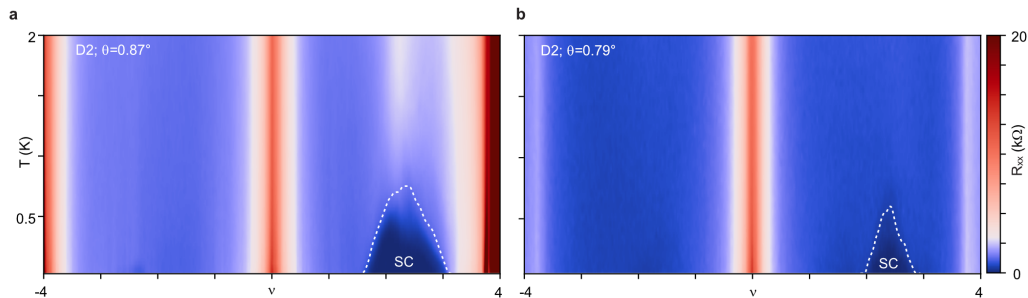


Figure 3.5: R_{xx} vs. T and ν for measured contact pairs with 0.87° (a) and 0.79° (b) twist angles.

For device D1, $\theta = 0.97^\circ$, a superconducting pocket emerges on the hole side near $\nu = -2$ with a maximal transition temperature $T_c \approx 0.8$ K. To our knowledge, this is the smallest angle for which superconductivity has been reported for hole doping. Careful inspection reveals another weak superconductivity pocket close to $\nu = +2$.

However, despite the small twist angle—falling outside the $\theta_M \pm 0.1^\circ$ range—the observed phase diagram resembles that of regular high-quality magic-angle hBN-TBG-hBN structures [20, 44]. Evidence of correlated insulators are also present in this device, visible as resistance peaks at $\nu = 2, 3$ and will be discussed more below.

Fig. 3.5 shows the temperature dependence of resistance over two TBG regions corresponding to angles $\theta = 0.87^\circ$ and $\theta = 0.79^\circ$; in both cases superconducting transitions are clearly visible, this time only on the electron side. The transition temperatures are $T_c \approx 600$ mK and 380 mK, respectively. Aside from the drop in longitudinal resistance (R_{xx}) to zero, it helps to have another tool for confirming the superconductivity. Otherwise, the resistance drop could possibly be explained by a phase transition to a low-resistance state [80]. In three-dimensional superconductors, one may measure the Meissner effect, or the expulsion of magnetic fields, but this is more difficult in a system consisting of two atomic layers (so very small magnetization) and that is potentially prone to vortices and other modulations or defects in the ideally uniform superconducting area.

Measurements of resistivity under a DC bias current and at a range of magnetic fields serve as a useful tool since they can reveal the robustness of the superconducting phase to magnetic field and phase coherence effects that manifest as oscillations as the magnetic field changes. These phase-coherent oscillations are reminiscent of a Josephson junction where two superconducting electrodes, decoupled by a non-superconducting element, exhibit predictable magnetic field oscillations. For an ideal rectangular geometry, the oscillations have a characteristic Fraunhofer pattern (similar to the pattern seen by diffracting light through a slit). Thus we call the diagrams Fraunhofer-like patterns, and we display the plots for three mentioned twist angles in Fig. 3.6. These are qualitatively similar to the typical hBN-TBG-hBN devices [20, 43, 44]. The shape is diamond-like, representing a finite phase space in DC bias current and magnetic field where superconductivity exists, and it exhibits small oscillations. In our devices, we typically see periods of 1.5–3 mT. If interpreted as an effective junction area, where oscillations are periodic in $B = \Phi_0/A$, where $\Phi_0 = h/2e$ is the superconducting flux quantum, and A is the junction area, we obtain $A \sim 0.67\text{--}1.33 \mu\text{m}^2$, consistent with the length scale of the device geometry. Josephson Junction behavior likely occurs when the superconductivity in the devices has some inhomogeneities, and more distinct oscillations are observed by measuring the patterns at ν closer to the edge of the superconducting regions [20]. Fig. 3.7 shows Fraunhofer-like patterns for D1 at other filling factors. Panel (a) shows what

a Fraunhofer-like pattern looks like for the weak superconductivity found on the electron side, and panel (b) shows more distinct oscillations due to being closer to the edge of the superconducting range.

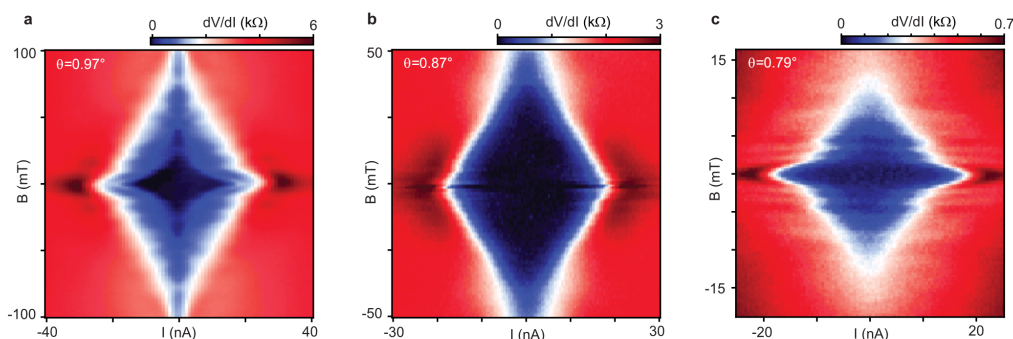


Figure 3.6: Fraunhofer-like patterns for the 0.97° region at $\nu = -2.4$ (a), 0.87° region at $\nu = 1.96$ (b), and 0.79° region at $\nu = 2.3$.

3.3 Disappearing correlated insulators and full-filling gaps at low twist angles

Starting at 0.97° , the presence of robust correlated insulating states observed at filling factors $\nu = +2, +3$ allows for further analysis based on the higher-temperature data shown in Fig. 3.8. As seen in panels (a),(b), the mentioned correlated insulators have an exponentially increasing resistance below a few Kelvin. However, small resistance peaks seen at other filling factors are less developed and do not show insulating behavior (Fig. 3.8c). Measurement of the activated gaps, explained in more detail below, determines the correlated insulator gaps to be $\Delta_{+2} = 0.68$ meV and $\Delta_{+3} = 0.08$ meV (see Fig. 3.9f).

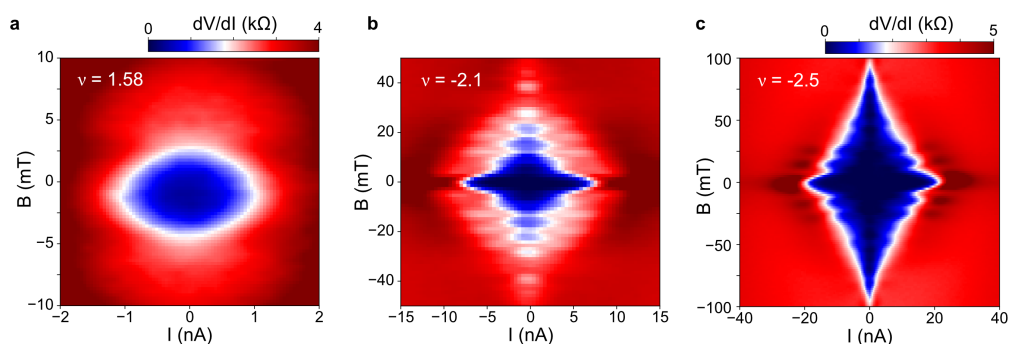


Figure 3.7: Additional data from device D1 (0.97°). (a) Fraunhofer-like pattern for electron doping, at $\nu = 1.58$. (b), (c) Additional Fraunhofer-like pattern for hole doping, $\nu = -2.1$ (b), and $\nu = -2.5$ (c).

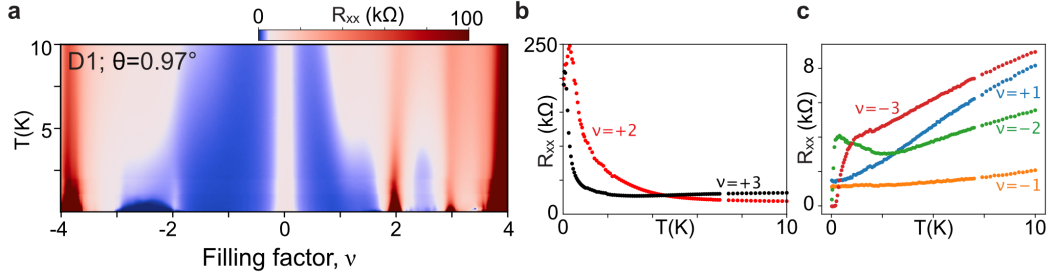


Figure 3.8: Additional temperature data for device D1 (0.97°). (a) R_{xx} as a function of ν and Temperature up to 10 K. (b) Temperature dependence of R_{xx} for $\nu = 2$ and $\nu = 3$ showing insulating behaviour. (c) At other partial integer filling factors R_{xx} increases with temperature, consistent with metallic behavior.

Although superconductivity persists for all three angles, the correlated insulators are quickly suppressed as the twist angle is reduced. This suppression is not surprising, as for angles below θ_M , the bandwidth increases rapidly and, moreover, the characteristic correlation energy scale $e^2/4\pi\epsilon L_m$ also diminishes due to an increase in the moiré periodicity $L_M = a/2 \sin(\theta/2)$ [10, 11, 65, 71–73]. For the lower angle of $\theta = 0.87^\circ$ correlated-insulating behavior is heavily suppressed at all filling factors. In Fig. 3.5a, a peak in longitudinal resistance versus density is visible only around $\nu = +2$ above the superconducting transition. Data for a larger temperature range (Fig. 3.9a,b) shows that the resistance peak near $\nu = +2$ survives up to $T = 30$ K, and also reveals a new peak near $\nu = +1$ in the temperature range 10–35 K. These observations suggest that electron correlations remain strong, though the corresponding states appear to be metallic as the overall resistance increases with temperature. The decreasing resistivity with T is in contrast to the correlated insulators observed in the 0.97° device (Fig. 3.9f).

Fig. 3.9e shows fitting for activation gaps at full filling for 0.87° with dark black/blue dots. The log conductivity (σ) vs. $1/T$ plot allows for linear fitting to exponential behavior of the form $\sigma \propto e^{-\Delta/2k_B T}$, shown with green lines (the same fit is applied to the 0.97° correlated insulators in panel f). At low temperatures (high $1/T$), however, the conductivity is known to saturate due to variable-range hopping, which takes the form $\sigma \propto \exp[-(T_0/T)^{1/3}]$ [61]. The red dotted lines show the fit to a model that includes both behaviors. For this angle, we measure activation gaps at full filling (i.e., at $\nu = \pm 4$) of $\Delta_{+4} = 8.3$ meV and $\Delta_{-4} = 2.8$ meV (the red line fits give 9.4 meV and 3.7 meV, respectively)—far smaller than the gaps around θ_M (for example, see Fig. 3.10 for full-filling gaps of $\Delta_{+4} = 29.2$ meV and $\Delta_{-4} = 21.1$ meV and also

activated behavior for correlated states at $\nu = \pm 2$). The trend represented in our devices at low twist angles is in line with previous results that report a disappearance of the band gap separating dispersive and flat bands at around $\theta = 0.8^\circ$ [81, 82]. This full-filling gap behavior also informs the interlayer tunneling parameters we used in our continuum model Hamiltonian $w_{AA} = 55$ meV and $w_{AB} = 105$ meV, as the gaps close near 0.8° as seen in Fig. 1.9, yet the magic angle is still in the range of $1\text{--}1.1^\circ$.

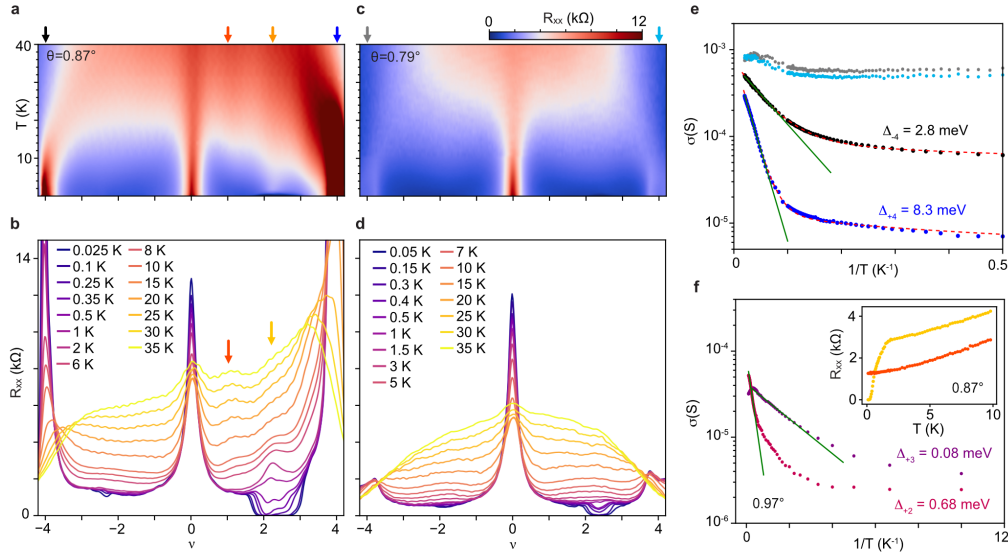


Figure 3.9: Larger-temperature-range data showing R_{xx} as a function of filling factor ν , for $\theta = 0.87^\circ$ (a), (b) and $\theta = 0.79^\circ$ (c), (d). Line cuts shown in (b) are taken from the same data set as (a), and line cuts shown in (d) are taken from (c). (e) Conductance vs. $1/T$ for full filling $\nu = \pm 4$ extracted from the data in (a) (blue and black) and (c) (cyan and gray). The behavior for $\theta = 0.79^\circ$ shows much smaller variation in temperature. (f) Conductance vs. $1/T$ for partial filling factors $\nu = +2, +3$ (shown with activated gap measurements) for 0.97° showing insulating behavior. In contrast, the inset shows that for 0.87° , partial fillings $\nu = 1, 2$ show metallic behavior.

Measurements at the smallest twist angle, $\theta = 0.79^\circ$, particularly confirm the full-filling gap trend. Along with the lack of insulating states at any partial filling, the resistance at full filling is even more reduced (Fig. 3.9c,d). The relatively low resistances < 2 k Ω , measured at full filling—which are less than 15% of the resistance at the charge neutrality point (CNP)—suggest a semi-metallic band structure around full filling, consistent with theoretical expectations for TBG at $\theta = 0.79^\circ$ [81] and the resistivity of a dilute 2D electron gas [83]. Surprisingly, despite the complete absence of both full-filling band gaps and correlated insulators, the

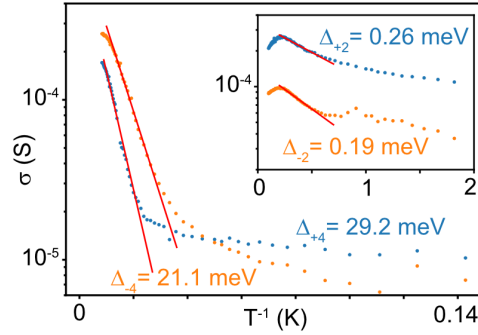


Figure 3.10: Activated gap measurements for the $\nu = \pm 4$ full filling gaps in device D3 at 1.04° . The higher temperatures required for this measurement were enabled by measuring this sample in a Quantum Design PPMS system with continuous temperature regulation from 1.7–300 K. Inset: activated gap measurements of the correlated states at $\nu = \pm 2$.

superconducting low-resistance pocket near $\nu = +2$ is clearly resolved (Fig. 3.5b, Fig. 3.6c).

We have also reproduced the finding in another device at a twist angle of 0.80° . Despite having a slight change in geometry, with WSe_2 on both top and bottom of TBG, we observe resistance at full-filling that is less than at the CNP, and superconductivity is found on the electron side (Fig. 3.11a). Fig. 3.11b shows another measurement commonly performed on two-dimensional superconductors. The dotted line marks the point where the I-V curve matches $V_{xx} \propto I^3$, which is known as the BKT (after Berezinskii, Kosterlitz, and Thouless) transition temperature, and is seen here near 250 mK. Fig. 3.11c shows the Fraunhofer-like pattern, further confirming superconductivity.

Both the disappearance of the correlated insulators and the vanishing gap between flat and dispersive bands for low angles suggest that the additional WSe_2 monolayer does not significantly change the magic angle (on the scale of angles considered here). Since superconductivity survives at much lower angles than the correlated insulating states, our observations strongly suggest the two phenomena have different origins [47, 48]. Note also that the close proximity of the dispersive bands does not seem to have a major impact on the superconducting phase. Our findings of superconductivity in TBG with metallic band structure put strong constraints on the proposed theoretical explanations and are the main result of this work. For example, our observations are in contrast with scenarios wherein superconductivity descends from a Mott-like insulating state as in high- T_c superconductors [7]

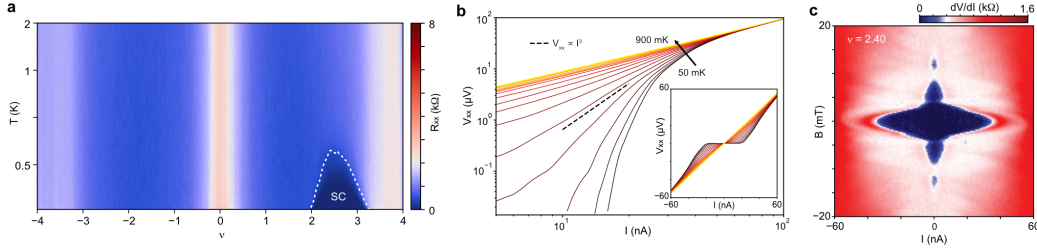


Figure 3.11: Additional data for device D4 (0.80°). (a) R_{xx} as a function of ν and temperature to 2 K, revealing a superconducting pocket over the range of $2 < \nu < 3.2$ and resistance at full filling ($\nu = |4|$) less than at the charge neutrality point. (b) Current vs. voltage at $\nu = 2.79$, at temperatures from 50 mK to 900 mK, in 50 mK steps. The main plot is on the log scale in both axes, revealing a BKT transition temperature near 250 mK. Inset: I-V dependence for the same temperatures. (c) Fraunhofer-like pattern for D4 at $\nu = 2.40$.

and more consistent with phonon-only mediated superconductivity [84–86]. We emphasise, however, that electron correlations may still prove important for the development of superconductivity. For instance, even for the smallest angle of $\theta = 0.79^\circ$, the superconducting pocket is seemingly pinned to the vicinity of $\nu = 2$. Additionally, as shown in Fig. 3.9, at higher temperatures residual R_{xx} peaks can still appear at certain integer filling factors despite the absence of gapped correlated insulating states. It is thus hard to rule out the possibility that superconductivity arises from correlated states of metallic nature that may be present at smaller angles and near integer values of ν in analogy to other exotic superconducting systems [87–89].

3.4 Weak antilocalization measurements in TBG-WSe₂

Measurements in finite magnetic field reveal further insights into the physics of TBG-WSe₂ structures. First, in small fields we observe a conductance peak at $B = 0$ mT, indicative of weak antilocalization (WAL) and consequently the presence of strong SOI. Previous works established that WSe₂ can induce large SOI into monolayer and bilayer graphene [29, 32, 77], and hence the generation of SOI in the proximitized layer of TBG is expected. In Fig. 3.12c, we see the WAL peak’s development in the flat bands as the temperature is lowered from 700 mK to 25 mK. Each peak is taken by averaging over a small range of gate voltages (shown in Fig. 3.12a, b, colored dots), which averages out the noise due to mechanisms such as universal conductance fluctuations [90]. The data taken at 900 mK—where the WAL peak has disappeared—has been subtracted from experimental points at other

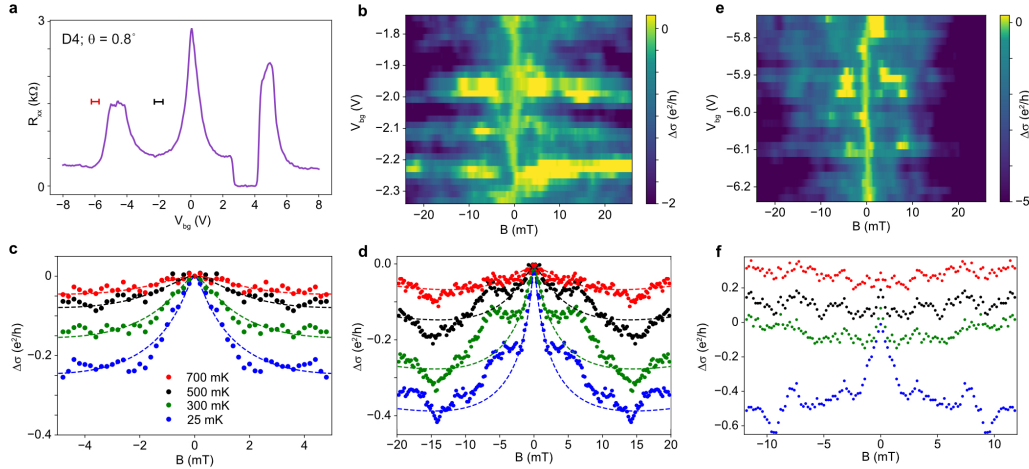


Figure 3.12: WAL data measured in D4 ($\theta = 0.80^\circ$). (a) R_{xx} as a function of backgate voltage, V_{bg} , for the 0.80° contacts of D4. The black line shows the voltage range used in the flat bands, which corresponds to the plots in (b)–(d). The red line, from the dispersive bands, corresponds to plots in (e), (f). (b) The change in conductivity, relative to the 0 mT point, as a function of magnetic field ($\Delta\sigma$) taken at the mentioned range of gate voltage at 25 mK. (c), (d) show averaged data from (b) for different field ranges. The data in (e), (f) show a WAL peak in the dispersive bands near $V_{bg} = -6$ V (red line in (a)). Data in (e) was taken at 25 mK. In (f), the data points at each temperature are offset by $0.1 e^2/h$ for clarity.

temperatures, and the data points have been symmetrized about 0 mT. The peak can be easily missed unless the averaging process mentioned above is performed, and the magnetic field sweeps very slowly.

In order to fit the peaks, we implemented the theory of WAL in monolayer graphene [91] since the low-energy band structure in TBG retains Dirac cones, although they have been flattened. The theory has been previously used in graphene-TMDC heterostructures [29, 90] as well as in bare monolayer graphene on SiO_2 [92]—but in the bare monolayer case, it only occurs close to the CNP and at temperatures > 5 K, ruling out this effect in TBG (since the WAL peaks we observe only occur below 1 K and persist away from the CNP). The relevant equation is

$$\Delta\sigma(B) = -\frac{e^2}{2\pi h} \left[F\left(\frac{\tau_B^{-1}}{\tau_\phi^{-1}}\right) - F\left(\frac{\tau_B^{-1}}{\tau_\phi^{-1} + 2\tau_{asy}^{-1}}\right) - 2F\left(\frac{\tau_B^{-1}}{\tau_\phi^{-1} + \tau_{so}^{-1}}\right) \right] \quad (3.3)$$

where $F(x) = \ln(x) + \psi(0.5 + x)$, ψ is the digamma function, and $\tau_B^{-1} = 4eDB/\hbar$. $D = v_F^2\tau/2$ is the diffusion constant, which is set by the Fermi velocity (in our

case we use $v_F \approx 1 \times 10^5$ m/s, reduced from the monolayer graphene value of 10^6 m/s) and the Drude scattering time $\tau = \frac{\mu m^*}{e} = \frac{\hbar \sigma}{v_F e^2} \sqrt{\frac{\pi}{|n|}}$, which is derived from the effective mass $m^* = \hbar \sqrt{\pi |n|} / v_F$ and measurements of mobility $\mu = \sigma / |n| e$ to be ~ 1.5 ps. Then we are left with three fit parameters: $\tau_\phi, \tau_{asy}, \tau_{so}$. The spin-orbit relaxation time parameters τ_{asy} —which results mostly from Ising-like asymmetric SOI—and $\tau_{so} = (\tau_{asy}^{-1} + \tau_{sym}^{-1})^{-1}$ —which combines symmetric (τ_{sym}) and asymmetric SOI terms—are intrinsic to the system and do not vary with temperature. However, the dephasing parameter τ_ϕ decreases with increasing temperature. Thus, we can constrain the fits by only varying τ_ϕ for curves at different temperatures.

Since there are several fit parameters, and the applicable range of Eq. (3.3) is difficult to determine precisely, two magnetic field ranges are shown, along with their dotted-line fits in Fig. 3.12c, d. Whereas the total spin-orbit scattering time $\tau_{so} \approx 10$ ps better reproduces the low-field data in panel (c), $\tau_{so} \approx 1\text{--}3$ ps captures the saturation at larger fields with asymmetric and symmetric relaxation time ratio (τ_{asy}/τ_{sym}) varying in range 0.3–3. The values of τ_{so} obtained here correspond to SOI energies [93] in the range of 0.5–1 meV. We note that, in the case of TBG, a more detailed analysis with a correct model for describing WAL in TBG is likely required for a more accurate quantitative comparison. Regardless, the WAL peaks are an indication of strong SOI in WSe₂/TBG heterostructures. Finally, we also see evidence of WAL in the dispersive bands, as shown in Fig. 3.12e, f.

3.5 Landau Fans

The second important finding that results from finite magnetic field measurements comes from Landau fan diagram measurements. For all angles measured in our range of $0.79^\circ\text{--}0.97^\circ$ we find that even at modest magnetic fields, above $B = 1$ T, gaps between Landau levels are well-resolved, showing a fan diagram that diverges from the CNP (Fig. 3.13). The slopes of the dominant sequence of R_{xx} minima correspond to even-integer Landau level fillings $\pm 2, \pm 4, \pm 6$, etc.—indicating broken four-fold (spin-valley flavor) symmetry. By contrast, the majority of previous transport experiments [20, 43–45, 47, 48, 54] near the magic angle report a Landau-fan sequence $\pm 4, \pm 8, \pm 12$ at the CNP (see Section 2.2), with broken-symmetry states being only occasionally observed at the lowest Landau level (corresponding to the ± 2 sequence) [44, 54, 66]. In addition to R_{xx} minima corresponding to the gaps between Landau levels, we also measured quantized Hall conductance plateaus with distinct quantization at $\pm 2, \pm 4, \pm 6$, shown in Fig. 3.14. The well quantized plateaus further corroborate the two-fold symmetry and indicate the low disorder in

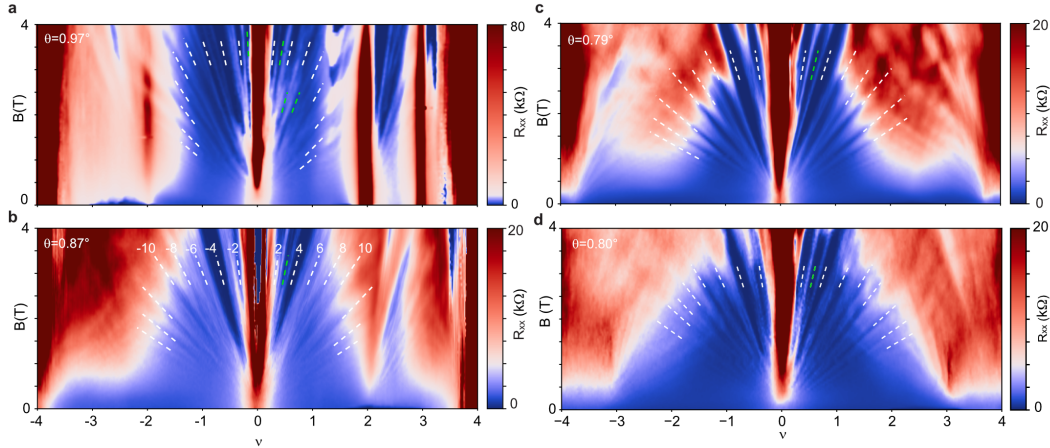


Figure 3.13: Longitudinal resistance R_{xx} as a function of magnetic field and ν for the four regions of twist angle 0.97° (a), 0.87° (b), 0.79° (c), and 0.80° (d). Here the dominant sequence in the Landau fan is $\pm 2, \pm 4, \pm 6, \pm 8, \pm 10$, as labeled in (b). After ± 10 , we find a sequence of $\pm 14, \pm 18$, and ± 22 , which can also be accounted for by the SOI, as shown in Fig. 3.17. These mentioned Landau levels up to ± 22 are marked by white lines in each plot. Additional slopes are found in (a) corresponding to Landau levels $-1, +3, -12$, as well as short segments corresponding to $+5$ and $+7$ that disappear as the field increases. In (b), (c) we find Landau level $+3$, but in (c) $+22$ seems to be missing. The odd levels are all marked with green lines.

the measured TBG areas. Note also that for the smallest angle ($\theta = 0.79^\circ$), we do not observe obvious signatures of correlated insulating states, which are sometime strengthened by magnetic fields, near $\nu = 2$ up to $B = 4$ T.

3.6 Discussion on spin-orbit coupling effects

The observation of additional Landau levels is also consistent with a scenario in which the TBG band structure is modified by SOI inherited from the WSe_2 monolayer. We included spin-orbit coupling in continuum-model calculations by adding a term to the top layer's interlayer Hamiltonian $H_t = H_{t,\text{Dirac}} + H_{t,\text{SO}}$, where the spin-orbit term is

$$H_{t,\text{SO}} = \int d\mathbf{k} \psi_t^\dagger(\mathbf{k}) e^{i\theta\sigma_z/4} \left(\frac{\lambda_I}{2} \tau_z s_z + \frac{\lambda_R}{2} (\tau_z \sigma_x s_y - \sigma_y s_x) + \frac{\lambda_{KM}}{2} \tau_z \sigma_z s_z \right) e^{-i\theta\sigma_z/4} \psi_t(\mathbf{k}). \quad (3.4)$$

The Ising (λ_I), Rashba (λ_R), and Kane-Mele spin-orbit parameters reported in the literature for proximitized SOI in monolayer graphene vary widely in density functional theory calculations [94, 95] and experimental studies [28, 29, 32, 76, 77,

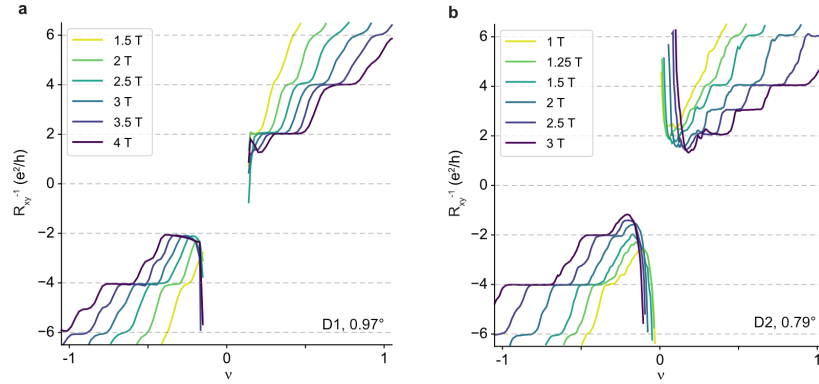


Figure 3.14: Hall conductance for devices D1 ($\theta = 0.97^\circ$, panel (a)) and D2 ($\theta = 0.79^\circ$, panel (b)) showing quantized steps around the CNP with steps corresponding to ± 2 , ± 4 and ± 6 (in units of e^2/h) being pronounced down to 1.5 T. The less developed $3e^2/h$ step has also been observed.

[93]. Ranges given include $\lambda_I \sim 1\text{--}5$ meV and $\lambda_R \sim 1\text{--}15$ meV. The wide ranges are mostly due to the relatively unconstrained parameters when fitting weak antilocalization data. While density functional theory does not predict strong Kane-Mele SOI, some experiments have suggested it could play a role near the CNP [29]. Since both Ising and Kane-Mele terms contribute similarly to the spin relaxation times [93], and the band structure of TBG is more complex in comparison to monolayer and bilayer graphene, it is challenging to distinguish their separate contribution in our weak antilocalization measurements, so we set it to zero. Although spin-orbit parameters have not been studied in TBG, the interfacial nature suggests we can translate the results from monolayer graphene in the way described above.

Fig. 3.15 shows the band structure at the two twist angles of 0.87° (panel (a)) and 0.79° (panel (b)) with $\lambda_I = 3$ meV and $\lambda_R = 4$ meV. These twist angles are sufficiently below the magic angle that Hartree correlations [96] are not expected to warp the bands significantly from their single-particle band structures, and there are no correlated insulating gaps in the system visible in Fig. 3.9. Closer to the magic angle, correlations significantly reconstruct the band structure and likely dominate over the SOI. Nevertheless, the displayed single-particle band structures show that the presence of SOI lifts the degeneracy of both flat and dispersive bands, thereby breaking four-fold spin-valley symmetry. In a finite magnetic field, the resulting Landau levels then descend from two-fold degenerate Kramers states. We emphasise that the fan diagram has been reproduced in multiple samples—including a device with WSe₂ on both the top and bottom (D4, 0.80° , Fig. 3.13d). The latter

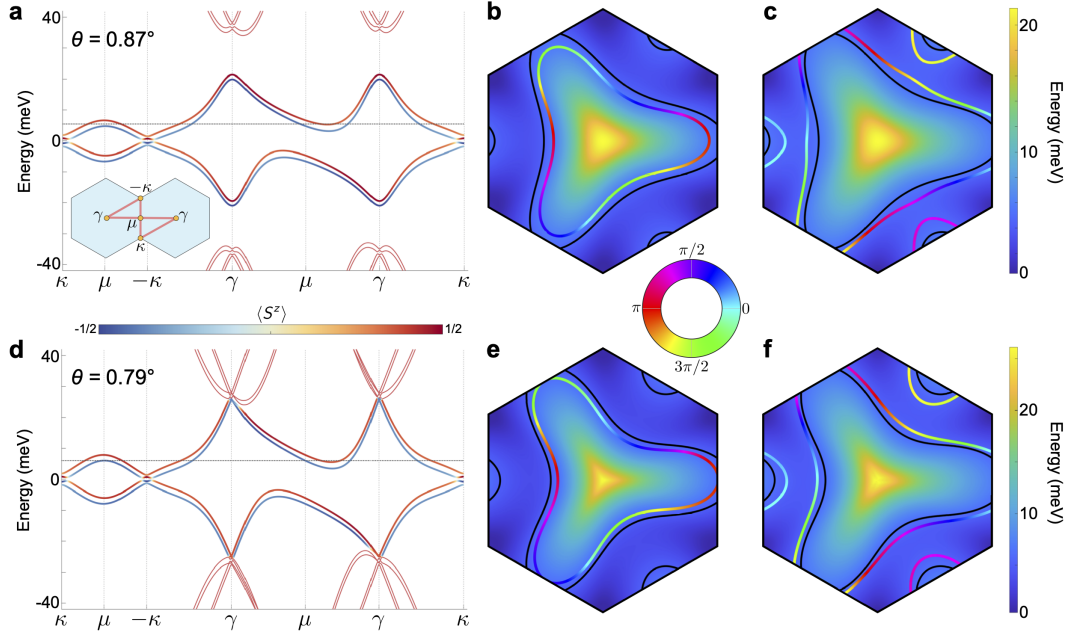


Figure 3.15: Continuum-model results for valley K that include Ising and Rashba spin-orbit coupling at 0.87° (a)–(c) and 0.79° (d)–(f) twist angles. (a), (d) Band structure along the high-symmetry directions of the Brillouin zone indicated in the inset. The line colour represents the out-of-plane spin projection, $\langle S_z \rangle$, and the dotted horizontal line denotes the chemical potential corresponding to $\nu = +2$. (b), (c) and (e), (f) Energy of the upper pair of flat conduction bands, including spin-orbit coupling. Coloured lines show the Fermi surfaces at $\nu = +2$, with the colour indicating the in-plane spin projection. The out-of-plane projection is largely constant along these surfaces and may therefore be deduced from (a), (d). Black lines correspond to the Fermi surface without SOI effects. The large spin-orbit-induced Fermi-surface deformation visible here reflects the flatness of the bands near the Fermi energy.

observation indicates that mirror symmetry breaking by WSe_2 placed on only one side of the TBG does not account for the observed degeneracy lifting. Odd steps—which are not generated by the SOI—are occasionally observed for low angles (green dashed lines in Fig. 3.13). We attribute these steps to additional symmetry breaking, possibly due to correlation effects originating either from flat-band physics or simply a magnetic-field-induced effect (e.g., Zeeman splitting or exchange interaction) at low electronic densities. The band structure is not overly dependent on the details of the SOI, as is explored in Fig. 3.16. Cases where only the Ising term (panel (c)), only the Kane-Mele term (panel (f)), and only the Rashba term (panel (h)) are considered relative to the case without any spin-orbit coupling (panel (a)). When both λ_I and λ_R are non-zero, the Dirac cones at $\pm\kappa$ generate masses. In contrast,

when λ_I , λ_R , λ_{KM} are individually the only non-zero SOI, only the Kane-Mele term results in a gapped spectrum at charge neutrality, as indicated in the inset of panel (f). Aside from this feature, the band structure when $\lambda_{KM} = 3$ meV is qualitatively identical to the band structure without SOI. Nevertheless, the dominant picture is that of spin-orbit split bands.

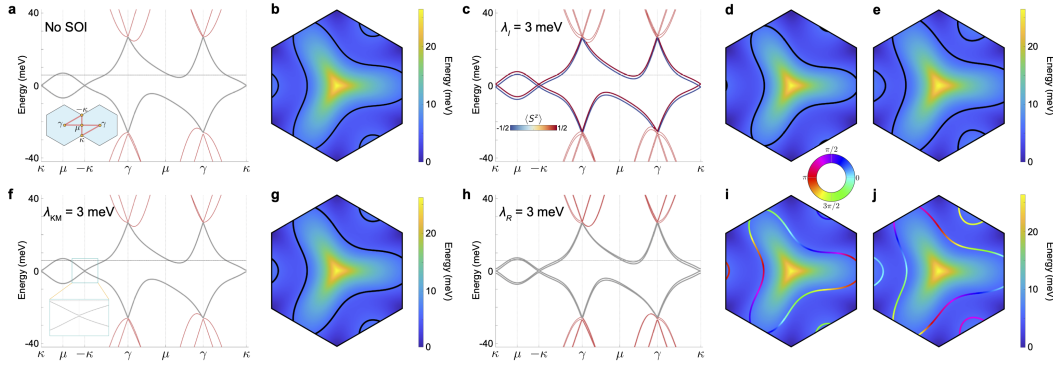


Figure 3.16: Continuum model band structure calculations for different SOI parameters. (a), (c), (f), (h) Flat-band energies similar to Fig. 3.15. (b), (d), (e), (g), (i), (j) $\nu = +2$ Fermi surfaces. We consider the cases where no SOI is present along with cases where only Ising, only Kane-Mele, and only Rashba are present. In (c)–(j), the non-zero SOI parameter is set to 3 meV. In (c), the bands possess an out-of-plane spin polarization ($\langle S^z \rangle$), which is displayed in colour as per the inset. In (i) and (j), the colour of the Fermi surfaces indicates the expectation value of the in-plane spin according to the wheel above (i). All other parameter sets have a zero in-plane spin projection.

In addition to the degeneracy splitting, our data reveal an apparent recurrence of 4-fold degeneracy for large Landau-level fillings, ± 14 , ± 18 , ± 22 , which are still offset from the usual sequence of ± 16 , ± 20 , ± 24 . The mechanism of SOI-induced degeneracy breaking can account for this recurrence as well, as seen in Fig. 3.17. The model used in this case considers a Dirac cone Hamiltonian at mini-valley κ and valley flavor K (and K' results are produced in a similar manner)

$$H = -\hbar v_{F,\text{renorm}}(i\partial_x\sigma_x + i\partial_y\sigma_y) + \frac{\tilde{\lambda}_I}{2}s_z + \frac{\tilde{\lambda}_R}{2}(\sigma_x s_y - \sigma_y s_x) + \frac{\tilde{\lambda}_{KM}}{2}\sigma_z s_z \quad (3.5)$$

with renormalized Fermi velocity $v_{F,\text{renorm}} \approx 10^5$ m/s, as is appropriate for the twist angles considered. The three spin-orbit terms in this case are *effective* SOI terms relevant to the moiré Dirac cones and not expected to be the same as the terms considered above. After including a magnetic field, solving for Landau levels,

and adding a broadening factor—outlined in more detail in the Supplementary Information of Ref. [46]—we calculate the results shown in Fig. 3.17a,c. The Landau level positions (solid lines) and gaps (dotted lines) are considered in panels (b) and (d). For reasonable SOI effective parameters, the experimental scenario is realized. SOI remains, so far, the simplest explanation for the additional even Landau levels observed, though other effects such as strain [62, 97] may contribute.

Induced SOI can additionally constrain the nature of the TBG phase diagram. Regardless of concrete SOI mechanism details, SOI acts as an explicit symmetry-breaking field that further promotes instabilities favoring compatible symmetry-breaking patterns while suppressing those that do not. For example, the relative robustness of the $\nu = 2$ correlated insulator in our $\theta = 0.97^\circ$ device suggests that interactions favor re-populating bands [74, 75] in a manner that also satisfies the spin-orbit energy. Furthermore, the survival of superconductivity with SOI constrains the plausible pairing channels—particularly given the dramatic spin-orbit-induced Fermi-surface deformations that occur at $\nu = +2$, shown in the 2D Fermi surface diagrams in Fig. 3.15b, d. Superconductivity in our low-twist-angle devices, for instance, is consistent with Cooper pairing of time-reversed partners that remain resonant with SOI. Thus the stability of candidate insulating and superconducting phases to the SOI provides additional nontrivial constraints for theory [85, 98–101]. The integration of monolayer WSe₂ demonstrates the impact of the van der Waals environment and proximity effects on the rich phase diagram of TBG. In a broader context, this approach opens the future prospect of controlling the range of novel correlated phases available in TBG and similar structures by carefully engineering the surrounding layers, and it highlights a key tool for disentangling the mechanisms driving the different correlated states.

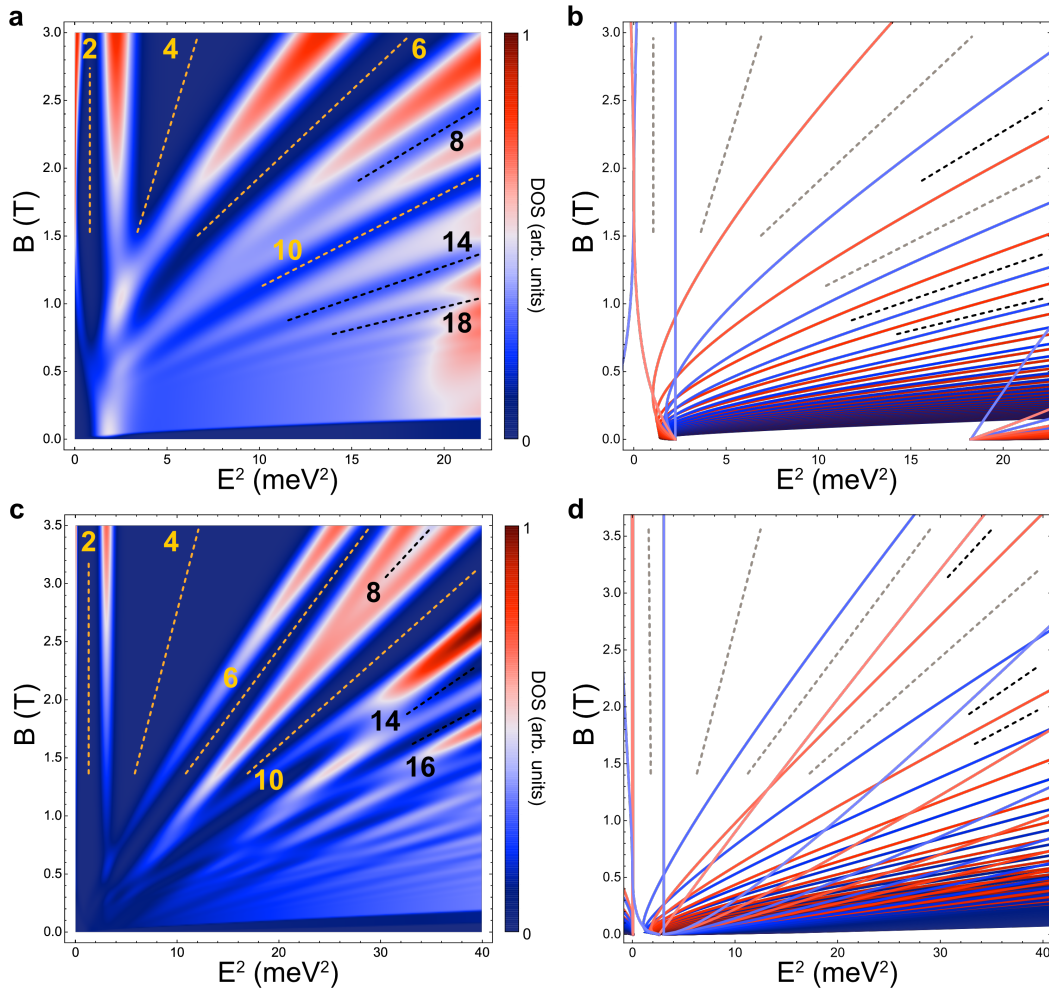


Figure 3.17: Simulated Landau fan diagrams with SOI. (a), (c) Color plot of the phenomenologically broadened density of states as a function of energy squared in $(\text{meV})^2$ (roughly equivalent to the electron density that is gate-tuned in the experiment) and the magnetic field in Tesla. (b), (d) The spectrum without taking broadening effects into account. Blue and red lines correspond to levels originating proximate to the $+\mathbf{K}$ and $-\mathbf{K}$ valleys, respectively. The parameters considered are $(\tilde{\lambda}_I, \tilde{\lambda}_R, \tilde{\lambda}_{\text{KM}}) = (3, 4, 0)$ meV with a broadening $\Gamma = 0.22$ meV and (a), (b) and $(\tilde{\lambda}_I, \tilde{\lambda}_R, \tilde{\lambda}_{\text{KM}}) = (1.5, 2.5, 2)$ meV with a broadening $\Gamma = 0.15$ meV (c), (d). We note that the Landau level sequence and energy levels on the hole-doped side are identical to those shown here for (a) and (b). When both $\tilde{\lambda}_I$ and $\tilde{\lambda}_{\text{KM}}$ are nonzero, as in (c) and (d), a slightly different Landau-level sequence is generically obtained at negative energies relative to the CNP.

HIERARCHY OF CORRELATIONS IN TWISTED BILAYER GRAPHENE-WSE₂ HETEROSTRUCTURES

The twisted bilayer graphene (TBG)-WSe₂ material system, with its stabilized superconductivity, shows promise for further studying the host of correlated phases and effects of the topological bands previously found in TBG [20, 43, 44, 46, 49, 50, 65–67]. Particularly, the increased angle range of superconductivity allows us to search for other phenomena linked to superconductivity. The twist angle serves the role of tuning the electronic interactions in the system [11, 65], so we particularly study the twist-angle dependence of a variety of correlation-related effects. We find a hierarchy of phases, with some phases, such as superconductivity, present over a wide twist angle range. Meanwhile, some phases are only present in a small range about the magic angle of 1.1°, i.e., where the strength of interactions is greatest. In this study, a number of devices have been measured in detail with the goal of distinguishing characteristics that are reproducible over multiple devices. Given the wide range of phenomena observed in these devices and others, our findings serve as an initial roadmap to further studies of correlated effects in TBG and give some clues about the mechanisms involved.

4.1 Devices studied

The devices studied in this chapter are of the same structure as in the previous chapter (Fig. 3.1 and the schematic is shown in Fig. 4.1a), TBG picked up with monolayer WSe₂, encapsulated with hBN, and placed on a Au back gate. Although the devices from the previous chapter have been included in considerations, several more devices have been added to the study, including the ones shown in Fig. 4.1. For a summary of devices used, see Table A.1. The new devices used WSe₂ from a commercial source (HQ graphene), which we found had a similar effect on our devices. Some of the devices included Au top gates, as shown in Fig. 4.1e. Since we are studying the trends through the range of twist angles, much of the summarizing data for each twist angle is left to the appendix.

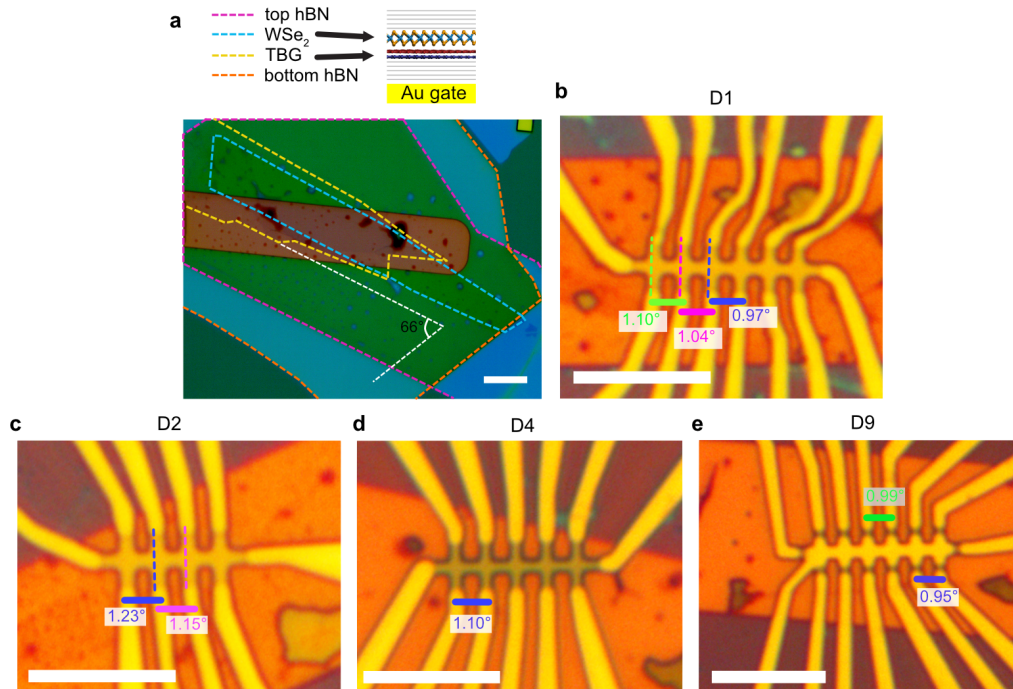


Figure 4.1: Device overview and optical images. (a) Schematic of the devices and example stack of flakes before cleanroom processing, showing the twist angle between the graphene and bottom hBN, showing no obvious alignment. (b)–(e) Optical images of finished devices.

4.2 Correlated phases at a range of twist angles

We first point out the phase diagram of correlated phases for the range of twist angles studied here, 0.79° – 1.23° , in Fig. 4.2. We find correlated insulators with well defined activation gaps for twist angles in the relatively narrow range of 0.97° – 1.15° , indicating that the addition of WSe₂ leaves the value of the magic angle unaffected. Unlike the correlated insulators, we find that the cascade of high-temperature symmetry breaking transitions [74, 75] (discussed in more detail below) and superconductivity near $\nu = \pm 2$ (where ν is the number of electrons per unit cell) persist over a much wider range of - twist angles (see also Fig. A.1 Ref. [46] for more data). While all devices exhibit pronounced electron-hole asymmetry and a peak T_c on the electron (hole) side which is shifted towards lower (higher) angles, superconductivity can be found well above ($\theta = 1.23^\circ$, D2) and below ($\theta = 0.88^\circ$, D3) the magic angle for both negative and positive filling factors. To the best of our knowledge, this is the largest reported range of twist angles exhibiting superconductivity for both electron and hole doping.

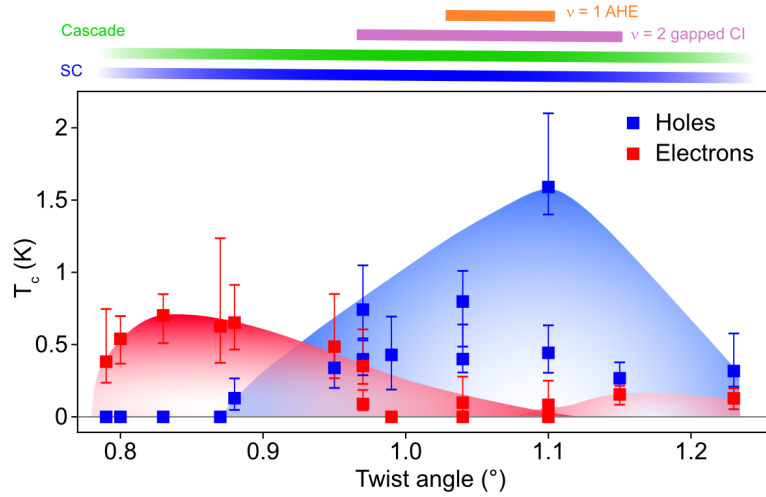


Figure 4.2: Phase diagram, focusing particularly on superconductivity. (Top) Phase diagram as a function of twist angle, indicating the regions which exhibit the anomalous Hall effect (AHE) due to ferromagnetism, $\nu = +2$ correlated insulators (CI), superconductivity (SC), and symmetry breaking cascade effects as deduced from R_{xx} peaks and Hall density resets. The cascade and superconductivity start to disappear on either side of the diagram, as indicated by the fading bar color. (Bottom) Critical temperatures T_c of superconductivity for both holes and electrons (squares indicate 50% R_n and the error bars 10% and 90% R_n ; for more details, see Fig. A.1). The gradient-filled domes are guides to the eye.

4.3 Link between superconductivity and Fermi surface reconstruction

Importantly, the observed superconducting regions are consistently accompanied by Fermi surface reconstructions around $\nu = \pm 2$, as manifested by a low-temperature reset in the Hall density. Consider, for example, the Hall density plots for the two lowest twist angles in Fig. 4.3 (blue and black curves). For 0.88° , hole-side SC around $\nu = -2$ has $T_c = 130$ mK and is accompanied by the formation of a kink in the Hall density (black arrow), which is separate from the van Hove singularity. At larger twist angles, the kink becomes a fully-developed Hall density reset to zero (colored arrows), corresponding to a more complete flavor symmetry breaking-induced Fermi surface reconstruction (see Fig. A.2 for more data). In contrast, the device with twist angle 0.79° reveals a linear Hall density on the hole side that extends well beyond $\nu = -2$, ultimately reaching a van Hove singularity [102]. This signals the absence of an interaction-driven Fermi surface reconstruction. Interestingly, we also no longer find hole-side superconductivity for this twist angle. On the electron side, both twist angles exhibit superconductivity and a kink in the Hall density due

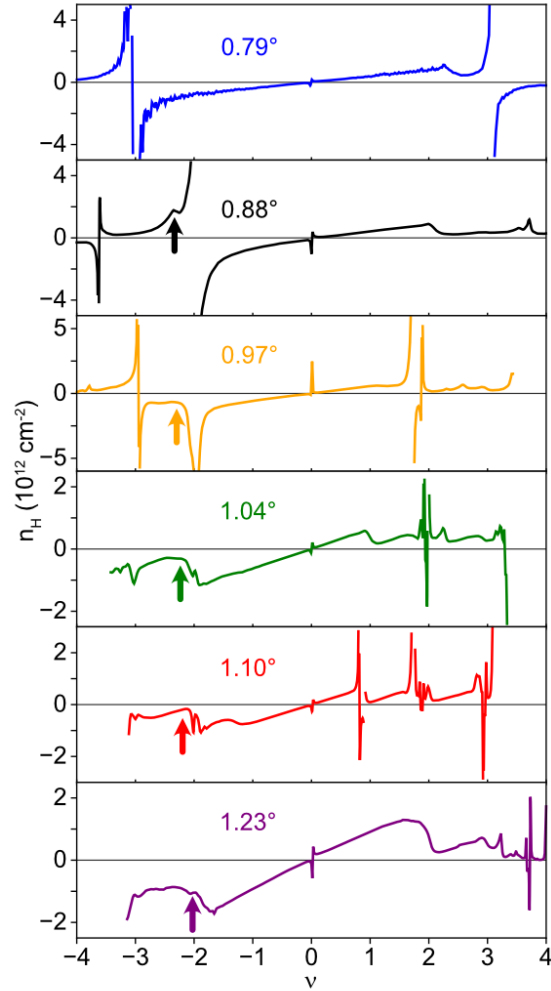


Figure 4.3: Hall density vs. ν . Flavor symmetry breaking correlations manifest as Hall density resets (as seen clearly for 1.04° – 1.23° on the hole side, indicated by colored arrows) and occasionally as singularities or hole-like regions (as seen at 1.10° and 0.97° on the electron side).

to Fermi surface reconstructions.

Our observations indicate that a fully flavor (i.e., spin and valley) symmetric state strongly disfavors the formation of superconductivity. This rules out the simplest scenario for superconductivity based on electron-phonon coupling, which relies only on the local density of states [103]. Alternatively, and independently of the pairing mechanism, in the case of multiflavor pairing, superconductivity and magnetism (i.e., flavor polarization) can be inherently connected. This connection emerges from a simple energetic argument. If two flavors pair, they could increase their condensation energy by exchanging particles with the other flavors, such that

they maximize their density of states. Roughly, this is captured through a term akin to $\Delta^2 M$ in the free energy, but with M (and Δ) being a matrix indicating the density of the various flavors on its diagonal, and correlations (pairing) in the off diagonal [104]. This term in the free energy implies that strong flavor polarization (manifested in M) will generally increase the superconducting gap, and thus T_c , of a multiflavor superconductor. Conversely, a finite superconducting order parameter could also induce polarization. Our experimental observation that enhanced superconductivity occurs only in regions with prominent Hall density resets is thus in line with multiflavor pairing. This could potentially reconcile experiments with electron-phonon mechanisms of superconductivity, although we note that our results do not rule out unconventional mechanisms based, for example, on flavor fluctuations [99] or the Kohn-Luttinger scenario [105].

4.4 Notes on the effects of adding WSe₂ and disorder

We note that the addition of WSe₂, while not changing the magic angle value, may help stabilize superconductivity over a wider range of angles. A few effects may be responsible. The first effect is a possible reduction in twist angle disorder. In all TBG devices studied so far, it appears that there are significant device-to-device variations that are often associated with disorder. In addition to disorder that is intrinsic to graphene (such as charge disorder originating from residual polymers and other impurities, disordered edges, strain from wrinkles or bubbles, strain from the substrate or back gate), in TBG twist angle disorder is believed to play an important role. As previously reported, it generates domains and gradual twist-angle shifts on length scales from 100 nm to a micron [54, 57]. In this context, characterizing TBG disorder through transport measurements is somewhat more elusive as transport averages over device length scales (a few μm).

It is important to emphasize that measurements of disorder that are typically used in a single layer of graphene and commonly detected through broadening of charge-neutrality peaks in longitudinal or Hall resistance (full width at half max—FWHM—of R_{xx}), do not correlate well with superconductivity or other features that may point towards disorder in the TBG samples. Fig. 4.4 shows that there is not an obvious correlation of superconducting T_c with the charge-neutrality peaks. However, the previously mentioned robust plateaus in our devices (Fig. 3.14) suggest that the added layer of WSe₂ decreases the amount of twist angle disorder, and we occasionally see devices with broadened features in Landau fan diagrams and a number of features near $\nu = 2$, suggesting twist angle disorder as the cause

(Fig. A.3d). We have also confirmed in separate devices that the twist angle disorder is reduced on the hundreds-of-nanometer to μm scale in STM measurements [57].

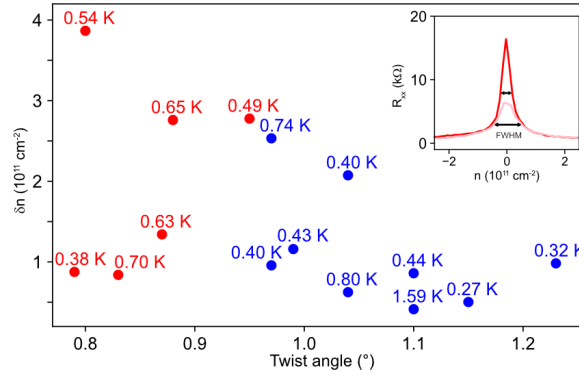


Figure 4.4: Widths of charge-neutrality peaks δn . The full-width half-max used for this plot is shown in the inset for the 1.10° data point with T_c of 1.59 K (red) and the 1.23° point (pink). Listed next to each data point is the maximum T_c measured for the twist angle, and the color corresponds to whether the superconductivity was on the hole (blue) or electron (red) side.

We find in the best devices that four-point measurements almost perfectly overlap for different contact configurations (Fig. 4.5b), signaling high twist angle uniformity. Moreover, in a dual-gated geometry no dependence on the displacement field is found (Fig. 4.5c). Although this device's twist angle (0.88°) is right on the edge of where superconductivity begins on the hole side (Fig. 4.2), we see clear signs of superconductivity on both electron and hole sides in Fig. 4.5.

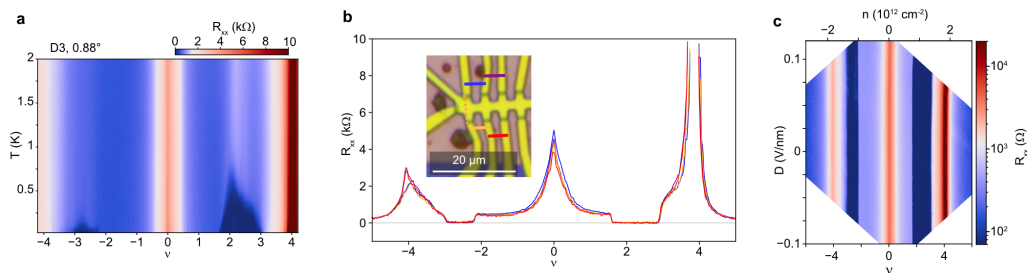


Figure 4.5: Data for device D3 at 0.88° . (a) A ν - T diagram of R_{xx} . (b) Linecuts at base temperature of R_{xx} for different contacts (colors corresponding to the inset) show little variation over a range of several μm . (c) Applying an electric field (D) shows no obvious D -field dependence.

This may explain our observation, in part, of superconductivity over a large angle range although the spin-orbit coupling may still play a role, particularly in the

electron-side superconductivity away from the magic angle where hBN encapsulated TBG data is lacking and comparison is not possible. We also point out that our recent study on Bernal bilayer graphene-WSe₂ heterostructures suggests that spin-orbit coupling from WSe₂ favors superconducting ground states at flavor polarization transitions in another graphene system [106]. This further bolsters the idea that WSe₂ plays a part in the stabilized superconductivity observed here. However, we suspect that the precise details could possibly depend on the precise twist angle difference between WSe₂ and graphene [107].

4.5 High-temperature features at a range of twist angles

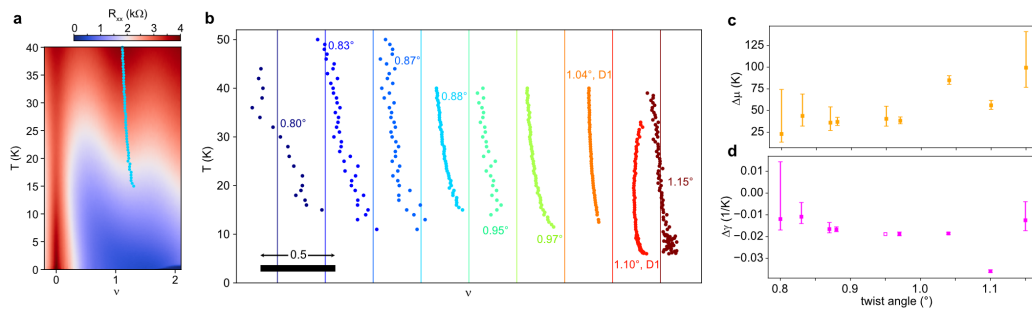


Figure 4.6: Pomeranchuk-effect phase transition peak fits. (a) Example of a peak fit at $\nu \approx 1$ for a device at twist angle 0.88° . (b) R_{xx} peak positions near filling factor $\nu \approx 1$ as a function of temperature for devices with various twist angles. The vertical colored lines represent the $\nu = 1$ filling factor for the respectively colored twist angle data. (c), (d) Fit parameters $\Delta\mu$ and $\Delta\gamma$ representing change in the chemical potential and specific heat, respectively, for the phase transition represented by the R_{xx} peaks in (b). Error bars are 95% confidence intervals. The hollow square for 0.95° was set to the same $\Delta\gamma$ value as the 0.97° device due to the unconstrained $\Delta\gamma$ value for the data points.

The principal features emerging at higher temperatures (above 5–10 K) in TBG, such as the cascade of phase transitions between symmetry broken states near integer filling factors and the linear-in-T dependence of R_{xx} , are also present over a wide range of angles. We focus first on the cascade of phase transitions, high-temperature R_{xx} peaks associated with phase transitions that repopulate the bands to favor certain flavors [74, 75]. In the case of $|\nu| \approx 1$, R_{xx} peaks (an example is shown in Fig. 4.6a, and panel (b) shows experimental data following the R_{xx} peaks at a range of twist angles) are associated with a Pomeranchuk-like phase transition [108, 109] between a flavor symmetric state near charge neutrality and a symmetry broken phase with free local spin moments (approximately 1 per moiré site) in analogy to

the Pomeranchuk effect in He^3 [108]. The evolution of this phase boundary with temperature can be fit using a simple thermodynamic model including the free energy of localized spins [109]. When considering the grand canonical potential approach, allowing the filling factor ν to change, and setting the magnetic field to zero, the phase transition line follows:

$$\nu = \frac{1}{\Delta\mu} \left[-\frac{1}{2}\Delta\gamma T^2 - \ln(2)T + \Delta\epsilon \right]. \quad (4.1)$$

The main parameters entering this model are the shift in the chemical potential $\Delta\mu$ due to the cascade transition and the change in specific heat $\Delta\gamma$ between the flavor symmetric and local moment phases. $\Delta\gamma$ is negative since the local moment phase has a smaller density of states. $\Delta\epsilon$ is a free parameter related to a reference energies of the phases. A strong carrier density reset, and therefore strong correlations, are related to a strong $\Delta\mu$. Only the electron-side transitions were mapped in this study because they were detectable in a wider range of twist angles.

Our data suggest that this description works reasonably well over the entire range of angles investigated here. Fig. 4.6c, d show the fit parameters for the data in panel (b). $\Delta\gamma$ appears to be roughly constant except for device D1 at 1.10° right at the magic angle, perhaps indicating additional correlation effects emerging for this angle. We note that this device also exhibits a metallic anomalous Hall phase near $\nu = 1$ at low temperatures, discussed below. The slowly increasing $\Delta\mu$ signals stronger shifts of the bands as the twist angle is increased toward the magic angle, a trend that is consistent with the strength of interactions. The appearance of superconductivity, high-temperature symmetry breaking cascade transitions, and in particular Pomeranchuk-like transitions over similar twist angle ranges (see Fig. A.1 and Ref. [46] to see the fading cascade at the limits of twist angles studied here) suggests a possible connection between these instabilities and points to similarities between TBG and heavy-fermion systems [110] which also show rich phase diagrams exhibiting similar phases [87, 111, 112].

The twist angle dependence of the linear-in-T resistivity behavior is shown in Fig. 4.7, with more examples in the appendix (Fig. A.4). A linear temperature dependence of the resistivity can be due to electron-phonon scattering, at least at higher temperatures (above 5–10K) [82, 86, 113]. Alternatively, this dependence has also been associated with strange metal behavior due to its onset at low temperatures and its strength near the $|\nu| = 2$ correlated phases [49, 114]. Our data show that

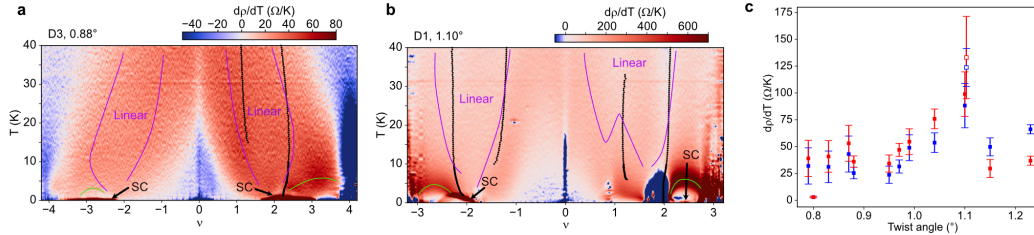


Figure 4.7: $\frac{d\rho}{dT}$ resistivity derivative data. (a), (b) $\frac{d\rho}{dT}$ 2D diagrams for devices at twist angles 0.88° and 1.10° , respectively. R_{xx} peaks corresponding to Pomeranchuk-like transitions are shown with black dots, superconducting (SC) pockets are shown with arrows, and the magenta lines are guides to the eye representing the approximate regions of T-linear resistivity. The green lines reveal the inflection points in ρ . (c) The resistivity slope $\frac{d\rho}{dT}$ for a range of twist angles, where red(blue) is for electrons(holes). The values come from the average derivative over the area spanned by $1.5 < \nu < 1.8$ ($-2 < \nu < -1.6$) for electrons (holes) and $15 < T < 38$ (error bars are the standard deviations). Device D4, twist angle 1.10° is represented by hollow squares.

the linear-in-T behavior is qualitatively similar in devices away from (Fig. 4.7a; see Fig. A.4 for more examples) and close to the magic angle (Fig. 4.7b).

Both cases exhibit broad regions of linear-in-T behaviour fanning out from approximately $|\nu| = 2$ (delineated by magenta lines). At lower $|\nu|$, this region is bordered by a broad region near charge neutrality, where the increase in resistance is quadratic (consistent with expectations for Fermi liquid behaviour). At higher $|\nu| > 2$, there is a region where the temperature dependence of the resistivity crosses over from strongly super-linear to sub-linear as temperature increases. The intermediate inflection points, shown as green lines in Fig. 4.7a, b appear to be intertwined with other TBG phases as they occasionally touch the superconducting domes (both for electrons and holes at 0.88° as well as for holes at 1.10°) or onset near $\nu \approx 2$, when a correlated insulating gap is present. This observation contrasts with the suggestion that the entire superconducting dome emerges below a linear-in-T phase [114].

Both the magnitude of the T dependence at $\nu > 2$ (as measured by the slope near the green lines) and the linear-in-T slope measured at higher temperatures (within the magenta regions, in the range of $1 < \nu < 2$) are enhanced near the magic angle (Fig. 4.7c). This is to be expected, as the Fermi velocity is minimized for this angle and could be even further reduced by interaction effects causing band flattening at nonzero filling [115]. Particularly, calculations with Hartree effects included are known to exhibit flattened regions of bands in the range of $|\nu| > 2$. Finally we note

that, in general, the linear-in-T slope peaks around the same angle value for both electrons and holes. This contrasts with the observed doping asymmetry of the twist angles at which the superconducting T_c becomes maximal, further highlighting the differences between high- and low-temperature symmetry breaking phenomena.

4.6 Strong correlations and a ferromagnetic state at 1.10°

For the remaining section of the chapter, we focus mostly on a magic-angle device with $\theta = 1.10^\circ$ (D1, Fig. 4.8). Upon cooldown, this device exhibits clear R_{xx} peaks below $T \approx 40$ K at every integer $0 < |\nu| < 4$. As temperature is lowered further, a correlated insulator (CI) develops near $\nu = +2$, while other resistance peaks remain metallic or disappear gradually (Fig. 4.8a, c). As is seen in Fig. 4.1a and Fig. 4.1c, there is not evidence of obvious alignment between hBN and TBG, which tends to produce a gap at the charge neutrality point. For hole doping (Fig. 4.8b), the corresponding superconducting dome near $\nu = -2$ reaches a maximal transition temperature of $T_c = 1.6$ K, featuring vanishing longitudinal resistance R_{xx} and a Fraunhofer-like pattern in line with previously reported hBN-encapsulated, high-quality magic-angle TBG devices [20, 43, 44, 47, 48].

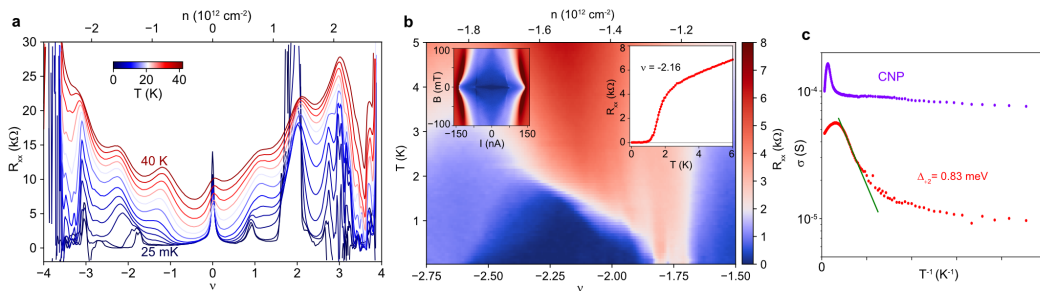


Figure 4.8: Data for the 1.10° region of D1. (a) Linecuts for a range of temperatures shown in the colorbar. (b) R_{xx} of the hole-side superconductivity dome, along with a linecut at $\nu = -2.16$ (right inset) and Fraunhofer-like pattern (left inset, $\nu = -2.3$). (c) Temperature dependence of the charge neutrality point and $\nu = 2$ peaks, showing the activated gap behavior at $\nu = 2$.

In contrast to the features at $\nu = \pm 2$, the evolution of R_{xx} near $\nu = \pm 1$ is more subtle. In the temperature range $6 \text{ K} < T < 40 \text{ K}$, the R_{xx} peaks near both $\nu = +1$ and $\nu = -1$ evolve towards lower filling factors $|\nu|$ as temperature increases, following the phase boundary discussed above (Fig. 4.8a, Fig. 4.9c). However, at lower temperatures, $T < 6 \text{ K}$, the two peaks show distinctly different behavior. While the hole-side peak completely disappears, reflecting simple metallic behavior from charge neutrality

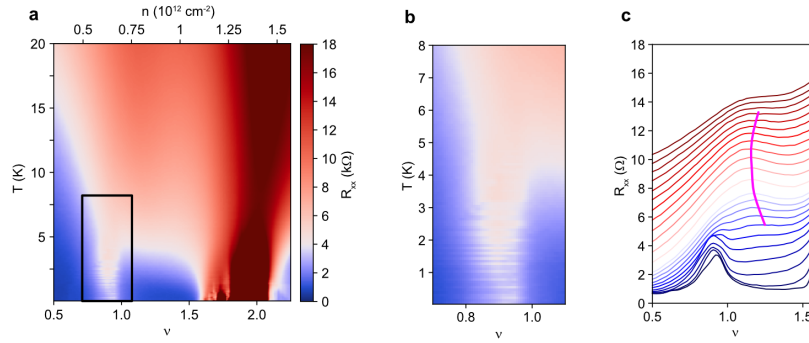


Figure 4.9: R_{xx} data focusing around $\nu = 1$. (a) R_{xx} vs. ν and T on the electron side for D1 at 1.10° . (b) A zoom into panel (a) around $\nu = 1$, revealing the switching behavior of the resistance. (c) Dense line-cut plots near $\nu = 1$, showing that the evolution of R_{xx} maxima above 10 K (magenta line) are distinct from the ferromagnetic peak.

to $\nu \approx -2$, the peak near $\nu = 1$ gradually gives way to another peak emerging in the filling range $0.8 < \nu < 0.95$ that persists to the lowest temperatures (Fig. 4.9a). Careful inspection reveals that R_{xx} exhibits switching behavior around the peak, discontinuous resistance changes between the same sweep across ν taken at slightly different temperatures (Fig. 4.9b) presumably due to switching of domains.

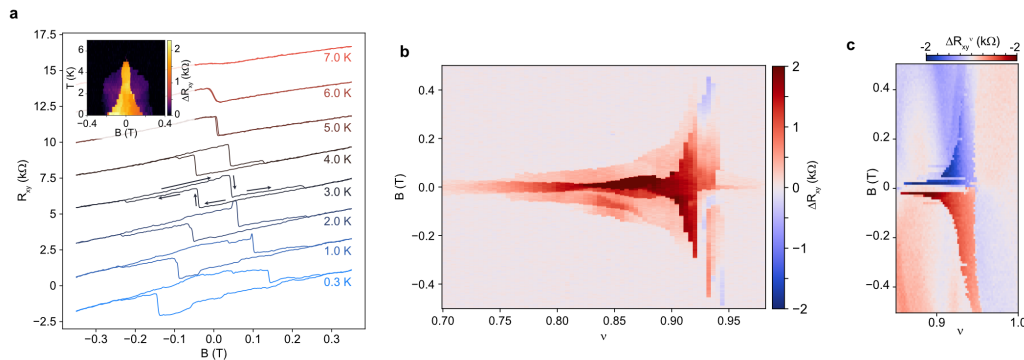


Figure 4.10: R_{xy} hysteresis data. (a) Hysteresis loops taken at $\nu = 0.9$ at a range of temperatures. Inset: the resistance jump ΔR_{xy} of hysteresis loops measured vs. B and T . (b) ΔR_{xy} measured as a function of ν and B at 1.5 K. For each ν , the line results from sweeping B up and down. (c) $\Delta R_{xy}^\nu = R_{xy}^{\nu\uparrow} - R_{xy}^{\nu\downarrow}$ measured as a function of the sweeping parameter ν and B , which was held constant.

Further measurements in the ν and temperature range of this low-temperature R_{xx} peak reveal an anomalous Hall effect (AHE). Fig. 4.10a shows hysteresis loops in the Hall resistance, R_{xy} , for $\nu = 0.9$ as measured from 0.3 K to 7 K. The loop

has a coercive field of up to about 150 mT and is centered about zero magnetic field. The jump in resistance $\Delta R_{xy} = R_{xy}^{B\uparrow} - R_{xy}^{B\downarrow}$ reaches a maximal value of 2.5 k Ω , significantly smaller than the resistance quantum, which persists until the Curie temperature ~ 5 K (Fig. 4.10a inset). Signatures of the AHE are also observed at twist angles of 1.04 $^\circ$ and 0.99 $^\circ$, as shown in Fig. A.5.

Importantly, the observed AHE phase appears well below filling factor $\nu = 1$, existing in the range $0.7 < \nu < 1$, with the maximal ΔR_{xy} occurring near $\nu = 0.88$ (Fig. 4.10b). Upon approaching $\nu = 0.95$, the filling at which R_{xx} peaks, the coercive field diverges accompanied by a sudden decrease in ΔR_{xy} . Additionally, hysteresis is observed when sweeping ν in opposite directions (Fig. 4.10c) and holding the magnetic field constant.

For a more detailed look, see Fig. 4.11. Panels (c)-(e) shows the picture of hysteresis seen as a result of sweeping either B or ν . Panel (b) shows that after $\nu > 0.95$, hysteresis loops sometimes appear in the opposite direction from that seen for $\nu < 0.95$ (in this case at 3.5 K but still with a similar ν -B diagram in panel (a)). The magnetism is also very stable, with domains remaining unflipped for up to hours after initializing them using magnetic field or ν (Fig. 4.11f).

Measurements of R_{xy} at elevated temperatures and over a wider doping range further reveal the unusual nature of the observed AHE phase (Fig. 4.12a). Surprisingly, within the range of ν exhibiting the AHE and up to magnetic fields greater than 1 T, the sign of R_{xy} is opposite to that of the surrounding doping range. Also, R_{xy} changes sign when the temperature reaches ~ 5 K, consistent with the measured AHE Curie temperature. While naively this behaviour might be due to a change of carrier type from electrons to holes, the measurements show a linear increase in R_{xy} with increasing magnetic field throughout the entire doping range (Fig. 4.10a and Fig. 4.12b), consistent with dominant electron conduction.

The observation of hysteresis signals the emergence of an orbital ferromagnetic phase that arises from a band carrying nonzero Chern number C [82, 116]. A finite Chern number is also expected to result in R_{xy} and R_{xx} features that follow the Streda formula in an out-of-plane magnetic field $B = \frac{h}{Ce}n$. We observe clear maxima and minima in R_{xx} approximately following the Streda formula at fields less than 3 T (Fig. 4.12c), and specifically point to the R_{xx} minimum following $C = -1$ that extrapolates to $\nu = 0.95$ at zero field, near where the coercivity diverges. The low-field features disappear by $B = 3-4$ T, where a finite-field Chern insulating phase corresponding to $C = 3$ takes over. The observed switch in Chern number

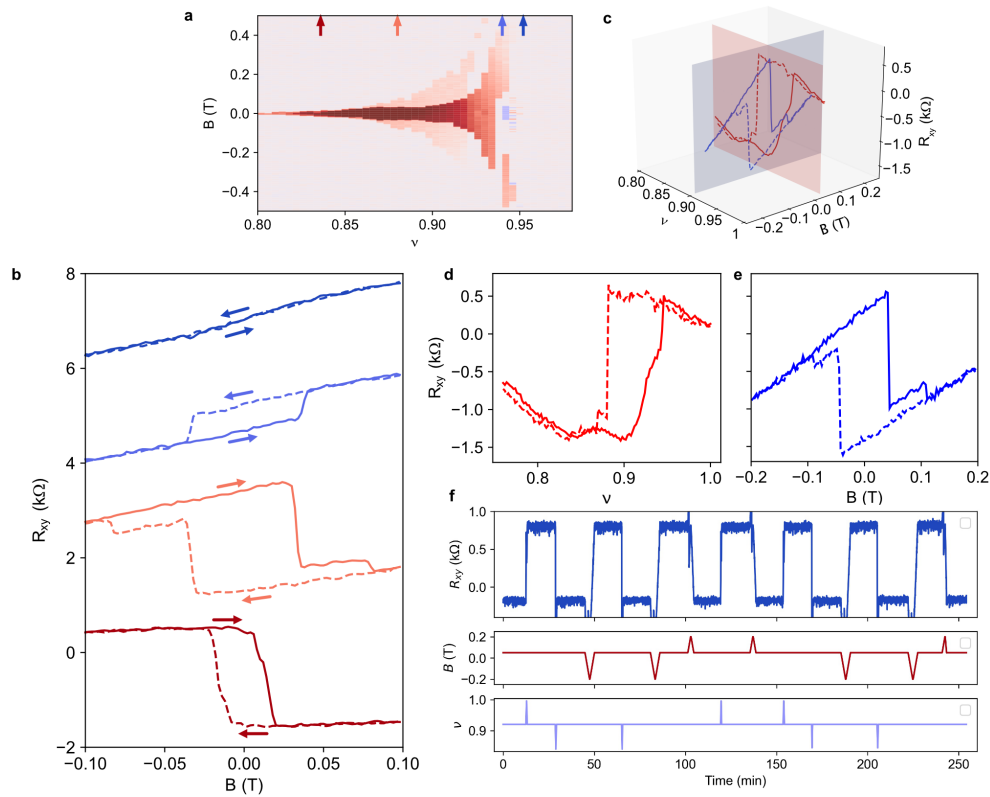


Figure 4.11: More details on hysteresis. (a) ΔR_{xy} vs. B and ν around filling factor 1 measured at 3.5 K. (b) Hysteresis loops measured at filling factors marked by arrows in (a). (c)-(e) Hysteresis loops as a function of ν and B . (c) The 3D perspective of (d) (ν sweep forward is solid, backward is dashed) and (e) (B sweep forward is solid, backward sweep is dashed). The density sweep in (d) was measured at 30 mT, after cycling to 200 mT to align the domains. (f) Pulses of B and ν showing reproducible switching of magnetic state, with bit-like switching of R_{xy} .

indicates the competing nature of these phases [47, 117].

However, our observations stand in contrast to discussions of zero-field Chern insulators, where the chemical potential falls into an insulating gap [47, 56, 117, 118]. Throughout the entire doping range, the AHE phase observed here appears metallic. This is implied by the electron-like Hall resistivity and the finite R_{xx} peak at 0 T that is small compared to h/e^2 and increases with temperature. This contrasts with the expected vanishing of R_{xx} for a gapped bulk with gapless edge channels [67] or a resistance $\sim h/e^2$ that can originate from domain walls extending between the contacts [119]. We note that while disorder effects and the presence of domains observed in Ref. [56] can, to some extent, explain the absence of a gap

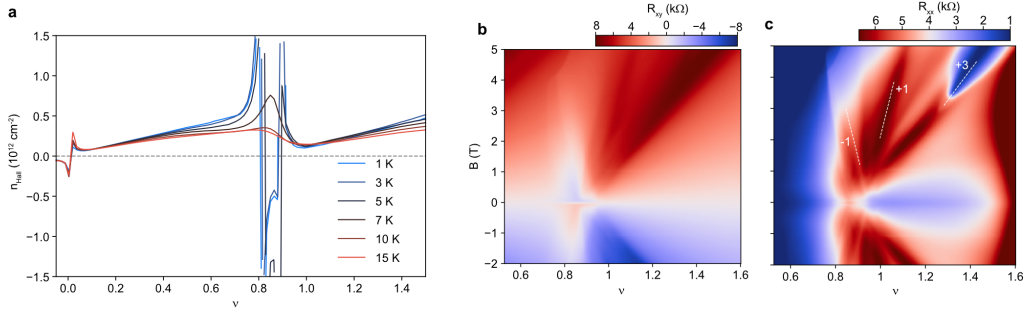


Figure 4.12: Hall effect and Chern number behavior near $\nu = 1$. (a) Hall density vs. ν measured at 0.5 T (the value shown is antisymmetrized $[R_{xy}(0.5T) - R_{xy}(-0.5T)]/2$). (b), (c) Magnetic field and ν dependence of R_{xy} and R_{xx} measured at 3 K. (c) contains dotted lines representing the $C = -1, +1, +3$. $C = -1$ and $+3$ lines originated from $\nu = 0.95$.

and imperfect quantization, local compressibility [75, 120] and scanning tunneling spectroscopy measurements [14, 121] typically do not resolve a gapped state near $\nu = 1$. In the following, we present a scenario which would be consistent with the metallicity as well as the electron-like behaviour of R_{xy} in the AHE phase seen in Fig. 4.10a and Fig. 4.12a. Our scenario relies on the fact that strong interactions can heavily deform the TBG bands, such that the Γ point of the mini-Brillouin zone can be inverted, as reported by local spectroscopy measurements [14].

4.7 Ten band Hartree-Fock model for TBG near $\nu = 1$

To model TBG, we employ a ten-band model [122] that includes short-range Coulomb interactions [10]. First we show that this model, which uses a Hartree-Fock approximation, can capture the existence of the symmetry breaking cascade [74, 75] and TBG band structure deformations [14, 102, 115, 123] (see Supplemental Material of Ref. [53] for more details). Flavor-resolved mean-field band structures at $\nu = 0.81$ are shown in Fig. 4.13a–d. Here, the symmetry breaking cascade occurs well before ν reaches 1, with one of the spin-valley flavor bands being almost filled while the other three develop a gap and are shifted back to the vicinity of the charge neutrality point. Focusing on the three gapped bands, one can obtain a total Chern number of $C = \pm 3$ or $C = \pm 1$ [117], depending on the exact symmetry breaking mechanism, when the chemical potential is within the gap. For example, broken \mathcal{T} symmetry naturally leads to $C = \pm 3$, and broken C_2 symmetry can give rise to $C = \pm 1$ phases [121].

Now consider the case displayed in Fig. 4.13 where the chemical potential for three

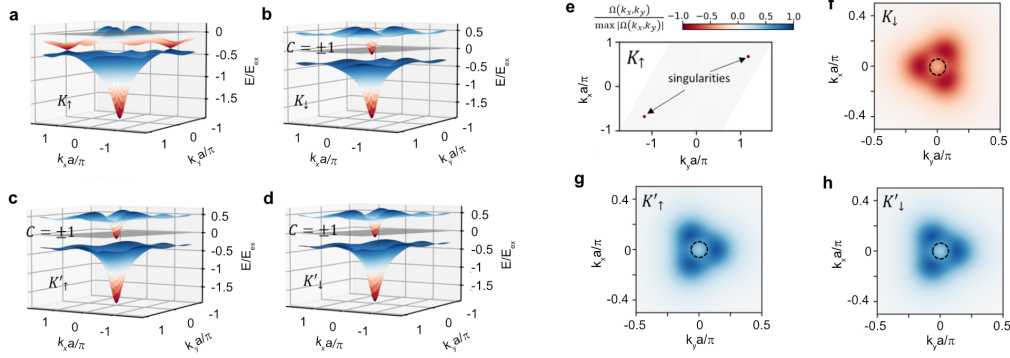


Figure 4.13: Ten-band model calculations. (a)–(d) The band structure obtained for each spin and mini-valley (K , K') flavor for the case of broken $C_2\mathcal{T}$ symmetry at $\nu \simeq 0.81$. The K_\uparrow flavor, which is nearly filled, preserves the Dirac-like band structure (a), whereas the other three flavors have a $C_2\mathcal{T}$ -broken mass (b)–(d). The gray planes represent the chemical potential. (e)–(h) Berry curvature Ω_{k_x, k_y} for the conduction flat band in the K_\uparrow flavor (e) and for K_\downarrow (f)–(h), where the Berry curvature is concentrated above the Γ pocket. The Fermi surface is plotted as a dotted circle.

flavors touches the bottom of the inverted electron pocket at the Γ point and still remains in the top of the band for the remaining flavor. Despite being slightly electron doped, the three flavors still contribute to the anomalous Hall conductance. Since the Berry curvature of the upper band is small near the bottom of the inverted electron pocket, as shown in Fig. 4.13g–h, the Chern number remains approximately conserved and contributes to magnetization in a way that is analogous to the description in Section 1.7. The consistently positive slope $\frac{dR_{xy}}{dB}$ of the Hall resistivity arises from the electron-like bands of the barely filled flavors, while the apparent hole-like sign of R_{xy} originates from the negative offset caused by the anomalous Hall effect. The experimentally observed hysteresis, in this scenario, would still be explained by orbital ferromagnetism [116]. Due the metallic nature of the system, the Streda formula with $C = -1$; $\nu = 1$ at $B = 0$ T is only approximately satisfied. We note, that while the mean-field calculations presented here successfully capture a possible metallic AHE phase, other ground states with similar characteristics may also be possible [102, 117, 124, 125] and are hard to rule out based on our data. Finally, a similar scenario to the one proposed here can also explain AHE phases observed recently near $\nu = \pm 2$ [118, 126].

Our results show that the robustness to deviations of the twist angle from the magic angle divides TBG phases into two categories. Superconductivity, cascade

transitions, as well as the linear-in-T dependence of the resistivity are robust over a wide range of twist angles, spanning at least $0.8^\circ \lesssim \theta \lesssim 1.23^\circ$. Moreover, the cascade transitions near $\nu = \pm 2$ appear to be a necessary prerequisite for the appearance of superconductivity, implying close relations between these two phases. In contrast, the correlated insulating and orbital ferromagnetic states require a more subtle interplay of strong interactions, kinetic energy scales, and possible breaking of spatial symmetries. Due to this sensitivity, these phases appear in a more immediate vicinity of the magic angle, where the close competition between various phases can result in differing behaviour of devices with the same twist angle (e.g., see Fig. A.6). This hierarchy of TBG phases will guide future theoretical frameworks aiming to explain the rich phenomenology of TBG and related structures.

PROMOTION OF SUPERCONDUCTIVITY IN MAGIC-ANGLE GRAPHENE MULTILAYERS

While we previously restricted our discussion to two layers of graphene with rotational misalignment, the discovery of a new heterostructure involving three graphene layers suggests that TBG may be just one in a family of graphene moiré superconductors. Twisted trilayer graphene (TTG) exhibits superconductivity with even more robust indicators of strong coupling or BEC-type superconductivity [127, 128] and large Pauli limit violation [129] along with the other indicators of robust superconductivity characteristic of TBG. This recent introduction of a new graphene moiré superconductor leads us to wonder if there could be more waiting to be discovered. Our work here introduces two new superconducting graphene systems by translating the concept of alternating twist angle in TTG to four- and five-layer devices.

5.1 Alternating twisted multilayer graphene heterostructures

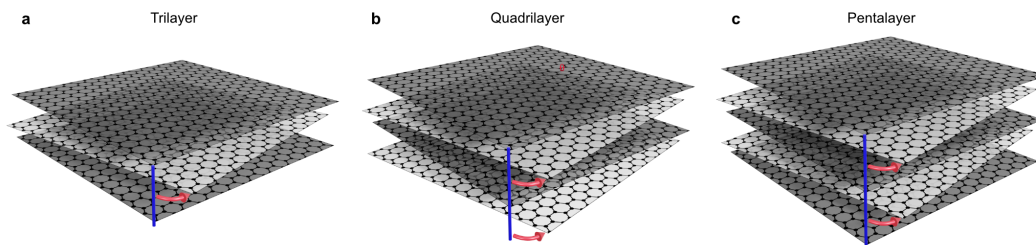


Figure 5.1: Schematics of the alternating twisted trilayer (a), quadrilayer (b), and pentalayer (c) graphene studied.

We investigate twisted graphene multilayers where each successive layer is twisted by an angle $\pm\theta$ relative to the previous one in an alternating sequence (Fig. 5.1). We denote the four- and five-layer structures twisted quadrilayer graphene (TQG) and twisted pentalayer graphene (TPG). For an even number n of layers, the spectrum at zero displacement field D is expected to separate into $n/2$ independent TBG-like bands, each characterized by a different effective twist angle. When the number of layers n is odd, in addition to $(n-1)/2$ TBG-like bands, one monolayer-graphene-like band (essentially a Dirac cone) is expected [130] (see Fig. 5.2, left side of

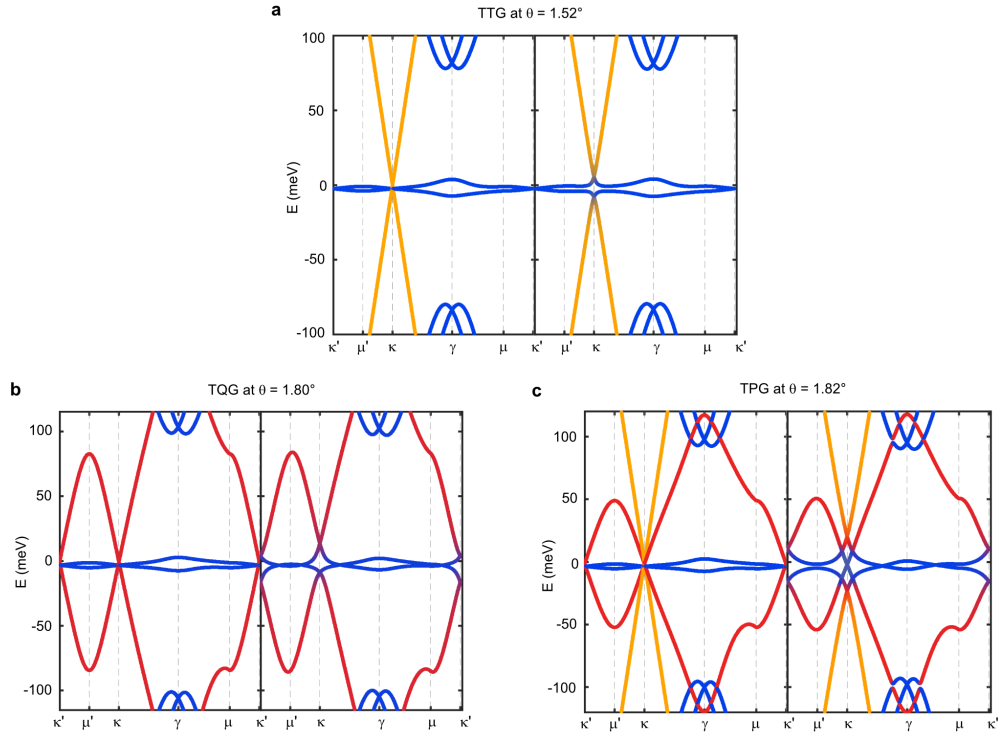


Figure 5.2: The non-interacting band structures calculated based on the continuum model for TTG (a), TQG (b), and TPG (c) near their respective magic angles. The colors represent the eigenstates associated with the flat bands (blue), Dirac cones (yellow), and dispersive TBG-like bands (red). On the left side of each diagram is the band structure with $D/\epsilon_0 = 0$, and the right side shows finite field $D/\epsilon_0 \approx 0.4$ V/nm.

each diagram, for examples when n is 3, 4 and 5). In twisted bilayer graphene, the continuum model Hamiltonian matrix looks like (see Section 1.4 for more details)

$$h_{TBG} = \begin{pmatrix} h_{D,1} & T \\ T^\dagger & h_{D,2} \end{pmatrix} \quad (5.1)$$

where along the diagonal are rotated Dirac Hamiltonians for the two layers, and the T is an interlayer tunneling term. It can be extended to twisted n -layer devices with a generalization

$$h_{Tn_{\text{layer}}G} = \begin{pmatrix} h_{D,1} & T_{1,2} & 0 & \dots \\ T_{1,2}^\dagger & h_{D,2} & T_{2,3} & \dots \\ 0 & T_{2,3}^\dagger & h_{D,3} & \dots \\ \vdots & \vdots & \vdots & \ddots \end{pmatrix}. \quad (5.2)$$

An important distinction between TBG and graphene moiré heterostructures containing additional layers is the band structure dependence of the relative layer displacement, which manifests as an extra phase factor in the tunneling terms. For the picture in Ref. [130] and Fig. 5.2, not only must the graphene sheets be stacked with alternating angles, but moreover, the emergence of independent TBG- and Dirac-like bands only occurs when all odd (even) layers are AA stacked, *i.e.*, stacked directly on top of one another.

In TTG, it has been numerically shown that this situation is energetically preferable: the system naturally relaxes into the odd/even aligned stacking configuration [131]. This result is further experimentally verified in transport [127] and local probe [132] measurements. A simple heuristic supports these results and permits a generalization to additional layers. Starting from a bilayer system, the moiré superlattice appears as a periodic variation between AA, AB, and BA stacking regions. The AA regions have a relatively high energy compared to the Bernal-like (AB and BA) regions, and the lattice accordingly responds by relaxing to minimize the AA-region area. We now consider adding a third layer with the same relative twist angle as the first layer, but for the moment arbitrarily displaced from that layer. A moiré superlattice is also generated between the new layer and the second layer, and the system once again seeks to minimize (maximize) the area of the AA (AB/BA) regions. Crucially, if the first and third layers are misaligned, the AA regions between the first and second layers are misaligned from the AA regions between the second and third layers, frustrating the ability of the lattice to relax. Only when the first and third layers are aligned will the AA region occur at the same locations and only then can the system optimize its energy through relaxation. As the layers are sequentially stacked, the argument generalizes to quadrilayer and pentalayer systems.

The theoretically predicted “magic” values needed to obtain one set of flat TBG-like bands are $\theta_{\text{TTG}}^{\text{magic}} = \sqrt{2}\theta_{\text{TBG}}^{\text{magic}} \approx 1.53^\circ$, $\theta_{\text{TQG}}^{\text{magic}} = (\sqrt{5} + 1)\theta_{\text{TBG}}^{\text{magic}}/2 \approx 1.75^\circ$, and $\theta_{\text{TPG}}^{\text{magic}} = \sqrt{3}\theta_{\text{TBG}}^{\text{magic}} \approx 1.87^\circ$ assuming an effective TBG twist angle $\theta_{\text{TBG}}^{\text{magic}} = 1.08^\circ$ [130]. The system may be conveniently modified through the application of a

displacement field D , which controllably hybridizes the different bands (Fig. 5.2 right side of each diagram). In our case, we add a potential difference U between the top and bottom layer—and linearly interpolate for layers in between—such that $U = 0.1(n - 1)eD/\epsilon_0 \times 0.33$ nm, where n is the number of layers. This provides agreement with experiment, but results do not rely on the specifics of the approximation.

In order to approximate the band structures of the experimental systems in this study, we use different interlayer tunneling parameters in Fig. 5.2. Since tunneling parameter w_{AB} also changes the magic angle, different tunneling parameters can be used to simulate systems slightly above and below the magic angle. The continuum model suggests that for the case where the twist angle is below the n -layer magic angle ($\theta < \theta_{n\text{layer}G}^{\text{magic}}$), a D field applied to the system quickly gaps out all states at the charge neutrality point (CNP) except for a dispersive monolayer graphene-like Dirac cone in odd-layer systems, and the density of states remains constant for larger D . However, for the case where $\theta > \theta_{n\text{layer}G}^{\text{magic}}$, the CNP becomes gradually more metallic as D is applied until a finite D where the bands are gapped out. For TTG the behavior is closer to the former case, justifying our use of $w_{AB} = 110$ meV, whereas TQG and TPG behave like the latter case, so we used $w_{AB} = 108$ and 102 meV, respectively. We use the same $w_{AA} = 60$ meV for all three band structures.

5.2 Introduction to the devices measured

Experimentally, we explore properties of alternating twisted trilayer, quadrilayer, and pentalayer graphene (TTG, TQG, and TPG) structures with $\theta = 1.52 \pm 0.02^\circ$ (device D1, trilayer), $\theta = 1.80 \pm 0.04^\circ$ (D2, quadrilayer), and $\theta = 1.82 \pm 0.05^\circ$ (D3, pentalayer), respectively. We also measured a second TQG device at $\theta = 1.64^\circ$, shown in the appendix (Fig. B.3). We find that TTG, TQG, and TPG all exhibit hallmark signatures of strong correlations (Fig. 5.3), including robust superconductivity on electron and hole sides and flavor symmetry breaking as revealed by pronounced resistance peaks around certain integer filling factors ν (number of electrons per moiré site). These peaks, particularly at higher temperature—such as at 7 K in Fig. 5.3c—look analogous to the cascade peaks in TBG.

Furthermore, each sample has a dependence on electric displacement field D shown in Fig. 5.4. The correlated features at $|\nu| < 4$ generally disappear at high D , likely due to strong hybridization between bands (as shown in Fig. 5.2 right panels) that tends to broaden and change the character of the flat bands. The hybridization in

each device also reveals a more resistive region in the $|\nu| \approx 4$ range between flat and dispersive bands since the dispersive low-energy bands (red and yellow in Fig. 5.2) are lifted, and Dirac cone-like structures (which have a low density of states near the cone) are raised above the flat bands.

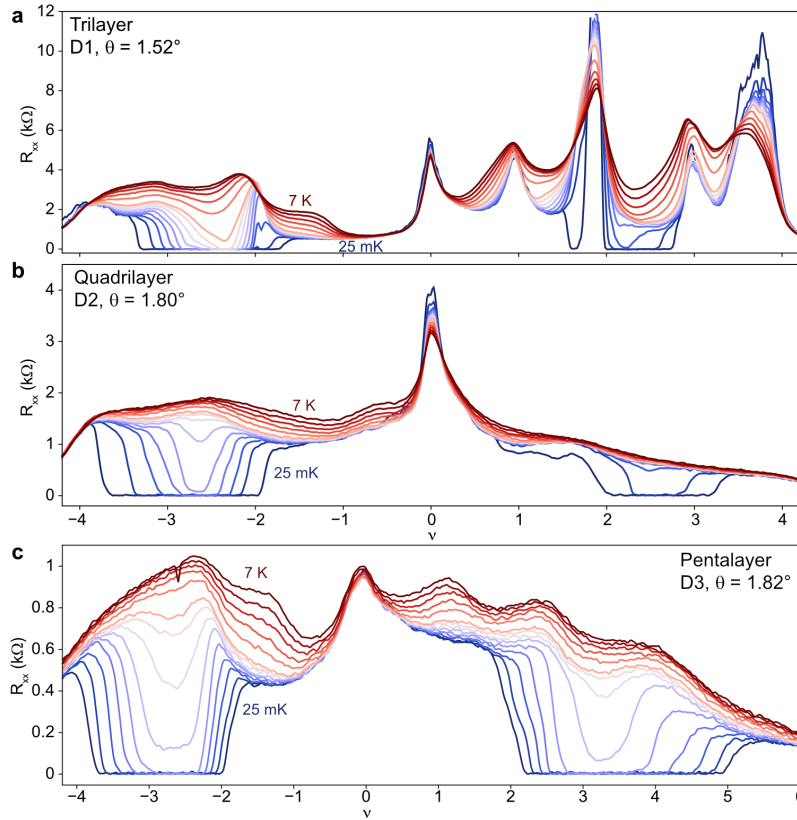


Figure 5.3: R_{xx} linecuts for TTTG device D1 (a), TQG device D2 (b), and TPG device D3 (c) at a range of temperatures (25 mK, every 0.25 K from 0.25 to 2 K, and then every 1 K from 3 to 7 K). The cuts were taken at constant D fields of $D/\epsilon_0 = 0.22$ V/nm (a), -0.15 V/nm (b), and 0 V/nm (c).

All devices investigated here show a high degree of twist angle homogeneity as characterized by four-point measurements between different pairs of contacts. Fig. 5.5 shows R_{xx} versus carrier density with fixed top-gate voltage ($V_{tg} = 0$ V), revealing that almost every pair of contacts shows superconductivity. More importantly, superconducting pockets from different pairs significantly overlap in the filling range, and resistance peaks at $|\nu| = 4$ appear at the same density. Moreover, all findings related to the extent of the superconducting phase and the occurrence of the symmetry-breaking transitions in the ν - D phase diagram are reproducible over multiple contact pairs. This also includes the observation of a gapped correlated in-

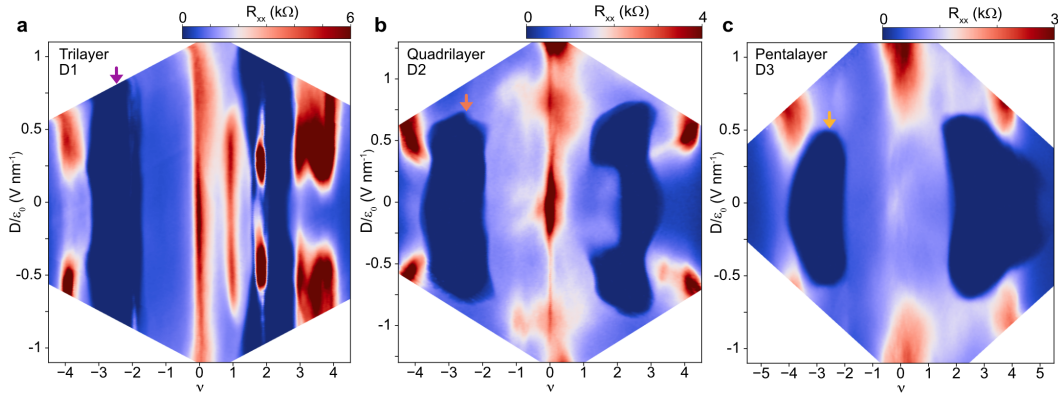


Figure 5.4: R_{xx} measurements as a function of ν and electric displacement field D for TTG (a), TQG (b), and TPG (c).

ulator at $\nu = +2$ in TTG, which has not been reported previously. In this context, we note that any significant twist-angle disorder would create conducting percolation pathways that quickly suppress insulating behavior.

We attribute the low level of disorder to the increased twist angle relative to TBG—which results in less twist angle relaxation—and the use of monolayer WSe₂ during device stacking, presumably originating from the increased lateral friction between WSe₂ and graphene (compared to the friction at the hBN-graphene interface). We note that this additional layer does not change the magic-angle condition [14, 46], and the induced spin-orbit interaction (SOI) energy scale is ~ 1 meV in twisted bilayers [46]. Therefore, SOI is likely too small to significantly affect the overall band structure and directly impact the cascade physics at the *magic angle* (though may play a more important role for stabilizing superconductivity far away from the magic angle [46]). Finally, we note that, in general, SOI is expected to manifest differently when the sign of the D field is reversed, a feature that has not been observed in the experiment. The absence of D -field asymmetry is probably due to the small energy scale of SOI compared to the interactions and the weak tendency to polarize wavefunctions with D field in magic-angle graphene multilayers.

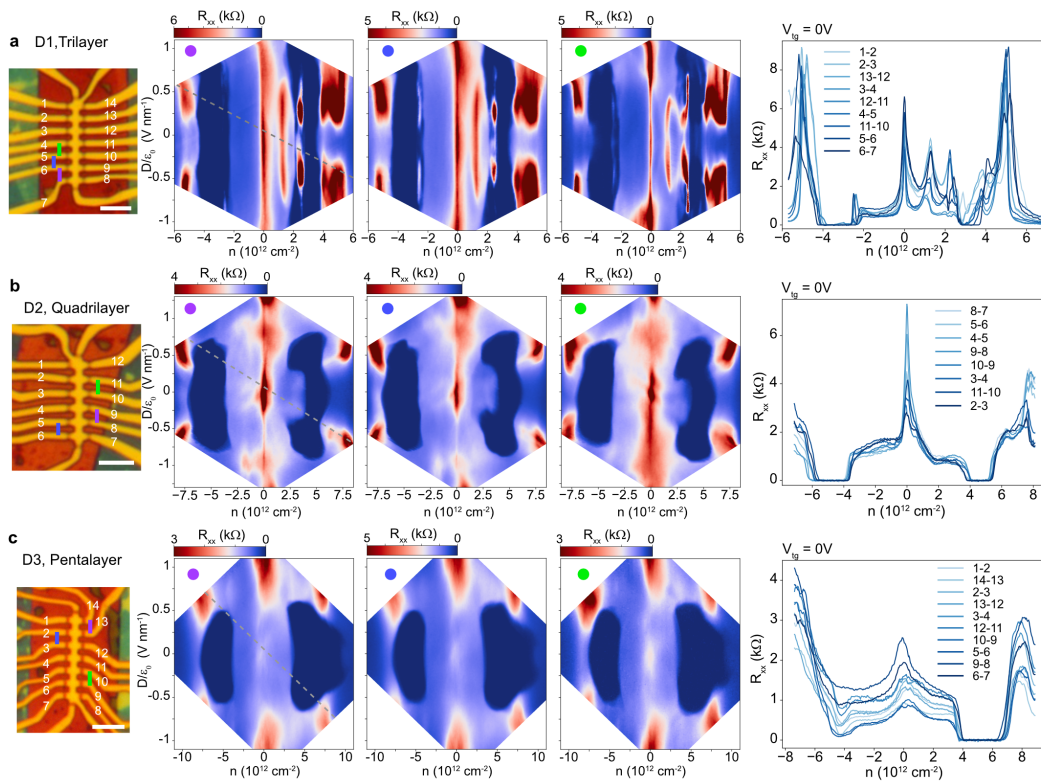


Figure 5.5: Leftmost optical images are devices D1–D3. The scale bar in each panel is $5 \mu\text{m}$. R_{xx} 2D diagrams (n – D) shown in the middle are obtained from electrodes marked with the corresponding colored lines. The electrodes marked with purple lines were used for measuring R_{xx} in the other figures of the text. Rightmost plots were taken at $V_{tg} = 0 \text{ V}$ (along the grey dashed lines in the n – D plots). All three devices have a high degree of homogeneity in twist angle with the same superconducting filling range and $|\nu| = 4$ carrier density for multiple contacts.

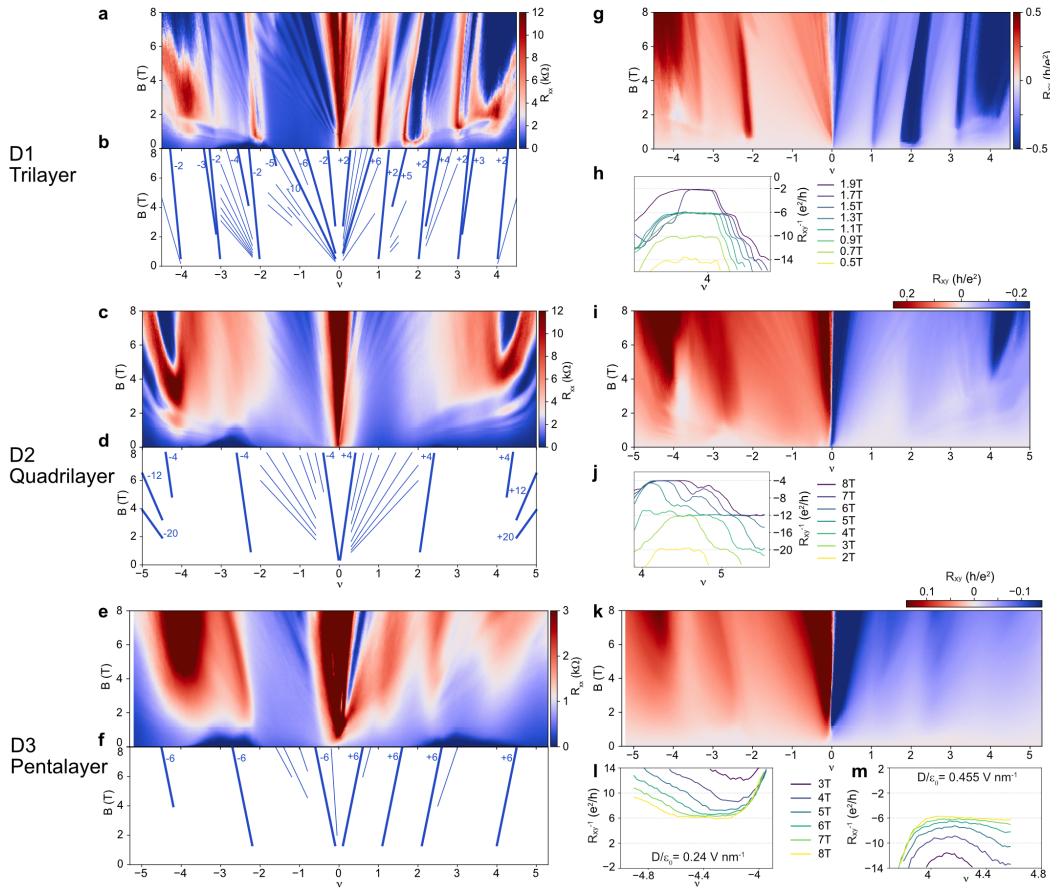


Figure 5.6: Landau fans of multilayer devices. (a)–(f) R_{xx} measured as a function of B field and ν from trilayer to pentalayer. The main sequences of the fan diagrams are labelled below the R_{xx} plots. Landau levels from the dispersive bands are visible as R_{xx} oscillations at low B fields in the fan diagrams. (g)–(m) R_{xy} measured as a function of B field and ν from trilayer to pentalayer. Below the 2D plots, we show Hall conductance linecuts around $|\nu| = 4$. The layer number n determines the resulting quantization. Since the dispersive bands of n -layer magic-angle graphene consist of $n - 2$ Dirac-like cones (at low energies), the $|\nu| = 4$ quantization is therefore expected to follow monolayer graphene sequence multiplied by $n - 2$. The plateaus in TTG and TQG clearly show this trend, while in TPG only the first plateau is observed. These observations however confirm the number of layers in each sample.

Twist angles were determined from high B field data and corresponding Landau-fan diagrams in a similar way as in TBG. From the slope of the Landau fan at charge neutrality (which is directly proportional to the gate-sample capacitance) and the voltage difference between charge-neutrality point (CNP) and $|\nu| = 4$ filling, the corresponding $|\nu| = 4$ electron density is obtained. We used two separate criteria for the assignment of $|\nu| = 4$. First, at high D fields, resistive features (peaks) emerge (Fig. 5.4), as discussed before. We interpret these peaks presumably as the opening of the hybridization ‘gaps’ and corresponding full filling ($|\nu| = 4$) of the ‘gapped’ bands. Even though the Dirac-like bands prevent full gaps, their low density of states should not change ν too drastically. Second, at high B fields, quantum Hall insulating states develop around $|\nu| = 4$, which typically cover a broader filling range where Hall conductance is quantized in accordance with the expectations from the dispersive bands (Fig. 5.6, also see discussion below). These high- B features can also be cross-checked with fan-like features coming from $|\nu| < 4$. The electron density of $|\nu| = 4$ directly determines the twist angle in the low-angle approximation $\theta^2 \approx \sqrt{3}a^2n_{|\nu|=4}/8$, where $a = 0.246$ nm is the graphene lattice constant.

In terms of mismatched twist angles between layers and twist angle disorder, it is difficult to experimentally determine the magnitude, but there are a few reasons that suggest our samples are close to the desired alternating twist angle structure, with matching twist angles for even/odd layers. When multiple distinct twist angles are present [133], the resulting band structure is expected to become very complex (notably, no sense of single moiré periodicity remains) and deviates significantly from the observed experimental results. Importantly, the resulting band structures noticeably deviate from the ones described in Fig. 5.2, where for n layers at zero D field, there are $n/2$ (for even n) or $(n-1)/2$ (for odd n) sets of overlapping TBG-like bands (one flat) and 1 Dirac cone if n is odd. Although the parameter space is too large to provide a thorough analysis, we provide some references with varying geometries that do not agree with our experimental observations [134–136].

We note that signatures of the dispersive bands are also observed in Landau-fan diagrams and vHs (Fig. 5.6 and Fig. 5.15). For example, emerging Landau levels from the dispersive bands are typically observed through oscillations at low magnetic field. Since at low energies, the dispersive bands (Fig. 5.2 left panels in yellow and red) can be effectively treated as decoupled monolayer graphene-like bands when considering the Landau level spectrum (see Section 2.2), the corresponding Hall conductance around $|\nu| = 4$ will be quantized in a way that depends on the number

of layers. As we see in Fig. 5.6g–m (particularly the linecuts), the $\nu \approx 4$ Landau level TTG sequence follows (2, 6, 10, etc.) as in monolayer graphene. For TQG, the sequence is roughly like two decoupled monolayers: 4, 12, 20, etc. Although the TPG sequence is less clear, the first level can be made out at 6, following three decoupled monolayers, as we would expect from the band structure (Fig. 5.2c). Furthermore, both TQG and TPG devices show vHs signatures at $|\nu| \approx 6$, consistent with the expectation for vHs from roughly half filling of the dispersive TBG-like bands (see Fig. 5.15).

5.3 Gaps in TTG and TQG

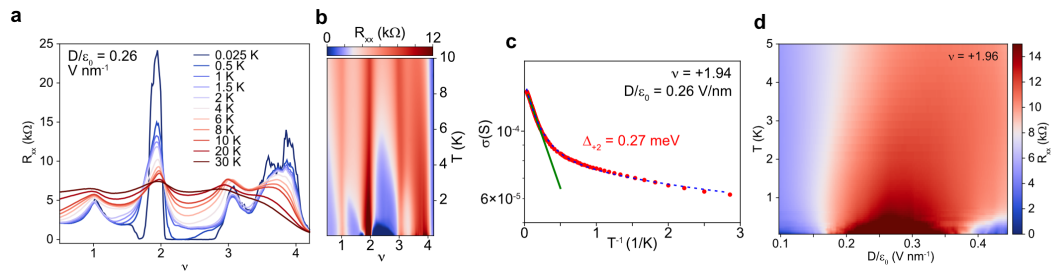


Figure 5.7: Measurements of the $\nu \approx 2$ insulator in TTG through linecuts (a), and equivalent 2D diagram (b). Activation gap measurement (c), and D dependence (d).

In addition to the symmetry-breaking transitions previously reported in TTG [51, 127, 128], our TTG structure (coupled to a tungsten diselenide (WSe₂) monolayer [46]) exhibits a previously unobserved correlated insulating state near $\nu = +2$ at finite D (Fig. 5.7). We note that this insulating state is more resistive than the other states in the vicinity Fig. 5.7a,b, and we determine it is gapped by its activated temperature dependent behavior in Fig. 5.7c. This behavior cannot arise at the non-interacting band theory level, which always predicts semimetallic bands, and is instead attributed to the interplay between an interaction-driven cascade transition and hybridization induced by the D field (e.g., as captured by Refs. [137, 138]). The D -dependence, particularly its finite extent at $0.2 < D/\epsilon_0 < 0.35$, is further shown in Fig. 5.7d.

The behavior is suppressed by an out-of-plane B field of $B_{\perp} > 0.4$ T but is mostly insensitive to the in-plane B field (the weak suppression by the in-plane B field could possibly originate from a non-ideal in-plane-field alignment of the sample), as shown in Fig. 5.8. These experimental observations are highly indicative of a gap that originates from strong interactions in TTG. We note, however, that the formation

of fully gapped states in TTG requires a mechanism that additionally gaps out the MLG-like band, which may explain the presence of the gap only at finite D fields. Moreover, suppression of the gap with an out-of-plane magnetic field is at odds with the C_2 breaking scenario [66, 67] and is more in line with incommensurate Kekulé spiral [124] or intervalley-coherent [117, 137–139] orders in the flat bands. The insensitivity to in-plane field is suggestive of a spin-polarized insulator or a phase that is otherwise insensitive to in-plane magnetic field. Finally, we can not rule out that the gap originates from induced SOI, since it is still possible that SOI promotes instabilities that favor the formation for certain $\nu = +2$ insulating states in TTG.

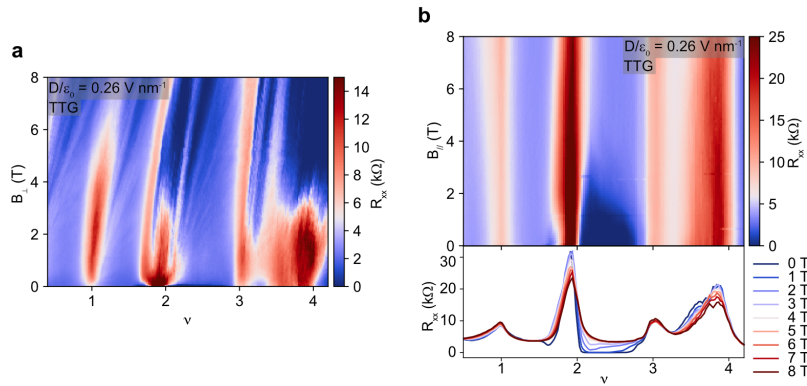


Figure 5.8: Magnetic field dependence of the TTG insulating state under out-of-plane magnetic field (a) and in-plane magnetic field (b). Linecuts at the bottom of (b) are for clarity.

We have also detected an insulating state developing at finite D fields in TQG near charge neutrality, as seen in Fig. 5.9a. The gap opens at $D/\epsilon_0 \approx 1.2$ V/nm, and it increases with increasing D . However, in contrast to TTG, the TQG insulating state can be explained through the D -induced hybridization only. As mentioned above, the continuum model predicts that in a sample with $\theta > \theta_{TTG}^{magic}$, the bands at the CNP are metallic until a finite D , where they gap out. And in TTG, there is no monolayer graphene-like Dirac cone to keep the bands metallic, so the result is predicted based on single-particle physics (Fig. 5.9c,d). The D field where the CNP is first gapped also serves as a constraint for modeling the system, helping determine w_{AB} . Note that the charge-neutrality gap is a good reference for matching the experimental D field with potential difference U (which we defined above) used in calculations since the interaction-driven Hartree correction vanishes at the CNP.

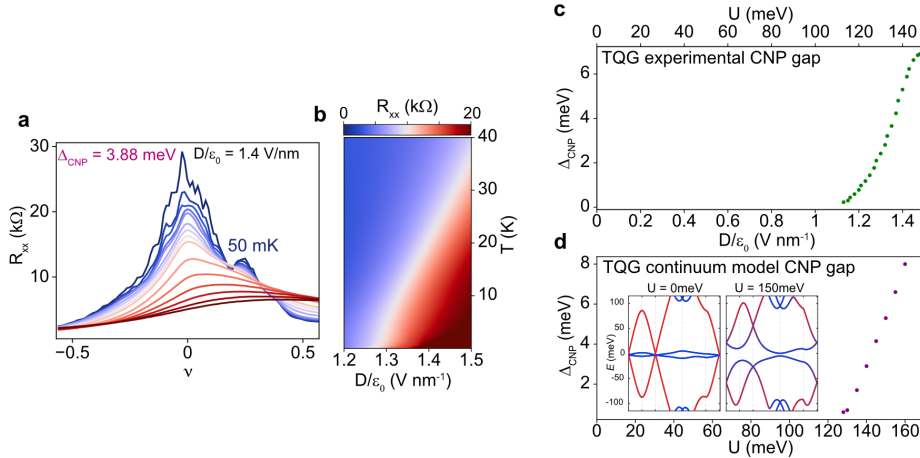


Figure 5.9: The R_{xx} gap behavior at charge neutrality in TQG revealed with temperature linecuts (a), and a D -temperature diagram (b). (c) Experimentally derived gaps with respect to D and (d) TQG continuum-model gaps. U is the top-bottom layer potential used.

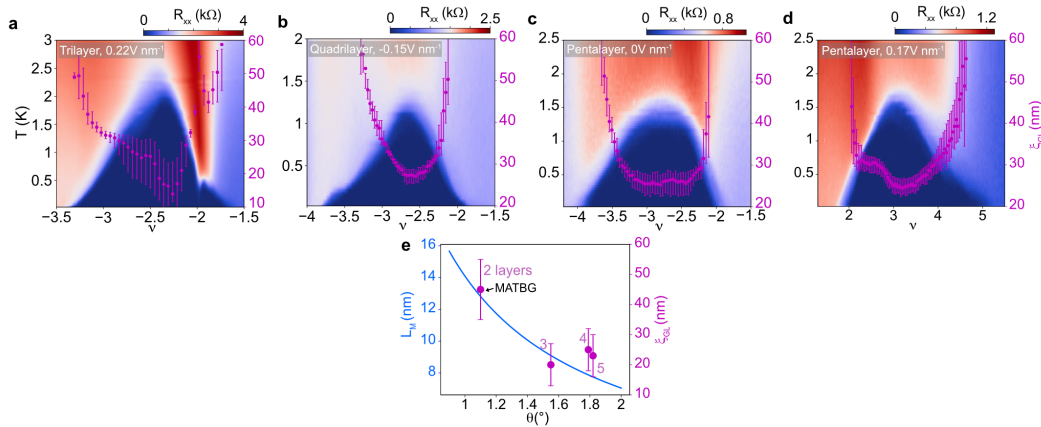


Figure 5.10: (a)–(d) Ginzburg–Landau coherence lengths ξ_{GL} (for details on determining ξ_{GL} , see Section B.1) versus ν for all three devices around $\nu = -2$ —and for $\nu = +2$ for TPG (d)—superimposed on the R_{xx} versus T and ν plots. (e) ξ_{GL} and moiré wavelength L_M versus twist angle of different layers, suggesting a possible relation between the two length scales.

5.4 Superconducting regions

The superconducting regions in all three structures extend over significantly larger filling factor ranges in comparison to TBG [20, 43, 46, 48] where superconductivity is typically observed within $2 < |\nu| < 3$. Moreover, superconductivity is ‘ascendant’ as the layer number is increased, in the sense that it emerges over successively broader regions of phase space, reaching $\nu \approx +5$ on the electron side for TPG

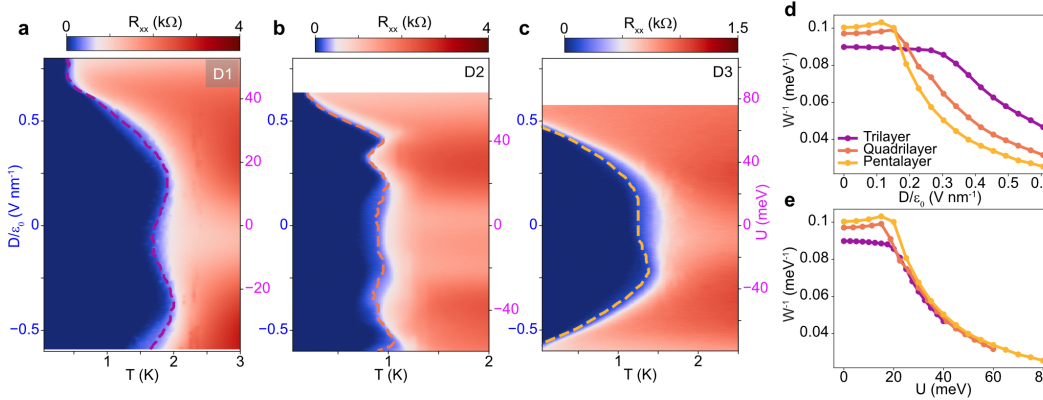


Figure 5.11: Critical temperature T_c is indicated by a dashed line that delineates 10% of the normal state resistance (see Section B.1 for details). T_c is maximized at finite D fields. Overall, superconductivity is suppressed more easily with D as the layer number is increased for both hole ((a)–(c)) and electron (Fig. B.2) doping. (d) Theoretical calculations of the inverse of the flat-band bandwidth for twisted trilayer, quadrilayer, and pentalayer graphene as a function of D/ϵ_0 (top) and potential difference U (bottom). For a fixed D , the bandwidth of the flat bands is larger for systems with more layers, but when expressed as a function of U , the flat-band broadening follows a similar trend across the different structures.

(Fig. 5.3). Along with a zero longitudinal resistance R_{xx} observed in the characteristic ν vs. T dome (Fig. 5.10), we also measure large critical currents (~ 400 nA) and Fraunhofer-like patterns, substantiating the robustness of phase coherence (shown in the appendix, Fig. B.1).

Moreover, high critical perpendicular magnetic fields B_c (typically ~ 0.8 T) indicate that the corresponding Ginzburg–Landau coherence lengths ξ_{GL} (approximately 10–30 nm) are significantly smaller than those observed in TBG (Fig. 5.10e) and deviate from the weak-coupling prediction, $\xi_{GL} \approx \hbar v_F / \pi \Delta$ with $\Delta \approx 1.76 k_B T_c$ —suggesting a strong-coupling origin of superconductivity [127, 128] (see Section B.1). When combined with other recent experiments [129, 132, 140], these observations affirm the unconventional nature of superconductivity within the entire class of graphene moiré systems. Further, the measurements on three to five layers indicate that the addition of layers promotes superconductivity over a broader filling window despite the coexisting dispersive bands as well as the ostensibly increased vulnerability to disorder—both from the additional twist angles as well as from the sensitivity to the relative displacement between layers.

In addition to the pronounced ν -dependence, the observed superconducting pockets are highly tunable with electric displacement field D . A comparison of the three structures reveals that TQG and TPG are more tunable than TTG. This is apparent both in the D -dependent evolution of the filling range where superconductivity is measured (Fig. 5.4) as well as in the critical temperature T_c (Fig. 5.11a–c). Notably, superconductivity in TQG and TPG is fully quenched for all fillings at $D/\epsilon_0 = 0.75 \text{ V nm}^{-1}$ and $D/\epsilon_0 = 0.6 \text{ V nm}^{-1}$, respectively. In the case of TTG, however, superconductivity is present up to the maximum accessible electric field $D/\epsilon_0 = 1 \text{ V nm}^{-1}$. Nevertheless, superconductivity is largely suppressed at optimal doping in all three heterostructures; further, they reveal that T_c forms a D -symmetric dome maximized at small finite D fields (for electron-side data showing similar behavior see Fig. B.2). We also note that TTG, TQG, and TPG all exhibit a similar variation of T_c when viewed as a function of the potential difference U (as defined in Section 5.3 and represented on the right side of panels (a)–(c) in Fig. 5.11) between the top and bottom layers. This layer-number invariance is consistent with non-interacting continuum-model calculations tracking the evolution of the inverse of the flat-band bandwidth with U (Fig. 5.11e). The dependence of T_c on D in all devices qualitatively matches the predictions of Ref. [103] for TTG with one marked exception: the observed vanishing of superconductivity and the decay of T_c appears to be linear in D (Fig. 5.11b,c and Fig. B.2), in line with predictions for multilayer graphene with rhombohedral stacking [141] and in contrast to the exponential ‘tail’ typically expected from the weak-coupling theory (and seen in the model of Ref. [103]).

5.5 Hall density analysis

Comparing the location of the superconducting regions with the evolution of the Hall density as a function of D and ν in TTG, TQG, and TPG provides further insight into the intricate relationship between the superconducting phase and the correlation-modified Fermi surface (Fig. 5.12). As in previous TBG and TTG measurements, we observe symmetry-breaking electronic transitions (a ‘cascade’ of transitions) that are signalled by sudden drops in the Hall density magnitude (a ‘reset’) without a change in sign (see Fig. B.4g–i for examples of these features). These resets (see dashed lines in Fig. 5.12) indicate a rearrangement of spin/valley sub-bands and typically occur near integer fillings of the flat bands [74, 75]. At low D fields, superconducting pockets onset around the $|\nu| = 2$ resets (purple dashed line), and the filling extent of superconductivity varies depending on the presence

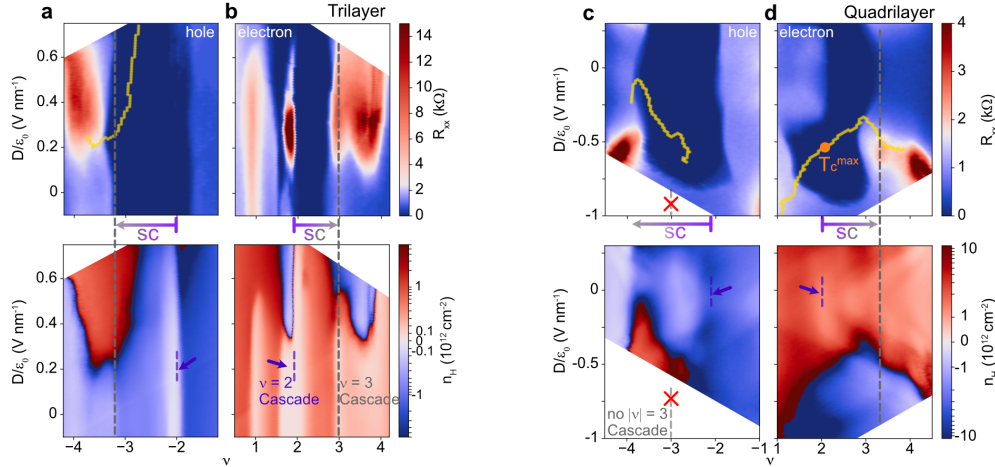


Figure 5.12: Comparison of Hall and longitudinal resistance in tri- and quadrilayer graphene devices. (a), (b) D field and ν dependence of R_{xx} (top) and Hall density (bottom, measured at $B = 0.9$ T) for TTG. Purple and grey dashed lines mark the filling factors where flavor symmetry-breaking transitions associated with $|\nu| = 2$ and $|\nu| = 3$ happen, respectively. The yellow line in (a) delineates the evolution of the vHs. (c), (d) Same for TQG (bottom, measured at $B = 1.5$ T). The superconducting T_c reaches its maximum (orange dot in (d)) exactly at the position of the vHs. When present, flavor symmetry-breaking transitions around $|\nu| \approx 3$ coincide with the termination of superconductivity. By contrast, superconductivity extends much further in the absence of a $|\nu| \approx 3$ reset (c).

or absence of a $|\nu| = 3$ flavor symmetry-breaking transition (grey dashed line). For electron- and hole-doped TTG as well as for electron-doped TQG (Fig. 5.12a, b, d), a flavor symmetry-breaking transition appears around $|\nu| = 3$ and superconductivity accordingly terminates, as previously noted in TTG [127]. By contrast, when signatures of the $|\nu| = 3$ reset are completely absent (for example in hole-doped TQG, Fig. 5.12c, or in TPG, Fig. 5.13), superconductivity extends much farther. Combined, these observations suggest that superconductivity is favored when only two out of the four flavors are predominantly populated ($|\nu| = 2$ cascade) and suppressed beyond $|\nu| = 3$ resets. This behavior can be understood within the simplest iteration of the cascade scenario: resets associated with $|\nu| = 3$ produce spin- and valley-polarized bands [125, 142, 143] and naturally disfavor Cooper pairing of time-reversed partners.

At high D fields, signatures of the cascade vanish and instead van Hove singularities (vHs) become more prominent, reflecting qualitative changes in the band structure (see yellow lines in Fig. 5.12 and Fig. B.4 that track the vHs). Consistent with

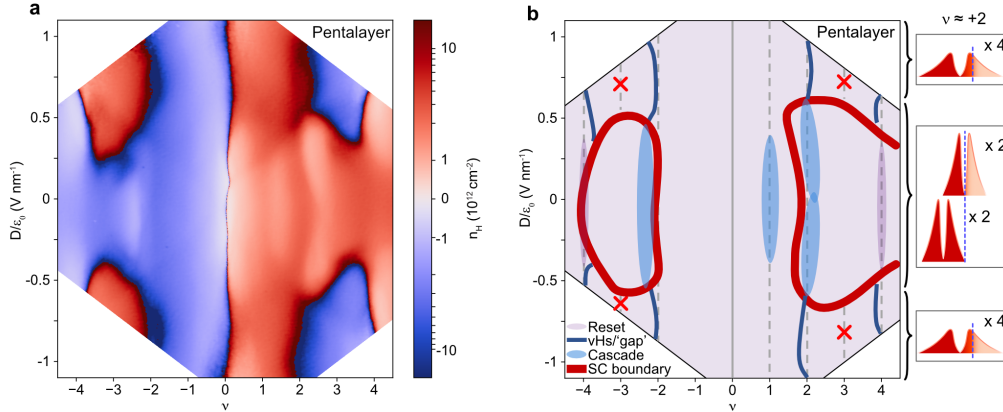


Figure 5.13: TPG device Hall density and phase diagram. (a) Hall density as a function of ν and D . (b) Schematic of features in the phase diagram of TPG, mapping out the cascade (present at low D but not present at high D), van Hove singularities, superconducting boundary, and $|\nu_{\text{flat}}| = 4$ Hall density resets. Sketches of the DOS around $\nu = +2$ for different D fields are shown on the right. The middle panel illustrates the flavor symmetry polarization observed in regions that support superconductivity. Flavor symmetry is preserved at higher D fields, as shown in the top and bottom panels.

previous TTG measurements [127, 128], the vHs in our TTG sample (as well as in TPG, see Fig. 5.13) crudely bound the superconducting regions. By contrast, the vHs in TQG cross well into the superconducting pockets—in fact, for electron doping, T_c reaches its maximum exactly at the position of the vHs (orange dot in Fig. 5.12d or see Fig. B.5d–f for more details). In our second TQG device, the vHs behavior crossed into the superconducting pocket, but it was not as pronounced as the first device (Fig. B.3), likely due to the smaller twist angle. The interplay between the vHs and superconducting boundaries, as revealed in Hall density measurements, is complex: T_c can be both enhanced and suppressed at the vHs depending on the layer number and possibly other details such as the precise twist angle.

Pentlayer measurements provide additional signatures that point towards a close relation between superconductivity and flavor symmetry-breaking cascades (Fig. 5.13). In contrast to TTG, in TPG we can access D fields that are large enough to stifle superconductivity—which occurs simultaneously with the onset of the vHs and the apparent suppression of the cascade transitions (see red and light blue lines in Fig. 5.13b that mark the superconducting boundaries and the cascade transitions, respectively). For example, at low D fields ($|D|/\epsilon_0 < 0.6 \text{ V nm}^{-1}$) around $\nu = +2$,

the Hall density resets close to zero, in line with a nearly complete flavor symmetry-breaking polarization. However, at higher D fields ($|D|/\epsilon_0 > 0.6 \text{ V nm}^{-1}$), the Hall density is dominated by a vHs around $\nu = +2$, while the cascade signatures are diminished. Superconductivity accordingly also vanishes. For hole doping, the disappearance of superconductivity similarly coincides with the weakening of the cascade. This on/off correspondence between the two phenomena suggests that they either share a common origin, such as a large density of states, or that the cascade serves as a prerequisite for robust superconductivity in graphene moiré superlattices.

5.6 Superconductivity extended to $\nu \approx 5$ in TPG

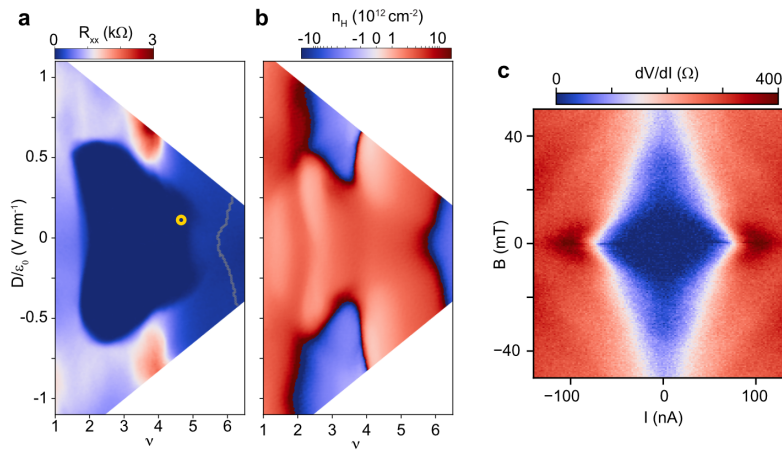


Figure 5.14: Electron-side superconductivity in TPG. (a), (b) 2D plots of R_{xx} and Hall density n_H , respectively, showing the extent of superconductivity, how it evolves with D and is associated with features in panel (b). (c), Fraunhofer-like pattern taken at the yellow point in (a).

As mentioned above, for low D fields in TPG, the superconducting pockets are extraordinarily large, spanning $-4 \lesssim \nu < -2$ for hole doping and $+2 \lesssim \nu \lesssim +5$ for electron doping (Fig. 5.10c,d, Fig. 5.4c, and Fig. 5.14). In particular, the electron-side range corresponds roughly to a density window of $6 \times 10^{12} \text{ cm}^{-2}$, which is the largest filling range so far reported in a graphene-based superconductor. The observed superconductivity exhibits similar values of T_c and B_c as the trilayer and quadrilayer samples and is likewise accompanied by a Fraunhofer-like pattern of critical current (Fig. 5.14c), confirming superconducting phase coherence. This contrasts TBG, where superconductivity originating at $|\nu| \approx 2$ almost always dies before about $|\nu| \approx 3$. We emphasize that the unprecedented persistence of superconductivity across a large filling factor range in TPG (and also TQG in comparison to TTG or TBG) cannot be explained in a minimal framework of alternating twisted

graphene multilayers [130, 144] without invoking the non-trivial role of the additional bands.

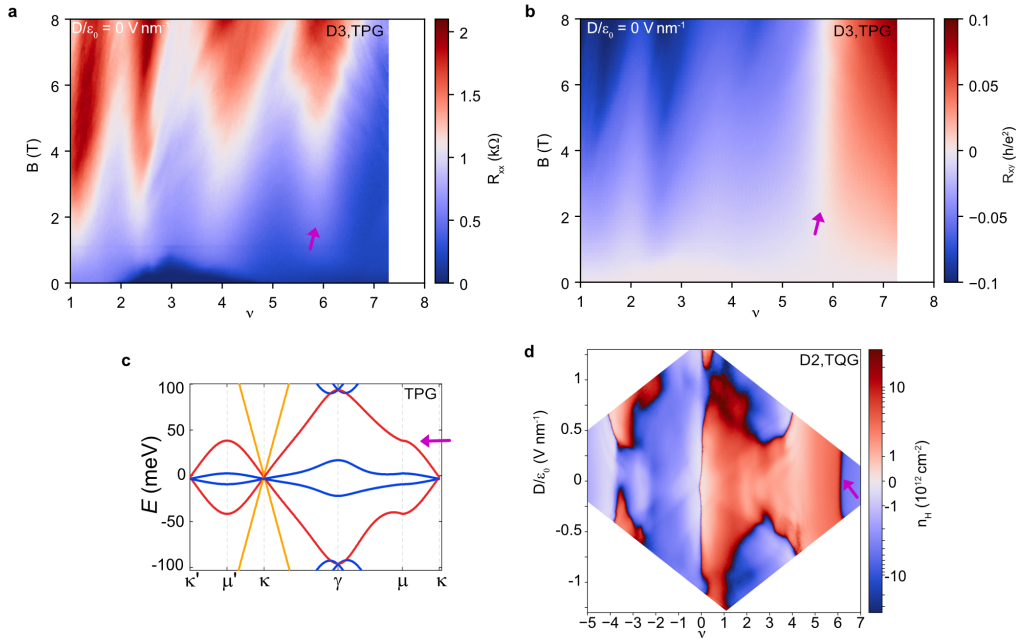


Figure 5.15: Observation of a vHs near $\nu = 6$. R_{xx} (a) and R_{xy} (b) for large ν in TPG at $D = 0$. The purple arrows show the vHs located in the dispersive TBG-like band near its half-filling point ($\nu \approx 6$), which is shown in the band structure of (e). The same vHs is also present in TQG (d), which also has a dispersive TBG-like band (compare to Fig. 5.14b).

The role of the additional bands in TPG deserves careful consideration due to the implications for the strength of interactions (such as Hartree effects) and the types of superconductivity the bands can plausibly support. Explanations for the enlarged superconducting intervals can generically be organized into three scenarios depending on the filling of the flat TBG-like bands ν_{flat} , relative to the total filling ν_{max} at which superconductivity terminates ($\nu_{\text{max}} = +5$ for electron-doped TPG and $|\nu_{\text{max}}| = 4$ for TQG and hole-doped TPG). Briefly, in scenario (i), ν_{max} corresponds to $\nu_{\text{flat}} \approx +3$, the flat-band filling at which superconductivity is typically suppressed in TBG, suggesting that the superconducting phase space is largely the same for different multilayer magic-angle structures when considering just the flattest TBG-like bands. In scenario (ii), ν_{max} coincides with $\nu_{\text{flat}} \approx +4$, precluding any simple analogy with TBG, although superconductivity can still be attributed to the flat bands. Finally, scenario (iii) assumes full filling of the flat bands *before* superconductivity

is suppressed at ν_{\max} . This scenario includes the possibility that the distinction between the different TBG- and MLG-like bands breaks down even at $D = 0$ due to hybridization as well as potential multi-band superconductivity [145–148]. In this case, superconductivity in TPG is a more general phenomenon than in TBG since it occurs in either mixed bands or new, more dispersive bands.

From the perspective of the non-interacting band structure, the three scenarios all seem implausible, therefore interactions must play a crucial role. In particular, although the presence of the dispersive bands implies that $|\nu| - |\nu_{\text{flat}}| > 0$, this effect is much smaller than needed for either scenario (i) or (ii). Coulomb interactions can significantly enhance $|\nu| - |\nu_{\text{flat}}|$, either by evening out the spatial charge distribution [14, 98, 115, 149, 150] or symmetry breaking. We developed a few simple models for TPG incorporating these mechanisms (for more details on the model including interactions, see the Supplementary Material in Ref. [58]) and show an outline of the results in Fig. 5.16 and 5.18. We now return to the three scenarios while considering the effects of interactions along with the experimental behavior near $\nu \approx 4$ shown in Fig. 5.20, 5.19 and the presence of vHs at $\nu \approx 6$ (Fig. 5.14b and Fig. 5.15). Note that in the discussion below, ν denotes the total number of electrons per moiré site, and ν_{flat} denotes the number of electrons per moiré site added to the flat TBG-like bands.

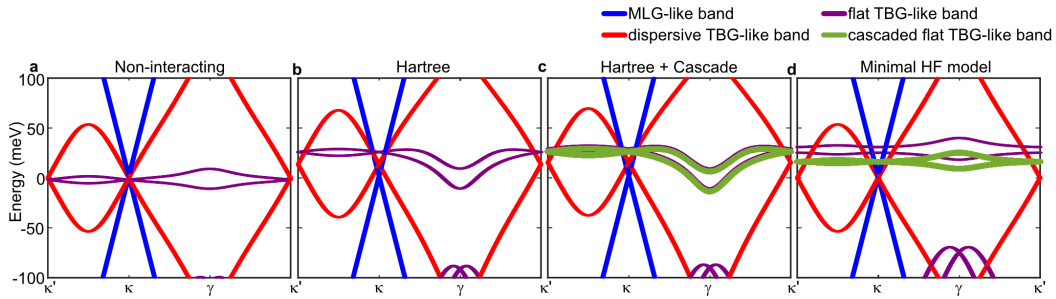


Figure 5.16: Depiction of different approximation schemes used to understand the role of interactions in TPG. Note that the Hartree correction shifts the flat band (purple) up in energy, and the chemical potential (for a given ν) consequently also shifts upward. Cascaded bands (bands that are totally filled as a result of symmetry breaking) in (c) and (d) are shown in green. (d) corresponds to a minimal model of Hartree and Fock effects characterized by a Hartree shift (Δ_H) and a Fock gap (Δ_F).

Scenario (i): flat TBG-like bands are filled to $\nu_{\text{flat}} = +3$ at $\nu = +5$

For TBG and TTG, the strongest superconducting pockets normally start from $|\nu| = 2$ and end around $|\nu| = 3$. Therefore, a conventional scenario would suggest that TPG could behave in a similar way, i.e., flat TBG-like bands are filled to $\nu_{\text{flat}} = +3$ when superconductivity is diminished at $\nu = +5$. This scenario implies that the additional two electrons per moiré site are distributed in the dispersive TBG- and MLG-like bands due to the Hartree interactions, with a large portion of the charge carriers being hosted by the dispersive TBG-like bands. Our modeling suggests a minimal flat-band occupation $\nu_{\text{flat}} \gtrsim +3.8$ at $\nu \approx +5$ (see Fig. 5.18a, c, which show that unphysically large Δ_H and Δ_F are required to allow for $\nu_{\text{flat}} < +3.8$), diminishing the plausibility of scenario (i) for electron-doped TPG which has $\nu_{\text{max}} \approx +5$. The relevance of this scenario is further undermined by the observation of vHs at $\nu \approx +6$ (Fig. 5.15): under the reasonable assumption that the non-interacting band structure remains valid for the dispersive TBG-like bands (apart from a Hartree shift), scenario (i) would instead place the observed vHs near $\nu \approx +5$ due to the vHs occurring near half filling of the TBG-like band. Taken together, these arguments effectively rule out scenario (i).

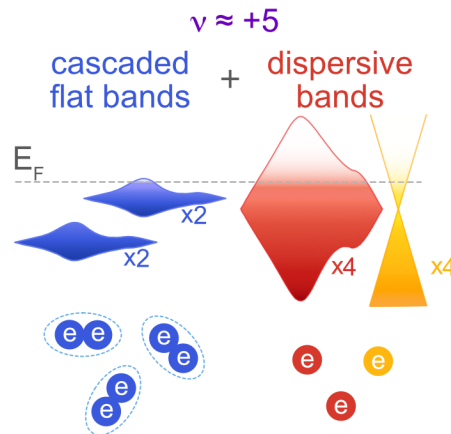


Figure 5.17: A schematic of the three bands contributing to ν . Superconductivity is expected in cascaded flat bands (blue). The schematic depicts scenario (ii), where the dispersive bands collect charge, keeping the flat bands from filling until $\nu \approx 5$, where superconductivity ends.

Scenario (ii): flat TBG-like bands are filled close to $\nu_{\text{flat}} = +4$ at $\nu = +5$

As a result of interactions, a fraction of electrons are preferentially distributed in the dispersive TBG- and MLG- like bands. It is therefore possible that for total filling of $\nu \approx +5$, the flat TBG-like bands are filled close to $\nu_{\text{flat}} \approx +4$, with the extra

one electron per moiré site being distributed in the other bands (see Fig. 5.17 for a schematic). Fig. 5.18a shows the filling correspondence between ν_{flat} and ν for various interaction terms given a reasonable dielectric constant under two methods of accounting for correlations. Whether using just Hartree correlations (solid lines) or including cascade effects (dashed lines), it is plausible that the dispersive bands could hold the extra electron necessary to keep superconductivity in the flat bands. In this scenario, the modeling suggests that the filling of the flat bands is nearly four ($\nu_{\text{flat}} > +3.8$) when $\nu \approx 5$, which is well outside the typical TBG superconducting range. However, the appearance of $\nu \approx \nu_{\text{flat}} = 4$ resistive states at high D suggests the filling ν_{flat} is modified at high D . This is shown in Fig. 5.18b, where the dashed lines indicate that the flat bands fill more quickly once a finite D has been applied. In this scenario, the flat bands are filled with 4 electrons per unit cell by $\nu \approx 5$, so by the time $\nu = 6$ is reached, 2 electrons per unit cell can be distributed to the dispersive bands. This allows for the appearance of the vHs in Fig. 5.15.

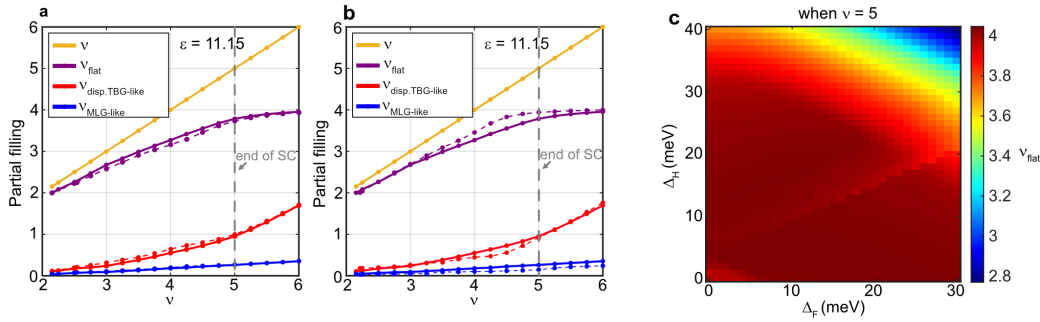


Figure 5.18: Model calculations, including interactions, of band filling. (a) Partial filling of each subsystem versus total filling ν for a fixed dielectric constant $\epsilon = 11.15$. Here, solid (dashed) lines correspond to a cascaded (uncascaded) solution with the cascade solution enabling higher filling of the flat-band subsystem. (b) Similar to (a) but the solid (dashed) lines correspond to a solution at potential difference $U = 0$ meV ($U = 34$ meV). Finite D allows the flat bands to fill more quickly. (c) filling of the flat-band subsystem as function of the Hartree and Fock terms, holding total ν constant. While (a), (b) are calculated using the model shown in panel (b), (c) of Fig. 5.16, (c) is calculated using the minimal Hartree-Fock model of panel (d) in Fig. 5.16.

Scenario (iii): flat TBG-like bands are fully filled to $\nu_{\text{flat}} = +4$ before $\nu = +5$ or hybridization of different bands obscures the distinction between them

The last scenario suggests either that the flat TBG-like bands are fully filled *before* the suppression of superconductivity, in which case superconductivity would exist in the more dispersive bands, *or* that the distinction between the different TBG- and MLG-like bands breaks down due to hybridization (i.e. mixing), even at $D = 0$. Such mixing between flat, dispersive TBG-like, and MLG-like bands obviates our definition of ν_{flat} , potentially allowing flavor polarization, and accompanying superconductivity, to persist well beyond $\nu = +4$. While such hybridization is expected for finite D fields, mixing between flat, dispersive TBG- and MLG-like bands for $|\nu| < |\nu_{\text{max}}|$ may occur even at $D = 0$ due to, for example, proximity to WSe_2 , layer-to-layer charge inhomogeneity, or distant-layer coupling.

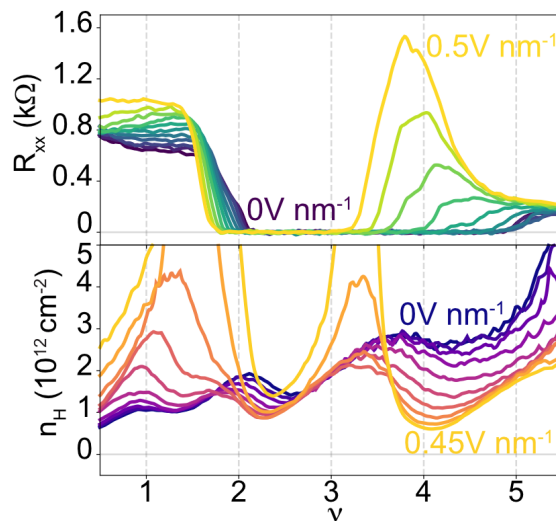


Figure 5.19: TPG measurements near $\nu = 4$. R_{xx} (top panel) and Hall density (bottom panel) measurements measured at D shown in the figure.

Assuming well-defined flat and dispersive bands, in scenario (iii) the former bands are completely filled, and superconductivity is supported fully by the latter non-flat bands. This assertion is at odds with the large dispersion of the remaining TBG- and MLG-like bands. However, while the exact mechanism underlying scenario (iii) is difficult to pin down, it is not without experimental support. For instance, a natural interpretation of the Hall density minimum around $\nu \approx +4$ (Fig. 5.19 for $|D| \lesssim 0.4 \text{ V nm}^{-1}$) is that it marks the complete filling of the flat bands, $\nu_{\text{flat}} \approx +4$.

Experimentally, starting from low D fields, we observe a drop in Hall density at

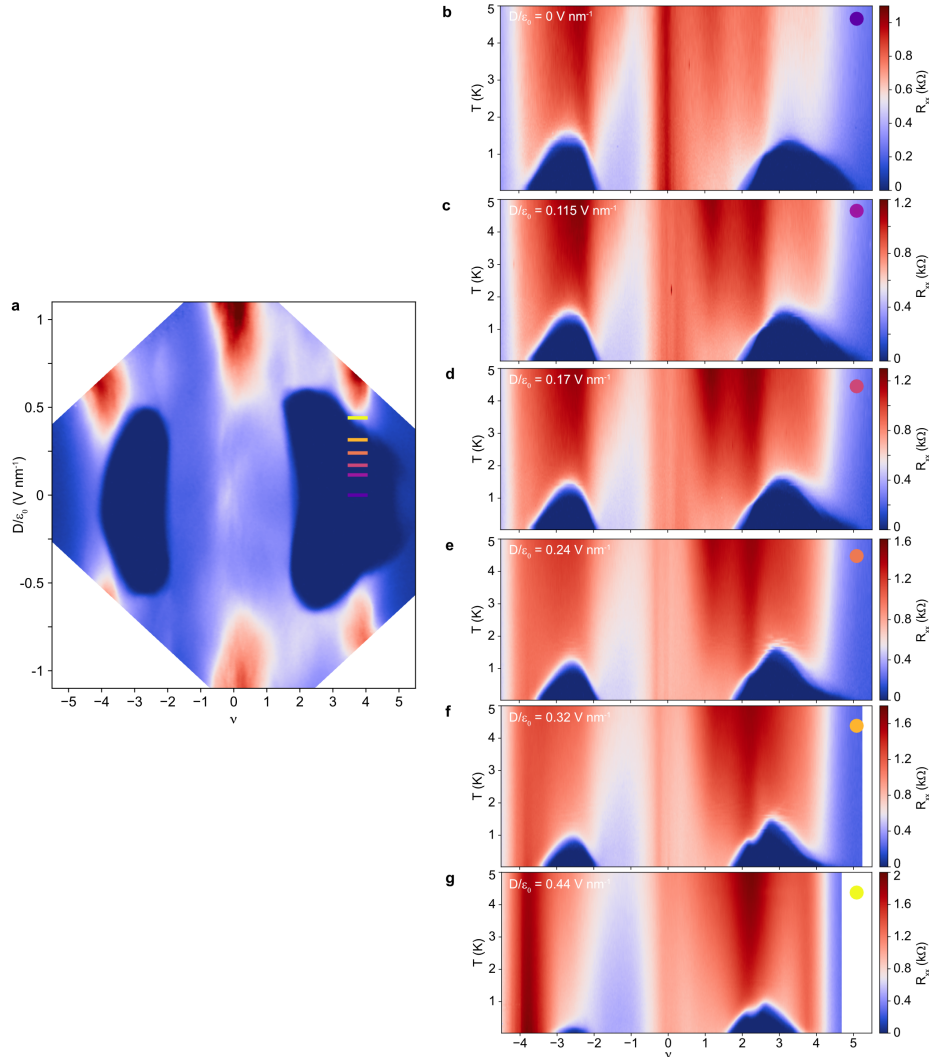


Figure 5.20: The D -dependence near $\nu = 4$. (a) R_{xx} vs. ν and D , showing the linecuts where (b)–(g) are taken from. (b)–(g) ν vs. temperature at a selected value of D , showing the evolution near $\nu \approx 4$.

$\nu \approx +4$ which surprisingly does not affect superconductivity in any abrupt way (superconductivity continuously evolves and is present until $\nu \approx +5$). As the D field is increased, this Hall density drop only varies slightly (Fig. 5.19) and is gradually replaced by a transition where Hall density changes sign (Fig. B.6). The high D -field transition can be interpreted as a ‘gap’ feature emerging in the band structure similar to TTG [127]. Further measurements of R_{xx} show that the corresponding $\nu \approx +4$ feature does not shift with temperature (Fig. 5.20) and is significantly broadened at high B fields, resembling the feature associated with the flat-band gap in TTG (Fig. 5.6, a and e). Fig. B.6 shows more evidence that the $\nu \approx 4$ behavior does

not vary strongly with added magnetic field or temperature. These observations indicate that the $\nu = +4$ feature is naturally explained as either marking the end of the flat bands or resulting from band details due to hybridization, which is in line with scenario (iii). In this context, the alternative possibility that $\nu = +4$ corresponds to a flavor-polarization reset at $\nu_{\text{flat}} = +3$ is highly unlikely, due to the limited movement of the features associated with $\nu \approx 4$ as D is varied. Finally, we note that this line of argument cannot fully rule out scenario (ii) due to the potential presence of small dispersive pockets in the flat bands that may remain unfilled near $\nu = +4$ (schematically depicted in Fig. 5.17).

Our measurements demonstrate the increasing predominance of superconductivity in twisted graphene multilayer structures as the number of layers is increased from three to five and highlight the close relationship between the flavor symmetry-breaking transitions and superconductivity. Moreover, our findings suggest a scenario in which the symmetry-broken $\nu = \pm 2$ state strongly favors the formation of the superconducting state while the cascade corresponding to $\nu = \pm 3$ suppresses it. Interestingly, this scenario is consistent not only with previous TBG [20, 43, 46–48, 53] and TTG [51, 127, 128] observations but also in part with the recently investigated ABC trilayers [151] and Bernal bilayers without [152] and with a WSe₂ substrate [106] where superconductivity is observed near or within phases in which two out of four flavors are predominantly filled. These common observations suggest that symmetry-broken states with similar types of polarization underlie superconductivity in all these graphene-based superconductors. In this context, the discovery of superconductivity in TQG and TPG together with recent work on untwisted bi- and trilayers dramatically expands the scope of graphene-based superconductors. This expansion holds promise for resolving important questions related to the nature of the pairing mechanism in these systems and provides guidance for developing novel graphene-based superconductors and their applications.

TOPOLOGY AND BAND ENGINEERING IN INAS/GASB-DERIVATIVE STRUCTURES

The 2D topological insulator (2DTI) phase serves an important role in condensed matter physics due to the protected helical edge states intrinsically present in materials exhibiting the phase. The phase exhibits topological properties without large magnetic fields (required for the quantum Hall effect) or ferromagnetic symmetry breaking. When coupled to superconductors, 2DTIs can provide a route to topological quantum computation with the elusive Majorana bound states [153–156]. Although graphene-based heterostructures show promise for examining electron correlations and topological phases, the potentially useful 2DTI (or quantum spin Hall) state has not been found in these systems, except at extreme conditions, such as a version of 2DTIs at high magnetic fields [9, 157] or in fragile forms that show only a few features of topological insulators [32].

Materials grown with molecular beam epitaxy, however, have shown promise as 2D topological insulators [158–161]. The flexibility in fabrication of these 2D electron gases (2DEGs), the achievable impurity levels, and favorable contacts with superconductors such as aluminum, allow for complex designs and a high degree of control over experimental parameters. Furthermore, 2DTIs in Josephson junctions show theoretical promise for studying the phase diagram of topological superconductivity [162, 163] and for a scalable route to networks of topological qubits [164, 165]. However, the field is still in its infancy and has many unresolved issues. After a brief introduction to 2DTIs, this section discusses the InAs/GaSb coupled quantum well material system and improvements our group has made toward tunable 2DTIs. Initial results on superconducting Josephson junctions with the material are also covered in the outlook section (Chapter 7). Particularly, we cover the promising coupled $\text{InAs}_{1-x}\text{Sb}_x/\text{In}_y\text{Ga}_{1-y}\text{Sb}$ platform that exhibits large resistance in the inverted band (potentially 2DTI) regime, measurements of valence band structure, and magnetic field dependence and comparison to theoretical expectations.

6.1 Introduction to 2D topological insulators (2DTIs)

Topological insulators are materials that behave as insulators in the bulk and host conductive edge states. The conductive edge states arise from the required closing of

the bulk insulating gap when going from the non-trivial topology inside the material to the trivial topology outside. The topological state does not break time-reversal symmetry and thus occurs at zero magnetic field, without any magnetism in the sample. The insulating gap results from time-reversal-symmetric spin-orbit coupling that splits two crossing bands into spin- \uparrow , $+\mathbf{k}$ (also spin- \downarrow , $-\mathbf{k}$) and spin- \downarrow , $+\mathbf{k}$ (also spin- \uparrow , $-\mathbf{k}$) bands, where $\pm\mathbf{k}$ refers to bands of electrons with opposite momenta. One way to represent this is with the schematic in Fig. 6.1, where the conduction and valence band edges are plotted along a line drawn through the sample. Outside the sample, conduction and valence bands are topologically trivial, but inside the sample, the two bands invert and exhibit non-trivial topology. The bands cross at the edges to form a Dirac point, resulting in a topologically protected conductive edge state. Due to the degeneracy of spin-orbit coupling, electrons traveling in one direction are spin polarized, and the electrons travelling in the opposite direction are oppositely spin polarized. This is what is meant by helical edge states. Furthermore, each edge should theoretically exhibit a robust quantized conductance of one quantum conductance unit e^2/h in each of the two directions (resulting in predictable nonlocal quantized conductance in devices according to Landauer-Büttiker theory), that is highly sensitive to time-reversal breaking perturbations such as magnetic field or magnetic impurities but not to other forms of disorder.

Only a few material systems have been shown to exhibit 2DTI behavior experimentally on a scale large enough to make electrical transport devices. The leading material systems are HgTe/CdTe quantum wells [158], the recently studied monolayer WTe₂ [166, 167], and InAs/GaSb quantum wells [159, 160, 168–172], the system studied in this thesis. Although several experimental signatures have been verified, including the quantized edge mode conductivity [158, 173], edge mode suppression under a magnetic field [158], helical spin transport [174], and imaging of the protected conductive edge modes [175, 176], several questions remain regarding 2DTIs. Namely, how robust are the helical edge states to disorder [177, 178], temperature [179], and magnetic field [180–182]? What is the role of interactions [183], and band structure [184] in each of these systems? Also, how well can these experimental signatures be accounted for using non-topological (trivial) mechanisms? The discussion on InAs/GaSb will touch these topics and point out the benefits of the InAs/GaSb system for studying 2DTIs due to its remarkable tunability.

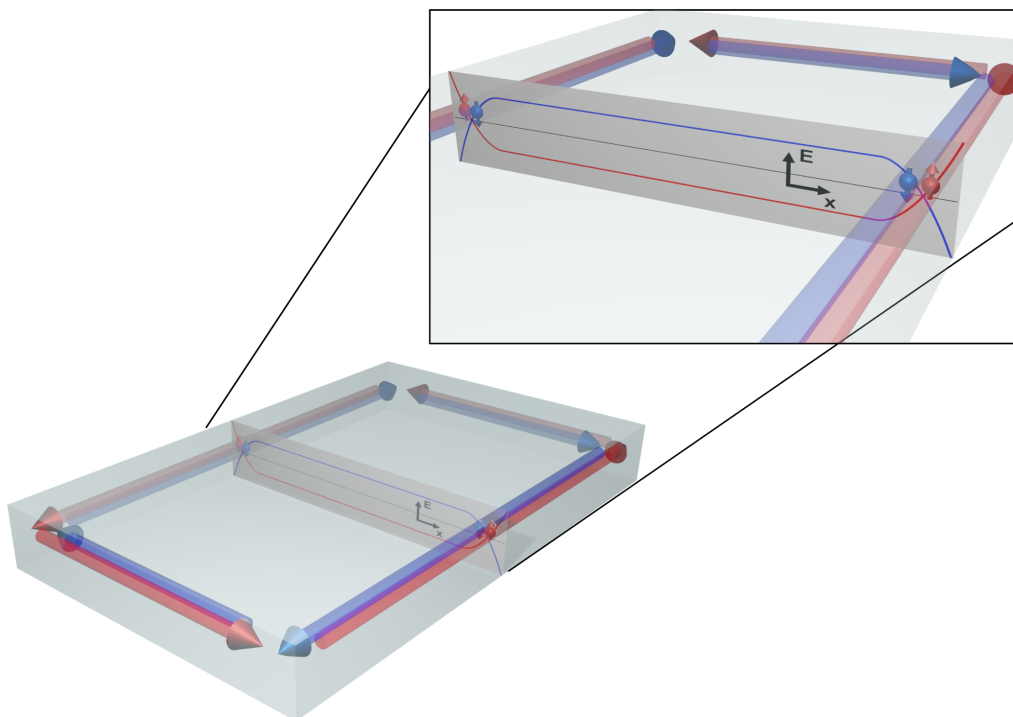


Figure 6.1: A schematic of a 2D topological insulator, demonstrating the inverted band structure with protected helical edge states. The close-up shows the spin polarization of the edge states in opposite directions, and the axes in the plot track the energy E , of the conduction and valence bands along the sample width x .

6.2 InAs/GaSb, a topological insulator candidate

Coupled intrinsically electron-doped InAs and hole-doped GaSb quantum wells offer an enticing route to further studying 2DTIs. The two semiconductor layers are deposited on top of one another using molecular beam epitaxy, resulting in geometries similar to those shown in Fig. 6.2. The AlSb layers, which have a larger bandgap than InAs or GaSb, serve as insulating barriers. Contacts are made to the quantum wells using selective wet etching to the InAs layer, followed by Ti/Au evaporation. Device shape can be controlled with an etch to the substrate. The gold topgate can then be fabricated after an Al_2O_3 dielectric layer is deposited.

The key to the InAs/GaSb material structure lies in (a) the broken-gap structure in which the bottom of the conduction band of InAs lies below the top of the valence band of GaSb, and (b) the gate tunability to both the electron-like InAs and hole-like GaSb layers. The full range of this tunability has been enabled by substrate engineering [186]. The GaSb substrate, which is deposited onto, is already lattice-matched with the GaSb quantum well (and only slightly off for InAs), resulting

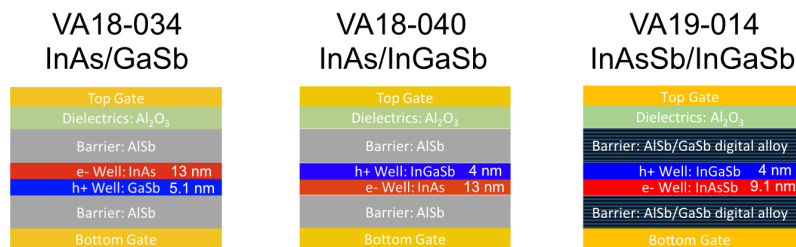


Figure 6.2: Schematics of the double quantum wells studied. Adapted from Ref. [185].

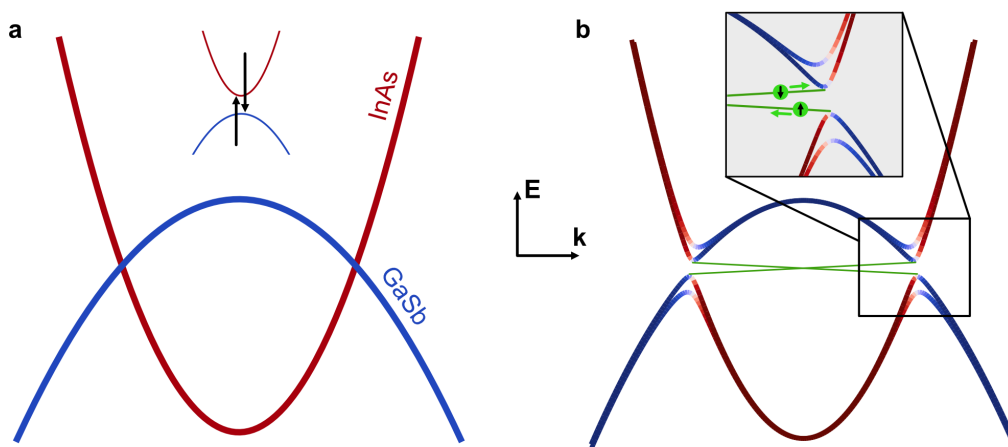


Figure 6.3: Schematic diagrams InAs/GaSb uncoupled/coupled quantum well band structure. (a) Uncoupled overlapping InAs and GaSb quantum wells and (b) coupled quantum wells with anticrossing points at finite k and spin-orbit coupling. The green lines represent the predicted topologically protected edge states of opposite spin and momentum combinations.

in both a reduction in strain dislocations and less deposition required between the substrate and the quantum well relative to GaAs substrates, for instance. Thus the backgate's higher capacitance enables greater density tuning in the quantum well, and the reduced strain improves mobility [160].

The conceptual idea behind the InAs/GaSb system is captured by first considering an effective band structure of the two layers when they are decoupled (e.g., by a small dielectric layer grown between them), as shown in Fig. 6.3a. InAs (red, electron band) has a lower effective mass than GaSb (blue, hole band), and their alignment can be tuned by the top and back gates. Applying an out-of-plane electric field can either further dope both the electron (InAs) and hole (GaSb) bands, causing the bands to further overlap, or it can push the bands apart. When the electron and hole

bands are no longer overlapping, as shown in the inset to Fig. 6.3a, there is a trivial energy gap between the bands.

However, when the two bands overlap, the InAs and GaSb layers are coupled. Once spin-orbit coupling is considered, anticrossing points occur at finite momenta, as shown in Fig. 6.3b. Electrons are still represented as red, and holes as blue in the band structure. The gaps have been shown theoretically to exhibit the quantum spin Hall effect [187], which prompted experimental efforts to observe 2DTI signatures. The nature of the edge states (green lines) is shown in the inset of Fig. 6.3b. When looking along one edge of a device, a channel of one spin species travels in the forward direction, and the opposite-spin channel travels in the reverse direction. The chemical potential must pass through both edge states when it is in the gap, and the Fermi velocity is controlled by the size of the gap and the momenta of the anticrossing points.

This can be modeled, to first-order, using a capacitance model [188] that considers the geometric capacitance of the wells to the top/back gates (C_t/C_b), the geometric capacitance between the electron and hole layers (C_m), and the quantum capacitance of the electron/hole layers ($C_{q,e}/C_{q,h}$), as shown in Fig. 6.4a. The quantum capacitance follows the density of states, D of the quadratic spin-degenerate bands, $C_{q,e(h)} = e^2 D_{e(h)}$, where $D_e(h) = \frac{m_{InAs(GaSb)}^*}{\pi\hbar^2}$. Then, the electron and hole densities (n and p) follow from the definitions of the chemical potential relative to the conduction band bottom, E_F , and the amount of band inversion, E_g , in Fig. 6.4b.

$$n = D_e E_F = \frac{C_{q,e}}{e^2} E_F \quad (6.1)$$

$$p = D_h (E_g - E_F) = \frac{C_{q,h}}{e^2} (E_g - E_F) \quad (6.2)$$

A schematic of the InAs (left) and GaSb (right) energy levels is shown in Fig. 6.4c. Also shown is the energy offsets, E_1 and H_1 , of the electron and hole bands due to quantum confinement from the finite layer thickness, which tunes the band overlap. This energy structure can be represented mathematically as

$$\mu_{tg} + e \frac{\sigma_{tg}}{C_t} - H_1 - E_g + E_F + \text{const.} = \mu \quad (6.3)$$

$$\mu_{bg} + e \frac{\sigma_{bg}}{C_b} + E_1 + E_F + \text{const.} = \mu. \quad (6.4)$$

Gauss's law determines the charge at each layer and the electric field between layers

$$ep + \sigma_{tg} = -\epsilon_0\epsilon_{QW}E_m \quad (6.5)$$

$$-en + \sigma_{bg} = \epsilon_0\epsilon_{QW}E_m \quad (6.6)$$

where ϵ_{QW} is the quantum well dielectric constant (which is nearly the same for InAs and GaSb), and E_m is the electric field in the middle of the quantum wells. Lastly, we have the following relations between E_m , μ , μ_{bg} , and μ_{tg} and other parameters:

$$eE_md_m = \Delta = E_g + \text{const.} \quad (6.7)$$

$$-eV_{bg} = \mu_{bg} - \mu \quad (6.8)$$

$$-eV_{tg} = \mu_{tg} - \mu. \quad (6.9)$$

If we leave offsets as experimentally determined constants, we can get equations relating n and p to topgate and backgate voltages V_{tg} . The capacitance model results in linear relationships between densities and gate voltages. There are three regimes of p and n to consider:

1. **$n > 0, p = 0$** : When one carrier type is absent, the dependence on gates comes from some simple modifications to geometric capacitance. For the topgate, the slope is

$$\frac{dn}{dV_{tg}} = \frac{C_{q,e}}{e} \frac{C'_t}{C'_t + C_{q,e} + C_b}, \quad (6.10)$$

where $C'_t = \left(\frac{1}{C_t} + \frac{1}{C_m}\right)^{-1}$ is the capacitance from the topgate to the bottom InAs layer. And for the backgate,

$$\frac{dn}{dV_{bg}} = \frac{C_{q,e}}{e} \frac{C_b}{C'_t + C_{q,e} + C_b}. \quad (6.11)$$

2. **$n = 0, p > 0$** : For the topgate,

$$\frac{dp}{dV_{tg}} = -\frac{C_{q,h}}{e} \frac{C_t}{C_t + C_{q,h} + C'_b}, \quad (6.12)$$

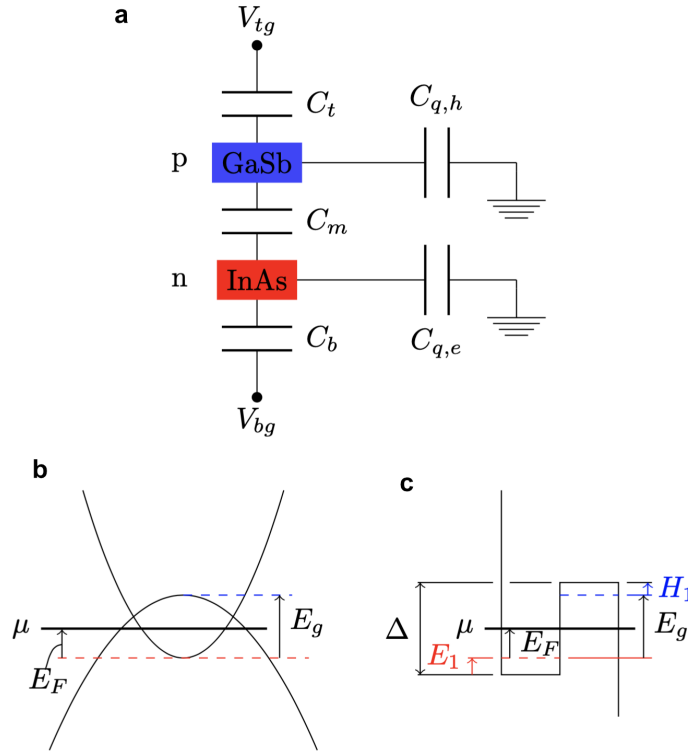


Figure 6.4: An electrostatic capacitance model that is a first approximation to the InAs/GaSb double quantum well's behavior under top and back gates. (a) shows a circuit schematic, and (b), (c) show the relevant parameters for the model, which are described in the text

where $C'_b = \left(\frac{1}{C_b} + \frac{1}{C_m}\right)^{-1}$. And for the backgate,

$$\frac{dp}{dV_{bg}} = -\frac{C_{q,h}}{e} \frac{C'_b}{C_t + C_{q,h} + C'_b}. \quad (6.13)$$

3. **n, p > 0**: When both carriers are present, the analysis takes a few more steps and results in the coupled equations

$$V_{tg} - V_{tg,0} = -\frac{ep}{C_t} - \frac{ep}{C_{q,h}} - \frac{eC_m}{C_t} \left(\frac{n}{C_{q,e}} + \frac{p}{C_{q,h}} \right) \quad (6.14)$$

$$V_{bg} - V_{bg,0} = \frac{en}{C_b} + \frac{en}{C_{q,e}} + \frac{eC_m}{C_b} \left(\frac{n}{C_{q,e}} + \frac{p}{C_{q,h}} \right). \quad (6.15)$$

These equations can be evaluated most easily by inverting the following derivatives, which are represented only in terms of constants:

$$\frac{dV_{tg}}{dp} = -e \left(\frac{1}{C_t} + \frac{1}{C_{q,h}} + \frac{C_m}{C_t C_{q,h}} \right) + e \frac{C_m^2}{C_t C_{q,h}} (C_{q,e} + C_b + C_m)^{-1} \quad (6.16)$$

$$\frac{dV_{tg}}{dn} = e \left(\frac{C_{q,h}}{C_m C_t} + \frac{1}{C_m} + \frac{1}{C_t} + \frac{C_b C_{q,h}}{C_m C_{q,e} C_t} + \frac{C_b}{C_m C_{q,e}} + \frac{C_b}{C_t C_{q,e}} + \frac{C_{q,h}}{C_{q,e} C_t} + \frac{1}{C_{q,e}} \right) \quad (6.17)$$

$$\frac{dV_{bg}}{dp} = e \frac{C_m}{C_b C_{q,h}} - e \left(\frac{1}{C_b} + \frac{1}{C_{q,e}} + \frac{C_m}{C_b C_{q,e}} \right) \left(\frac{C_{q,e}}{C_m} + \frac{C_t C_{q,e}}{C_m C_{q,h}} + \frac{C_{q,e}}{C_{q,h}} \right) \quad (6.18)$$

$$\frac{dV_{bg}}{dn} = e \left(\frac{1}{C_b} + \frac{1}{C_{q,e}} + \frac{C_m}{C_b C_{q,e}} \right) - e \frac{C_m^2}{C_b C_{q,e}} (C_{q,h} + C_t + C_m)^{-1}. \quad (6.19)$$

When these three regimes are patched together with reasonable material parameters, described more below, the result is the phase diagram shown in Fig. 6.5. The lines of constant n (black) and p (gray) reveal that increasing the topgate and backgate voltages leads to more electrons in the system, and decreasing the gate voltages leads to more holes in the system. In the bottom right of the diagram, an electric field results in depopulated electron and hole bands, and a trivial gap along the green line. The top left of the diagram, between the red and blue lines, marks the gate space where electron and hole bands overlap, or the inverted band regime. The blue and red lines represent the edge of the hole and electron bands, respectively. As shown in Fig. 6.5b,c, the hole and electron bands, respectively, are completely depopulated beyond these lines. Finally, the green line in the top left marks where we should find the topological gap.

The novelty of InAs/GaSb as a 2DTI comes from the ability to electrically tune between a topological gap, with helical edge states, and a trivial gap without protected edge states. The inverted regime was explored in [168, 170, 189], and the transition from inverted to non-inverted bands was further explored in [160, 190] due to enhanced growth techniques [186] and tuning the layer thicknesses close to the crossover point. A 2D diagram formed from using both top and back gates allows

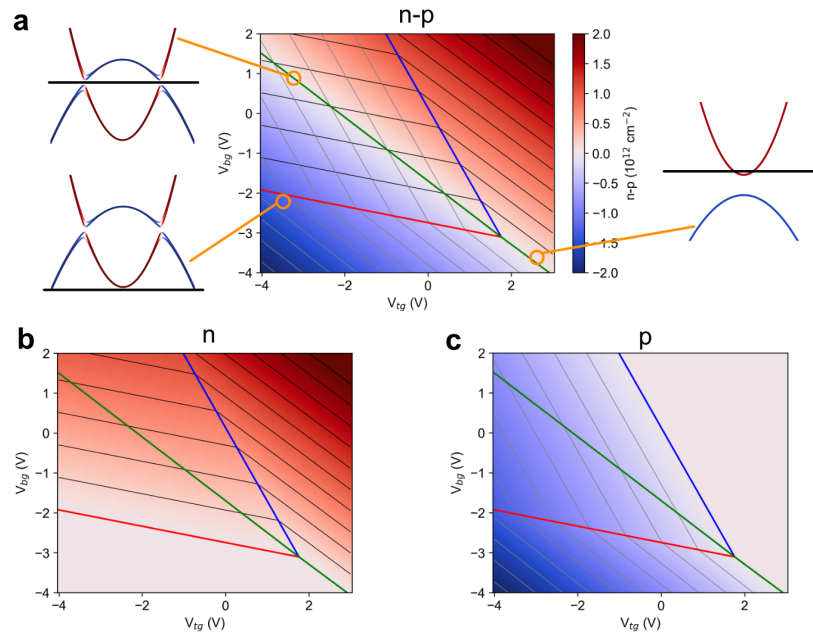


Figure 6.5: 2D gate plots of electron and hole densities. (a) $n - p$, (b) n , and (c) $-p$, using the capacitance model. The color bar is the same in all plots, except plot (b) has the p contribution removed. (c) has the n contribution removed. The band schematics plotted next to (a) reveal the general behavior of the bands and chemical potential at various points in the phase diagram.

for a better determination of band structure. The inverted regime for InAs/GaSb behaves similarly to our reference device, VA18-034 (schematic in Fig. 6.2a), for which we show the topgate Landau fan diagram in Fig. 6.6. Large topgate values result in electron-like behavior very similar to that expected in an InAs quantum well. Close to the resistance peak, when charge carriers are maximally depleted and equal (the charge neutrality point or CNP), the Landau fan shows evidence of both electron and hole-like features, as expected for the mixed electron and hole bands. The presence of multiple peaks at $B = 0$ also indicates mixed bands due to the added van Hove singularities when bands cross through each other to form mixed electron-hole states.

A few problems arose over the past several years, however:

1. The resistance peak in InAs/GaSb only reaches in the range of a few $\text{k}\Omega$, indicating the lack of a bulk gap. One explanation of the bulk resistivity is a combination of (a) the low gap of $\sim 4 \text{ meV}$ and (b) anisotropy in the band when considering more realistic band structure calculations [170, 191]. Although there may be a gap at each point in momentum space, the hole band

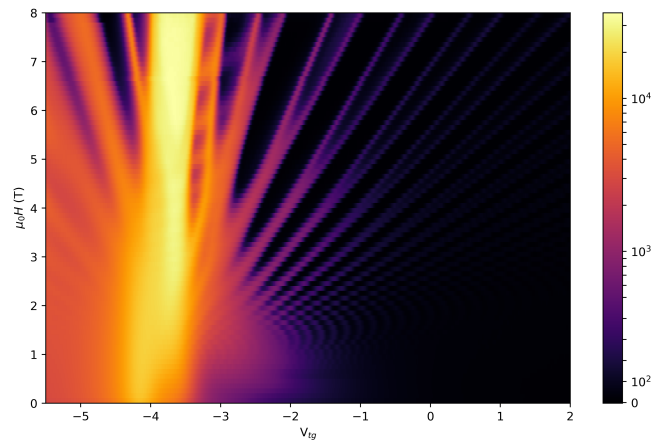


Figure 6.6: Landau fan of an InAs/GaSb device VA18-034 showing electron-like/InAs behavior on the right and hole-like behavior on the left, with some evidence of mixing/inverted bands.

at a given momentum may overlap with the conduction band at a different momentum point, resulting in semimetallic behavior.

2. The ability to tune between inverted (ideally topological) and non-inverted (trivial) band structures provides a cross check to ensure the 2DTI edge mode properties don not arise from trivial effects. However, studies indicate that many of the features previously associated with topological edge conductance can also be found when the gap is trivial [171, 192]. The reported trivial edge conductance can be attributed to phenomena related to Fermi level pinning at the edge of the device in the InAs layer. The nature of these trivially conductive edges were further revealed to persist over 100s of μm and exhibit n-type behavior [193].
3. The finite momentum of the quantum spin Hall gaps should die as parallel magnetic field is applied. Additionally, the time-reversal symmetry-protected edge states should allow backscattering with an applied magnetic field, as it does in HgTe/CdTe quantum wells [158]. Nevertheless, some devices lack the expected in-plane magnetic field dependence of the bulk resistivity and edge state conductance [159]. Although explanations have been suggested for this robustness to magnetic fields due to strain or correlated phases [180–183], the mechanisms often complicate or preclude characterizing the system as a standard 2DTI [184]. Additionally, the lack of robustness to magnetic field in some samples [160, 172] suggests other mechanisms at work.

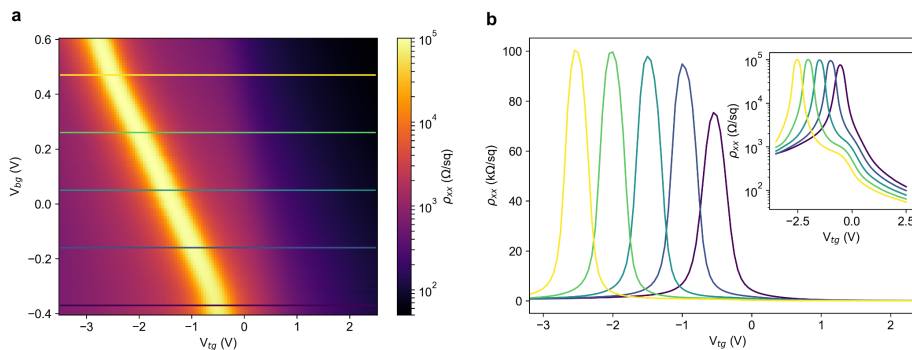


Figure 6.7: VA19-014 R_{xx} characterization. (a) R_{xx} plot measured with respect to topgate voltage V_{tg} and backgate voltage V_{bg} . (b) Linecuts from (a) on a linear scale and log scale in the inset.

4. Lastly, a more realistic band structure using, e.g., an 8-band Kane model suggests spin-orbit coupling may play a larger role than initially thought since it splits results in large splitting of the hole band. However, the precise role of the spin-orbit splitting has contrasting explanations [191, 194, 195] due to the dominant electron conduction in the devices studied. Understanding the hole band spin-orbit splitting will help with material development and characterization and lead to more accurate predictions regarding 2DTI physics.

These problems call into question some of the claims of 2DTI behavior, call for more careful characterization, and suggest goals for future material development.

6.3 InAs/In_xGa_{1-x}Sb and InAs_{1-x}Sb_x/In_yGa_{1-y}Sb impurity doped systems

The first problem of a conductive bulk has been explored by doping the material system. Strain in the GaSb layer was soon discovered to increase the gap size and the peak resistivity [159, 196], and an effective method of inducing strain is through modifying the effective lattice constant in GaSb relative to the substrate by adding indium to make a quantum well of In_xGa_{1-x}Sb [169, 172, 194] or by changing the substrate's lattice constant [161]. Bulk resistivity at the inverted gap, with these modifications, has been enhanced to hundreds of kΩ, and the gap estimates are in the range of tens of meV, about an order of magnitude larger than estimates on the InAs/GaSb system. However the possible effects of trivial edge states have not been extensively studied in the strained-layer systems.

Additionally, adding Sb to lone quantum well of InAs, making InAs_{1-x}Sb_x, likely

reduces the n-type trivial edge states [185] and lifts the electron band bottom from the InAs level without having to reduce the thickness. Thus, a double quantum well of $\text{InAs}_{1-x}\text{Sb}_x/\text{In}_y\text{Ga}_{1-y}\text{Sb}$ has the potential to simultaneously reduce the effects of bulk conductivity and trivial edge states. As such, we studied the structures shown in the middle and on the right in Fig. 6.2. The VA18-040 structure included 4 nm of $\text{In}_{0.33}\text{Ga}_{0.67}\text{Sb}$ grown on 13 nm InAs. The VA19-014 structure was grown with 4 nm of $\text{In}_{0.33}\text{Ga}_{0.67}\text{Sb}$ grown on top of 9.1 nm of $\text{InAs}_{0.9}\text{Sb}_{0.1}$. The results showed many similarities, but due to the smaller band overlap in the latter, we will focus here mostly on the VA19-014 structure. A 2D gate map is shown in Fig. 6.7, with linecuts revealing a max resistivity of 100 k Ω and a shoulder (seen in the inset of b) related to the hole band edge. The resistivity of the CNP peak also increases toward the top left of the diagram in Fig. 6.7a, indicating a larger gap as the electron and hole bands further overlap.

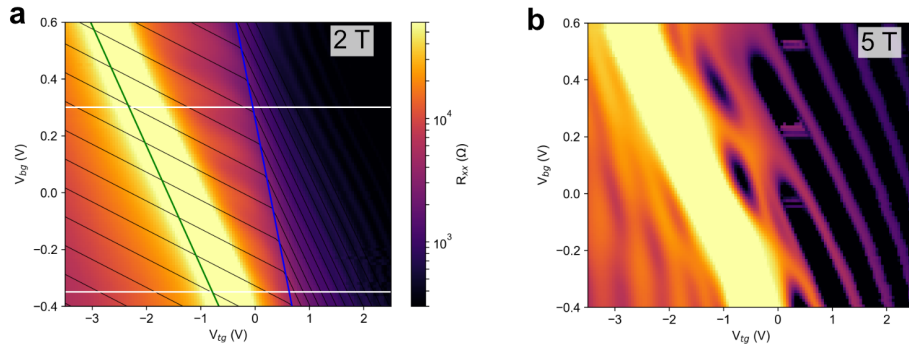


Figure 6.8: Comparing 2D Landau diagrams with constant- n lines. (a) 2D gate diagram taken at 2 T to show the Landau levels of constant n on the right side. (b) 2d gate diagram taken at 5 T to clarify the Landau level behavior.

Using the capacitance model, combined with 2D gate maps at 2 T we can determine the gate phase diagram, as shown in Fig. 6.8a. The visible Landau levels (peaks in the 2D plot) at the top-right of the diagram are due to a single electron band, so they represent lines of constant- n and therefore follow the lines of constant n derived from the capacitance model, represented as black lines. Furthermore, to the left of the hole band edge (blue line, as derived from the capacitance model), in the inverted regime, the electron Landau levels are still visible and further constrain the phase diagram. The green line represents the CNP from the capacitance model, which also aligns with the R_{xx} peak. The parameters used in the capacitance model here are $m_e = 0.045m_0$, $m_h = 0.09m_0$ and $C_t = 0.054$, $C_b = 0.13$, and $C_m = 2.1$ $\mu\text{F}/\text{cm}^2$, derived roughly from the device dimensions. Fig. 6.8a shows the same

diagram taken at 5 T to more clearly reveal the Landau levels and the signs of mixed electron and hole bands to the left of where the blue line is in panel a.

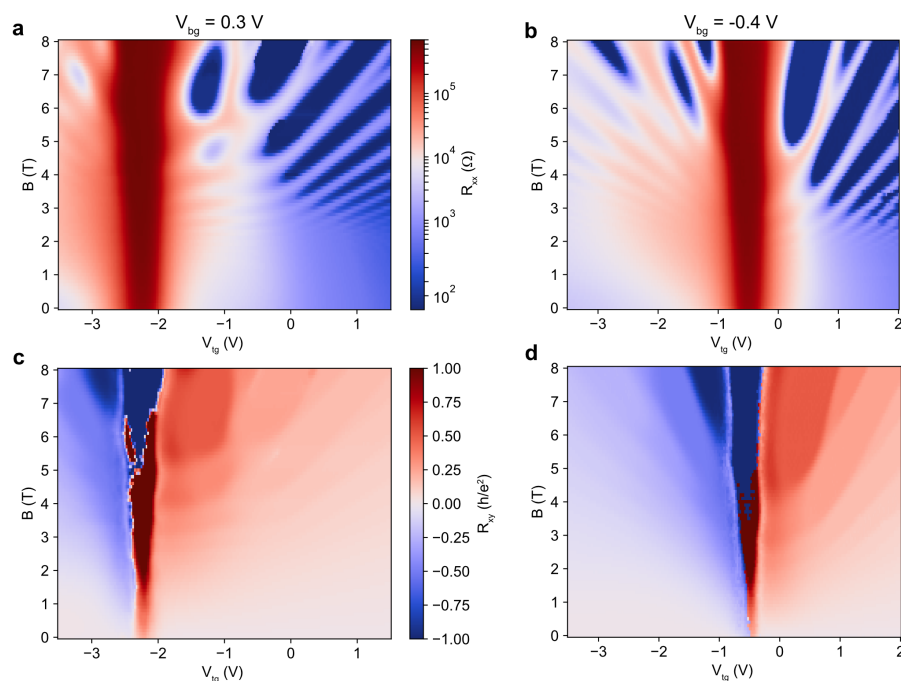


Figure 6.9: Landau fan diagrams. (a) R_{xx} and (b) R_{xy} Landau fan diagrams for two different values of V_{bg} , taken by sweeping V_{tg} .

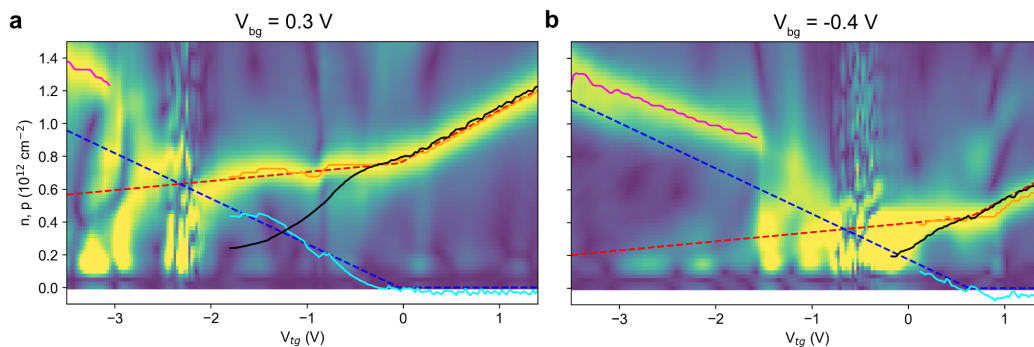


Figure 6.10: Fourier transforms (y-axis densities n and p are derived from $2f_1/Be/h$) of the data in Fig. 6.9(a), (b).

A further look at the Landau fan diagrams (Fig. 6.9) following two linecuts of constant V_{bg} (shown as white lines in Fig. 6.8a) further reveals the nature of the band filling. As with the InAs/GaSb device in Fig. 6.6, the right side of the diagram reveals electron behavior, and there is evidence of hole-like behavior left of the CNP peak. In this device, the large resistance of the CNP peak hides some of the

mixed-band behavior in R_{xx} plots although the crossing bands on the right side of the CNP and positive-to-negative switch in the lower left of the R_{xy} diagrams reveal signatures of inverted bands.

Using a Fourier transform of the Shubnikov-de Haas (SdH) oscillations reveals peaks in frequencies that are related to the Fermi surface area of the bands, as seen in Fig. 6.10. The Fourier transform is taken using the R_{xx} Landau fan diagrams that have been represented in $1/B$, up-sampled, subtracted by a polynomial fit, zero-padded, and windowed (as is commonly done in these measurements [197]) before applying the Fourier transform. Then each Fourier transform is normalized to its largest magnitude to give the plots in Fig. 6.10. The frequencies can be converted to electron n and hole p densities using the relation $n(p) = 2ef_{1/B}/h$ (assuming an isotropic, spin-degenerate 2D Fermi surface). The solid orange and magenta lines follow the peaks of the main features in the data while the black solid lines mark the Hall density-derived total carrier density $|n - p|$, which is measured in two-carrier systems through the slope of the linear R_{xy} regime at intermediate fields ($\sim 1.75\text{--}4$ T). By subtracting the black curve ($|n - p|$) from the orange curve n , we derive the hole density (cyan curve) [160] when two carriers are involved. The red and blue dashed lines mark the capacitance model densities n and p , respectively, which show reasonable agreement with experiment on the right side of the CNP in both diagrams. To the left of the CNP, the oscillation-derived features distinctly contrast the capacitance model predictions due to the spin-split valence bands discussed next.

6.4 8-band Kane model band structure including strain

Although the capacitance model works well for the conduction bands, its assumption of quadratic and spin-degenerate bands oversimplifies the band structure of the valence bands. A more realistic model can be constructed using the 8-band Kane model Hamiltonian applied to the materials involved. The 8×8 $k \cdot p$ Hamiltonian, discussed in detail elsewhere [184, 191], is derived based on the symmetry of the zincblende semiconductor systems grown in the [001] direction and has empirically derived material-dependent parameters found in Refs. [198–200]. The eight bands include two from an s-like orbital for the conduction band, denoted Γ_{6c} with total angular momentum $L = 1/2$ and z-component $L_z = \pm 1/2$, and a p-like orbital for the valence band. The valence band can be broken up into two bands with total angular momentum $L = 1/2$ (Γ_{7v}), and $L = 3/2$ for the four remaining bands ($L_z = \pm 3/2$, $L_z = \pm 1/2$, the Γ_{8v} bands).

For a stoichiometrically pure system, like InAs/GaSb, the Hamiltonian for the 2D system is calculated by discretizing into a grid in the z direction, with the Hamiltonian for each point reflecting the appropriate material parameters. Stoichiometric impurities can be modeled by appropriate interpolation of the parameters [200]. While most parameters can be linearly interpolated, a few, such as band gap E_g and spin-orbit parameter Δ , have quadratic components. For our $\text{InAs}_{1-x}\text{Sb}_x/\text{In}_y\text{Ga}_{1-y}\text{Sb}$ devices, Fig. 6.11a shows the geometry of the discretized lattice used for the Hamiltonian (with 9 nm $\text{InAs}_{1-x}\text{Sb}_x$ and 4 nm $\text{In}_y\text{Ga}_{1-y}\text{Sb}$). The grid spacing (0.5 nm) and the AlSb barrier thicknesses (5 nm) used are sufficient for the model, and the band structure does not change much if they are varied. Fig. 6.11b shows the resulting band structure, where $k = 0$ on the x-axis refers to the Γ point, and the positive (negative) k sides of the graph plot out the band structure along the [100] ([110]) direction. The calculations here are incomplete since they do not incorporate strain effects into the Hamiltonian. As such, the band structure is very similar to that of stoichiometrically pure InAs/GaSb. The code for the band structure calculations is modified from Ref. [201].

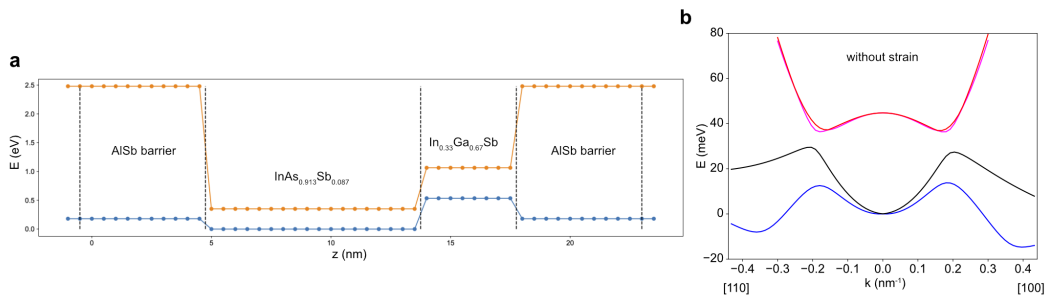


Figure 6.11: $k \cdot p$ calculation details. (a) The 1D lattice in the growth direction used in the 8-band calculations. Each point has its own Hamiltonian with the appropriate material parameters, and they are linked through the k_z variable. (b) The resulting band structure without including strain effects yet.

The addition of stoichiometric impurities not only changes the Kane Hamiltonian parameters but also adds strain to the lattice by changing the bulk lattice constant a_0 of the material. In our case, epitaxial growth restricts the lattice constant of the grown materials a_{eff} to approximately the same lattice constant as the GaSb substrate. When the large indium atoms are added, the bulk material lattice constant a_0 increases, and thus the lattice undergoes compressive strain in order to grow epitaxially according to the substrate lattice constant a_{eff} . The effect of this compressive strain can be accounted for using the strain parameters a_c, a_v, b provided

by Ref. [200], along with the in-plane strain in one direction

$$\epsilon_{xx} = \frac{a_{eff} - a_0}{a_0}. \quad (6.20)$$

The strain in the remaining directions can be determined, due to the [001] direction of epitaxial growth, to be [202–204]

$$\epsilon_{yy} = \epsilon_{xx} \quad (6.21)$$

$$\epsilon_{zz} = -\frac{\epsilon_{xx}}{\sigma} = -2\epsilon_{xx} \frac{c_{12}}{c_{11}} \quad (6.22)$$

where $\sigma = c_{11}/2c_{12}$ is Poisson's ratio. The appropriate strain matrix shifts the conduction band according to the hydrostatic strain, or trace of the strain $\epsilon_{tr} = \epsilon_{xx} + \epsilon_{yy} + \epsilon_{zz} = 2\epsilon_{xx}(c_{11} - c_{12})/c_{11}$, multiplied by a constant a_c . The valence band also shifts following $-a_v\epsilon_{tr}$. Note that under compressive strain ($\epsilon_{tr} < 0$), the conduction band moves upward, and the valence band moves downward ($a_c, a_v < 0$) due to these diagonal components. Other terms come into play in the valence bands due to the transformation from the p-orbital $|X\rangle, |Y\rangle, |Z\rangle$ basis into the $|L, L_Z\rangle$ basis. The total strain matrix for the valence bands, following Pikus and Bir [202–204], is

$$\begin{pmatrix} |3/2, 3/2\rangle & |3/2, 1/2\rangle & |3/2, -1/2\rangle & |3/2, -3/2\rangle & |1/2, 1/2\rangle & |1/2, -1/2\rangle \\ -a_v\epsilon_{tr} + \epsilon_b & 0 & 0 & 0 & 0 & 0 \\ 0 & -a_v\epsilon_{tr} - \epsilon_b & 0 & 0 & \sqrt{2}\epsilon_b & 0 \\ 0 & 0 & -a_v\epsilon_{tr} - \epsilon_b & 0 & 0 & -\sqrt{2}\epsilon_b \\ 0 & 0 & 0 & -a_v\epsilon_{tr} + \epsilon_b & 0 & 0 \\ 0 & \sqrt{2}\epsilon_b & 0 & 0 & -a_v\epsilon_{tr} & 0 \\ 0 & 0 & -\sqrt{2}\epsilon_b & 0 & 0 & -a_v\epsilon_{tr} \end{pmatrix} \quad (6.23)$$

where $\epsilon_b = \frac{b}{2}(\epsilon_{xx} + \epsilon_{yy} - 2\epsilon_{zz}) = b\epsilon_{xx}(c_{11} + 2c_{12})/c_{11}$. After interpolating the material parameters (strain parameters a_c, a_v , and b and the lattice constant a_0 can be linearly interpolated [200]) and adding the strain term to the Hamiltonian, the band structure is significantly modified, as shown in Fig. 6.12. The band structure is approximately matched to the experimental results by finding the band overlap that produces the density n_{cross} at the CNP taken from the capacitance model, which

can be translated into a wavevector $k_{\text{cross}} = \sqrt{2\pi n_{\text{cross}}}$. The gate points $V_{bg} = 0.3V$ and $V_{bg} = -0.4V$ correspond approximately to $k_{\text{cross}} = 0.2 \text{ nm}^{-1}$ (panel a) and $k_{\text{cross}} = 0.16 \text{ nm}^{-1}$ (panel b), respectively.

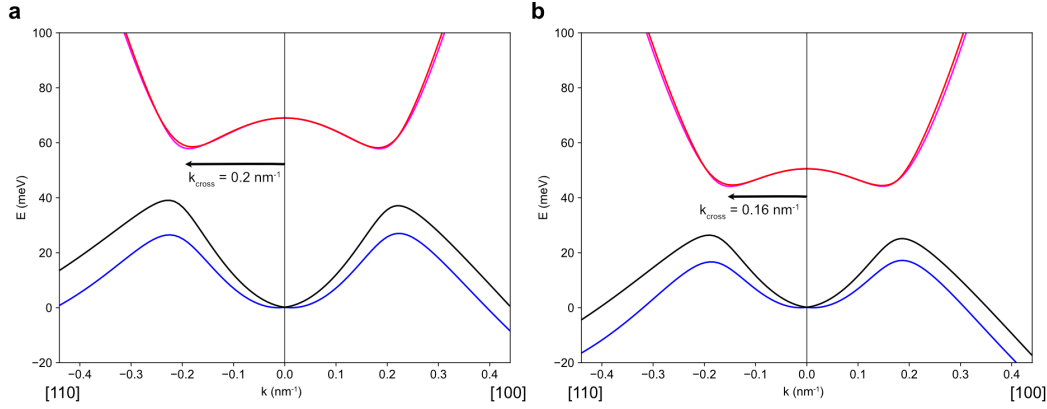


Figure 6.12: The $k \cdot p$ 8-band model calculation with strain included for $\text{InAs}_{0.913}\text{Sb}_{0.087}/\text{In}_{0.33}\text{Ga}_{0.67}\text{Sb}$ at two levels of band overlap corresponding to $k_{\text{cross}} = 0.2$ and 0.16 nm^{-1} . The positive side of the k axis refers to k in the $[100]$ direction, and the negative side to the $[110]$ direction.

The main effect on the band structure of the Sb impurity in the $\text{InAs}_{1-x}\text{Sb}_x$ layer is to modify the effective mass of the electron-like bands, and otherwise the band structure is similar to previously studied $\text{InAs}/\text{In}_x\text{Ga}_{1-x}\text{Sb}$ structures [169, 172, 194], with an increased band gap in the range of tens of meV and split valence bands. The band gap also increases with the overlapping of the bands in the calculated band structure, contrary to the narrowing of the band gap with increasing band overlap that occurs in InAs/GaSb systems [160, 189]. This is confirmed by the increasing resistance of the CNP at higher backgate values in Fig. 6.7.

Considering the anisotropy involved (the valence bands are more squarelike in $k_x - k_y$ space rather than circular parabolas), the relevant quantity to compare with SdH oscillations is the Fermi surface area, shown in Fig. 6.13a. The slopes give the cyclotron effective mass (the mass relevant for SdH oscillations) through the formula

$$m^* = \frac{\hbar^2}{2\pi} \frac{dA}{dE} \quad (6.24)$$

and are also shown in Fig. 6.13b,c. Although the topgate dependence will vary from the dependence on energy, the picture of the valence band realized by the 8-band

Hamiltonian with strain reveals a few points that can clarify the behavior of the SdH oscillations left of the CNP in Fig. 6.10. Due to the large splitting of the valence bands, we can expect a finite Fermi level range where only one electron and one hole band are filled. In this range, the lower density of states should result in the bands quickly filling and then filling more slowly when the second valence band has been reached.

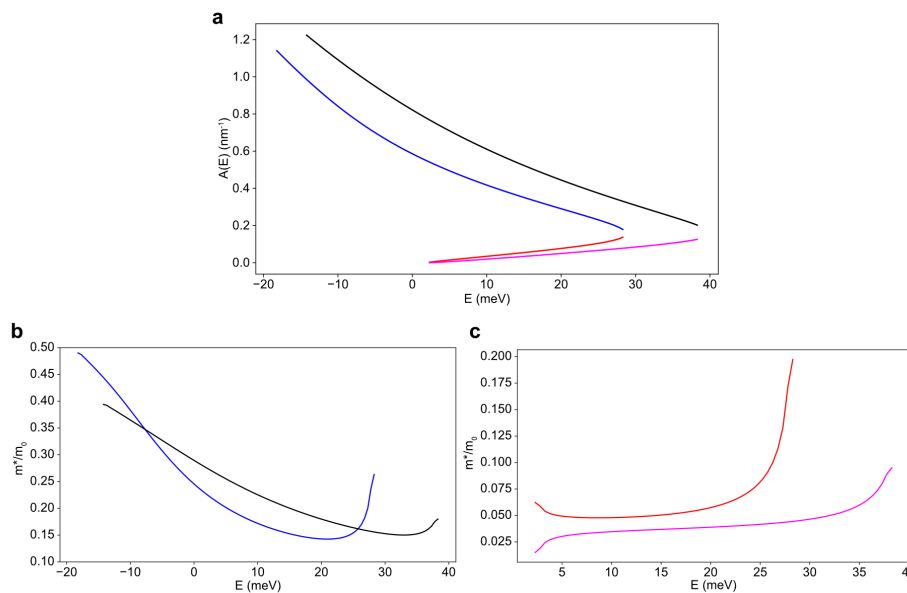


Figure 6.13: Fermi surface properties deduced from the $k \cdot p$ model with $k_{\text{cross}} = 0.2 \text{ nm}^{-1}$. (a) displays the Fermi surface areas. The red and magenta curves are for the heavy and light electron bands, respectively, and the black and blue are for heavy and light holes, respectively. (b), (c) The effective masses calculated from (a) for holes and electrons.

6.5 Effective model for the valence band Fermi surface area

The relation of the gate voltages to the valence band filling can be qualitatively captured with a modified capacitance model, shown in Fig. 6.14. The model still assumes quadratic bands but allows for two offset hole-like bands and two electron-like bands, with different effective masses in each band. The electron bands still move together, and the hole bands move together as the gate voltages are changed. The quadratic band assumption allows the same analysis above to work by modifying the quantum capacitances and breaking the valence band into three ranges based on the Fermi level position.

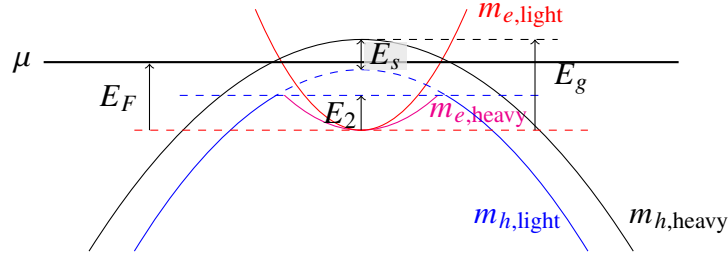


Figure 6.14: Modified quadratic band structure now introducing a heavy and light hole band along with heavy and light electron bands. The light electron band and heavy hole band start at a certain energy E_2 , whereas the heavy hole and light electron bands start at the band gap, which is approximately where μ is. We have just included the part above μ for the sake of better identifying these as parabolas and for the sake of the definition of E_g .

- (i) $E_F > E_2$: Here there is just the heavy hole and and light electron band. The model is the same as before, just with quantum capacitances due to singly degenerate bands. Although perhaps the hole band is offset some as well, our main concern is with the slopes dp/dV_{tg} and dn/dV_{tg} , which we can find using Eq. (6.17), (6.16) with modified quantum capacitances

$$C_{q,e(h),\text{light(heavy)}} = \frac{e^2 m_{e(h),\text{light(heavy)}}^*}{2\pi\hbar^2} \text{ as follows}$$

$$C_{q,h} \rightarrow C_{q,h,\text{heavy}} \quad (6.25)$$

$$C_{q,e} \rightarrow C_{q,e,\text{light}}. \quad (6.26)$$

Then we can get the Fermi surface areas $A_{e,\text{light}} = 4\pi^2 n$ and $A_{h,\text{heavy}} = 4\pi^2 p$. The only constraint used here is that the heavy-hole and light-electron bands start with approximately the same k_F , so the same electron/hole densities, resulting in $n_{\text{light}} = p_{\text{heavy}}$ at the top of the valence band.

- (ii) $0 < E_F < E_2$: With the addition of the heavy electron band and heavy hole band, the quantum capacitances are updated with

$$C_{q,h} \rightarrow C_{q,h,\text{light}} + C_{q,h,\text{heavy}} \quad (6.27)$$

$$C_{q,e} \rightarrow C_{q,e,\text{light}} + C_{q,e,\text{heavy}}. \quad (6.28)$$

Then a few constraints help with deriving the Fermi surface areas. First, the two electron-like bands share the same band bottom, so they share the same Fermi energy

$$E_F = \frac{\hbar^2 k_{F,e,\text{light}}^2}{2m_{e,\text{light}}} = \frac{\hbar^2 k_{F,e,\text{heavy}}^2}{2m_{e,\text{heavy}}}. \quad (6.29)$$

Given the total $n = n_{\text{light}} + n_{\text{heavy}}$, retrieved from the capacitance equations, and some algebra, we get

$$A_{e,\text{light}} = 4\pi^2 n_{\text{light}} = \frac{4\pi^2 n}{1 + \frac{m_{e,\text{heavy}}}{m_{e,\text{light}}}} \quad (6.30)$$

$$A_{e,\text{heavy}} = 4\pi^2 n_{\text{heavy}} = \frac{4\pi^2 n}{1 + \frac{m_{e,\text{light}}}{m_{e,\text{heavy}}}}. \quad (6.31)$$

For holes, the case is similar, except the light hole band is offset from the heavy hole band by a constant E_s :

$$E_{\text{light}} = E_{\text{heavy}} - E_s \quad (6.32)$$

$$\frac{\hbar^2 k_{F,h,\text{light}}^2}{2m_{h,\text{light}}} = \frac{\hbar^2 k_{F,h,\text{heavy}}^2}{2m_{h,\text{heavy}}} - E_s. \quad (6.33)$$

Then we can derive

$$p = p_{\text{heavy}} + p_{\text{light}} \quad (6.34)$$

$$= p_{\text{heavy}} \left(1 + \frac{m_{h,\text{light}}}{m_{h,\text{heavy}}} \right) - \frac{2m_{h,\text{light}} E_s}{4\pi\hbar^2} \quad (6.35)$$

$$= p_{\text{light}} \left(1 + \frac{m_{h,\text{heavy}}}{m_{h,\text{light}}} \right) + \frac{2m_{h,\text{heavy}} E_s}{4\pi\hbar^2}, \quad (6.36)$$

from which we can get $A_{h,\text{light}} = 4\pi^2 p_{\text{light}}$ and $A_{h,\text{heavy}} = 4\pi^2 p_{\text{heavy}}$. The only other constraint used is that p_{heavy} and n_{light} are continuous from region (i).

- (iii) $E_F < 0$: This range below the bottom of the electron-like bands is similar to regime 2 above, where $C_{q,h}$ is the combined quantum capacitance of the hole bands. The only difference here is that the two bands will be filled to different densities, but we stop the discussion here since this range of E_F is not reached in our devices.

Focusing on just V_{tg} dependence to match our two SdH oscillation diagrams, we get the Fermi surface areas in Fig. 6.15. It is apparent that the low density of states in region (i) results in quicker band filling, and the bands fill more slowly once all four bands are involved in region (ii). The parameters used here are $m_{e,\text{light}} = 0.04m_0$, $m_{e,\text{heavy}} = 0.05m_0$, $m_{h,\text{light}} = 0.15m_0$, $m_{h,\text{heavy}} = 0.16m_0$, $E_s = 3$ meV.

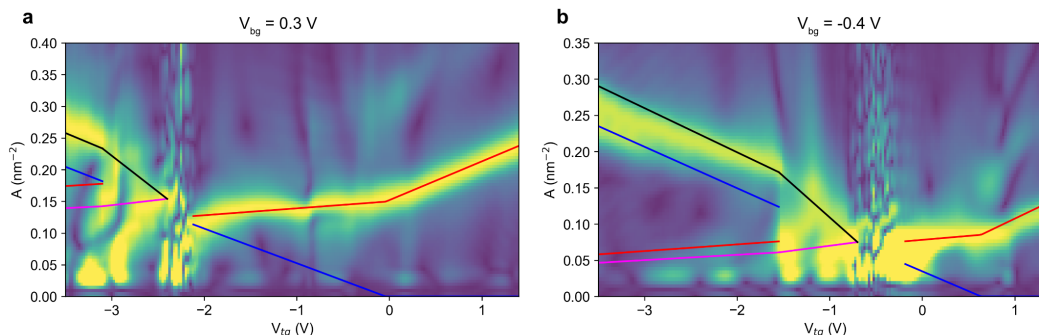


Figure 6.15: Plots of the Fourier transforms of the SdH oscillations (represented as Fermi surface area), along with the capacitance model (right side lines) and split-band effective model (left side lines) fits to the data. Taken for V_{tg} linecuts at two V_{bg} points.

To further visualize the valence band filling, we show the quadratic band schematics for three gate points on the $V_{bg} = -0.4V$ linecut in Fig. 6.16, using the same parameters as in the fits above. All three diagrams show in bold the maximum and minimum filling of each band, and the black line represents the Fermi level. Since the electric field changes with V_{tg} , the bands shift relative to each other. Fig. 6.16a shows the top of the heavy hole and light electron bands, Fig. 6.16b shows the onset of the light hole and heavy electron bands, and Fig. 6.16c shows the far left point in V_{tg} .

Although the inclusion of more fitting parameters into the model introduces more play in the model, and imperfections in the bands will likely change the behavior slightly, a few trends can be noted. The low slope in the left side of the diagrams indicates we have reached region (ii), where both heavy and light electron and hole bands are involved. We also have a ballpark indication of the splitting of the two valence bands, with E_s being in the range of a few meV, and $E_{h,\text{heavy},\text{top}} - E_2 \sim 10$ meV (seen in Fig. 6.16b) as another measure.

The VA18-040 structure, with thicker InAs (13 nm, without impurity Sb) shows similar SdH oscillation behavior. Since the backgate showed signs of saturation at high and low values, visible as a curving CNP in Fig. 6.17a, the model fitting

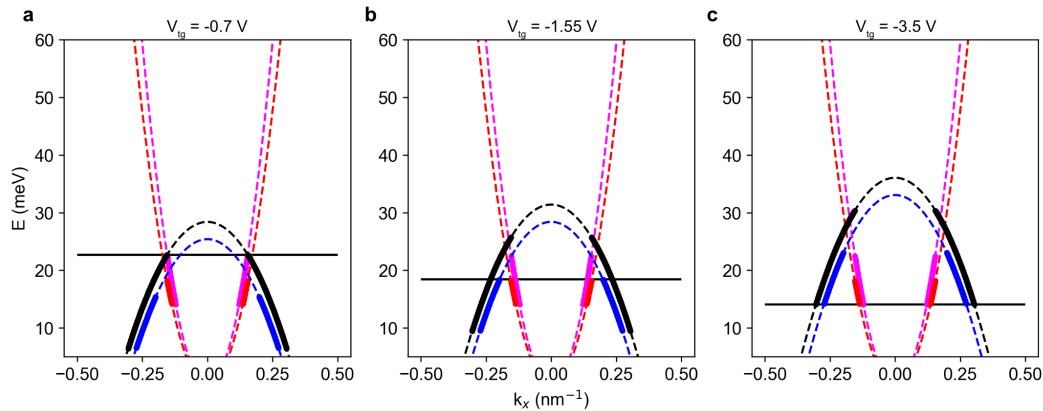


Figure 6.16: The four quadratic bands used in the effective model and the Fermi level (black line) as seen at three different V_{tg} points for $V_{bg} = -0.4V$.

cannot be made as precise, but signs of both light and heavy hole bands are visible in the SdH oscillations (Fig. 6.17c). The larger hole density here is allowed by the larger electron-hole band overlap, which results from the thicker InAs layer (providing less quantum confinement energy). Interestingly, $k \cdot p$ theory for this structure predicts a non-monotonic hybridization gap behavior as the electron-hole band overlap increases (Fig. 6.17b). The non-monotonic behavior is consistent with experiment, where the resistance of the CNP increases along with V_{bg} when $V_{bg} < 0$ and decreases with V_{bg} on the positive side. We leave the in-depth study of the hybridization gap for future studies, but the variance in behavior observed in the two structures—both theoretically and experimentally—suggest a high degree of tunability in such structures by varying stoichiometry and material thickness.

The observation of the valence band transition from one electron/one hole band to two electron/two hole band behavior is a step forward for InAs/GaSb-derivative structures. Previous measurements have either lacked high-quality hole-like SdH oscillations required for reliable determination of the valence band behavior [191] or have not yet reached the point where there is evidence of two electron and two hole bands [194]. The measurements we report serve as indicators of clean heterostructures and well working top and back gates, which allow for wide ranges of density tuning. The combination of sample quality and resistive bulk make these strained heterostructures worthwhile candidates for more rigorous study regarding the 2DTI phase, both theoretically [184] and experimentally in terms of trivial vs. topological edge state conductance [192].

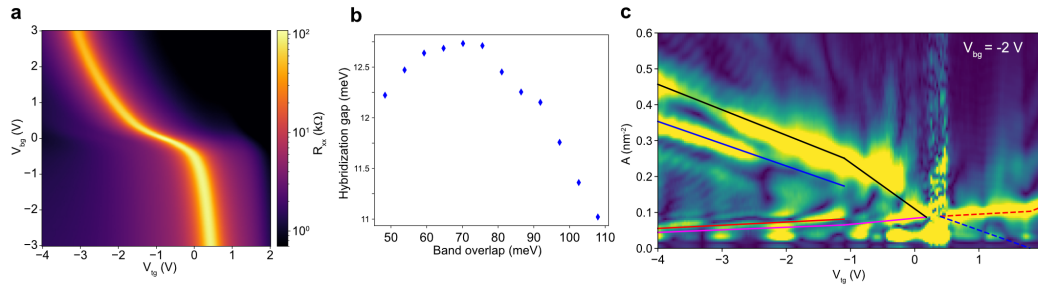


Figure 6.17: Results for a VA18-040 Hallbar. (a) A 2D topgate and backgate map of longitudinal resistance. (b) Hybridization gaps derived from the 8-band $k \cdot p$ model for the approximate range of electron-hole band overlap (top of hole band minus bottom of electron band) seen in experiment. (c) SdH oscillations-derived Fermi surface areas for a linecut at $V_{bg} = -2$ V. The colored lines were calculated from the same models as in Fig. 6.15, but with parameters $C_b = 0.06$, $C_t = 0.08$, $C_m = 1.62 \mu\text{F}/\text{cm}^2$, $E_s = 4$ meV, and the same effective masses except for $m_{h,\text{light}} = 0.14m_0$ in the valence band and $m_h = 0.1m_0$ in the conduction band.

To finish the discussion on strained InAs/GaSb devices, we turn to the in-plane magnetic field dependence, which is another useful determinant of inverted vs. non-inverted bands [160]. The orbital effect of the magnetic field shifts the k midline of the electron and hole bands in opposite directions relative to each other and perpendicular to the applied field following $\Delta k_x \sim eB_y \langle z \rangle / \hbar$, where $\langle z \rangle$ is the distance between the centers of the electron and hole wells (half the overall thickness). Although the larger hybridization gap in the strained devices will make them more impervious to Δk_x shifts, the shifting bands and diminishing bandgap should be apparent, which is confirmed experimentally in Fig. 6.18. Both the VA19-014 and VA18-040 devices show similar trends when the magnetic field is applied approximately along the same direction as the R_{xx} measurement. A gradual resistance decrease is seen, consistent with a slowly closing gap.

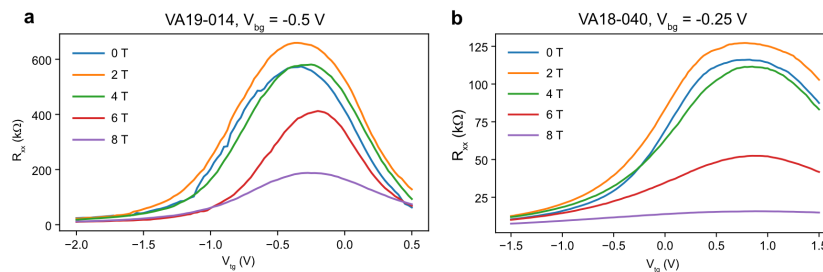


Figure 6.18: In-plane field dependent topgate curves for Hallbar devices with the structure of (a) VA19-014 and (b) VA18-040.

Chapter 7

OUTLOOK

7.1 Twisted moiré heterostructure devices

Research on superconducting twisted graphene moiré heterostructures has just begun. There are wide-ranging theories about the mechanism of superconductivity in TBG alone (Refs. [19, 84–86, 110, 125, 137, 205, 206] represent a small sample), and whether the same mechanisms can be applied to layer number greater than 2 remains to be explored. Additionally, we have only looked at a small range of twist angles in TTG, TQG, and TPG. More phenomena can be found from tuning the interactions through the twist angle of these structures, as has been done with TBG in Chapter 4, or from experimenting with the presence/absence of WSe₂ in heterostructures. Another question remains: are there more graphene moiré heterostructures supporting superconductivity? Twisted structures with layer number up to 5 allow for many more degrees of freedom to be explored.

A range of studies remain to be done, as well, to further probe the superconductivity in graphene moiré heterostructures. The nematicity seen in TBG [207] has not yet been reported in three-five layer systems. If it is unique to TBG, then the question of why remains. Electrical transport measurements with vector magnets and multidirectional contacts could reveal much about superconductivity in multilayer systems. Capacitance measurements, which have been relatively unproductive in TBG systems limited by twist angle disorder, could be useful to determine the phase diagram of other multilayer systems. Due to the higher homogeneity seen in our samples consisting of three and more layers, capacitive measurements of compressibility [151, 152, 208] could more directly and accurately reveal the density of states in these systems. Tunnel junctions and Josephson junctions in interesting geometries can reveal clues about the pairing mechanisms and character of superconductivity [18, 209]. While initial studies on transport devices [68] and STM measurements [132, 140] have revealed the unconventional character of superconductivity in TBG and TTG, careful experimental studies of utilizing a range of geometries could reveal more about the superconducting state.

Devices interfacing superconductivity with other correlated and topological phases are highly sought-after [165]. The unique ability of graphene moiré heterostruc-

tures to host both superconductivity and other correlated states places them in a unique position for studying interfacial phenomena. Since structures such as TBG, TTG, and TQG can exhibit superconductivity, flavor polarized states, and insulating behavior in the same device, problems of imperfect contacts between different materials can be minimized. Interfaces between states can be made by electrically gating selected areas. A few studies have been conducted on TBG Josephson junctions [68, 69] and Josephson junctions involving magnetic regions [210, 211]. However, reproducibility and lack of control over the correlated states available in TBG plague current efforts. The homogeneity and reproducibility of TTG and TQG, along with the new finding of insulating states, could allow for exploring impressive device physics while minimizing the problems inherent to TBG. Gating can not only tune between superconducting and insulating states at different electron densities but also carefully tune the bandwidth and correlations by using electric field. The level of control is unprecedented and would incorporate the unique properties such as high in-plane critical magnetic fields [129] and tunable coherence length. These sorts of devices would allow for further study of superconductivity and for potentially observing new phenomena entirely. For instance, the unique symmetry-broken states in TBG can potentially lead to Majorana bound states [212], and further topological superconducting states could be realized by considering moiré patterns with other materials, such as magnetic van der Waals layers [213].

7.2 Superconductivity stabilization in other graphene systems

Naturally occurring Bernal bilayer graphene (BBG) has recently been found to host superconductivity at high electric fields, with a low transition temperature of ~ 30 mK [152] and only existing at finite in-plane magnetic fields. BBG devices can have high mobility, they are not plagued by the twist-angle inhomogeneity of twisted graphene heterostructures, and they are easy to fabricate in a range of device geometries and sizes. The discovery of superconductivity in BBG, and specifically its link to symmetry breaking transitions allowed by high electric fields, brings to question whether other electronic systems can host superconductivity with an origin analogous to TBG.

We fabricated double-gated BBG devices with monolayer WSe₂ in proximity to the graphene. The phase diagram of R_{xx} with respect to electric displacement field D and electron density n is shown in Fig. 7.1. We focus on the hole side of the phase diagram ($n < 0$). When $D > 0$, the holes are drawn toward the WSe₂, and they are pushed away for $D < 0$. The leftward fan arises from a combination of

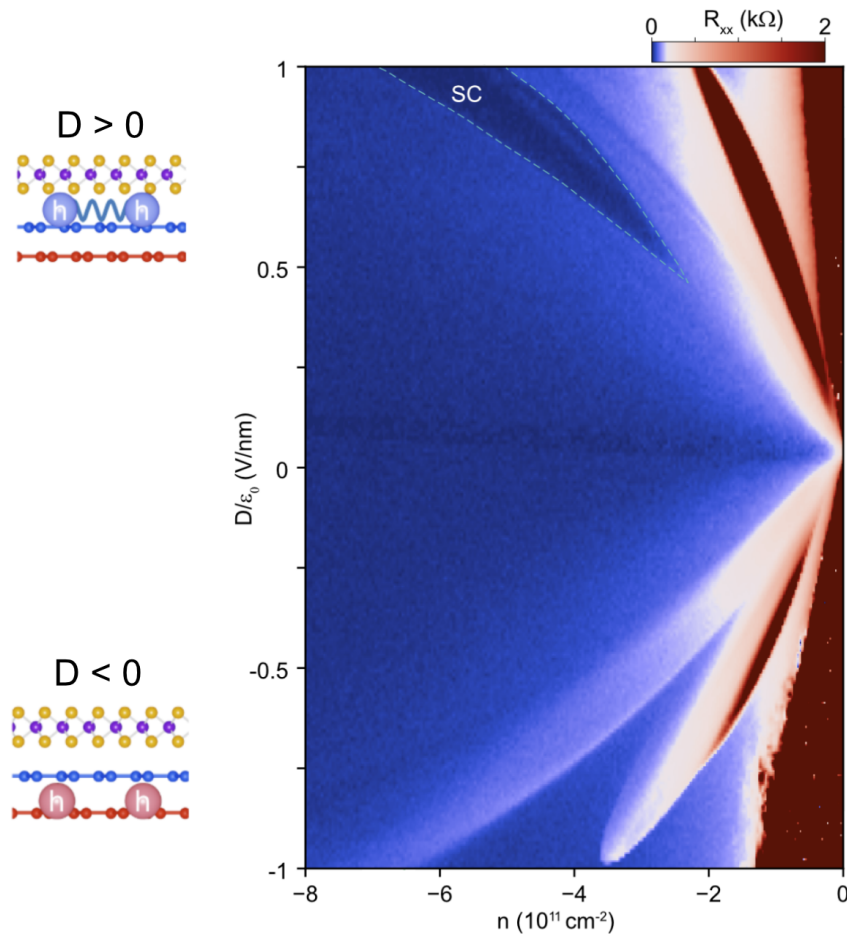


Figure 7.1: 2D R_{xx} plot vs. D and n . The left schematics show the setup of WSe₂ on top of BGG and the direction holes are pulled with each sign of D field.

Fermi surface changes (single-particle) and electronic correlation-driven symmetry breaking.

We find, interestingly, a broad zero-resistance feature on the $D > 0$ side of the phase diagram but not on the $D < 0$ side at zero magnetic field. This superconducting region displays a T_c (T_{BKT}) of 260 mK (Fig. 7.2a), almost an order of magnitude higher than the T_c in BGG without WSe₂. The superconductivity shows a diamond-like Fraunhofer-like pattern (Fig. 7.2b), and the critical field $B_{c\perp} \approx 15$ mT at base temperature yields a corresponding Ginzburg-Landau coherence length $\xi_{GL} = \sqrt{\Phi_0/(2\pi B_{c\perp})} \approx 150$ nm. This is much smaller than the mean free path ℓ_{mf} of BLG-WSe₂, measured using magnetic focusing [106] to be around $10 \mu\text{m}$, placing the superconductivity in the clean limit.

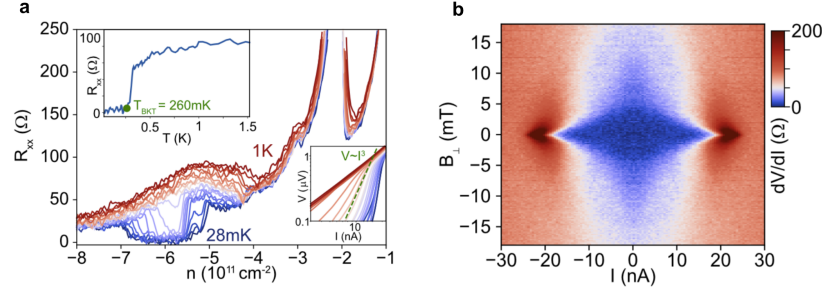


Figure 7.2: Superconductivity characterization under changes in temperature and magnetic field. (a) Temperature linecuts at $D/\epsilon_0 = 1$ V/nm, showing BKT behavior (right bottom inset) with a transition temperature 260 mK (green), along with R_{xx} vs. temperature at $n = -5.75 \times 10^{11}$ cm^{-2} (upper left inset). (b) Fraunhofer-like pattern at $D/\epsilon_0 = 0.9$ V/nm and $n = -5.05 \times 10^{11}$ cm^{-2} .

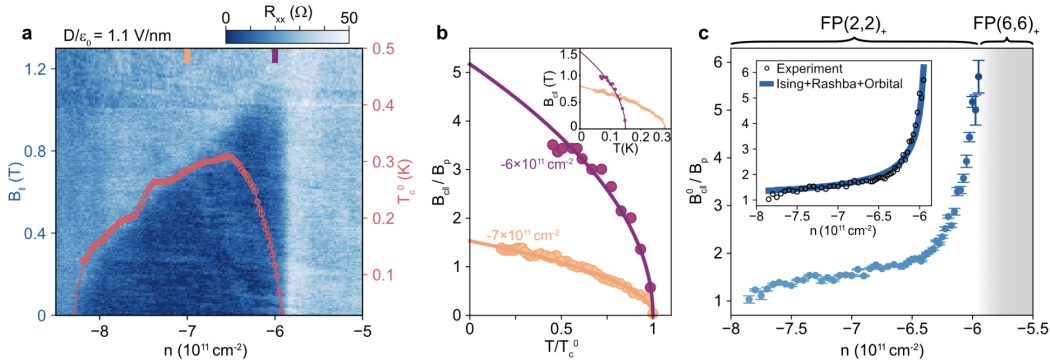


Figure 7.3: Anomalous magnetic-field dependence of superconductivity. (a) A map of the superconducting dome showing the dependence of R_{xx} on in-plane field (B_{\parallel} in the y-axis, left) and n . The zero-field T_c curve vs. n is plotted alongside (right y-axis). (b) Critical in-plane field normalized by the Pauli critical field, as a function of temperature normalized by T_c (inset is un-normalized data). Each curve was taken at a different density, and the solid lines are fit curves. (c) The Pauli violation ratio at a number of densities, with error bars being the standard deviation of the model fits. The doping trend of the PVR is well captured by a model (blue line in the inset) taking into account fixed Ising SOC together with doping-dependent Rashba SOC and constant orbital depairing

We then directed the magnetic field in the plane of the device (B_{\parallel}) and mapped out the superconductivity across the density range, shown in Fig. 7.3. The critical field and T_c curves should be approximately proportional if the superconductor is of the weak-coupling spin-singlet character, since the critical field should follow the Pauli limit $B_p = 1.86 \text{ T/K} \times T_c^0$. However, we find that they diverge on the low-density side of the diagram. When we look into it further (Fig. 7.3b), we

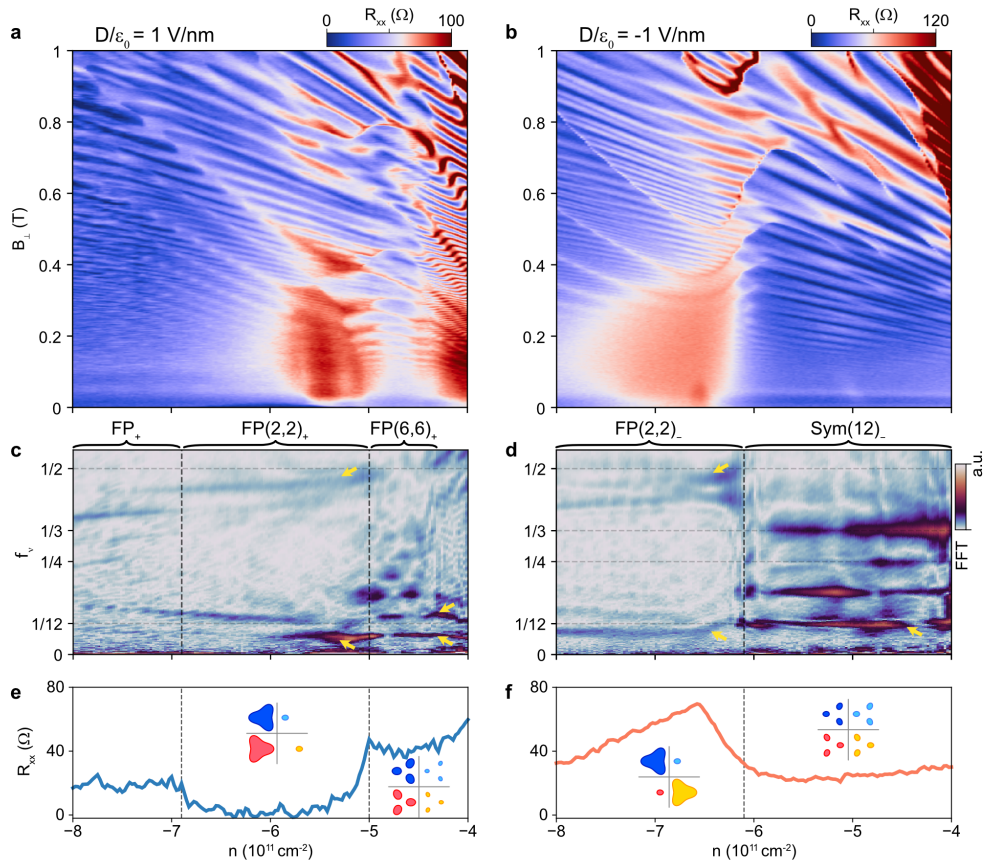


Figure 7.4: Landau fans and corresponding Fourier transforms. (a), (b) Landau fans measured for BBG-WSe₂ at $D/\epsilon_0 = 1$ V/nm and -1 V/nm, respectively. (c), (d) matching normalized Fourier transforms. (e), (f) R_{xx} plots at the same D along with Fermi surface schematics.

find that the critical field-temperature relation at different densities follow the same phenomenological model $T/T_c^0 = 1 - (B_{c\parallel}/B_{c\parallel}^0)^2$. However, the projected critical field at zero temperature $B_{c\parallel}^0$ for the orange curve is very near the Pauli limit, whereas $B_{c\parallel}^0$ for the purple curve shows a strong Pauli violation ratio $B_{c\parallel}^0/B_p \sim 5$. A large Pauli limit violation implies an unconventional pairing mechanism that is less susceptible to magnetic fields. The Pauli violation ratio is mapped across densities in Fig. 7.3c, showing continuous tunability from near-Pauli-limit superconductivity to superconductivity with a Pauli violation ratio up to ~ 6 .

We also measured Landau fan diagrams at $D/\epsilon_0 = 1$ V/nm and $D/\epsilon_0 = -1$ V/nm to map out the Fermi surface in Fig. 7.4a, b, respectively. Fig. 7.4c, d show the Fourier transforms, which have been normalized so that a single Fermi surface should show a line at a value of $f_\nu = 1$. BBG without WSe₂ [152] shows very similar Fermi

surfaces to the case here where $D/\epsilon_0 = -1$ (Fig. 7.4d). A peak of $f_\nu = 1/12$ at low densities represents a state where 12 pockets are being equally filled (3 because of trigonal warping \times 4 flavors), a symmetric 12-fold state ($Sym(12)_-$, with a subscript denoting that $D < 0$). This symmetric state transitions into a flavor-polarized state we call $FP(2, 2)_-$. $FP(2, 2)_-$ contains two pockets of larger density and two pockets of smaller density that are similar in size to the $Sym(12)_-$ pockets.

The $D > 0$ case at low densities, however, shows states at slightly higher and lower frequencies than $1/12$, suggesting the 12-fold degenerate state split in half to form six states with slightly higher and six with slightly lower density than the $Sym(12)_-$. We call this the $FP(6, 6)_+$ state (subscript now denoting that $D > 0$). The $FP(2, 2)_+$ state, although it is very similar to $FP(2, 2)_-$, exists throughout the superconducting range (Fig. 7.4c) and then quickly transitions out to a more complex polarized state at higher densities. This contrasts the larger phase space occupied by $FP(2, 2)_-$ and its transition into a more easily recognized 4-fold symmetric state. Furthermore, superconductivity seen throughout the range of the symmetry broken $FP(2, 2)_+$ state contrasts the appearance of superconductivity in BBG without WSe_2 only on the boundary of the $FP(2, 2)$ and $Sym(12)$ states.

Our observation of zero-field superconductivity throughout the range of the approximately 2-fold symmetry broken state, and the D field asymmetry suggests that spin-orbit coupling could play an important role in stabilizing superconductivity. Furthermore, the symmetry broken state with two out of four flavors filled suggests a similarity with TBG and other moiré systems exhibiting superconductivity. BBG, where spin-orbit coupling's effects are more easily seen than in TBG, could provide a new foundation for studying the effects of WSe_2 , such as how the spin-orbit coupling depends on relative twist angle, and how multiple-layer vs. monolayer WSe_2 effects the system. Since our initial studies already revealed links between the superconductivity, symmetry breaking, and the effects of WSe_2 , more studies will likely further unlock our understanding of the competing phases at play.

7.3 InAs/GaSb-derivative Josephson junction devices

Now we switch to the outlook for InAs/GaSb-based materials. Pairing well controlled 2DTI materials with superconductors is one of the next steps for fully exploiting their unique properties. 2DTIs in Josephson junctions show theoretical promise for studying the phase diagram of topological superconductivity [162, 163] and for a scalable route to networks of topological qubits [164, 165]. So far, promising efforts

have been made in a few material systems [214–216]. However, recent studies [217, 218] have called into question some of the methods used in the past to distinguish between topological and trivial states in Josephson junctions. The gate tunability of InAs/GaSb-derivative systems could offer an electric switch between trivial and topological states with similar qualities, in order to weed out shared effects. Previous results in InAs/GaSb systems [219] can likely be improved upon with the enhanced material quality, strained materials, and gate ranges available now. However, many details still need to be worked out in terms of material compatibility, making transparent contacts to the material, and reducing disorder resulting from etching and deposition steps.

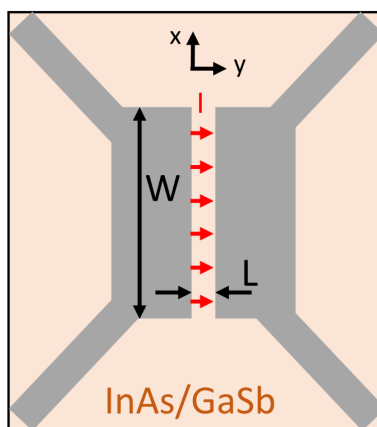


Figure 7.5: Geometry of Josephson junction devices fabricated from InAs/GaSb-derivative quantum well wafers. Shown are the Al electrodes (gray) and quantum well (orange).

To this end, we recently fabricated Josephson Junction devices with the general geometry shown in Fig. 7.5. With batch processing, devices of many widths W and lengths L were fabricated, and we have experimented briefly with the etch geometry around the devices. The processing works roughly as follows. The (capped) quantum wells are selectively etched to the InAs layer, and Al contacts are deposited in the etched area. Then the contacts are separated (except near the junction) by etching through the quantum wells. A dielectric layer is placed on top (usually Si_3N_4 or Al_2O_3), followed by thicker bond pad layers and top gates. So far we have only measured working devices with two quantum well geometries: VA20-004 with 5.1 nm GaSb on 13 nm $\text{InAs}_{0.9}\text{Sb}_{0.1}$ and VA21-010 with 13 nm $\text{InAs}_{0.6}\text{Sb}_{0.4}$ on 5 nm GaSb.

A number of the devices so far reveal reasonable critical currents and resistance measured above critical currents (or in the normal metal state) R_n , as shown in Fig. 7.6. $I_c R_n$ is a measure used for comparing the quality of the Josephson junction, so it is displayed with each figure. However, without much gate voltage dependence and a proper determination of where in the phase diagram we are (metallic, bordering on insulating, etc.), the values can't properly be compared with other devices.

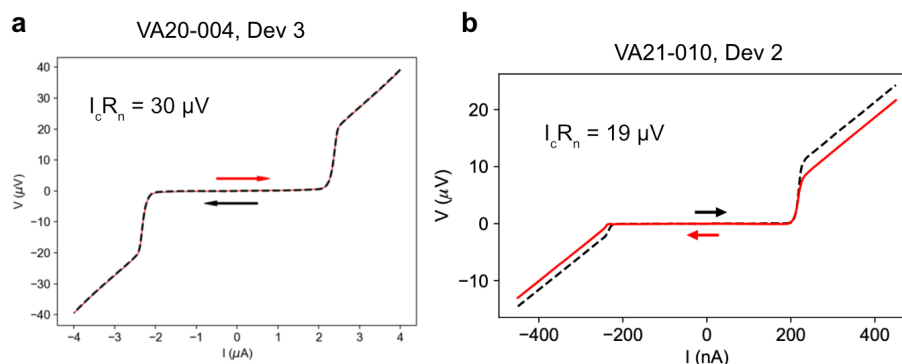


Figure 7.6: I - V curves for two representative devices: (a) from VA20-004 with dimensions $L = 0.15 \mu\text{m}$ and $W = 4 \mu\text{m}$, and (b) from VA21-010 with dimensions $L = 0.3 \mu\text{m}$ and $W = 2 \mu\text{m}$.

The Al-InAsSb/GaSb devices exhibit robust Fraunhofer patterns, as shown in Fig. 7.7a,b. These patterns can be used to determine the approximate current distribution in the device, and the period of the oscillations reflects the device area through the approximate relationship $\Delta BA = \Phi_0$, where the period in magnetic field is ΔB , the area of the device across which supercurrent travels (which is usually offset by a factor due to flux focusing from the contacts) is A , and $\Phi_0 = h/(2e)$ is the flux quantum. We see both oscillation periods that correspond to device geometry and evidence of fairly uniform supercurrent in each device (Fig. 7.7c,d). Well resolved and useful Fraunhofer patterns require several oscillations before the critical field of the superconductor is reached, here around 10 mT, but if the oscillations are too rapid, the magnetic field resolution may not be fine enough to measure a smooth pattern. This, and the fact that longer junctions make it harder for supercurrent to pass, place approximate limitations on the geometry of $L \sim 0.1\text{--}0.5 \mu\text{m}$ and $W \sim 2\text{--}6 \mu\text{m}$, with longer junctions requiring less width. The supercurrent distribution can be derived using the Dynes-Fulton approach [220, 221], and is a useful tool for determining of supercurrent is concentrated on the edges.

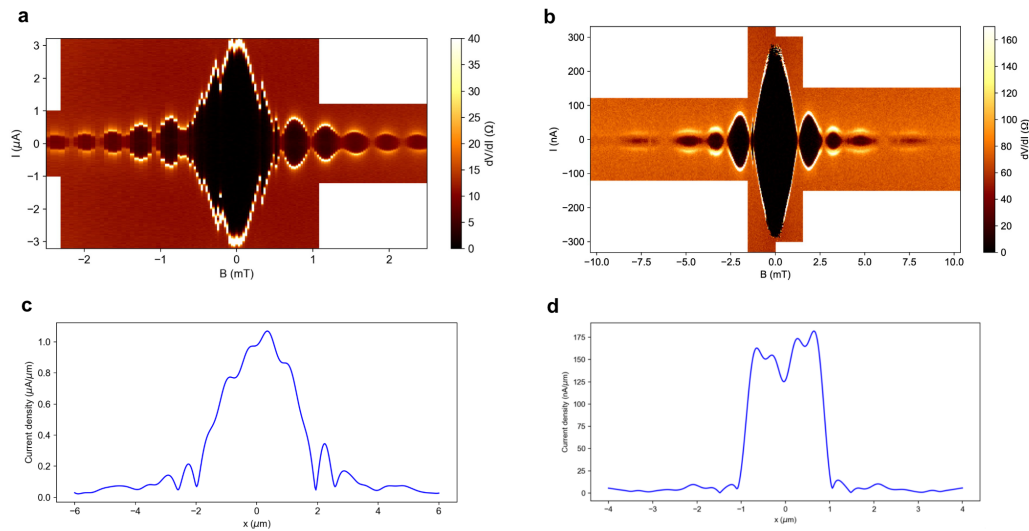


Figure 7.7: Fraunhofer patterns measured for two Josephson junctions. (a) Dev 3 from VA20-004 and (b) Dev 2 from VA21-010. The Dynes-Fulton-based estimates, derived from the Fraunhofer patterns above, of current density along the width of the Josephson junctions are shown in the lower panels.

Although some optimization is needed for larger gate ranges, some progress has been made. Fig. 7.8 and Fig. 7.9 show two devices with gate dependence suggesting that we are on the electron side of the phase diagram since R_n increases with decreasing V_{tg} . Interestingly, the $I_c R_n$ product in Fig. 7.8a increases as electrons are removed from the system. Although the critical current is small in Fig. 7.9, this device shows both topgate (panel a) and backgate dependence (panel b) to the critical current. The topgate range allows for large modulation of I_c , from full suppression to ~ 50 nA. R_n was also measured by killing the superconductivity with an out-of-plane field of 50 mT (panel c), showing both topgate and backgate dependence. The saturation of R_n at small V_{tg} and large resistance (~ 10 s of k Ω) suggest that the device quality is close to showing the transition from the conduction to the valence band.

The Josephson junction devices shown already suggest promising results with finer tuning of geometries, fabrication details, and material properties. These considerations along with the promise of strained InAs/GaSb-derivative quantum wells offer significant prospects for further study and could easily offer improvements into the understanding of superconducting devices with 2DTI candidates. Potential next steps are measuring Shapiro steps resulting from the irradiation of microwave-frequency excitations on Josephson junctions [219, 222, 223], measuring the current-phase relationship with more complex geometries [214, 224], and looking for phase

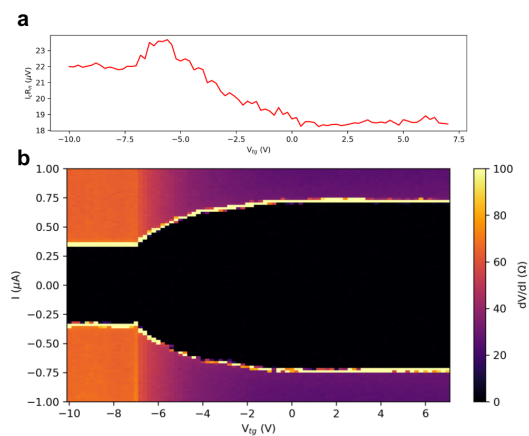


Figure 7.8: Critical current vs. gate voltage. $I_c R_n$ (a) and dV/dI data (b) for Josephson junction device 013 from VA21-010 ($L = 0.3 \mu\text{m}$ and $W = 4 \mu\text{m}$) showing topgate dependence. The saturation of the critical current left of $V_{tg} = -7\text{V}$ is likely due to screening in the gate.

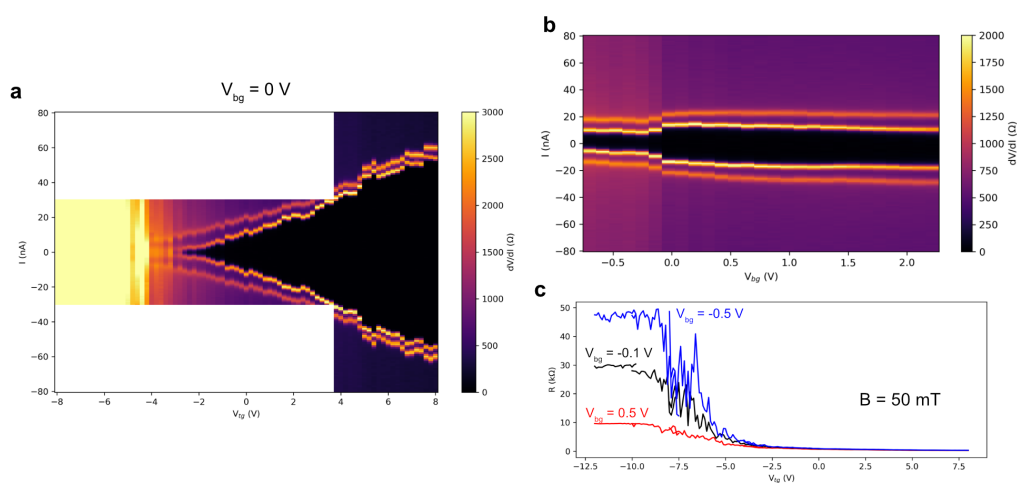


Figure 7.9: Changing critical current with topgate and backgate. (a) dV/dI data for Josephson junction 212 from VA21-010 ($L = 0.2 \mu\text{m}$ and $W = 4 \mu\text{m}$) showing I_c from 0 to $\sim 50 \text{ nA}$ as the topgate is tuned. (b) dV/dI and (c) resistance taken at 50 mT to kill superconductivity, showing modulation with back gate.

transitions that can be associated with topological superconductivity and Majorana bound states [156, 163, 165, 214, 216, 225].

BIBLIOGRAPHY

1. Castro Neto, A. H., Guinea, F., Peres, N. M. R., Novoselov, K. S. & Geim, A. K. The electronic properties of graphene. *Reviews of Modern Physics* **81**, 109–162. ISSN: 00346861. arXiv: [0709.1163](https://arxiv.org/abs/0709.1163) (2009).
2. Novoselov, K. S. *et al.* Electric field effect in atomically thin carbon films. *Science* **306**, 666–669. ISSN: 0036-8075. arXiv: [cond-mat/0410550](https://arxiv.org/abs/cond-mat/0410550). <http://www.sciencemag.org/cgi/doi/10.1126/science.1102896> (2004).
3. Novoselov, K. S. *et al.* Two-dimensional atomic crystals. *Proceedings of the National Academy of Sciences* **102**, 10451–10453. ISSN: 0027-8424. <http://www.pnas.org/cgi/doi/10.1073/pnas.0502848102> (2005).
4. Du, X., Prober, D. E., Vora, H. & Mckitterick, C. B. Graphene-based bolometers. *Graphene and 2D Materials* **1**, 1–22. ISSN: 2299-3134. arXiv: [1308.4065](https://arxiv.org/abs/1308.4065). <https://access.portico.org/stable?au=pgjm3g0nj6> (2014).
5. Young, A. F. & Kim, P. Quantum interference and Klein tunnelling in graphene heterojunctions. *Nature Physics* **5**, 222–226. ISSN: 1745-2473. arXiv: [0808.0855](https://arxiv.org/abs/0808.0855). <https://www.nature.com/articles/nphys1198> (2009).
6. Ashcroft, N. & Mermin, N. D. *Solid State Physics* ISBN: 978-0-03-083993-1 (Brooks/Cole, Cengage Learning, 1976).
7. Lee, P. A., Nagaosa, N. & Wen, X.-G. Doping a Mott insulator: Physics of high-temperature superconductivity. *Reviews of Modern Physics* **78**, 17–85. ISSN: 0034-6861. arXiv: [0410445](https://arxiv.org/abs/0410445). <https://link.aps.org/doi/10.1103/RevModPhys.78.17> (2006).
8. Cohen, M. L. & Louie, S. G. *Fundamentals of Condensed Matter Physics* ISBN: 978-0-521-51331-9 (Cambridge University Press, 2016).
9. Young, A. F. *et al.* Tunable symmetry breaking and helical edge transport in a graphene quantum spin Hall state. *Nature* **505**, 528–532. ISSN: 0028-0836. arXiv: [1307.5104](https://arxiv.org/abs/1307.5104). <http://www.nature.com/articles/nature12800> (2014).
10. Choi, Y. *et al.* Electronic correlations in twisted bilayer graphene near the magic angle. *Nature Physics* **15**, 1174–1180. ISSN: 1745-2473. <https://www.nature.com/articles/s41567-019-0606-5> (2019).
11. Bistritzer, R. & MacDonald, A. H. Moire bands in twisted double-layer graphene. *Proceedings of the National Academy of Sciences* **108**, 12233–12237. ISSN: 0027-8424. arXiv: [1009.4203](https://arxiv.org/abs/1009.4203). <http://www.pnas.org/cgi/doi/10.1073/pnas.1108174108> (2011).

12. Lopes dos Santos, J. M. B., Peres, N. M. R. & Castro Neto, A. H. Graphene bilayer with a twist: Electronic structure. *Physical Review Letters* **99**, 256802. ISSN: 0031-9007. arXiv: [0704.2128](https://arxiv.org/abs/0704.2128). <https://link.aps.org/doi/10.1103/PhysRevLett.99.256802> (2007).
13. Nam, N. N. T. & Koshino, M. Lattice relaxation and energy band modulation in twisted bilayer graphene. *Physical Review B* **96**, 075311. ISSN: 2469-9969. arXiv: [1706.03908](https://arxiv.org/abs/1706.03908). <https://link.aps.org/doi/10.1103/PhysRevB.96.075311> (2017).
14. Choi, Y. *et al.* Interaction-driven band flattening and correlated phases in twisted bilayer graphene. *Nature Physics* **17**, 1375–1381. ISSN: 1745-2473. arXiv: [2102.02209](https://arxiv.org/abs/2102.02209). <https://www.nature.com/articles/s41567-021-01359-0> (2021).
15. Bardeen, J., Cooper, L. N. & Schrieffer, J. R. Theory of superconductivity. *Physical Review* **108**, 1175–1204. ISSN: 0031-899X. <https://link.aps.org/doi/10.1103/PhysRev.108.1175> (1957).
16. Bednorz, J. G. & Müller, K. A. Perovskite-type oxides—The new approach to high- T_c superconductivity. *Reviews of Modern Physics* **60**, 585–600. ISSN: 0034-6861. <https://link.aps.org/doi/10.1103/RevModPhys.60.585> (1988).
17. Tinkham, M. *Introduction to Superconductivity* ISBN: 978-0-486-43503-9 (Dover Publications, 1996).
18. Van Harlingen, D. J. Phase-sensitive tests of the symmetry of the pairing state in the high-temperature superconductors—Evidence for $d_{x^2-y^2}$ symmetry. *Reviews of Modern Physics* **67**, 515–535. ISSN: 0034-6861. <https://link.aps.org/doi/10.1103/RevModPhys.67.515> (1995).
19. Khalaf, E., Chatterjee, S., Bultinck, N., Zaletel, M. P. & Vishwanath, A. Charged skyrmions and topological origin of superconductivity in magic-angle graphene. *Science Advances* **7**, 1–11. ISSN: 23752548. arXiv: [2004.00638](https://arxiv.org/abs/2004.00638). <https://www.science.org/doi/10.1126/sciadv.abf5299> (2021).
20. Cao, Y. *et al.* Unconventional superconductivity in magic-angle graphene superlattices. *Nature* **556**, 43–50. ISSN: 0028-0836. arXiv: [1803.02342](https://arxiv.org/abs/1803.02342). <http://www.nature.com/articles/nature26160> (2018).
21. Randeria, M. & Taylor, E. Crossover from Bardeen-Cooper-Schrieffer to Bose-Einstein condensation and the unitary Fermi gas. *Annual Review of Condensed Matter Physics* **5**, 209–232. ISSN: 1947-5454. <https://www.annualreviews.org/doi/10.1146/annurev-conmatphys-031113-133829> (2014).

22. Uemura, Y. J. *et al.* Basic similarities among cuprate, bismuthate, organic, Chevrel-phase, and heavy-fermion superconductors shown by penetration-depth measurements. *Physical Review Letters* **66**, 2665–2668. ISSN: 0031-9007. <https://link.aps.org/doi/10.1103/PhysRevLett.66.2665> (1991).
23. Talantsev, E. F., Maitra, R. C. & Crump, W. P. Classifying superconductivity in moiré graphene superlattices. *Scientific Reports* **10**, 212. ISSN: 2045-2322. <http://www.nature.com/articles/s41598-019-57055-w> (2020).
24. Nakagawa, Y. *et al.* Gate-controlled BCS-BEC crossover in a two-dimensional superconductor. *Science* **372**, 190–195. ISSN: 0036-8075. <https://www.sciencemag.org/lookup/doi/10.1126/science.abb9860> (2021).
25. Kane, C. L. & Mele, E. J. Quantum spin Hall effect in graphene. *Physical Review Letters* **95**, 1–4. ISSN: 00319007. arXiv: [0411737v2](https://arxiv.org/abs/0411737v2). <https://link.aps.org/doi/10.1103/PhysRevLett.95.226801> (2005).
26. Ihn, T. *Semiconductor Nanostructures: Quantum States and Electronic Transport* ISBN: 978-0-19-953443-2 (Oxford University Press, 2010).
27. Haldane, F. D. M. Model for a quantum hall effect without Landau levels: Condensed-matter realization of the “parity anomaly”. *Physical Review Letters* **61**, 2015–2018. ISSN: 1079-7114. <https://link.aps.org/doi/10.1103/PhysRevLett.61.2015> (1988).
28. Wang, Z. *et al.* Origin and magnitude of ‘designer’ spin-orbit interaction in graphene on semiconducting transition metal dichalcogenides. *Physical Review X* **6**, 041020. ISSN: 2160-3308. arXiv: [1606.01789](https://arxiv.org/abs/1606.01789). <https://link.aps.org/doi/10.1103/PhysRevX.6.041020> (2016).
29. Wakamura, T. *et al.* Spin-orbit interaction induced in graphene by transition metal dichalcogenides. *Physical Review B* **99**, 1–12. ISSN: 2469-9969. <https://link.aps.org/doi/10.1103/PhysRevB.99.245402> (2019).
30. Wakamura, T., Guéron, S. & Bouchiat, H. Novel transport phenomena in graphene induced by strong spin-orbit interaction. arXiv: [2112.07813](https://arxiv.org/abs/2112.07813). <http://arxiv.org/abs/2112.07813> (2021).
31. Qiao, Z. *et al.* Quantum anomalous Hall effect in graphene from Rashba and exchange effects. *Physical Review B* **82**, 161414. ISSN: 2469-9969. arXiv: [1005.1672](https://arxiv.org/abs/1005.1672). <https://link.aps.org/doi/10.1103/PhysRevB.82.161414> (2010).
32. Island, J. O. *et al.* Spin-orbit-driven band inversion in bilayer graphene by the van der Waals proximity effect. *Nature* **571**, 85–89. ISSN: 0028-0836. arXiv: [1901.01332](https://arxiv.org/abs/1901.01332). <http://www.nature.com/articles/s41586-019-1304-2> (2019).

33. Semenoff, G. W. Condensed-matter simulation of a three-dimensional anomaly. *Physical Review Letters* **53**, 2449–2452. ISSN: 0031-9007. <https://link.aps.org/doi/10.1103/PhysRevLett.53.2449> (1984).
34. Xiao, D., Yao, W. & Niu, Q. Valley-contrasting physics in graphene: Magnetic moment and topological transport. *Physical Review Letters* **99**, 1–4. ISSN: 0031-9007. arXiv: [0709.1274](https://arxiv.org/abs/0709.1274). <https://link.aps.org/doi/10.1103/PhysRevLett.99.236809> (2007).
35. Liu, C.-X., Zhang, S.-C. & Qi, X.-L. The quantum anomalous Hall effect: Theory and experiment. *Annual Review of Condensed Matter Physics* **7**, 301–321. ISSN: 1947-5454. <https://www.annualreviews.org/doi/10.1146/annurev-conmatphys-031115-011417> (2016).
36. Zou, L., Po, H. C., Vishwanath, A. & Senthil, T. Band structure of twisted bilayer graphene: Emergent symmetries, commensurate approximants, and Wannier obstructions. *Physical Review B* **98**, 085435. ISSN: 24699969. arXiv: [1806.07873](https://arxiv.org/abs/1806.07873). <https://link.aps.org/doi/10.1103/PhysRevB.98.085435> (2018).
37. Gorbachev, R. V. *et al.* Detecting topological currents in graphene superlattices. *Science* **346**, 448–451. ISSN: 0036-8075. <http://www.sciencemag.org/cgi/doi/10.1126/science.1254966> (2014).
38. Dean, C. R. *et al.* Boron nitride substrates for high-quality graphene electronics. *Nature Nanotechnology* **5**, 722–726. ISSN: 1748-3387. arXiv: [1005.4917](https://arxiv.org/abs/1005.4917). <http://www.nature.com/articles/nnano.2010.172> (2010).
39. Xue, J. *et al.* Scanning tunnelling microscopy and spectroscopy of ultra-flat graphene on hexagonal boron nitride. *Nature Materials* **10**, 282–285. ISSN: 1476-1122. <http://www.nature.com/articles/nmat2968> (2011).
40. Wang, L. *et al.* One-dimensional electrical contact to a two-dimensional material. *Science* **342**, 614–617. ISSN: 0036-8075. <https://www.science.org/doi/10.1126/science.1244358> (2013).
41. Purdie, D. G. *et al.* Cleaning interfaces in layered materials heterostructures. *Nature Communications* **9**, 5387. ISSN: 2041-1723. arXiv: [1803.00912](https://arxiv.org/abs/1803.00912). <http://www.nature.com/articles/s41467-018-07558-3> (2018).
42. Kim, K. *et al.* Van der Waals heterostructures with high accuracy rotational alignment. *Nano Letters* **16**, 1989–1995. ISSN: 1530-6984. <https://pubs.acs.org/doi/10.1021/acs.nanolett.5b05263> (2016).
43. Yankowitz, M. *et al.* Tuning superconductivity in twisted bilayer graphene. *Science* **363**, 1059–1064. ISSN: 0036-8075. arXiv: [1808.07865](https://arxiv.org/abs/1808.07865). <https://www.science.org/doi/10.1126/science.aav1910> (2019).

44. Lu, X. *et al.* Superconductors, orbital magnets, and correlated states in magic angle bilayer graphene. *Nature* **574**, 20–23. ISSN: 1476-4687. arXiv: [1903.06513](https://arxiv.org/abs/1903.06513). <https://www.nature.com/articles/s41586-019-1695-0> (2019).
45. Codecido, E. *et al.* Correlated insulating and superconducting states in twisted bilayer graphene below the magic angle. *Science Advances* **5**, 1–6. ISSN: 2375-2548. arXiv: [1902.05151](https://arxiv.org/abs/1902.05151). <https://www.science.org/doi/10.1126/sciadv.aaw9770> (2019).
46. Arora, H. S. *et al.* Superconductivity in metallic twisted bilayer graphene stabilized by WSe₂. *Nature* **583**, 379–384. ISSN: 0028-0836. <https://www.nature.com/articles/s41586-020-2473-8> (2020).
47. Stepanov, P. *et al.* Untying the insulating and superconducting orders in magic-angle graphene. *Nature* **583**, 375–378. ISSN: 0028-0836. arXiv: [1911.09198](https://arxiv.org/abs/1911.09198). <http://www.nature.com/articles/s41586-020-2459-6> (2020).
48. Saito, Y., Ge, J., Watanabe, K., Taniguchi, T. & Young, A. F. Independent superconductors and correlated insulators in twisted bilayer graphene. *Nature Physics* **16**, 926–930. ISSN: 1745-2473. <https://www.nature.com/articles/s41567-020-0928-3> (2020).
49. Cao, Y. *et al.* Strange metal in magic-angle graphene with near Planckian dissipation. *Physical Review Letters* **124**, 076801. ISSN: 0031-9007. arXiv: [1901.03710](https://arxiv.org/abs/1901.03710). <https://link.aps.org/doi/10.1103/PhysRevLett.124.076801> (2020).
50. Stepanov, P. *et al.* Competing zero-field Chern insulators in superconducting twisted bilayer graphene. *Physical Review Letters* **127**, 197701. ISSN: 0031-9007. arXiv: [2012.15126](https://arxiv.org/abs/2012.15126). <https://link.aps.org/doi/10.1103/PhysRevLett.127.197701> (2021).
51. Liu, X., Zhang, N. J., Watanabe, K., Taniguchi, T. & Li, J. I. A. Coulomb screening and thermodynamic measurements in magic-angle twisted trilayer graphene, 1–23. arXiv: [2108.03338](https://arxiv.org/abs/2108.03338). <http://arxiv.org/abs/2108.03338> (2021).
52. Das, I. *et al.* Symmetry-broken Chern insulators and Rashba-like Landau-level crossings in magic-angle bilayer graphene. *Nature Physics* **17**, 710–714. ISSN: 1745-2473. <http://www.nature.com/articles/s41567-021-01186-3> (2021).
53. Polski, R. *et al.* Hierarchy of symmetry breaking correlated phases in twisted bilayer graphene. arXiv: [2205.05225](https://arxiv.org/abs/2205.05225). <http://arxiv.org/abs/2205.05225> (2022).
54. Uri, A. *et al.* Mapping the twist-angle disorder and Landau levels in magic-angle graphene. *Nature* **581**, 47–52. ISSN: 0028-0836. <http://www.nature.com/articles/s41586-020-2255-3> (2020).

55. Shi, J., Zhu, J. & MacDonald, A. H. Moiré commensurability and the quantum anomalous Hall effect in twisted bilayer graphene on hexagonal boron nitride. *Physical Review B* **103**, 075122. ISSN: 2469-9950. arXiv: [2011.11895](https://arxiv.org/abs/2011.11895). <https://link.aps.org/doi/10.1103/PhysRevB.103.075122> (2021).
56. Grover, S. *et al.* Imaging Chern mosaic and Berry-curvature magnetism in magic-angle graphene. arXiv: [2201.06901](https://arxiv.org/abs/2201.06901). <http://arxiv.org/abs/2201.06901> (2022).
57. Choi, Y. *et al.* Correlation-driven topological phases in magic-angle twisted bilayer graphene. *Nature* **589**, 536–541. ISSN: 0028-0836. <http://www.nature.com/articles/s41586-020-03159-7> (2021).
58. Zhang, Y. *et al.* Ascendance of superconductivity in magic-angle graphene multilayers. arXiv: [2112.09270](https://arxiv.org/abs/2112.09270). <http://arxiv.org/abs/2112.09270> (2021).
59. Zhang, Y., Tan, Y.-W., Stormer, H. L. & Kim, P. Experimental observation of the quantum Hall effect and Berry’s phase in graphene. *Nature* **438**, 201–204. ISSN: 0028-0836. arXiv: [cond-mat/0509355](https://arxiv.org/abs/cond-mat/0509355) [cond-mat]. <http://www.nature.com/articles/nature04235> (2005).
60. Novoselov, K. S. *et al.* Two-dimensional gas of massless Dirac fermions in graphene. *Nature* **438**, 197–200. ISSN: 0028-0836. arXiv: [0509330](https://arxiv.org/abs/0509330) [cond-mat]. <http://www.nature.com/articles/nature04233> (2005).
61. Cao, Y. *et al.* Superlattice-induced insulating states and valley-protected orbits in twisted bilayer graphene. *Physical Review Letters* **117**, 116804. ISSN: 0031-9007. arXiv: [1607.05147](https://arxiv.org/abs/1607.05147). <https://link.aps.org/doi/10.1103/PhysRevLett.117.116804> (2016).
62. Zhang, Y.-H., Po, H. C. & Senthil, T. Landau level degeneracy in twisted bilayer graphene: Role of symmetry breaking. *Physical Review B* **100**, 125104. ISSN: 2469-9969. arXiv: [1904.10452](https://arxiv.org/abs/1904.10452). <https://link.aps.org/doi/10.1103/PhysRevB.100.125104> (2019).
63. Krinner, S. *et al.* Engineering cryogenic setups for 100-qubit scale superconducting circuit systems. *EPJ Quantum Technology* **6**, 2. ISSN: 2662-4400. arXiv: [1806.07862](https://arxiv.org/abs/1806.07862). <https://epjquantumtechnology.springeropen.com/articles/10.1140/epjqt/s40507-019-0072-0> (2019).
64. Kou, A. *Microscopic Properties of the Fractional Quantum Hall Effect* PhD thesis (Harvard University, Cambridge, MA, 2013).
65. Cao, Y. *et al.* Correlated insulator behaviour at half-filling in magic-angle graphene superlattices. *Nature* **556**, 80–84. ISSN: 0028-0836. arXiv: [1802.00553](https://arxiv.org/abs/1802.00553). <http://www.nature.com/articles/nature26154> (2018).

66. Sharpe, A. L. *et al.* Emergent ferromagnetism near three-quarters filling in twisted bilayer graphene. *Science* **365**, 605–608. ISSN: 1095-9203. arXiv: [1901.03520](https://arxiv.org/abs/1901.03520). <https://www.science.org/doi/10.1126/science.aaw3780> (2019).
67. Serlin, M. *et al.* Intrinsic quantized anomalous Hall effect in a moiré heterostructure. *Science* **367**, 900–903. ISSN: 0036-8075. arXiv: [1907.00261](https://arxiv.org/abs/1907.00261). <https://www.science.org/doi/10.1126/science.aay5533> (2020).
68. Rodan-Legrain, D. *et al.* Highly tunable junctions and non-local Josephson effect in magic-angle graphene tunnelling devices. *Nature Nanotechnology* **16**, 769–775. ISSN: 1748-3387. <http://www.nature.com/articles/s41565-021-00894-4> (2021).
69. De Vries, F. K. *et al.* Gate-defined Josephson junctions in magic-angle twisted bilayer graphene. *Nature Nanotechnology* **16**, 760–763. ISSN: 17483395. arXiv: [2011.00011](https://arxiv.org/abs/2011.00011). <https://www.nature.com/articles/s41565-021-00896-2> (2021).
70. Park, J. M., Cao, Y., Watanabe, K., Taniguchi, T. & Jarillo-Herrero, P. Flavour Hund’s coupling, Chern gaps and charge diffusivity in moiré graphene. *Nature* **592**, 43–48. ISSN: 0028-0836. <http://www.nature.com/articles/s41586-021-03366-w> (2021).
71. Xie, Y. *et al.* Spectroscopic signatures of many-body correlations in magic-angle twisted bilayer graphene. *Nature* **572**, 101–105. ISSN: 0028-0836. arXiv: [1906.09274](https://arxiv.org/abs/1906.09274). <http://www.nature.com/articles/s41586-019-1422-x> (2019).
72. Kerelsky, A. *et al.* Maximized electron interactions at the magic angle in twisted bilayer graphene. *Nature* **572**, 95–100. ISSN: 0028-0836. <http://www.nature.com/articles/s41586-019-1431-9> (2019).
73. Jiang, Y. *et al.* Charge order and broken rotational symmetry in magic-angle twisted bilayer graphene. *Nature* **573**, 91–95. ISSN: 0028-0836. arXiv: [1904.10153](https://arxiv.org/abs/1904.10153). <http://www.nature.com/articles/s41586-019-1460-4> (2019).
74. Wong, D. *et al.* Cascade of electronic transitions in magic-angle twisted bilayer graphene. *Nature* **582**, 198–202. ISSN: 0028-0836. <http://www.nature.com/articles/s41586-020-2339-0> (2020).
75. Zondiner, U. *et al.* Cascade of phase transitions and Dirac revivals in magic-angle graphene. *Nature* **582**, 203–208. ISSN: 1476-4687. arXiv: [1912.06150](https://arxiv.org/abs/1912.06150). <https://www.nature.com/articles/s41586-020-2373-y> (2020).
76. Zihlmann, S. *et al.* Large spin relaxation anisotropy and valley-Zeeman spin-orbit coupling in WSe₂/graphene/h-BN heterostructures. *Physical Review B* **97**, 1–10. ISSN: 2469-9969. arXiv: [1712.05678](https://arxiv.org/abs/1712.05678). <https://link.aps.org/doi/10.1103/PhysRevB.97.075434> (2018).

77. Wang, D. *et al.* Quantum Hall effect measurement of spin-orbit coupling strengths in ultraclean bilayer graphene/WSe₂ heterostructures. *Nano Letters* **19**, 7028–7034. ISSN: 1530-6992. arXiv: [1909.10931](https://arxiv.org/abs/1909.10931). <https://pubs.acs.org/doi/10.1021/acs.nanolett.9b02445> (2019).
78. Kretinin, A. V. *et al.* Electronic properties of graphene encapsulated with different two-dimensional atomic crystals. *Nano Letters* **14**, 3270–3276. ISSN: 1530-6984. <https://pubs.acs.org/doi/10.1021/nl5006542> (2014).
79. Wilson, N. R. *et al.* Determination of band offsets, hybridization, and exciton binding in 2D semiconductor heterostructures. *Science Advances* **3**, 1–8. ISSN: 2375-2548. <https://www.science.org/doi/10.1126/sciadv.1601832> (2017).
80. He, M. *et al.* Symmetry breaking in twisted double bilayer graphene. *Nature Physics* **17**, 26–30. ISSN: 1745-2473. <https://www.nature.com/articles/s41567-020-1030-6> (2021).
81. Koshino, M. *et al.* Maximally localized Wannier orbitals and the extended Hubbard model for twisted bilayer graphene. *Physical Review X* **8**, 031087. ISSN: 2160-3308. arXiv: [1805.06819](https://arxiv.org/abs/1805.06819). <https://link.aps.org/doi/10.1103/PhysRevX.8.031087> (2018).
82. Polshyn, H. *et al.* Large linear-in-temperature resistivity in twisted bilayer graphene. *Nature Physics* **15**, 1011–1016. ISSN: 1745-2473. <https://www.nature.com/articles/s41567-019-0596-3> (2019).
83. Lilly, M. P. *et al.* Resistivity of dilute 2D electrons in an undoped GaAs heterostructure. *Physical Review Letters* **90**, 056806. ISSN: 0031-9007. arXiv: [0210155](https://arxiv.org/abs/0210155). <https://link.aps.org/doi/10.1103/PhysRevLett.90.056806> (2003).
84. Wu, F., Macdonald, A. H. & Martin, I. Theory of phonon-mediated superconductivity in twisted bilayer graphene. *Physical Review Letters* **121**, 257001. ISSN: 1079-7114. arXiv: [1805.08735](https://arxiv.org/abs/1805.08735). <https://link.aps.org/doi/10.1103/PhysRevLett.121.257001> (2018).
85. Lian, B., Wang, Z. & Bernevig, B. A. Twisted bilayer graphene: A phonon-driven superconductor. *Physical Review Letters* **122**, 257002. ISSN: 10797114. arXiv: [1807.04382](https://arxiv.org/abs/1807.04382). <https://link.aps.org/doi/10.1103/PhysRevLett.122.257002> (2019).
86. Wu, F., Hwang, E. & Das Sarma, S. Phonon-induced giant linear-in-T resistivity in magic angle twisted bilayer graphene: Ordinary strangeness and exotic superconductivity. *Physical Review B* **99**, 1–13. ISSN: 2469-9969. arXiv: [1811.04920](https://arxiv.org/abs/1811.04920). <https://link.aps.org/doi/10.1103/PhysRevB.99.165112> (2019).
87. Stewart, G. R. Heavy-fermion systems. *Reviews of Modern Physics* **56**, 755–787. ISSN: 0034-6861. <https://link.aps.org/doi/10.1103/RevModPhys.56.755> (1984).

88. Ardavan, A. *et al.* Recent topics of organic superconductors. *Journal of the Physical Society of Japan* **81**, 011004. ISSN: 0031-9015. <http://journals.jps.jp/doi/10.1143/JPSJ.81.011004> (2012).
89. Stewart, G. R. Superconductivity in iron compounds. *Reviews of Modern Physics* **83**, 1589–1652. ISSN: 0034-6861. <https://link.aps.org/doi/10.1103/RevModPhys.83.1589> (2011).
90. Wang, Z. *et al.* Strong interface-induced spin–orbit interaction in graphene on WS₂. *Nature Communications* **6**, 8339. ISSN: 2041-1723. arXiv: [1508.02912](https://arxiv.org/abs/1508.02912). <http://www.nature.com/articles/ncomms9339> (2015).
91. McCann, E. & Fal’ko, V. I. z→-z symmetry of spin-orbit coupling and weak localization in graphene. *Physical Review Letters* **108**, 166606. ISSN: 0031-9007. arXiv: [1111.5267](https://arxiv.org/abs/1111.5267). <https://link.aps.org/doi/10.1103/PhysRevLett.108.166606> (2012).
92. Tikhonenko, F. V., Kozikov, A. A., Savchenko, A. K. & Gorbachev, R. V. Transition between electron localization and antilocalization in graphene. *Physical Review Letters* **103**, 226801. ISSN: 0031-9007. arXiv: [0903.4489](https://arxiv.org/abs/0903.4489). <https://link.aps.org/doi/10.1103/PhysRevLett.103.226801> (2009).
93. Cummings, A. W., Garcia, J. H., Fabian, J. & Roche, S. Giant spin lifetime anisotropy in graphene induced by proximity effects. *Physical Review Letters* **119**, 206601. ISSN: 0031-9007. arXiv: [1705.10972](https://arxiv.org/abs/1705.10972). <https://link.aps.org/doi/10.1103/PhysRevLett.119.206601> (2017).
94. Gmitra, M. & Fabian, J. Graphene on transition-metal dichalcogenides: A platform for proximity spin-orbit physics and optospintronics. *Physical Review B* **92**, 155403. ISSN: 2469-9969. arXiv: [1506.08954](https://arxiv.org/abs/1506.08954). <https://link.aps.org/doi/10.1103/PhysRevB.92.155403> (2015).
95. Gmitra, M., Kochan, D., Högl, P. & Fabian, J. Trivial and inverted Dirac bands and the emergence of quantum spin Hall states in graphene on transition-metal dichalcogenides. *Physical Review B* **93**, 155104. ISSN: 2469-9969. arXiv: [1510.00166](https://arxiv.org/abs/1510.00166). <https://link.aps.org/doi/10.1103/PhysRevB.93.155104> (2016).
96. Goodwin, Z. A. H., Corsetti, F., Mostofi, A. A. & Lischner, J. Twist-angle sensitivity of electron correlations in moiré graphene bilayers. *Physical Review B* **100**, 121106. ISSN: 2469-9969. <https://link.aps.org/doi/10.1103/PhysRevB.100.121106> (2019).
97. Bi, Z., Yuan, N. F. Q. & Fu, L. Designing flat bands by strain. *Physical Review B* **100**, 035448. ISSN: 2469-9969. <https://link.aps.org/doi/10.1103/PhysRevB.100.035448> (2019).

98. Guinea, F. & Walet, N. R. Electrostatic effects, band distortions, and superconductivity in twisted graphene bilayers. *Proceedings of the National Academy of Sciences* **115**, 13174–13179. ISSN: 0027-8424. arXiv: [1806.05990](https://arxiv.org/abs/1806.05990). <https://pnas.org/doi/full/10.1073/pnas.1810947115> (2018).
99. You, Y.-Z. & Vishwanath, A. Superconductivity from valley fluctuations and approximate SO(4) symmetry in a weak coupling theory of twisted bilayer graphene. *npj Quantum Materials* **4**, 16. ISSN: 2397-4648. arXiv: [1805.06867](https://arxiv.org/abs/1805.06867). <http://www.nature.com/articles/s41535-019-0153-4> (2019).
100. Kozii, V., Isobe, H., Venderbos, J. W. F. & Fu, L. Nematic superconductivity stabilized by density wave fluctuations: Possible application to twisted bilayer graphene. *Physical Review B* **99**, 144507. ISSN: 2469-9969. arXiv: [1810.04159](https://arxiv.org/abs/1810.04159). <https://link.aps.org/doi/10.1103/PhysRevB.99.144507> (2019).
101. Gu, X. *et al.* Antiferromagnetism and chiral d-wave superconductivity from an effective t-J-D model for twisted bilayer graphene. *Physical Review B* **101**, 180506. ISSN: 2469-9969. arXiv: [1902.00029](https://arxiv.org/abs/1902.00029). <https://link.aps.org/doi/10.1103/PhysRevB.101.180506> (2020).
102. Xie, M. & MacDonald, A. H. Weak-field Hall resistivity and spin-valley flavor symmetry breaking in magic-angle twisted bilayer graphene. *Physical Review Letters* **127**, 196401. ISSN: 0031-9007. arXiv: [2010.07928](https://arxiv.org/abs/2010.07928). <https://link.aps.org/doi/10.1103/PhysRevLett.127.196401> (2021).
103. Qin, W. & MacDonald, A. H. In-plane critical magnetic fields in magic-angle twisted trilayer graphene. *Physical Review Letters* **127**, 097001. ISSN: 0031-9007. arXiv: [2104.14026](https://arxiv.org/abs/2104.14026). <https://link.aps.org/doi/10.1103/PhysRevLett.127.097001> (2021).
104. Cherng, R. W., Refael, G. & Demler, E. Superfluidity and magnetism in multicomponent ultracold fermions. *Physical Review Letters* **99**, 130406. ISSN: 0031-9007. <https://link.aps.org/doi/10.1103/PhysRevLett.99.130406> (2007).
105. González, J. & Stauber, T. Kohn-Luttinger superconductivity in twisted bilayer graphene. *Physical Review Letters* **122**, 026801. ISSN: 0031-9007. arXiv: [1807.01275](https://arxiv.org/abs/1807.01275). <https://link.aps.org/doi/10.1103/PhysRevLett.122.026801> (2019).
106. Zhang, Y. *et al.* Spin-orbit enhanced superconductivity in Bernal bilayer graphene. arXiv: [2205.05087](https://arxiv.org/abs/2205.05087). <http://arxiv.org/abs/2205.05087> (2022).
107. Li, Y. & Koshino, M. Twist-angle dependence of the proximity spin-orbit coupling in graphene on transition-metal dichalcogenides. *Physical Review*

- B* **99**, 075438. ISSN: 2469-9969. arXiv: [1901.06769](https://arxiv.org/abs/1901.06769). <https://link.aps.org/doi/10.1103/PhysRevB.99.075438> (2019).
108. Saito, Y. *et al.* Isospin Pomeranchuk effect in twisted bilayer graphene. *Nature* **592**, 220–224. ISSN: 0028-0836. arXiv: [arXiv: 2008.10830](https://arxiv.org/abs/2008.10830). <https://www.nature.com/articles/s41586-021-03409-2> (2021).
109. Rozen, A. *et al.* Entropic evidence for a Pomeranchuk effect in magic-angle graphene. *Nature* **592**, 214–219. ISSN: 0028-0836. arXiv: [2009.01836](https://arxiv.org/abs/2009.01836). <http://www.nature.com/articles/s41586-021-03319-3> (2021).
110. Song, Z.-D. & Bernevig, B. A. MATBG as topological heavy fermion: I. Exact mapping and correlated insulators. arXiv: [2111.05865](https://arxiv.org/abs/2111.05865). <http://arxiv.org/abs/2111.05865> (2021).
111. Lonzarich, G., Pines, D. & Yang, Y.-f. Toward a new microscopic framework for Kondo lattice materials. *Reports on Progress in Physics* **80**, 024501. ISSN: 0034-4885. <https://iopscience.iop.org/article/10.1088/1361-6633/80/2/024501> (2017).
112. Continentino, M. A. & Ferreira, A. S. Pomeranchuk effect in unstable materials based on YbInCu₄. *Physical Review B* **69**, 233104. ISSN: 2469-9969. <https://link.aps.org/doi/10.1103/PhysRevB.69.233104> (2004).
113. Sarma, S. D. & Wu, F. Strange metallicity of moiré twisted bilayer graphene. arXiv: [2201.10270](https://arxiv.org/abs/2201.10270). <http://arxiv.org/abs/2201.10270> (2022).
114. Jaoui, A. *et al.* Quantum critical behaviour in magic-angle twisted bilayer graphene. *Nature Physics*. ISSN: 1745-2473. arXiv: [2108.07753](https://arxiv.org/abs/2108.07753). <https://www.nature.com/articles/s41567-022-01556-5> (2022).
115. Goodwin, Z. A. H., Vitale, V., Liang, X., Mostofi, A. A. & Lischner, J. Hartree theory calculations of quasiparticle properties in twisted bilayer graphene. *Electronic Structure* **2**, 034001. ISSN: 2516-1075. arXiv: [2004.14784](https://arxiv.org/abs/2004.14784). <https://iopscience.iop.org/article/10.1088/2516-1075/ab9f94> (2020).
116. Zhu, J., Su, J.-J. & MacDonald, A. H. Voltage-controlled magnetic reversal in orbital Chern insulators. *Physical Review Letters* **125**, 227702. ISSN: 0031-9007. arXiv: [2001.05084](https://arxiv.org/abs/2001.05084). <https://link.aps.org/doi/10.1103/PhysRevLett.125.227702> (2020).
117. Lian, B. *et al.* Twisted bilayer graphene. IV. Exact insulator ground states and phase diagram. *Physical Review B* **103**, 205414. ISSN: 2469-9969. <https://link.aps.org/doi/10.1103/PhysRevB.103.205414> (2021).
118. Lin, J.-X. *et al.* Spin-orbit–driven ferromagnetism at half moiré filling in magic-angle twisted bilayer graphene. *Science* **375**, 437–441. ISSN: 0036-8075. arXiv: [2102.06566](https://arxiv.org/abs/2102.06566). <https://www.science.org/doi/10.1126/science.abh2889> (2022).

119. Polshyn, H. *et al.* Topological charge density waves at half-integer filling of a moiré superlattice. *Nature Physics* **18**, 42–47. ISSN: 1745-2473. arXiv: [2104.01178](https://arxiv.org/abs/2104.01178). <https://www.nature.com/articles/s41567-021-01418-6> (2022).
120. Yu, J. *et al.* Correlated Hofstadter spectrum and flavor phase diagram in magic angle graphene. arXiv: [2108.00009](https://arxiv.org/abs/2108.00009). <http://arxiv.org/abs/2108.00009> (2021).
121. Nuckolls, K. P. *et al.* Strongly correlated Chern insulators in magic-angle twisted bilayer graphene. *Nature* **588**, 610–615. ISSN: 0028-0836. arXiv: [2007.03810](https://arxiv.org/abs/2007.03810). <https://www.nature.com/articles/s41586-020-3028-8> (2020).
122. Po, H. C., Zou, L., Senthil, T. & Vishwanath, A. Faithful tight-binding models and fragile topology of magic-angle bilayer graphene. *Physical Review B* **99**, 195455. ISSN: 2469-9969. arXiv: [1808.02482](https://arxiv.org/abs/1808.02482). <https://link.aps.org/doi/10.1103/PhysRevB.99.195455> (2019).
123. Cea, T. & Guinea, F. Band structure and insulating states driven by Coulomb interaction in twisted bilayer graphene. *Physical Review B* **102**, 2–7. ISSN: 2469-9969. arXiv: [2004.01577](https://arxiv.org/abs/2004.01577). <https://link.aps.org/doi/10.1103/PhysRevB.102.045107> (2020).
124. Kwan, Y. H. *et al.* Kekulé spiral order at all nonzero integer fillings in twisted bilayer graphene. *Physical Review X* **11**, 041063. ISSN: 2160-3308. arXiv: [2105.05857](https://arxiv.org/abs/2105.05857). <https://link.aps.org/doi/10.1103/PhysRevX.11.041063> (2021).
125. Shavit, G., Berg, E., Stern, A. & Oreg, Y. Theory of correlated insulators and superconductivity in twisted bilayer graphene. *Physical Review Letters* **127**, 247703. ISSN: 1079-7114. arXiv: [2107.08486](https://arxiv.org/abs/2107.08486). <https://link.aps.org/doi/10.1103/PhysRevLett.127.247703> (2021).
126. Tseng, C.-C. *et al.* Anomalous Hall effect at half filling in twisted bilayer graphene, 1–13. arXiv: [2202.01734](https://arxiv.org/abs/2202.01734). <http://arxiv.org/abs/2202.01734> (2022).
127. Park, J. M., Cao, Y., Watanabe, K., Taniguchi, T. & Jarillo-Herrero, P. Tunable strongly coupled superconductivity in magic-angle twisted trilayer graphene. *Nature* **590**, 249–255. ISSN: 0028-0836. <https://www.nature.com/articles/s41586-021-03192-0> (2021).
128. Hao, Z. *et al.* Electric field-tunable superconductivity in alternating-twist magic-angle trilayer graphene. *Science* **371**, 1133–1138. ISSN: 0036-8075. arXiv: [2012.02773](https://arxiv.org/abs/2012.02773). <https://www.sciencemag.org/lookup/doi/10.1126/science.abg0399> (2021).

129. Cao, Y., Park, J. M., Watanabe, K., Taniguchi, T. & Jarillo-Herrero, P. Pauli-limit violation and re-entrant superconductivity in moiré graphene. *Nature* **595**, 526–531. ISSN: 0028-0836. <http://www.nature.com/articles/s41586-021-03685-y> (2021).
130. Khalaf, E., Kruchkov, A. J., Tarnopolsky, G. & Vishwanath, A. Magic angle hierarchy in twisted graphene multilayers. *Physical Review B* **100**, 085109. ISSN: 2469-9969. arXiv: [1901.10485](https://arxiv.org/abs/1901.10485). <https://link.aps.org/doi/10.1103/PhysRevB.100.085109> (2019).
131. Carr, S. *et al.* Ultraheavy and ultrarelativistic dirac quasiparticles in sandwiched graphenes. *Nano Letters* **20**, 3030–3038. ISSN: 1530-6984. <https://pubs.acs.org/doi/10.1021/acs.nanolett.9b04979> (2020).
132. Kim, H. *et al.* Spectroscopic signatures of strong correlations and unconventional superconductivity in twisted trilayer graphene. arXiv: [2109.12127](https://arxiv.org/abs/2109.12127). <http://arxiv.org/abs/2109.12127> (2021).
133. Zhu, Z., Carr, S., Massatt, D., Luskin, M. & Kaxiras, E. Twisted trilayer graphene: A precisely tunable platform for correlated electrons. *Physical Review Letters* **125**, 116404. ISSN: 0031-9007. arXiv: [2006.00399](https://arxiv.org/abs/2006.00399). <https://link.aps.org/doi/10.1103/PhysRevLett.125.116404> (2020).
134. Tritsarlis, G. A. *et al.* Electronic structure calculations of twisted multi-layer graphene superlattices. *2D Materials* **7**. ISSN: 20531583. arXiv: [2001.11633](https://arxiv.org/abs/2001.11633). <https://iopscience.iop.org/article/10.1088/2053-1583/ab8f62> (2020).
135. Mora, C., Regnault, N. & Bernevig, B. A. Flatbands and perfect metal in trilayer moiré graphene. *Physical Review Letters* **123**, 026402. ISSN: 0031-9007. arXiv: [1901.05469](https://arxiv.org/abs/1901.05469). <https://link.aps.org/doi/10.1103/PhysRevLett.123.026402> (2019).
136. Xie, B., Peng, R., Zhang, S. & Liu, J. Alternating twisted multilayer graphene: Generic partition rules, double flat bands, and orbital magnetoelectric effect. *npj Computational Materials* **8**, 110. ISSN: 2057-3960. arXiv: [2111.06292v1](https://arxiv.org/abs/2111.06292v1). <https://www.nature.com/articles/s41524-022-00789-5> (2022).
137. Christos, M., Sachdev, S. & Scheurer, M. S. Correlated insulators, semimetals, and superconductivity in twisted trilayer graphene. *Physical Review X* **12**, 21018. ISSN: 2160-3308. arXiv: [2106.02063](https://arxiv.org/abs/2106.02063). <https://link.aps.org/doi/10.1103/PhysRevX.12.021018> (2021).
138. Xie, F., Regnault, N., Călugăru, D., Bernevig, B. A. & Lian, B. Twisted symmetric trilayer graphene. II. Projected Hartree-Fock study. *Physical Review B* **104**, 115167. ISSN: 2469-9969. <https://link.aps.org/doi/10.1103/PhysRevB.104.115167> (2021).

139. Bultinck, N. *et al.* Ground state and hidden symmetry of magic-angle graphene at even integer filling. *Physical Review X* **10**, 31034. ISSN: 2160-3308. arXiv: [1911.02045](https://doi.org/10.1103/PhysRevX.10.031034). <https://doi.org/10.1103/PhysRevX.10.031034> (2020).
140. Oh, M. *et al.* Evidence for unconventional superconductivity in twisted bilayer graphene. *Nature* **600**, 240–245. ISSN: 0028-0836. arXiv: [2109.13944](https://www.nature.com/articles/s41586-021-04121-x). <https://www.nature.com/articles/s41586-021-04121-x> (2021).
141. Kopnin, N. B., Heikkilä, T. T. & Volovik, G. E. High-temperature surface superconductivity in topological flat-band systems. *Physical Review B* **83**, 1–4. ISSN: 2469-9969. arXiv: [1103.2033](https://link.aps.org/doi/10.1103/PhysRevB.83.220503). <https://link.aps.org/doi/10.1103/PhysRevB.83.220503> (2011).
142. Potasz, P., Xie, M. & MacDonald, A. H. Exact diagonalization for magic-angle twisted bilayer graphene. *Physical Review Letters* **127**, 147203. ISSN: 10797114. arXiv: [2102.02256](https://link.aps.org/doi/10.1103/PhysRevLett.127.147203). <https://link.aps.org/doi/10.1103/PhysRevLett.127.147203> (2021).
143. Xie, F. *et al.* Twisted bilayer graphene. VI. An exact diagonalization study at nonzero integer filling. *Physical Review B* **103**, 1–41. ISSN: 2469-9969. <https://link.aps.org/doi/10.1103/PhysRevB.103.205416> (2021).
144. Ledwith, P. J. *et al.* TB or not TB? Contrasting properties of twisted bilayer graphene and the alternating twist n -layer structures ($n = 3, 4, 5, \dots$). arXiv: [2111.11060](http://arxiv.org/abs/2111.11060). <http://arxiv.org/abs/2111.11060> (2021).
145. Suhl, H., Matthias, B. T. & Walker, L. R. Bardeen-Cooper-Schrieffer theory of superconductivity in the case of overlapping bands. *Physical Review Letters* **3**, 552–554. ISSN: 0031-9007. <https://link.aps.org/doi/10.1103/PhysRevLett.3.552> (1959).
146. Dolgov, O. V., Mazin, I. I., Parker, D. & Golubov, A. A. Interband superconductivity: Contrasts between Bardeen-Cooper-Schrieffer and Eliashberg theories. *Physical Review B* **79**, 060502. ISSN: 2469-9969. <https://link.aps.org/doi/10.1103/PhysRevB.79.060502> (2009).
147. Hirschfeld, P. J., Korshunov, M. M. & Mazin, I. I. Gap symmetry and structure of Fe-based superconductors. *Reports on Progress in Physics* **74**, 124508. ISSN: 0034-4885. arXiv: [1106.3712](https://iopscience.iop.org/article/10.1088/0034-4885/74/12/124508). <https://iopscience.iop.org/article/10.1088/0034-4885/74/12/124508> (2011).
148. Chen, X., Maiti, S., Linscheid, A. & Hirschfeld, P. J. Electron pairing in the presence of incipient bands in iron-based superconductors. *Physical Review B* **92**, 224514. ISSN: 2469-9969. arXiv: [1508.04782](https://link.aps.org/doi/10.1103/PhysRevB.92.224514). <https://link.aps.org/doi/10.1103/PhysRevB.92.224514> (2015).

149. Rademaker, L., Abanin, D. A. & Mellado, P. Charge smoothening and band flattening due to Hartree corrections in twisted bilayer graphene. *Physical Review B* **100**, 205114. ISSN: 2469-9969. arXiv: [1907.00940](https://arxiv.org/abs/1907.00940). <https://link.aps.org/doi/10.1103/PhysRevB.100.205114> (2019).
150. Calderón, M. J. & Bascones, E. Interactions in the 8-orbital model for twisted bilayer graphene. *Physical Review B* **102**, 155149. ISSN: 2469-9969. arXiv: [2007.16051](https://arxiv.org/abs/2007.16051). <https://link.aps.org/doi/10.1103/PhysRevB.102.155149> (2020).
151. Zhou, H., Xie, T., Taniguchi, T., Watanabe, K. & Young, A. F. Superconductivity in rhombohedral trilayer graphene. *Nature* **598**, 434–438. ISSN: 0028-0836. arXiv: [2106.07640](https://arxiv.org/abs/2106.07640). <https://www.nature.com/articles/s41586-021-03926-0> (2021).
152. Zhou, H. *et al.* Isospin magnetism and spin-polarized superconductivity in Bernal bilayer graphene. *Science* **375**, 774–778. ISSN: 0036-8075. arXiv: [2110.11317](https://arxiv.org/abs/2110.11317). <https://www.science.org/doi/10.1126/science.abm8386> (2022).
153. Fu, L. & Kane, C. L. Superconducting proximity effect and Majorana fermions at the surface of a topological insulator. *Physical Review Letters* **100**, 096407. ISSN: 0031-9007. arXiv: [0707.1692](https://arxiv.org/abs/0707.1692). <https://link.aps.org/doi/10.1103/PhysRevLett.100.096407> (2008).
154. Akhmerov, A. R., Nilsson, J. & Beenakker, C. W. J. Electrically detected interferometry of Majorana fermions in a topological insulator. *Physical Review Letters* **102**, 216404. ISSN: 0031-9007. arXiv: [0903.2196](https://arxiv.org/abs/0903.2196). <https://link.aps.org/doi/10.1103/PhysRevLett.102.216404> (2009).
155. Oreg, Y., Refael, G. & von Oppen, F. Helical liquids and Majorana bound states in quantum wires. *Physical Review Letters* **105**, 177002. ISSN: 0031-9007. arXiv: [1003.1145](https://arxiv.org/abs/1003.1145). <https://link.aps.org/doi/10.1103/PhysRevLett.105.177002> (2010).
156. Alicea, J. New directions in the pursuit of Majorana fermions in solid state systems. *Reports on Progress in Physics* **75**, 076501. ISSN: 0034-4885. arXiv: [1202.1293](https://arxiv.org/abs/1202.1293). <https://iopscience.iop.org/article/10.1088/0034-4885/75/7/076501> (2012).
157. Sanchez-Yamagishi, J. D. *et al.* Helical edge states and fractional quantum Hall effect in a graphene electron–hole bilayer. *Nature Nanotechnology* **12**, 118–122. ISSN: 1748-3387. arXiv: [1602.06815](https://arxiv.org/abs/1602.06815). <https://www.nature.com/articles/nnano.2016.214> (2017).
158. König, M. *et al.* Quantum spin Hall insulator state in HgTe quantum wells. *Science* **318**, 766–770. ISSN: 0036-8075. <http://www.sciencemag.org/cgi/doi/10.1126/science.1148047> (2007).

159. Du, L., Knez, I., Sullivan, G. & Du, R.-R. Robust helical edge transport in gated InAs/GaSb bilayers. *Physical Review Letters* **114**, 096802. ISSN: 0031-9007. <https://link.aps.org/doi/10.1103/PhysRevLett.114.096802> (2015).
160. Qu, F. *et al.* Electric and magnetic tuning between the trivial and topological phases in InAs/GaSb double quantum wells. *Physical Review Letters* **115**, 036803. ISSN: 0031-9007. arXiv: [1502.05714](https://arxiv.org/abs/1502.05714). <https://link.aps.org/doi/10.1103/PhysRevLett.115.036803> (2015).
161. Irie, H. *et al.* Impact of epitaxial strain on the topological-nontopological phase diagram and semimetallic behavior of InAs/GaSb composite quantum wells. *Physical Review B* **101**, 075433. ISSN: 2469-9969. <https://link.aps.org/doi/10.1103/PhysRevB.101.075433> (2020).
162. Lee, S.-P., Michaeli, K., Alicea, J. & Yacoby, A. Revealing topological superconductivity in extended quantum spin Hall Josephson junctions. *Physical Review Letters* **113**, 197001. ISSN: 0031-9007. arXiv: [1403.2747](https://arxiv.org/abs/1403.2747). <https://link.aps.org/doi/10.1103/PhysRevLett.113.197001> (2014).
163. Pientka, F. *et al.* Topological superconductivity in a planar Josephson junction. *Physical Review X* **7**, 021032. ISSN: 2160-3308. arXiv: [1609.09482](https://arxiv.org/abs/1609.09482). <http://link.aps.org/doi/10.1103/PhysRevX.7.021032> (2017).
164. Mi, S., Pikulin, D. I., Wimmer, M. & Beenakker, C. W. J. Proposal for the detection and braiding of Majorana fermions in a quantum spin Hall insulator. *Physical Review B* **87**, 241405. ISSN: 2469-9969. arXiv: [1304.1685](https://arxiv.org/abs/1304.1685). <https://link.aps.org/doi/10.1103/PhysRevB.87.241405> (2013).
165. Hegde, S. S. *et al.* A topological Josephson junction platform for creating, manipulating, and braiding Majorana bound states. *Annals of Physics* **423**, 168326. ISSN: 1096035X. arXiv: [1907.02935](https://arxiv.org/abs/1907.02935). <https://doi.org/10.1016/j.aop.2020.168326> (2020).
166. Wu, S. *et al.* Observation of the quantum spin Hall effect up to 100 Kelvin in a monolayer crystal. *Science* **359**, 76–79. ISSN: 0036-8075. arXiv: [1711.03584](https://arxiv.org/abs/1711.03584). <https://www.science.org/doi/10.1126/science.aan6003> (2018).
167. Fei, Z. *et al.* Edge conduction in monolayer WTe₂. *Nature Physics* **13**, 677–682. ISSN: 1745-2473. arXiv: [1610.07924](https://arxiv.org/abs/1610.07924). <http://www.nature.com/articles/nphys4091> (2017).
168. Knez, I., Du, R.-R. & Sullivan, G. Evidence for helical edge modes in inverted InAs/GaSb quantum wells. *Physical Review Letters* **107**, 136603. ISSN: 0031-9007. arXiv: [1105.0137](https://arxiv.org/abs/1105.0137). <https://link.aps.org/doi/10.1103/PhysRevLett.107.136603> (2011).

169. Du, L. *et al.* Tuning edge states in strained-layer InAs/GaInSb quantum spin Hall insulators. *Physical Review Letters* **119**, 056803. ISSN: 0031-9007. arXiv: [1608.06588](https://arxiv.org/abs/1608.06588). <http://link.aps.org/doi/10.1103/PhysRevLett.119.056803> (2017).
170. Suzuki, K., Harada, Y., Onomitsu, K. & Muraki, K. Edge channel transport in the InAs/GaSb topological insulating phase. *Physical Review B* **87**, 235311. ISSN: 2469-9969. arXiv: [1306.4234](https://arxiv.org/abs/1306.4234). <https://link.aps.org/doi/10.1103/PhysRevB.87.235311> (2013).
171. Mueller, S. *et al.* Edge transport in InAs and InAs/GaSb quantum wells. *Physical Review B* **96**, 075406. ISSN: 2469-9969. arXiv: [1706.00320](https://arxiv.org/abs/1706.00320). <http://link.aps.org/doi/10.1103/PhysRevB.96.075406> (2017).
172. Irie, H. *et al.* Energy gap tuning and gate-controlled topological phase transition in InAs/In_xGa_{1-x}Sb composite quantum wells. *Physical Review Materials* **4**, 104201. ISSN: 2475-9953. arXiv: [2008.00664](https://arxiv.org/abs/2008.00664). <https://link.aps.org/doi/10.1103/PhysRevMaterials.4.104201> (2020).
173. Roth, A. *et al.* Nonlocal transport in the quantum spin Hall state. *Science* **325**, 294–297. ISSN: 0036-8075. <https://www.science.org/doi/10.1126/science.1174736> (2009).
174. Brüne, C. *et al.* Spin polarization of the quantum spin Hall edge states. *Nature Physics* **8**, 485–490. ISSN: 1745-2473. <http://dx.doi.org/10.1038/nphys2322><http://www.nature.com/doi/10.1038/nphys2322><http://www.nature.com/articles/nphys2322> (2012).
175. Nowack, K. C. *et al.* Imaging currents in HgTe quantum wells in the quantum spin Hall regime. *Nature Materials* **12**, 787–791. ISSN: 14764660. <https://www.nature.com/articles/nmat3682> (2013).
176. Shi, Y. *et al.* Imaging quantum spin Hall edges in monolayer WTe₂. *Science Advances* **5**, 1–7. ISSN: 2375-2548. arXiv: [1807.09342](https://arxiv.org/abs/1807.09342). <https://www.science.org/doi/10.1126/sciadv.aat8799> (2019).
177. König, M. *et al.* Spatially resolved study of backscattering in the quantum spin Hall state. *Physical Review X* **3**, 021003. ISSN: 2160-3308. arXiv: [1211.3917](https://arxiv.org/abs/1211.3917). <https://link.aps.org/doi/10.1103/PhysRevX.3.021003> (2013).
178. Väyrynen, J. I., Goldstein, M., Gefen, Y. & Glazman, L. I. Resistance of helical edges formed in a semiconductor heterostructure. *Physical Review B* **90**, 1–37. ISSN: 2469-9969. arXiv: [1406.6052](https://arxiv.org/abs/1406.6052) (2014).
179. Schmidt, T. L., Rachel, S., von Oppen, F. & Glazman, L. I. Inelastic electron backscattering in a generic helical edge channel. *Physical Review Letters* **108**, 156402. ISSN: 0031-9007. arXiv: [1201.0278](https://arxiv.org/abs/1201.0278). <https://link.aps.org/doi/10.1103/PhysRevLett.108.156402> (2012).

180. Hu, L.-H., Xu, D.-H., Zhang, F.-C. & Zhou, Y. Effect of in-plane magnetic field and applied strain in quantum spin Hall systems: Application to InAs/GaSb quantum wells. *Physical Review B* **94**, 085306. ISSN: 2469-9969. <https://link.aps.org/doi/10.1103/PhysRevB.94.085306> (2016).
181. Hu, L. H., Chen, C. C., Liu, C. X., Zhang, F. C. & Zhou, Y. Topological charge-density and spin-density waves in InAs/GaSb quantum wells under an in-plane magnetic field. *Physical Review B* **96**, 2–7. ISSN: 2469-9969. <https://link.aps.org/doi/10.1103/PhysRevB.96.075130> (2017).
182. Du, L. *et al.* Evidence for a topological excitonic insulator in InAs/GaSb bilayers. *Nature Communications* **8**, 1–8. ISSN: 20411723. <https://www.nature.com/articles/s41467-017-01988-1> (2017).
183. Pikulin, D. I. & Hyart, T. Interplay of exciton condensation and the quantum spin Hall effect in InAs/GaSb bilayers. *Physical Review Letters* **112**, 176403. ISSN: 0031-9007. arXiv: [1311.1111](https://arxiv.org/abs/1311.1111). <https://link.aps.org/doi/10.1103/PhysRevLett.112.176403> (2014).
184. Skolasinski, R., Pikulin, D. I., Alicea, J. & Wimmer, M. Robust helical edge transport in quantum spin Hall quantum wells. *Physical Review B* **98**, 201404. ISSN: 2469-9969. arXiv: [1709.04830](https://arxiv.org/abs/1709.04830). <https://link.aps.org/doi/10.1103/PhysRevB.98.201404> (2018).
185. Nguyen, B.-M. *Suppressing Trivial Edge Conductance in Antimonide-Based Quantum Spin Hall Materials* Presentation at the APS March Meeting. 2021.
186. Nguyen, B.-M., Yi, W., Noah, R., Thorp, J. & Sokolich, M. High mobility back-gated InAs/GaSb double quantum well grown on GaSb substrate. *Applied Physics Letters* **106**, 032107. ISSN: 0003-6951. <http://aip.scitation.org/doi/10.1063/1.4906589> (2015).
187. Liu, C., Hughes, T. L., Qi, X. L., Wang, K. & Zhang, S. C. Quantum spin Hall effect in inverted type-II semiconductors. *Physical Review Letters* **100**, 1–4. ISSN: 00319007. <https://link.aps.org/doi/10.1103/PhysRevLett.100.236601> (2008).
188. Karalic, M. *Electronic Transport in Hybridized Electron-Hole Bilayers* PhD thesis (ETH Zurich, 2019).
189. Knez, I., Du, R. R. & Sullivan, G. Finite conductivity in mesoscopic Hall bars of inverted InAs/GaSb quantum wells. *Physical Review B* **81**, 201301. ISSN: 2469-9969. <https://link.aps.org/doi/10.1103/PhysRevB.81.201301> (2010).
190. Suzuki, K., Harada, Y., Onomitsu, K. & Muraki, K. Gate-controlled semimetal-topological insulator transition in an InAs/GaSb heterostructure. *Physical Review B* **91**, 245309. ISSN: 2469-9969. <https://link.aps.org/doi/10.1103/PhysRevB.91.245309> (2015).

191. Nichele, F. *et al.* Giant spin-orbit splitting in inverted InAs/GaSb double quantum wells. *Physical Review Letters* **118**, 016801. ISSN: 0031-9007. arXiv: [1605.01241](https://link.aps.org/doi/10.1103/PhysRevLett.118.016801). <https://link.aps.org/doi/10.1103/PhysRevLett.118.016801> (2017).
192. Nichele, F. *et al.* Edge transport in the trivial phase of InAs/GaSb. *New Journal of Physics* **18**, 083005. ISSN: 1367-2630. <https://iopscience.iop.org/article/10.1088/1367-2630/18/8/083005> (2016).
193. Nguyen, B.-M. *et al.* Decoupling edge versus bulk conductance in the trivial regime of an InAs/GaSb double quantum well using Corbino ring geometry. *Physical Review Letters* **117**, 077701. ISSN: 0031-9007. <https://link.aps.org/doi/10.1103/PhysRevLett.117.077701> (2016).
194. Akiho, T. *et al.* Engineering quantum spin Hall insulators by strained-layer heterostructures. *Applied Physics Letters* **109**, 192105. ISSN: 0003-6951. <http://aip.scitation.org/doi/10.1063/1.4967471> (2016).
195. Beukman, A. J. A. *et al.* Spin-orbit interaction in a dual gated InAs/GaSb quantum well. *Physical Review B* **96**, 241401. ISSN: 2469-9969. <https://link.aps.org/doi/10.1103/PhysRevB.96.241401> (2017).
196. Charpentier, C. *et al.* Suppression of bulk conductivity in InAs/GaSb broken gap composite quantum wells. *Applied Physics Letters* **103**, 112102. ISSN: 0003-6951. <http://aip.scitation.org/doi/10.1063/1.4821037> (2013).
197. Nichele, F. *et al.* Insulating state and giant nonlocal response in an InAs/GaSb quantum well in the quantum Hall regime. *Physical Review Letters* **112**, 036802. ISSN: 0031-9007. <https://link.aps.org/doi/10.1103/PhysRevLett.112.036802> (2014).
198. Lawaetz, P. Valence-band parameters in cubic semiconductors. *Physical Review B* **4**, 3460–3467. ISSN: 0556-2805. <https://link.aps.org/doi/10.1103/PhysRevB.4.3460> (1971).
199. Halvorsen, E. & Galperin, Y. Optical transitions in broken gap heterostructures. *Physical Review B* **61**, 16743–16749. ISSN: 01631829. arXiv: [cond-mat/0003231](https://arxiv.org/abs/cond-mat/0003231) [cond-mat]. <https://link.aps.org/doi/10.1103/PhysRevB.61.16743> (2000).
200. Vurgaftman, I., Meyer, J. R. & Ram-Mohan, L. R. Band parameters for III–V compound semiconductors and their alloys. *Journal of Applied Physics* **89**, 5815–5875. ISSN: 0021-8979. <http://aip.scitation.org/doi/10.1063/1.1368156> (2001).
201. Skolasinski, R., Nijholt, B. & Weston, J. *Semicon: Python package for numerical calculation of semiconductors' band structures* <https://gitlab.kwant-project.org/semicon/semicon> (Nov. 15, 2021).
202. Pikus, G. E. & Bir, G. L. *Soviet Physics, Solid State* **1**, 1502 (1959).

203. Bir, G. L. & Pikus, G. E. *Symmetry and strain-induced effects in semiconductors* ISBN: 0470073217 (Wiley, New York, 1974).
204. Hinckley, J. M. & Singh, J. Influence of substrate composition and crystallographic orientation on the band structure of pseudomorphic Si-Ge alloy films. *Physical Review B* **42**, 3546–3566. ISSN: 01631829. <https://link.aps.org/doi/10.1103/PhysRevB.42.3546> (1990).
205. Fischer, A., Klebl, L., Honerkamp, C. & Kennes, D. M. Spin-fluctuation-induced pairing in twisted bilayer graphene. *Physical Review B* **103**, L041103. ISSN: 2469-9950. arXiv: [2008.12532](https://arxiv.org/abs/2008.12532). <https://link.aps.org/doi/10.1103/PhysRevB.103.L041103> (2021).
206. Huang, C., Wei, N., Qin, W. & MacDonald, A. Pseudospin paramagnons and the superconducting dome in magic angle twisted bilayer graphene. **78712**. arXiv: [2110.13351](https://arxiv.org/abs/2110.13351). <http://arxiv.org/abs/2110.13351> (2021).
207. Cao, Y. *et al.* Nematicity and competing orders in superconducting magic-angle graphene. *Science* **372**, 264–271. ISSN: 0036-8075. arXiv: [2004.04148](https://arxiv.org/abs/2004.04148). <https://www.science.org/doi/10.1126/science.abc2836> (2021).
208. Hunt, B. M. *et al.* Direct measurement of discrete valley and orbital quantum numbers in bilayer graphene. *Nature Communications* **8**, 948. ISSN: 2041-1723. arXiv: [1607.06461](https://arxiv.org/abs/1607.06461). <http://www.nature.com/articles/s41467-017-00824-w> (2017).
209. Kwon, H. J., Sengupta, K. & Yakovenko, V. M. Fractional ac Josephson effect in p- and d-wave superconductors. *European Physical Journal B* **37**, 349–361. ISSN: 14346028. arXiv: [0210148](https://arxiv.org/abs/0210148). <https://link.springer.com/article/10.1140/epjb/e2004-00066-4> (2004).
210. Diez-Merida, J. *et al.* Magnetic Josephson junctions and superconducting diodes in magic angle twisted bilayer graphene. arXiv: [2110.01067](https://arxiv.org/abs/2110.01067). <http://arxiv.org/abs/2110.01067> (2021).
211. Lin, J.-X. *et al.* Zero-field superconducting diode effect in small-twist-angle trilayer graphene. arXiv: [2112.07841](https://arxiv.org/abs/2112.07841). <http://arxiv.org/abs/2112.07841> (2021).
212. Thomson, A., Sorensen, I. M., Nadj-Perge, S. & Alicea, J. Gate-defined wires in twisted bilayer graphene: From electrical detection of intervalley coherence to internally engineered Majorana modes. *Physical Review B* **105**, 1–7. ISSN: 24699969. arXiv: [2105.02891](https://arxiv.org/abs/2105.02891) (2022).
213. Kezilebieke, S. *et al.* Moiré-enabled topological superconductivity. *Nano Letters* **22**, 328–333. ISSN: 15306992. arXiv: [2011.09760](https://arxiv.org/abs/2011.09760) (2022).
214. Ren, H. *et al.* Topological superconductivity in a phase-controlled Josephson junction. *Nature* **569**, 93–98. ISSN: 0028-0836. arXiv: [1809.03076](https://arxiv.org/abs/1809.03076). <http://www.nature.com/articles/s41586-019-1148-9> (2019).

215. Fornieri, A. *et al.* Evidence of topological superconductivity in planar Josephson junctions. *Nature* **569**, 89–92. ISSN: 14764687. arXiv: [1809.03037](https://arxiv.org/abs/1809.03037). <https://www.nature.com/articles/s41586-019-1068-8> (2019).
216. Dartiailh, M. C. *et al.* Phase signature of topological transition in Josephson junctions. *Physical Review Letters* **126**, 036802. ISSN: 0031-9007. arXiv: [1906.01179](https://arxiv.org/abs/1906.01179). <https://link.aps.org/doi/10.1103/PhysRevLett.126.036802> (2021).
217. De Vries, F. K. *et al.* h/e superconducting quantum interference through trivial edge states in InAs. *Physical Review Letters* **120**, 047702. ISSN: 0031-9007. arXiv: [1709.03727](https://arxiv.org/abs/1709.03727). <https://link.aps.org/doi/10.1103/PhysRevLett.120.047702> (2018).
218. Dartiailh, M. C. *et al.* Missing Shapiro steps in topologically trivial Josephson junction on InAs quantum well. *Nature Communications* **12**. ISSN: 20411723. arXiv: [2005.00077](https://arxiv.org/abs/2005.00077). <https://www.nature.com/articles/s41467-020-20382-y> (2021).
219. Pribiag, V. S. *et al.* Edge-mode superconductivity in a two-dimensional topological insulator. *Nature Nanotechnology* **10**, 593–597. ISSN: 17483395. <https://www.nature.com/articles/nnano.2015.86> (2015).
220. Dynes, R. C. & Fulton, T. A. Supercurrent density distribution in Josephson junctions. *Physical Review B* **3**, 3015–3023. ISSN: 0556-2805. <https://link.aps.org/doi/10.1103/PhysRevB.3.3015> (1971).
221. Hart, S. *et al.* Induced superconductivity in the quantum spin Hall edge. *Nature Physics* **10**, 638–643. ISSN: 1745-2473. <http://www.nature.com/articles/nphys3036> (2014).
222. Bocquillon, E. *et al.* Gapless Andreev bound states in the quantum spin Hall insulator HgTe. *Nature Nanotechnology* **12**, 137–143. ISSN: 1748-3387. arXiv: [1601.08055](https://arxiv.org/abs/1601.08055). <http://www.nature.com/articles/nnano.2016.159> (2017).
223. Jiang, L. *et al.* Unconventional Josephson signatures of Majorana bound states. *Physical Review Letters* **107**, 1–5. ISSN: 00319007. arXiv: [1107.4102](https://arxiv.org/abs/1107.4102) (2011).
224. Mayer, W. *et al.* Gate controlled anomalous phase shift in Al/InAs Josephson junctions. *Nature Communications* **11**. ISSN: 20411723. arXiv: [1905.12670](https://arxiv.org/abs/1905.12670). <https://www.nature.com/articles/s41467-019-14094-1> (2020).
225. Beenakker, C. W., Pikulin, D. I., Hyart, T., Schomerus, H. & Dahlhaus, J. P. Fermion-parity anomaly of the critical supercurrent in the quantum spin-Hall effect. *Physical Review Letters* **110**, 1–5. ISSN: 00319007. <https://link.aps.org/doi/10.1103/PhysRevLett.110.017003> (2013).

Appendix A

CHAPTER 4 SUPPLEMENTARY DATA: HIERARCHY OF CORRELATIONS IN TWISTED BILAYER GRAPHENE-WSE₂ HETEROSTRUCTURES

The data for TBG devices is available in a public repository at <https://doi.org/10.22002/D1.20151>, and the code (including Binder support for the Jupyter notebooks) for replication of the results can be found at <https://doi.org/10.22002/D1.20169>.

Table A.1: Device Table. The superconducting transition temperatures (SC T_c), $\nu = 2$ correlated insulator (CI) gap, and $\nu = 1$ correlated state parameters measured for the devices used to plot the phase diagram in Fig. 4.2 sorted by twist angle.

Twist angle (± 0.02)	Device	Hole SC T_c (K)	Electron SC T_c (K)	$\nu=2$ CI (meV)	$\nu=1$ state
0.79	D6 (M20)	N/A	0.382	N/A	N/A
0.80	D7 (W5)	N/A	0.54	N/A	N/A
0.83	D6 (M20)	N/A	0.702	High-T peak	High-T peak
0.87	D6 (M20)	N/A	0.626	High-T peak	High-T peak
0.88	D3 (S3)	0.129	0.652	High-T peak	High-T peak
0.95	D9 (M30)	0.339	0.486	$\Delta=0.186$	High-T peak
0.97	D5 (M08)	0.742	0.089	$\Delta=0.68$	High-T peak
0.97	D1 (S13)	0.398	0.352	$\Delta=0.09$	High-T peak
0.99	D9 (M30)	0.429	N/A	$\Delta=0.11$	Low-T peak, switching
1.04	D1 (S13)	0.798	N/A	$\Delta=0.89$	Low-T peak, hysteresis
1.04	D8 (M12)	0.4	0.098	$\Delta=0.26$	Low-T peak
1.10	D1 (S13)	1.59	0.083	$\Delta=0.84$	FM to 7K
1.10	D4 (W3)	0.443	N/A	$\Delta=0.27$	Low-T peak
1.15	D2 (S12)	0.267	0.155	$\Delta \sim 0.17$ to SC	High-T peak
1.23	D2 (S12)	0.317	0.128	Disappearing	N/A

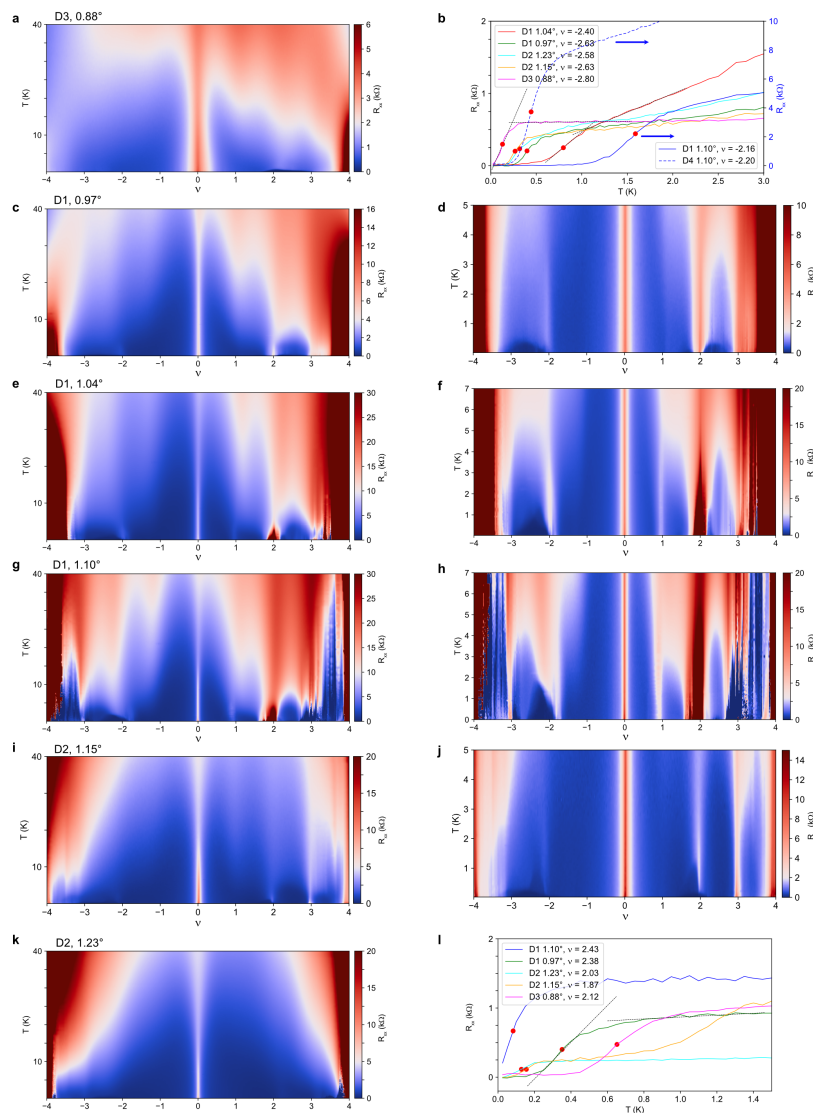


Figure A.1: Figures in the left column show the high-temperature (to 40 K) R_{xx} vs. the moiré filling factor for a number of devices across the angle range. The corresponding figures in the right column reduce the temperature range to emphasize the correlated insulators and superconductivity appearing at low temperature. (b) shows extracted T_c on the hole side for each of the angles represented here. The resistance was much larger for device D1 at 1.10°, as well as another device D4 at the same twist angle, so the y-axis for these curves is on the right of the plot. The extreme sensitivity of the correlations and superconductivity to the twist angle, cleanliness, homogeneity, and other factors occasionally results in different T_c values for devices of the same angle. (l), The electron-side superconductivity T_c values. T_c was derived from 50% R_n , where R_n is defined as the intersection of line fits to the highly sloped region and the normal region just above the transition (line fits shown for selected curves as dashed black lines). The same method was used to determine the error-bars at 10% and 90% R_n in Fig. 4.2.

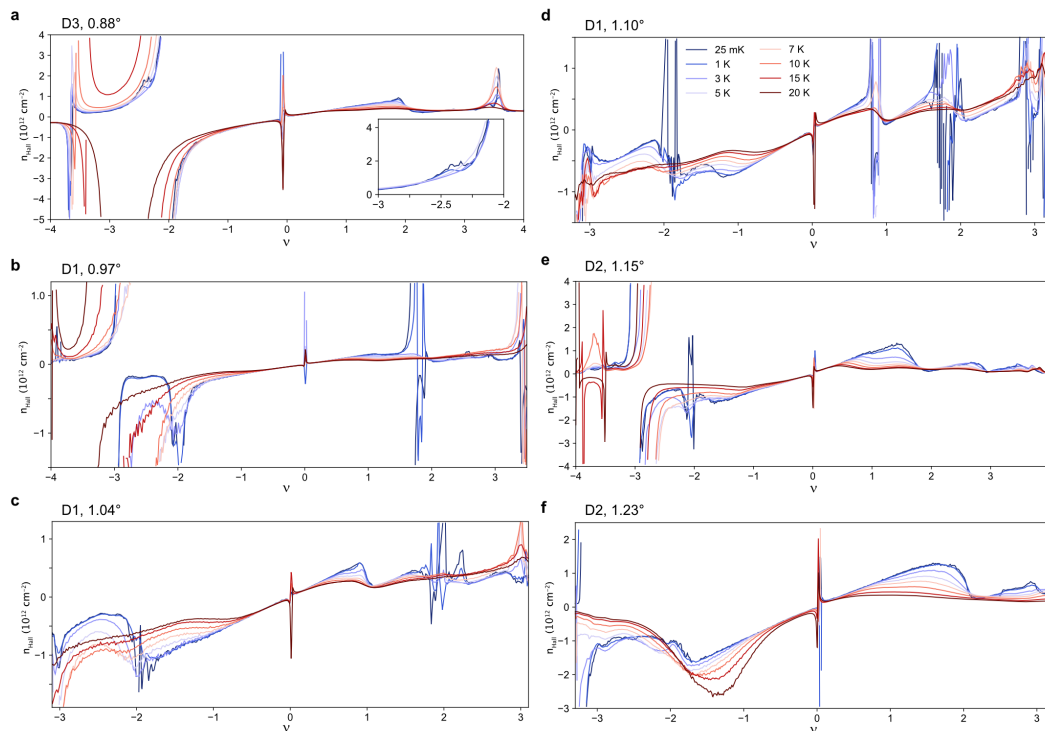


Figure A.2: More detailed Hall density data for the mentioned devices, taken at the the range of temperatures displayed in (b). The only deviation from these panels is in (a), where the lowest-temperature curve was measured at 50 mK instead of 25 mK. The inset of (a) displays the $\nu \approx -2$ region for the 0.88° device as it evolves at temperatures up to 5 K, revealing the appearance of the feature mentioned in the main text and Fig. 4.3, which corresponds with the onset of hole-side superconductivity. This small feature, indicative of the onset of a cascade, survives to only around 2 K. The rest of the panels reveal clear cascades, where the Hall density returns to near 0, at both $\nu = -2$ and $+2$ at low temperatures.

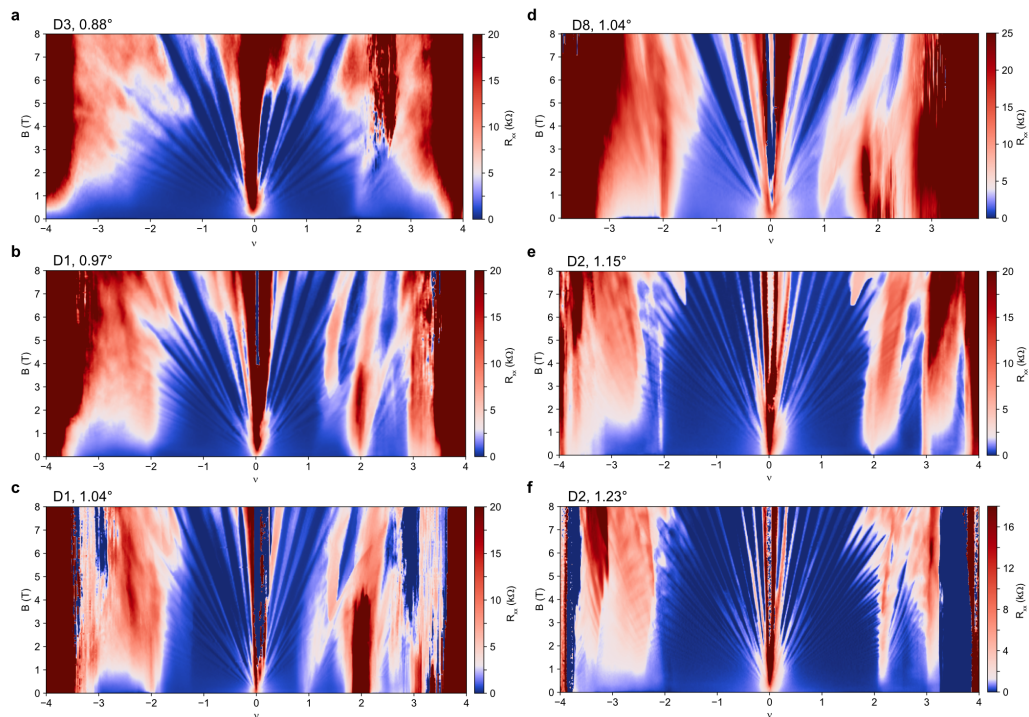


Figure A.3: R_{xx} measured as a function of magnetic field B and moiré filling factor ν for a collection of twist angles. One can see high-resistance states near $\nu = 2$ just near the magic angle (0.97° to 1.15°) and near $\nu = 1$ only in a very small range near 1.10° (by 1.04° , it is already disappearing, and it is gone at 1.15° here). On the edge of the magic angle, (such as at 0.97°) the $\nu = 2$ state develops with a small magnetic field. The hole-side $\nu = -2$ insulator is always smaller than the electron-side $\nu = 2$ insulator, and it is not fully developed at 0 magnetic field in these diagrams. The noisy features commonly seen for $|\nu| > 3$ and occasionally for other values of ν at high field are likely due to contact/geometry effects near the insulating states.

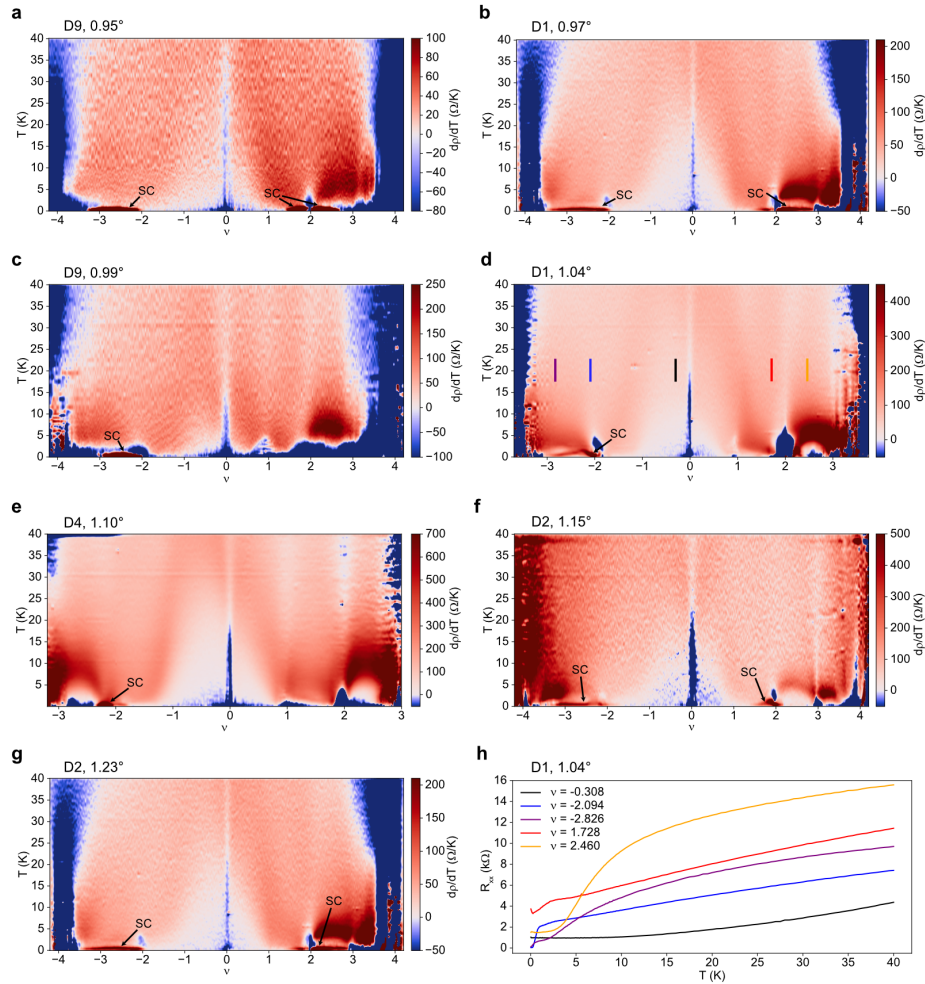


Figure A.4: Linear-in-T behavior of TBG. (a)–(g) Derivatives of resistivity with respect to temperature up to 40 K for twist angles from 0.95° to 1.23° . (h) Selected linecuts of R_{xx} vs. temperature for the 1.04° twist angle (filling factor values also shown as coloured lines in (d)). The linecuts show the broad positive-curvature zone near charge neutrality (black line), the linear resistivity that persists down to a few Kelvin (although often blocked by a correlated insulator, superconducting, or other symmetry-broken state at low temperatures) near $|\nu| = 2$ (red and blue lines), and the super-linear low temperature to sub-linear high temperature states at $|\nu| > 2$ (purple and orange lines), which have large transition regions that prevent linear behavior until high temperatures. The curve at $\nu = -2.826$ (purple) shows an example where the higher-temperature positive-curvature zone is seen as the superconducting dome is phasing out (small T_c).

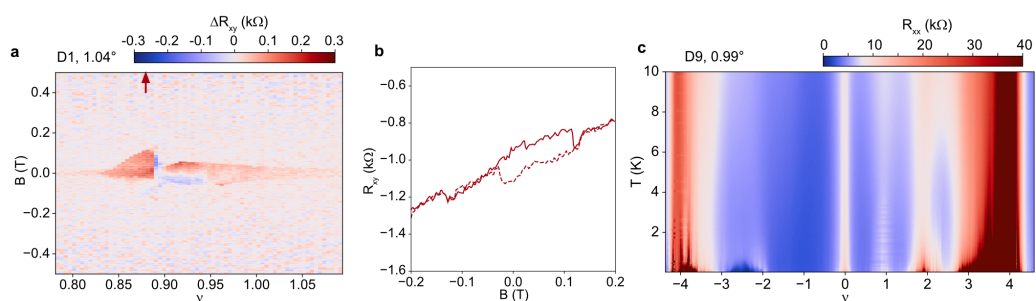


Figure A.5: Other signatures of ferromagnetism in TBG. (a) ΔR_{xy} vs. B and ν around filling factor 1 measured with twist angle 1.04° in device D1 at $1.5K$. (b) Line cut of R_{xy} versus B at $\nu = 0.87$ (red arrow) for the same device. (c) Temperature dependence of another device D9, twist angle 0.99° , showing evidence of switching behavior (similar to that seen in Fig. 4.9b) and therefore possible ferromagnetism near $\nu = 1$. Bad contacts prevented us from measuring R_{xy} data in this device.

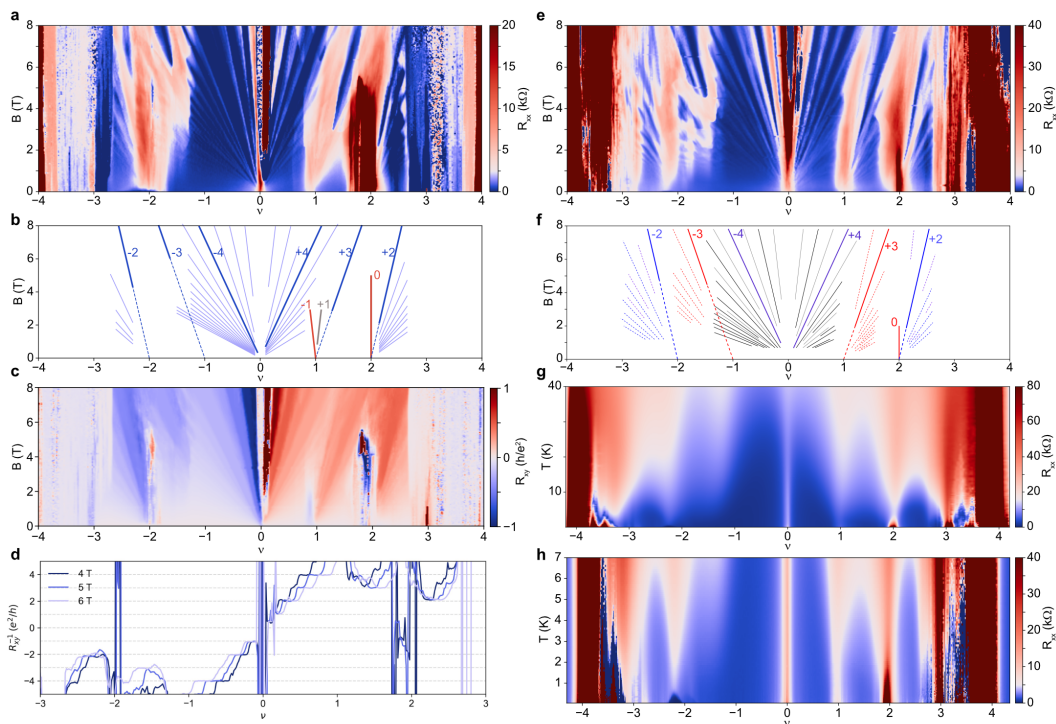


Figure A.6: Comparison of two devices at 1.10° . (a), (c) R_{xx} and R_{xy} versus filling factor and magnetic field up to 8 T for D1. (b) Schematics showing correlated Chern insulators (bold blue lines) and zero-field competing Chern insulators (red lines) at the magic angle. (d) Hall conductance showing well-quantized Chern insulators emanating from charge neutrality (broadest plateaus at $C = \pm 4$), $\nu = \pm 1$ ($C = \pm 3$) and $\nu = \pm 2$ ($C = \pm 2$). (e), (f) Landau fan of D4 and schematic of visible Landau levels along with correlated Chern insulators (bold lines). Notice the fan around charge neutrality does not show the usual clear 4-fold degeneracy preference represented by a wider Landau level plateau in (a), and the fan emanating from $\nu = 1$ persists to lower fields. This variance in magnetic field dependence reveals the sensitivity of the symmetry-broken states near 1.10° , particularly near $\nu = 1$. (g), (h) T-dependence of D4 at high and low temperatures, respectively. Contrast this with the T-dependence of D1 in Fig. 4.8 and Fig. A.1.

Appendix B

**CHAPTER 5 SUPPLEMENTARY DATA: ASCENDANCE OF
SUPERCONDUCTIVITY IN MAGIC-ANGLE GRAPHENE
MULTILAYERS**

B.1 Determining T_c and Hall density

T_c and the coherence length: T_c is determined by the following procedures. First, the high temperature R_{xx} data is fitted using a linear function $R(T) = AT + B$. Then, T_c is defined by the value where $R_{xx}(T)$ is a certain fraction (typically 10% as in Fig. 5.11) of $R(T)$. Ginzburg-Landau coherence lengths ξ_{GL} are obtained from the B dependence of T_c , by fitting the Ginzburg-Landau relation $T_c/T_{c0} = 1 - (2\pi\xi_{GL}^2/\Phi_0)B_{\perp}$, where $\Phi_0 = h/(2e)$ is the superconducting flux quantum and T_{c0} is the critical temperature at zero magnetic field. We get ξ_{GL} from the T_c vs. B linear fit, where the intercept at the B axis is equal to $\Phi_0/(2\pi\xi_{GL}^2)$. Following Ref. [127], we use T_c defined by 40% of the normal state resistance to evaluate the coherence length data in Fig. B.1e (corresponding error bars are evaluated by using T_c defined by 30% and 50% of the normal state resistance). As mentioned in the main text, $\xi_{GL}(B_c)$ is much smaller (higher) in the twisted graphene multilayers compared to TBG. One possibility for the reduction of ξ_{GL} is the relative decrease of the characteristic moiré wavelength (see Fig. B.1f).

B.2 Figures

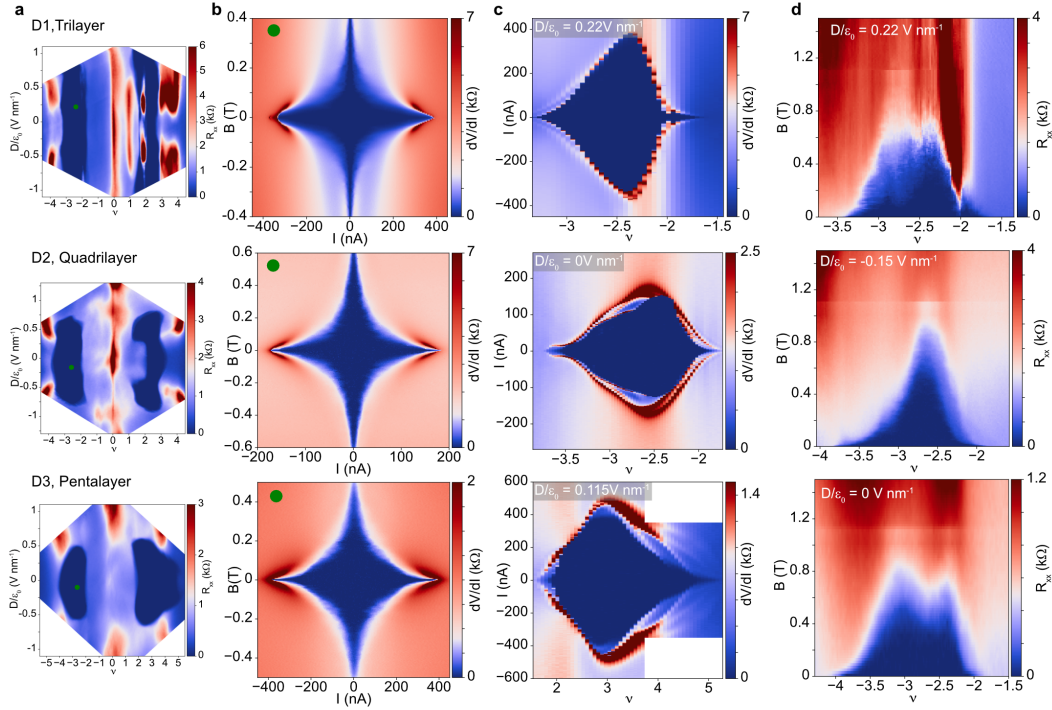


Figure B.1: Magnetic field dependence of twisted multilayer graphene samples. Column (a) shows R_{xx} versus ν and D phase diagrams, and the green dots indicate the positions where the corresponding I versus B plots shown in (b) are measured for D1–D3. Column (c) shows the critical current I_c versus ν at the optimal D fields for D1–D3. Column (d) shows R_{xx} versus ν and B around $\nu = -2$ for D1–D3, highlighting the high critical magnetic fields in these systems. Superconductivity in the twisted graphene multilayers has a higher B_c (~ 0.8 T or higher) than in TBG.

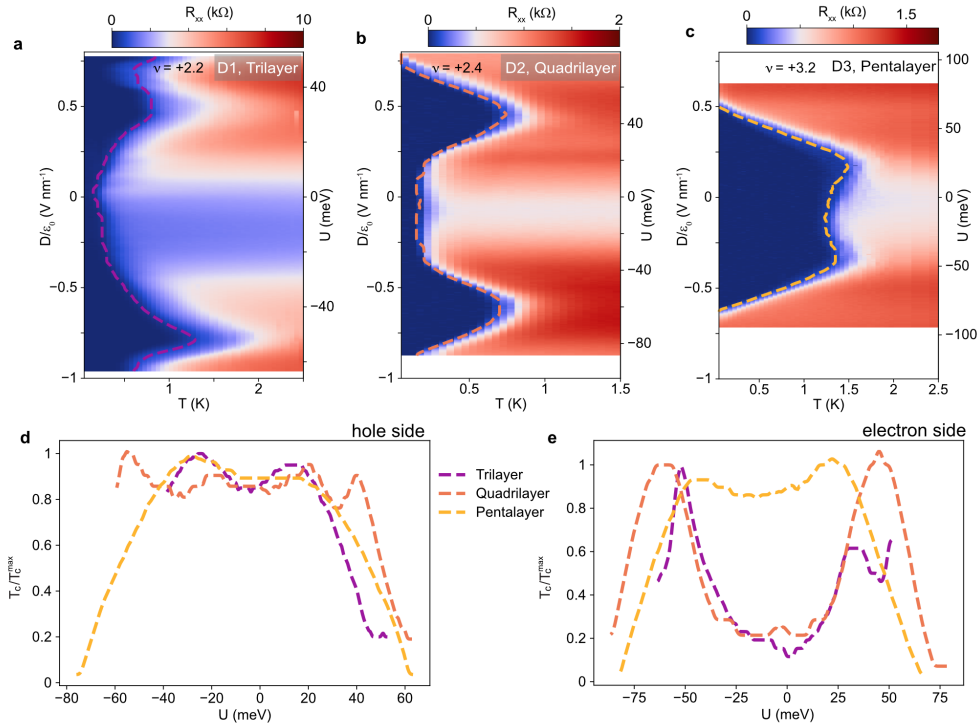


Figure B.2: D - T dependence of multilayer samples. (a)–(c) R_{xx} as a function of T and D field for D1–D3 at filling factor $\nu = +2.2, +2.4,$ and $+3.2$, respectively. Superconducting T_c is indicated by a dashed line that delineates 10% of the normal state resistance (see section B.1 for details). (d)–(e) T_c/T_c^{max} versus potential energy difference U for TTG, TQG, and TPG around hole-side (d) and electron-side (e) optimal doping, respectively. U is converted from D using $U = 0.1 \times (n - 1) \times 0.33 \text{ nm} \times eD$, where e is the electron charge and $n - 1$ is the number of graphene interfaces.

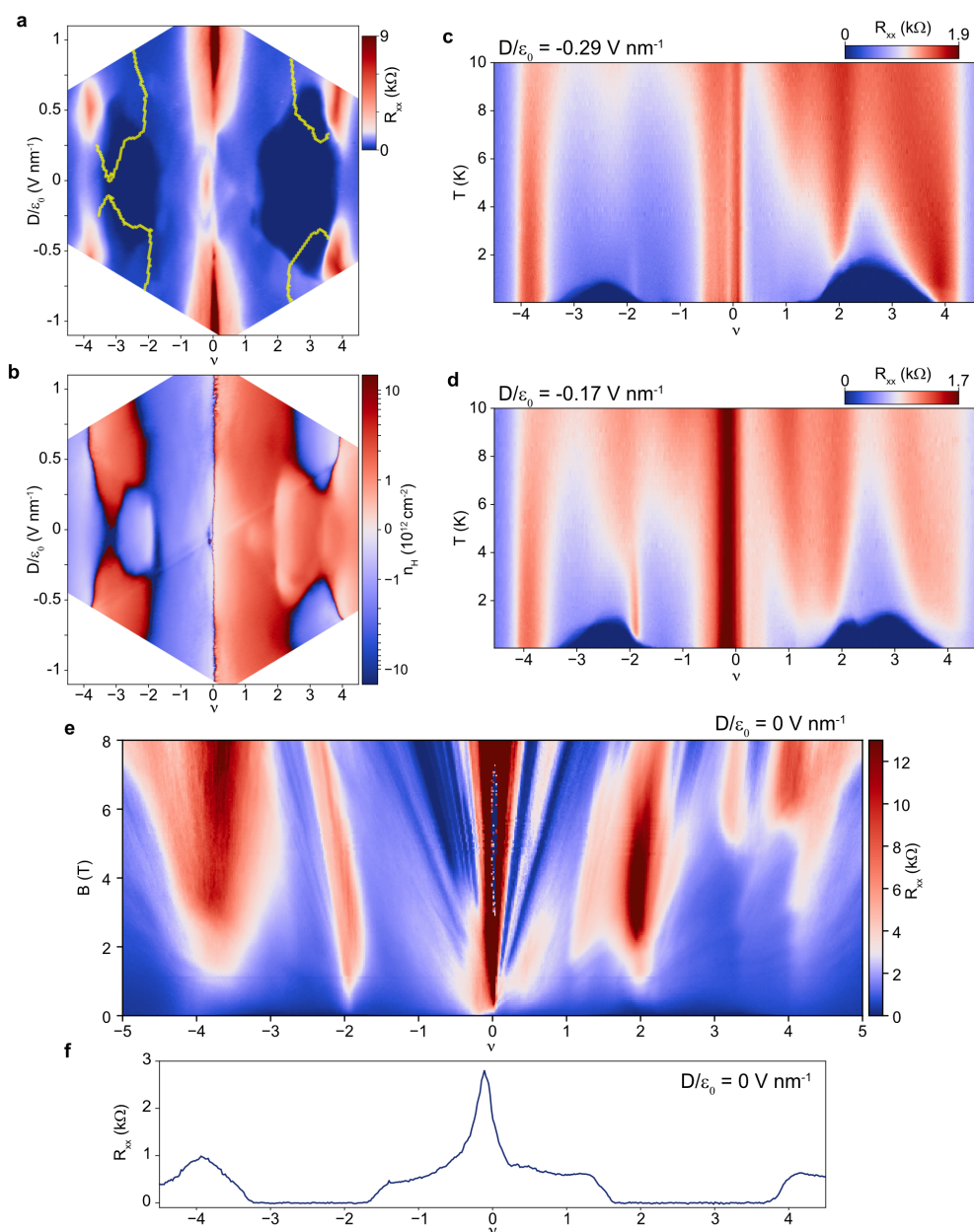


Figure B.3: Data for the second TQG device with twist angle $\theta \approx 1.64^\circ$. (a) R_{xx} and (b) Hall density versus filling factor ν and displacement field D . Yellow lines in (a) track the evolution of vHs features in Hall density. R_{xx} versus ν and temperature measured at $D/\epsilon_0 = -0.29 \text{ V nm}^{-1}$ (c) and -0.17 V nm^{-1} (d). (e) R_{xx} Landau fan measured at zero D field. (f) R_{xx} versus ν measured at zero D field and zero magnetic field. R_{xy} phase diagram measurements (b) and the Landau fan (e) reveal more correlated behavior ($|\nu| < 4$) than the TQG device at 1.80° twist angle.

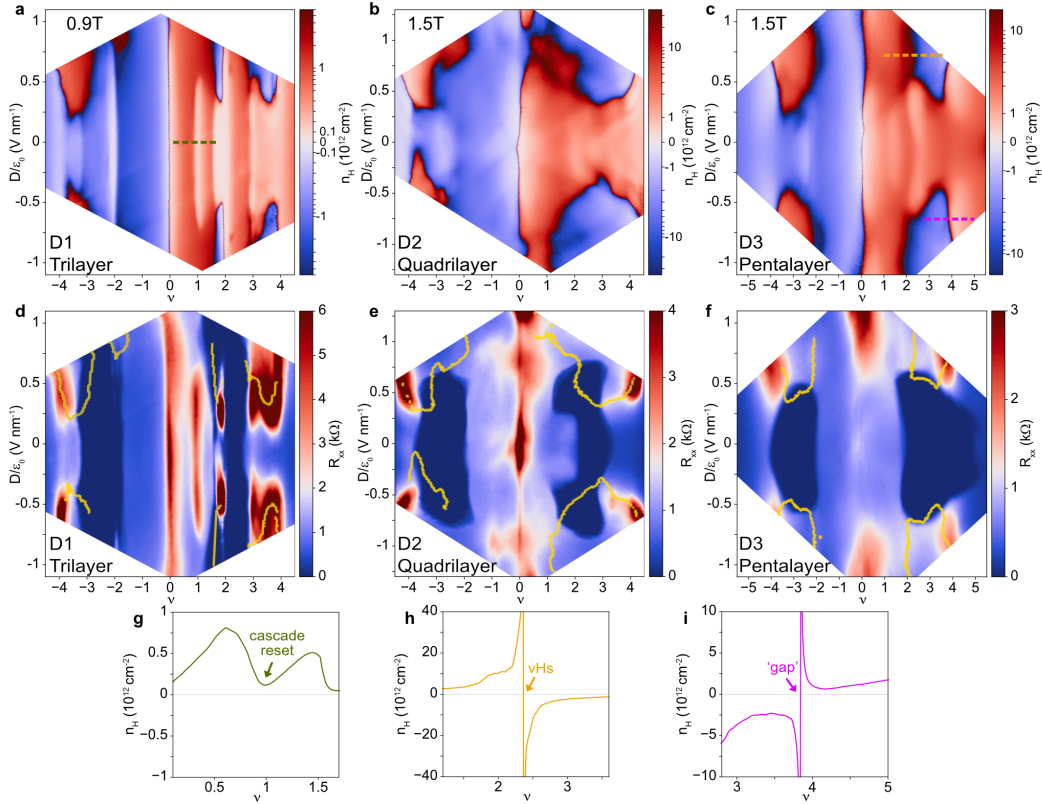


Figure B.4: Detailed tracking of Hall density for multilayer samples. Hall density (a)–(c) and R_{xx} (d)–(f) as a function of ν and D for TTG, TQG, and TPG. Hall density maps are measured at $B = 0.9$ T, 1.5 T, and 1.5 T, respectively. Yellow lines in (d)–(f) track the evolution of ν Hs/‘gap’ features where Hall density changes sign. Examples are shown of Hall density near the cascade transition reset (g), the ν Hs (h), and the ‘gap’ (i) following the definitions in Ref. [127]. Filling ranges for the line cuts are marked by the corresponding colored dashed lines in (a), (c).

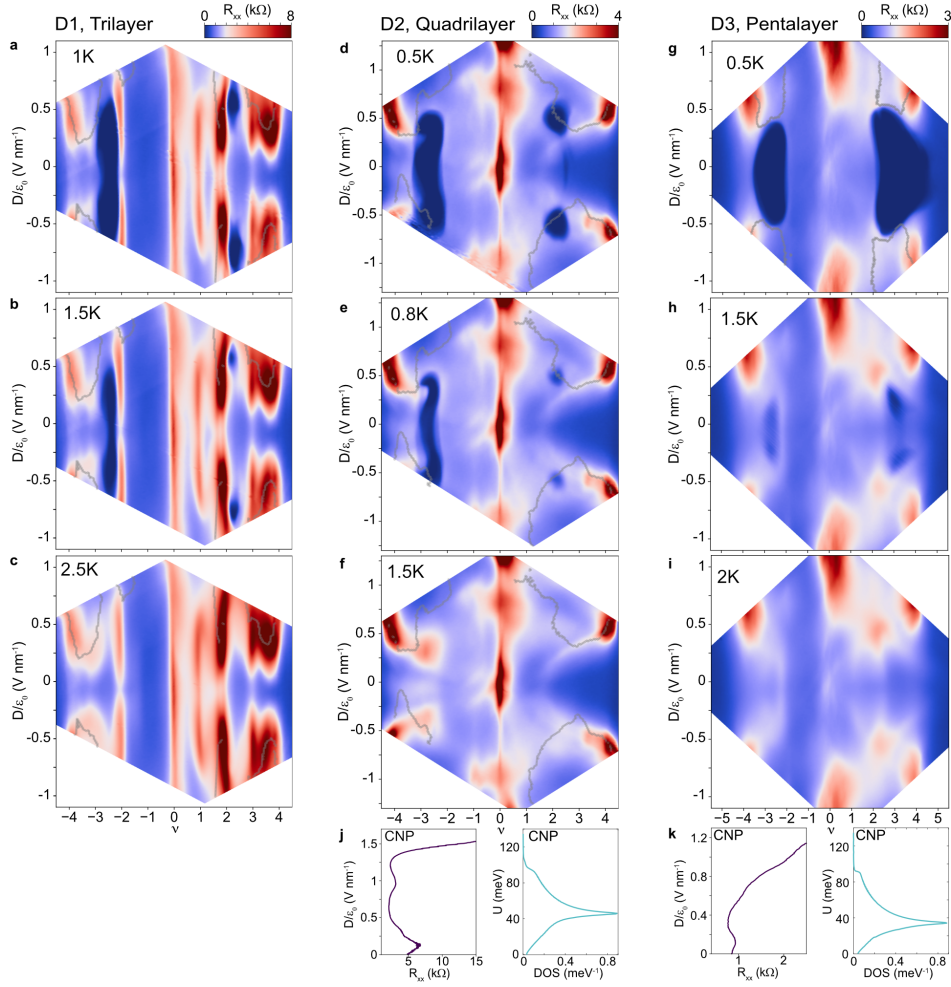


Figure B.5: R_{xx} as a function of ν and D measured at different temperatures. Plots for TTG (a)–(c), TQG (d)–(f), and TPG (g)–(i). Grey lines track the evolution of the vHs/‘gap’ features. (j) The plot on the left shows a line cut of R_{xx} versus D at charge neutrality for TQG. The plot on the right shows corresponding density of states (DOS) at charge-neutrality point (CNP) calculated using non-interacting continuum model. In the regions where DOS is high, resistance is expected to be low and vice versa. (k) Equivalent plots as in (j) for TPG.

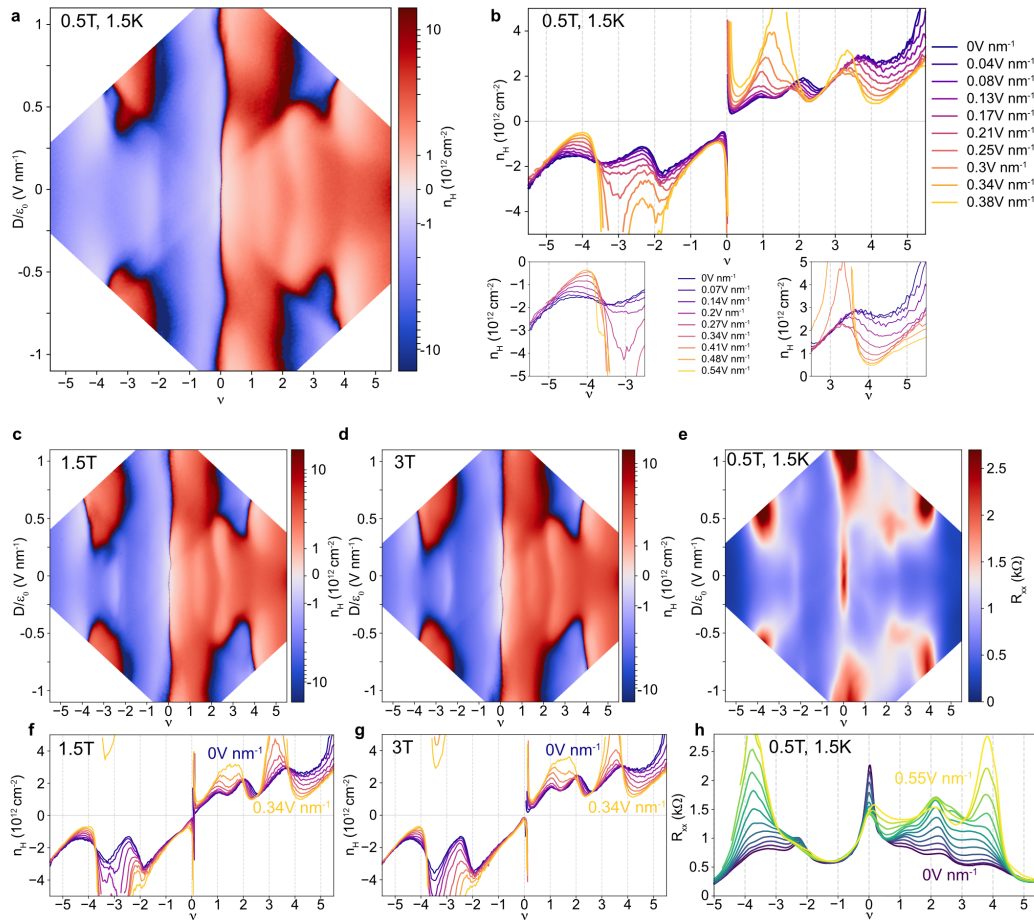


Figure B.6: Detailed Hall effect and temperature dependence data for TPG. (a) Hall density versus D and ν at $B = 0.5 \text{ T}$. (b) Line cuts from (a). Panels below zoom in on the evolution of Hall density resets near $|\nu| = 4$. (c) and (d) Hall density versus D and ν measured at $B = 1.5 \text{ T}$ (c) and 3 T (d), with respective line cuts shown in (f) and (g). (e) R_{xx} versus D and ν measured at $T = 1.5 \text{ K}$, $B = 0.5 \text{ T}$ (line cuts are shown in (h)). From all the above line cuts, Hall density resets and R_{xx} resistive features consistently exist around $\nu = +4$.